

---

**ZIRCON GEOCHRONOLOGY OF VOLCANIC ROCKS FROM THE TRANS-  
PECOS OROGENIC BELT, WESTERN TEXAS: TIMING THE CESSATION OF  
LARAMIDE FOLDING, UPLIFT, AND POST FLAT-SLAB IGIMBRITE  
FLARE-UPS**

-----  
A Thesis Presented to  
the Faculty of the Department of Earth and Atmospheric Sciences  
University of Houston

-----  
In Partial Fulfillment  
of the Requirements for the Degree  
Master of Science

-----  
By  
Melissa Elizabeth Davidson

May, 2014

---

**ZIRCON GEOCHRONOLOGY OF VOLCANIC ROCKS FROM THE TRANS-  
PECOS OROGENIC BELT, WESTERN TEXAS: TIMING THE CESSATION OF  
LARAMIDE FOLDING, UPLIFT, AND POST FLAT-SLAB IGNIMBRITE  
FLARE-UPS**

---

Melissa Elizabeth Davidson

APPROVED:

---

John F. Casey, Ph.D.

---

Thomas J. Lapen, Ph.D.

---

John F. Dewey, Ph.D.

---

Terry L. Pavlis, Ph.D.

---

---

Dan Wells, Ph.D.

Dean, College of Natural Sciences and Mathematics

---

## ACKNOWLEDGMENTS

I'd like to acknowledge and deeply thank Dr. John Casey for his unfaltering dedication to furthering my knowledge and development as a geologist, and as a student. My research and depth of comprehension was his top priority, and he *always* put my education and understanding first. I could not have asked for a better advisor, and am very fortunate and blessed to have had the opportunity to work with him. He went above and beyond his role as an advisor in every possible way and has made a lasting impact on me and my career as a geologist.

I'd like to thank Dr. Tom Lapen for the countless hours he spent helping with analysis on the LA-ICP-MS and with the reduction of my data.

A special thanks to Dr. Gao for his time and sincere efforts in furthering my knowledge and understanding of the ICP-MS, and for often putting my research and analysis ahead of his own.

My research would not have been possible without the help of Adrian Gittens who selflessly assisted me with much of my fieldwork throughout Trans-Pecos Texas.

Final thanks to the geologist that started it all, my father, Robert Davidson. Some people call him Maurice.

---

**ZIRCON GEOCHRONOLOGY OF VOLCANIC ROCKS FROM THE TRANS-  
PECOS OROGENIC BELT, WESTERN TEXAS: TIMING THE CESSATION OF  
LARAMIDE FOLDING, UPLIFT, AND POST FLAT-SLAB IGNIMBRITE  
FLARE-UPS**

-----  
An Abstract of a Thesis

Presented to

the Faculty of the Department of Earth and Atmospheric Sciences

University of Houston

-----  
In Partial Fulfillment

of the Requirements for the Degree

Master of Science

-----  
By

Melissa Elizabeth Davidson

May, 2014

---

## **Abstract**

This study refines regional differences in the cessation of Laramide compressional deformation and the subsequent initiation of episodic slab-asthenosphere influenced ignimbrite-rhyolite volcanism in West Texas by utilizing LA-ICP-MS U-Pb zircon geochronology. Ages have been obtained for volcanic rock samples that occur both above and below the angular unconformity demarcating compressional deformation structures below and a lack of contractional structures above, as well as the maximum depositional ages for Tertiary siliciclastic formations present below the unconformity. By assessing the provenance of the detritus age-spectra from the siliciclastic formations the eastward migration of the magmatic arc, subsequent uplift, and arrival of the flat-slab to the Texas-New Mexico border (~47 Ma) and beyond has been tracked by assessing the increasing abundances more proximal detritus in each progressively younger formation. The volcanic results suggest cessation of shortening associated with Laramide-style deformation and uplift in the northern Trans-Pecos region occurred by ~38-36.5 Ma (Eocene), but persisted in the south e.g., in the Big Bend National Park region until ~31 Ma (Oligocene).

Pre-Basin and Range Tertiary volcanism and compressional deformation associated with the Laramide orogeny in the Trans-Pecos region of West Texas is attributed to: 1) the subduction of thick, buoyant oceanic crust on the Farallon slab causing a major slab flattening period that resulted in magmatic arc volcanic activity progressively migrating eastward to Trans-Pecos Texas; 2) Laramide compression, uplift, and accelerated erosion directly preceding or synchronous

---

with arrival of the flat-slab; 3) a quiescent period or gap in volcanism upon arrival of the flat-slab associated with an extensive Farallon-North American lithosphere contact; and, 4) renewed volcanism usually in the form of ignimbrite flare-ups associated with the transition to steep slab and subsequent rollback. The marked age difference in post-angular unconformity ignimbrite deposits from north to south documented here is attributed to the early abutment and steepening of the flat-slab against a pronounced ancient cratonic lithospheric mantle keel east of the Davis Mountains in the north followed by rollback. A later related steepening perhaps facilitated by tearing of the slab in the southern Trans-Pecos area likely occurred with no direct collision of the flat-slab against a keel because of a less buoyant subducted lithosphere and less pronounced or absent cratonic lithospheric mantle keel to the south.

---

## TABLE OF CONTENTS

1. Introduction.....	1
2. Regional Geologic Background.....	6
3. Sample Preparation and Analytical Technique	
i. Crushing and Sieving.....	13
ii. Washing and Magnetic Separation.....	14
iii. Heavy Liquid Mineral Separation.....	15
iv. Heavy Liquid Reclamation.....	16
v. Hand Picking and Grain Mounting.....	17
vi. LA-ICP-MS Analysis and Data Reduction.....	18
4. Tertiary Siliciclastic Results and Implications	
a. Big Bend National Park: Tornillo Flat.....	22
i. Black Peaks Formation.....	28
ii. Hannold Hill Formation.....	33
iii. Canoe Formation.....	39
iv. Discussion.....	50
5. Tertiary Volcanic Sample Results and Implications	
a. Introduction.....	60
b. Eagle Mountains.....	62
i. Lower Rhyolite.....	66
c. Indio and Van Horn Mountains.....	70
i. Hogeys Tuff.....	74
ii. Bell Valley Andesite.....	78

---

d. Davis Mountains.....	82
i. Huelster Formation.....	86
ii. Star Rhyolite.....	89
e. Rio Grande River Area.....	91
i. Vieja Group: Buckshot Ignimbrite.....	91
f. Alamito Creek and Green Valley Area.....	95
i. Tascotal Formation.....	95
g. Chinati Mountains.....	100
i. Morita Ranch Formation.....	104
h. Big Bend National Park: Chisos Mountains.....	109
i. Chisos Formation.....	111
ii. South Rim Formation.....	118
iii. Burro Mesa Formation.....	121
i. Discussion.....	124
6. Evolution of Laramide Orogen in Texas	
i. The Cretaceous-Tertiary Laramide Orogen.....	137
ii. Evidence of Buoyant Farallon Slab Segments.....	139
iii. Magmatism and its Migration through Time.....	143
iv. Arrival of Flat-Slab to Texas and Collision against Keel...	147
v. West Texas Ignimbrite Flare-Ups and Slab Retreat.....	152
References.....	166
Appendix I .....	185

---

## INDEX OF FIGURES

**Figure 1.1:** Major Cenozoic volcanic fields, calderas, and Basin and Range province in Colorado, New Mexico, and the Trans-Pecos region of Texas (p.2)

**Figure 2.1:** Andean-arc eastward subduction beneath North America (p.7)

**Figure 2.2:** Palinspastic map displaying the southwest Cordilleran active margin and Laramide foreland during Late Cretaceous time with temperature field overlain (p.9)

**Figure 2.3:** Location of calderas and generalized tectonic setting of the Trans-Pecos Texas igneous province (p.10)

**Figure 4.1:** Reference map of Big Bend National Park (p.23)

**Figure 4.2:** Stratigraphic column displaying the geologic formations in relation to major tectonic episodes that occurred in the Big Bend National Park region (p.24)

**Figure 4.3:** Black Peaks Formation (WTX-BB 16), Hannold Hill Formation (WTX-BB 15), and Canoe Formation (WTX-BB 17& WTX-BB 22) sample locations (p.29)

**Figure 4.4:** Field-photograph displaying sample locality of the Black Peaks Formation (p.30)

**Figure 4.5:** Black Peaks Formation U-Pb age probability distribution plot (p.32)

**Figure 4.6:** Field-photograph displaying sample locality of the Hannold Hill Formation (p.35)

**Figure 4.7:** Hannold Hill Formation U-Pb age probability distribution plot (p.37)

**Figure 4.8: A)** Field-photograph displaying sample locality of the capping basalt of the Canoe Formation (WTX-BB 22), and **B)** the detrital sample collected and analyzed from the Canoe Formation (WTX-BB 17) (p.39)

**Figure 4.9:** Reference map showing location of Las Delicias basin and flanking volcanic arc (p.43)

**Figure 4.10:** Canoe Formation: WTX-BB 17 U-Pb age probability distribution plot (p.46)

**Figure 4.11:** Map displaying location of Tornillo Flat Syncline affecting Hannold Hill and Canoe Formations (p.47)

---

**Figure 4.12:** Stereonet of the measurements taken on the limbs of the Tornillo Flat Syncline affecting Hannold Hill and Canoe Formations (p.48)

**Figure 4.13:** High resolution aerial image displaying location of double-plunging syncline affecting Hannold Hill and Canoe Formations (p.49)

**Figure 4.14:** Location of North American crustal provinces (p.51)

**Figure 4.15:** **A.** Probability distribution function of arc-derived detrital zircons in Lakowski and others study (2013). **B.** Velocity and age at the subduction interface of the Farallon plate. **C.** Relative flux curves from exposures of igneous rock along the Cordilleran magmatic arc including the Coast Mountains Batholith and Sierra Nevada and Cascades Batholith (p.54)

**Figure 4.16:** Location of detrital zircon samples and boundaries of the four sampling regions, including the Four Corners, Uinta, Montana, and Canada in Lakowski *et al.*'s study (p.57)

**Figure 4.17:** Combined detrital analyses from Black Peaks, Hannold Hill, and Canoe Formations (p.58)

**Figure 4.18:** Composite normalized U-Pb age probability plot for the Wilcox Group in southeastern Texas (p.59)

**Figure 5.1:** Sample location of the Lower Rhyolite (WTX-EAGLE 1A) on the southeastern flank of the Eagle Mountains (p.63)

**Figure 5.2:** Stratigraphic column displaying the Cretaceous geologic formations exposed in the Eagle Mountains (p.64)

**Figure 5.3:** Field-photograph displaying sample locality of the Lower Rhyolite/ Carpenter Canyon (p.67)

**Figure 5.4:** Lower Rhyolite/ Carpenter Canyon Tuff: WTX-EAGLE 1A Tera-Wasserberg plot (p.69)

**Figure 5.5:** Reference map of the Indio Mountains (p.71)

**Figure 5.6:** **A)** An exposure of the Hogeye Tuff that was analyzed in this study (WTX-INDIO 5A, 5B, and 7B) and **B)** a field-photograph displaying sample locality of the Bell Valley Andesite (WTX-INDIO 1A) (p.75)

**Figure 5.7:** Map displaying Van Horn Mountains Caldera Complex in relation to the Indio Mountains (p.77)

**Figure 5.8:** Hogeye Tuff: WTX-INDIO 5A Tera-Wasserberg plot (p.79)

- 
- Figure 5.9:** Hogeeye Tuff: WTX-INDIO 5B Tera-Wasserburg plot (p.80)
- Figure 5.10:** Hogeeye Tuff: WTX-INDIO 7B Tera-Wasserburg plot (p.81)
- Figure 5.11:** Bell Valley Andesite: WTX-INDIO 1A Tera-Wasserburg plot (p.81)
- Figure 5.12:** Sample location of WTX-NDAVIS 1B (Hueslter Fm.) and WTX-NDAVIS 2B (Star Mountain Rhyolite) located in the Davis Mountains (p.83)
- Figure 5.13:** N-S diagrammatic stratigraphic section and average  $^{40}\text{Ar}/^{39}\text{Ar}$  ages (Ma) of the Davis Mountains volcanic field (p.85)
- Figure 5.14:** Field photograph displaying the sample location of the Huelster Formation and overlying Star Mountain Rhyolite (p.87)
- Figure 5.15:** Huelster Formation: WTX-NDAVIS 1B Tera-Wasserburg plot (p.88)
- Figure 5.16:** Sample location of WTX-SEAST 1(Buckshot Ignimbrite) (p.93)
- Figure 5.17:** Buckshot Ignimbrite: WTX-SEAST 1 Tera-Wasserburg plot (p.94)
- Figure 5.18: A)** A field-photograph displaying the Tascotal Mesa and Tascotal Formation (WTX-SEAST 4) and **B)** a field-photograph displaying sample locality of the Tascotal Formation (p.96)
- Figure 5.19:** Sample location of WTX-SEAST 4 (Tascotal Formation) (p.97)
- Figure 5.20:** Tascotal Formation: WTX SEAST-4 Tera-Wasserburg plot (p.99)
- Figure 5.21:** Field-photograph displaying relationship of Morita Ranch Formation above and underlying Cretaceous Shafter Formation (p.101)
- Figure 5.22:** Stratigraphy of the Morita Ranch Formation (p.102)
- Figure 5.23:** Morita Ranch Formation: WTX BB-10 sample location (p.106)
- Figure 5.24:** Morita Ranch Formation: WTX BB-10 Tera-Wasserburg plot (p.108)
- Figure 5.25:** Generalized volcanic stratigraphy of the Big Bend National Park Group (p.112)
- Figure 5.26:** Map displaying sample locations of the Chisos Formation (WTX-BB 19) and South Rim Formation (WTX-BB 18) (p.114)
- Figure 5.27:** Field-photograph displaying sample location of Tule Mountain Trachyandesite in relation to the flat-lying South Rim Formation above (p.116)

---

**Figure 5.28:** Field-photograph documenting compressional deformation associated with the Laramide orogeny (p.117)

**Figure 5.29:** Chisos Formation: WTX BB-19 Tera-Wasserburg plot (p.118)

**Figure 5.30:** Field-photograph displaying relationship of the flat-lying South Rim Formation above and underlying tilted Chisos Group (p.121)

**Figure 5.31:** South Rim Formation: WTX BB-18 Tera-Wasserburg plot (p.122)

**Figure 5.32:** Map displaying sample location of the Wasp Spring Member of the Burro Mesa Formation (WTX-BB 4B) (p.124)

**Figure 5.33:** Field-photography displaying sample location of the Wasp Spring Member of the Burro Mesa Formation (WTX-BB 4B) (p.125)

**Figure 5.34:** Regional map displaying sample location and U/Pb age of analyzed volcanic samples collected from directly above and below the unconformity (p.128)

**Figure 5.35:** Regional map displaying Precambrian exposures associated with the Grenville orogeny and other Proterozoic aged uplifts of the Carrizo Mountain Group found in the Van Horn Mountains and neighboring areas (p.131)

**Figure 5.36:** Plot emphasizing the age variation of all volcanic rocks analyzed in this study from northwest to southeast along the section line A-A' drawn on Fig.5.33 (p.132)

**Figure 5.37:** Displays the varying erosional level or vacuity based on the age of sub-unconformity rocks and the age of each basal volcanic unit in several localities listed on the A-A' section line in Fig.5.33 (p.134)

**Figure 6.1:** Plate reconstruction compiled by Liu *et al.* (2010) of the Shatsky and Hess conjugate plateau (p.142)

**Figure 6.2:** Palinspastic map displaying the southwest Cordilleran active margin and Laramide foreland during Late Cretaceous time with temperature field overlain (p.146)

**Figure 6.3:** Joint inversion S- and P- wave velocity models at depths of 100 and 200 km modeled by Sigloch *et al.* (2008) (p.148)

**Figure 6.4:** North American model for vertically polarized shear wave velocity ( $V_{sv}$ ) plotted at depths of 70 and 110 km determined by Nettles and Dziewonski (2008) (p.149)

---

**Figure 6.5:** The trajectory of the Hess Rise conjugate plateau has been projected on to the base map from Liu *et al.* (2010) to indicate where it would have initial and most prolonged impact on West Texas (although uncertainties exist in the age capsules of its projection (p.153)

**Figure 6.6:** Diagram displaying The Hess conjugate plateau and associated magmatic activity with slab dehydration and melting of the mantle wedge is projected to have reached the present-day Texas-New Mexico border at ~47 Ma (p.155)

**Figure 6.7:** Diagram displaying the Arc magmatism shutting off briefly across the western United States around 40 Ma when flat-slab Farallon-North American lithosphere contact extends across the western margin and before collision with the continental interiors stable craton (p.156)

**Figure 6.8:** Diagram displaying the flat-slab and steeper components of the Farallon plate descending beneath North America in the southern Trans-Pecos Texas region near present-day Big Bend National Park (p.157)

**Figure 6.9:** Diagram displaying Collision of the Farallon slab against the keel facilitated steepening and forced the buoyant lithosphere to descend into the mantle causing roll-back and rapid westward retreat of ignimbrite flare-ups (p.158)

**Figure 6.10:** Displays the distribution of over 3,000 radiometric ages (U/Pb, Ar/Ar, K/Ar, Rb/Sr, Sr/Sr, Sr/Nd, and Nd/Nd) for plutonic and volcanic samples collected from the IEDA-EarthChem Portal plotted with the U/Pb data obtained in this study as a function of time (p.160)

**Figure 6.11:** Inlay of Fig. 6.10 that displays the equations for each best-fit line trend in addition to the relationship between the U/Pb data in this study and the retreating volcanic and plutonic activity trend line (p.161)

**Figure 6.12:** Histogram of K-Ar and  $^{40}\text{Ar}/^{39}\text{Ar}$  ages of igneous rocks in New Mexico from Late Cretaceous to present-day compiled by Chapin *et al.*(2004) that clearly displays the pulses of ignimbrite volcanism (p.162)

**Figure 6.13:** Three-dimensional views provided by Sigloch *et al.* (2008) of the subducted Farallon plate beneath North America (p.164)

---

## INDEX OF TABLES

**Table 1.1:** Site of collection, sample identification, and brief lithology of samples analyzed in this study (p.4)

**Table 5.1:** Volcanic stratigraphy of the western Eagle Mountains (p.65)

**Table 5.2:** Summary of the volcanic stratigraphy of the Garren Group in the Chispa Mountain Quadrangle (p.72)

**Table 5.3:** Summary of the volcanic stratigraphy of the Sierra Vieja Group in the Rim Rock Country along the Rio Grande River (p.91)

**Table 5.4:** Displays age, error, and sample location of formations successfully analyzed in this study (p.127)

---

## **Chapter 1:**

### **Introduction**

The Laramide orogeny is hypothesized to have been the result of low angle- or flat-slab subduction of the Farallon Plate beneath western North America caused by the combined effects of subduction of a buoyant oceanic plateau and associated seamounts and increased suction in the mantle wedge initiated by the Farallon slab approaching the North American cratonic keel between 75-35 Ma (Coney and Reynolds, 1977; Dickinson and Snyder, 1978; Bird, 1988; Humphreys, 2009). Following the compressional deformation associated with this low-angle subduction event and subsequent removal of the Farallon slab, the rising asthenospheric/lithospheric contact resulted in intense volcanic episodes throughout the western region of Texas (Fig.1.1). The variations in composition from large-scale calc-alkaline ignimbritic to smaller-scale effusive almost exclusively mafic volcanic rocks exposed in the Trans-Pecos region are regarded as direct evidence of a change from the compressive subduction related stress regime of the Laramide orogeny to an extensional Basin and Range environment. A transition that is regarded in this study to have initially occurred with ignimbrite flare-ups associated with the steepening of the Farallon slab and subsequent asthenospheric upwelling. Price and Henry (1984) have suggested this transition occurred in the Oligocene between 31-28 Ma.

Tertiary flat-lying volcanic units found in the northern Trans-Pecos igneous province lacking thrust faults exposed in the Eagle and Indio Mountains unconformably overlie Laramide-style faulted and folded rocks of Turonian

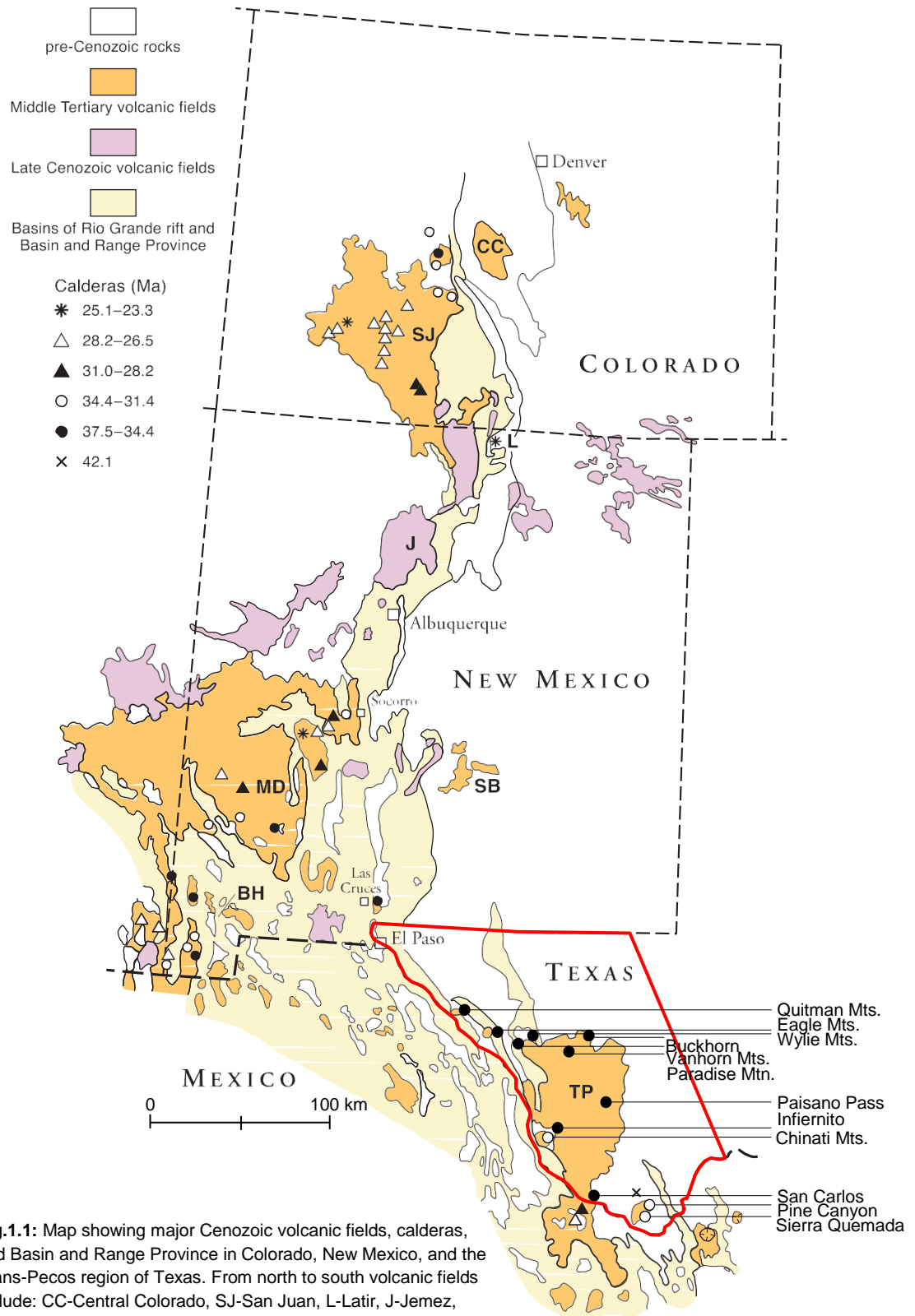


**Fig.1.1:** Map showing major Cenozoic volcanic fields, calderas, and Basin and Range Province in Colorado, New Mexico, and the Trans-Pecos region of Texas. From north to south volcanic fields include: CC-Central Colorado, SJ-San Juan, L-Latir, J-Jemez, MD-Mongollon-Datil, SB-Sierra Blanca, BH-Boot Heel, and TP-Trans Pecos. Map modified from Muehlberger (1992), Lipman (2000), McIntosh and Chapin and others (2004).

---

age, suggesting emplacement towards the waning stages of contraction. Some tilting in these volcanic units has been documented but is associated with major Basin and Range normal faulting (Duex and Henry, 1981). A more extensive and age complete stratigraphic sequence is exposed in the southwestern region of Big Bend National Park and consists of Tertiary flat-lying volcanic members of the South Rim and Burro Mesa Formations resting unconformably on tilted Tertiary volcanic units of the Chisos Formation. The Chisos Formation displays the same Laramide-style folding and thrust fault deformation as Early Tertiary, Cretaceous, and Paleozoic sedimentary units observed throughout the entire Trans-Pecos igneous province. It is widely accepted that the earliest magmatism in the Trans-Pecos igneous province took place in a compressional stress regime from 47-32 Ma during active subduction (Price and Henry, 1984), and intrusive dikes associated with a subsequent Basin and Range extensional environment have yielded younger isotopic ages of 24-17 Ma (Henry and Price, 1986). However, the timing of the transition from compression to extension, whether there was a quiescent period between, as well as the theories of the mechanics behind slab steepening, removal, and the extension that followed are still in question. The purpose of this study is to improve on the timing estimates of the age of Laramide-style deformation, compressional uplift, and pre- and post-unconformity volcanic events to help clarify these transitions associated with major tectonic events related to subduction and compression and late Basin and Range extension.

This study investigates the regional differences in the cessation of

Laramide folding, the extent of uplift or continued basin subsidence, and episodic slab-asthenosphere influenced volcanism in West Texas by utilizing LA- ICP-MS U/Pb zircon geochronology. Ages have been measured for volcanic rock samples that occur both above and below the ‘Laramide’ angular unconformity in Texas; those above including: the Lower Rhyolite or basal unit of the Carpenter Canyon Tuff from the Eagle Mountains, the Hogeeye Tuff and Bell Valley Andesite from the Garren Group in the Indio Mountains, the Huelster Formation and Star Mountain Rhyolite from the Davis Mountains, the Morita Ranch Formation from the Chinati Mountains, the Tascotal Formation from the Alamito Creek and Green Valley area, the Vieja Group from the Rio Grande River area, and the South Rim, Burro Mesa, and Chisos Formations of the Chisos Mountains in Big Bend National Park.

Sample Site	Sample ID	Latitude	Longitude	Lithology
Eagle Mountains	WTX-EAGLE 1A	30.91382	-105.03985	Lower Rhyolite (Rhyolite)
Indio Mountains	WTX-INDIO 5A	30.75056	-105.00417	Garren Gp. (Hogeeye Tuff-Welded Tuff)
	WTX-INDIO 5B	30.75056	-105.00417	Garren Gp. (Hogeeye Tuff-Welded Tuff)
	WTX-INDIO 7B	30.74028	-105.00056	Garren Gp. (Hogeeye Tuff-Welded Tuff)
Davis Mountains	WTX-INDIO 1A	30.74690	-104.99679	Garren Gp. (Bell Valley Andesite-Andesite)
	WTX-NDAVIS 1B	30.86547	-103.79678	Huelster Fm. (Reworked Tuff)
	WTX-NDAVIS 1B2	30.86547	-103.79678	Star Mountain Rhyolite (Rhyolite)
Rio Grande River Area	WTX-SEAST 2	30.19257	-104.26791	Undivided Vieja Gp. (Rhyolite)
Alamito Creek and Green Valley Area	WTX-SEAST 1	30.19019	-104.27943	Tascotal Fm. (Tuffaceous Sandstone)
Chinati Mountains	WTX-BB 11	29.87272	-104.28577	Morita Ranch Fm. (Rhyolite)
Big Bend National Park	WTX-BB 15	29.43258	-103.13862	Black Peaks Fm. (Sandstone)
	WTX-BB 15	29.40085	-103.14441	Hannold Hill Fm. (Sandstone)
	WTX-BB 17	29.38329	-103.14992	Canoe Fm. (Sandstone)
	WTX-BB 22	29.40491	-103.14036	Canoe Fm. (Basalt)
	WTX-BB 18	29.26879	-103.29823	Chisos Fm. (Trachyandesite)
Chisos Mountains	WTX-BB 19	29.27095	-103.30025	South Rim Fm. (Rhyolite)
	WTX-BB 20	29.14520	-103.49918	Burro Mesa Fm. (Ash-Fall Tuf)
	WTX-BB 21	29.26533	-103.37259	Burro Mesa Fm. (Rhyolite Tuff)

**Table 1.1:** Displays site of collection, sample identification, and brief lithology of samples analyzed in this study.

In addition, ages for detrital zircons have been obtained from sandstones below the unconformity within the Tertiary Black Peaks, Hannold Hill, and Canoe Formations to constrain the age of the maximum depositional age. In addition, these detrital zircons limit the range of igneous zircon ages sampled as well as the age of western U.S. volcanic activity from fluvial source regions. Samples

---

have been dated in an attempt to more precisely constrain the age of cessation of Laramide shortening and following ignimbrite flare-ups after cessation of flat-slab subduction across or near West Texas (Table 1.1). Based on our results, we suggest cessation of shortening associated with Laramide-style deformation and uplift in the northern Trans-Pecos region occurred by ~38 Ma (Eocene) and persisted in the south e.g., in the Big Bend region until ~31 Ma (Oligocene).

---

## Chapter 2: Regional Geologic Setting

Three major overlapping deformational events have affected the west-central United States since Cretaceous time. The Sevier Orogeny resulted in the displacement of thick sections of sedimentary rock that were telescoped eastward for tens of kilometers on bedding-plane thrusts with west dipping ramps between ~119-50 Ma (Bird, 1998). Widespread compression related to the Laramide Orogeny resulted in a shortening episode throughout the interior of North America between ~75-35 Ma (Bird, 1998) that has largely been attributed to the flat-slab subduction of the Farallon plate beneath the North American Plate (Fig.2.1). Inverse convection models have identified two large seismic anomalies on the recovered Farallon slab within the mantle that are believed to represent the buoyant Shatsky and Hess oceanic plateau pairs (Liu *et al.*, 2010). The Shatsky conjugate is predicted to extend from 900-1,400 km depth spanning an area of 1,000 km from north-south and 500 km from east-west; whereas the Hess conjugate stays above 1,000 km in depth with a cross-sectional dimension of 500 km (Liu *et al.*, 2010). These two prominent seismic anomalies have been paired with reconstructions of plate motions to coincide paleogeographically with the reconstructed positions of the Shatsky and Hess conjugate plateaus at the age of formation. Liu *et al.* (2010) inferred based upon the geometry of the preserved plateaus, the age of underlying ocean lithosphere, and the associated mid-ocean ridge system that the Shatsky Rise formed at the Pacific-Farallon-Izanagi trip junction between ~145-130 Ma and the Hess Rise formed along the



---

Pacific-Farallon ridge at ~110 Ma. They have been suggested to have initially subducted beneath the North American plate at 84 Ma and 64 Ma respectively, with a predominantly northeast trajectory (Fig.2.2) (Liu *et al.*, 2010). The subduction of these two oceanic plateaux is suggested to be responsible for initial slab-flattening at the beginning of the Laramide orogeny given the added buoyancy associated with thickened oceanic crust of the subducted slab and subsequently transgressed eastward through time.

Ignimbritic volcanism occurred in three regionally synchronous pulses (37.5-31.4, 29.3-26.8, 25.1-23.3 Ma) from Trans-Pecos Texas to central Colorado, a distance of 1,100 km during the late Eocene and Oligocene with two temporal gaps (31.4-29.3 and 26.8-25.1 Ma) proposed to separate the pulses (Chapin *et al.*, 2004). Twelve calderas occurring in two north-northwest trending belts and ranging in size from 4-30 km were the dominant volcanic sources in the Trans-Pecos region (Fig.2.3) (Henry and Price, 1984). Four calderas are categorized into an eastern alkalic belt, and eight, including two in neighboring Chihuahua, Mexico occur in a western alkali-calcic belt (Henry and Price, 1984). The eastern belt is predominantly alkalic and includes the Buckhorn, Paisano Pass, Pine Canyon, and Sierra Quemada calderas of the Davis and Chisos Mountains (Henry and Price, 1984). The volcanic rocks of the western belt are calc-alkaline in composition and are found in the Quitman Mountains, Eagle Mountains, Van Horn Mountains, Wylie Mountains, Chinati Mountains, Infiernito, San Carlos, and Santiago calderas (Henry and Price, 1984; Peacock, 1931). The compositional variations of volcanic rocks in Trans-Pecos Texas are attributed to

## Shatsky and Hess Rise Conjugate Plateau Trajectories

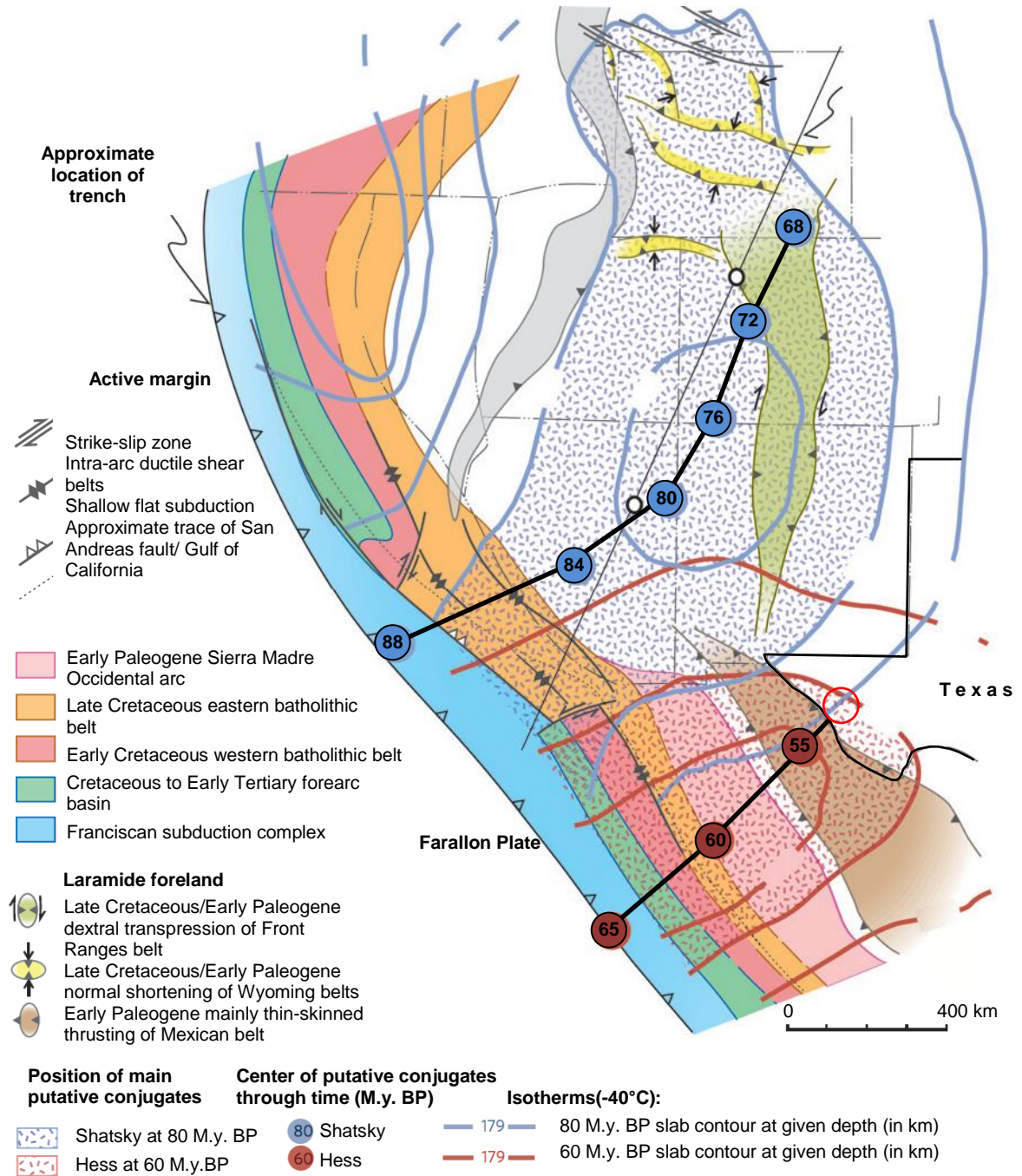


**Fig.2.2:** Palinspastic map displaying the southwest Cordilleran active margin and Laramide foreland during Late Cretaceous time with temperature field overlain. Shatsky and Hess conjugate plateaus initially subducted beneath the North American plate 88 and 65 Ma. The Hess conjugate plateau trajectory has been extended into the West Texas region and the ages of its trajectory path are believed to have errors of  $\pm 5$  My. Modified from Liu and others (2010).

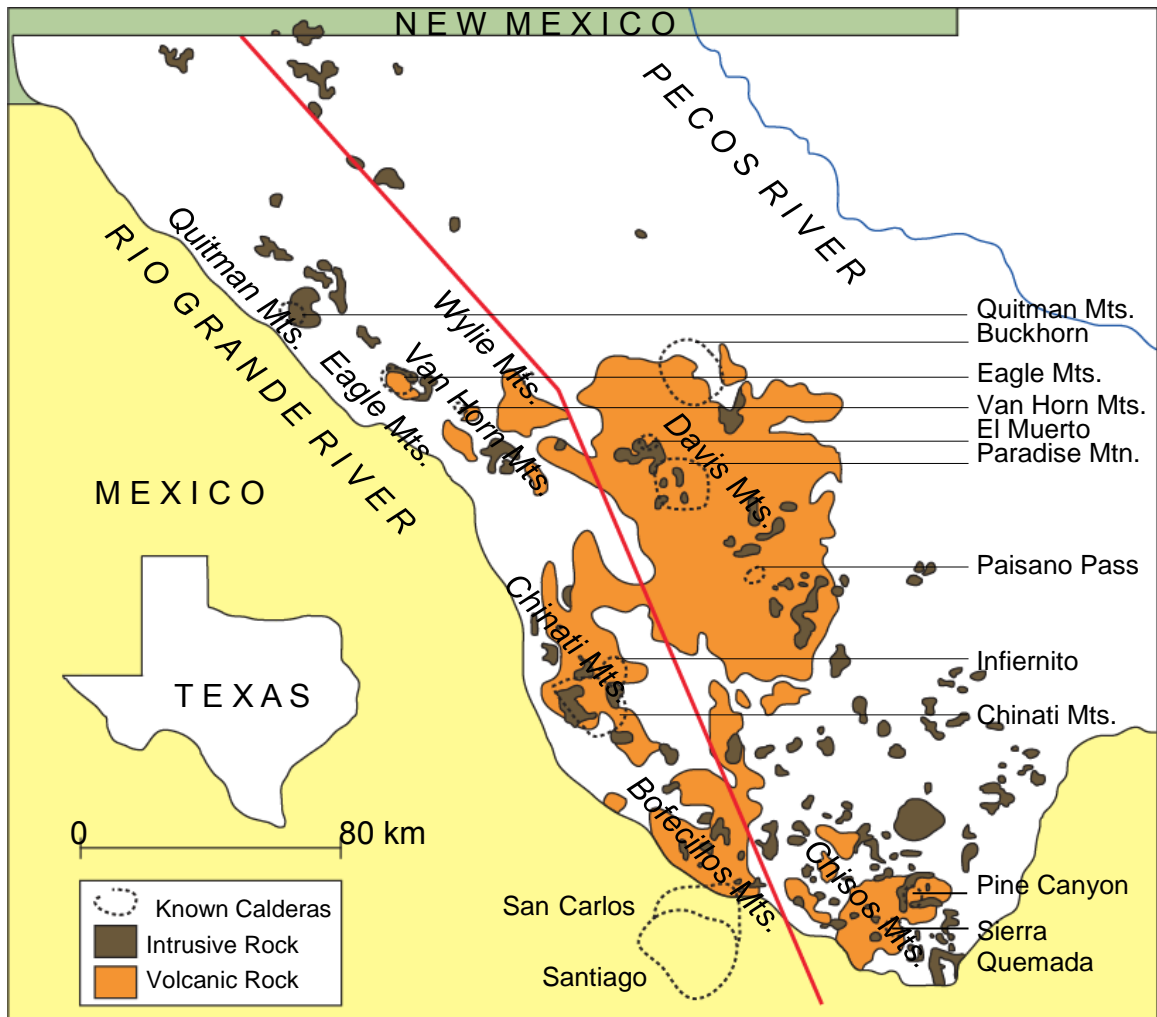


**Fig.2.3:** Location of calderas and Tertiary volcanic and plutonic rock in the Trans-Pecos Texas igneous province. The red line signifies the line between predominantly alkalic deposits to the east vs. calc-alkaline volcanic ignimbrite deposits to the west. Modified from Befus and others (2009).

processes of generation at varying depths in the mantle which causes melts to transition from an alkalic to calc-alkaline composition with increasing depth of formation (Dickinson and Snyder, 1978). All calderas are believed to have formed between 42 and 28 Ma, excluding the two calderas found in Chihuahua that formed between 30 and 28 Ma that display significant differences in composition and eruptive style from the earlier calderas found in West Texas (Henry and Price, 1984).

---

The caldera cycle and associated volcanism in the region was highly variable and the calderas are believed to have been underlain by individual magma chambers that were only active for about 1 m.y. (Henry and Price, 1984). Minor volcanism was common and tumescence, or swelling of the magma chamber is documented to have occurred in at least two calderas as common precursor to ash-flow tuff eruption and caldera collapse (Henry and Price, 1984). Thick, intracaldera tuffs interbedded with breccias shed from caldera walls indicate that ash-flow eruption and collapse were simultaneous in all calderas. Westward younging of linear caldera complexes is likely indicative of a trenchward retreat of subducted slabs and reflects plate-margin control of volcanism rather than intraplate controls (Chapin *et al.*, 2004). As documented by the high-angle tilt of the Cretaceous to Early Tertiary units in much of the region, the principal shortening direction in the Trans-Pecos region of West Texas throughout Laramide deformation was in an east-west to northeast-southwest direction (Price and Henry, 1984). The earliest magmatism in the region is associated with the emplacement of an andesitic suite of intrusive rocks located in El Paso, Texas. The suite is post-Cretaceous in age, and is found cropping out on the campus of The University of Texas at El Paso. The pluton dated using K-Ar geochronology has yielded an age of  $47.1 \pm 2.3$  Ma (Hoffer, 1970), slightly older than volcanism to the east.

The timing of the change from compression to extension, whether there was a quiescent period between, as well as the theories of the mechanics behind slab steepening, removal, and extension that followed in the Trans-Pecos

---

igneous province are still in question. The purpose of this study is to improve on the timing of compressional uplift and volcanic events to help clarify these transitions associated with major tectonic events. In order to improve on the timing of compressional uplift and volcanic episodes, sample sites were chosen in several mountain ranges and surrounding areas throughout the Trans-Pecos igneous province including, from north to south, the Eagle Mountains, Indio and Van Horn Mountains, Davis Mountains, the southwestern Rio Grande River area, the Alamito Creek and Green Valley area, Chinati Mountains, and Chisos Mountains. Volcanic and siliciclastic rock samples that occur both above and below the Laramide unconformity collected and analyzed throughout the duration of this study include the Lower Rhyolite from the Eagle Mountains; the Garren Group from the Indio and Van Horn Mountains; the Huelster Formation and Star Rhyolite from the Davis Mountains; the Undivided Vieja Group of the southwestern Rio Grande River area; the Tascotal Tuff from the Alamito Creek and Green Valley area; the Morita Ranch Formation from the Chinati Mountains; and the Black Peaks, Hannold Hill, Canoe, Chisos, South Rim, and Burro Mesa Formations of the Chisos Mountains located in Big Bend National Park. In the subsequent chapters I will explain the local geology of each sample site, the analyzed sample, and its acquired analytical results in addition to a discussion of the compiled data and summary.

---

**Chapter 3:**  
**Sample Preparations and Analytical Technique**

**i. Crushing and Sieving**

Individual samples varying in weight from 0.5 kg to 4.0 kg (1-8 lbs.) were broken into small fragments using a 2.5 kg (5 lbs) sledgehammer and subsequently crushed and pulverized into coarse to fine granules (sand to clay sized particles) using a BICO-Braun “Chipmunk” steel jaw crusher and disk mill. The pulverized sample was size graded into two fractions:  $250\ \mu\text{m} < x < 500\ \mu\text{m}$  and  $x < 250\ \mu\text{m}$  (Tyler Mesh #60-32). Large efforts were made to avoid contamination from previous samples on the BICO-Braun “Chipmunk” steel jaw crusher, disk mill, collection pans and  $250\ \mu\text{m} < x < 500\ \mu\text{m}$  and  $x < 250\ \mu\text{m}$  (Tyler Mesh #60-32) sieves. Before and after use, the stationary and moving steel plates of the BICO-Braun “Chipmunk” steel jaw crusher, in addition to the entire machine and table it is mounted on were vacuumed, brushed with a steel brush and water, and blown clean with compressed air. The Bico-BRAUN steel disk mill was cleaned before and after use by blowing compressed air into the entrance port, vacuuming the entire machine and table it is mounted on, washing with water, and then blowing with compressed air once more. The  $250\ \mu\text{m} < x < 500\ \mu\text{m}$  and  $x < 250\ \mu\text{m}$  (Tyler Mesh #60-32) sieves were washed with water, brushed thoroughly with a steel brush, and then blown with compressed air. The table at which sieving occurred was vacuumed, washed, and blown dry with compressed air and always with multiple pieces of clean paper to avoid contamination from any remaining particles.

---

## **ii. Washing and Magnetic Separation**

A minimum of 3.5 oz. (115 g) of each homogenized sample was washed using water and acetone to remove clay-sized particles and other potential unwanted contaminants. Following the washing process each sample was thoroughly dried for 24 hours by utilizing suction from a vacuum line. All glassware that the samples were washed in were sanitized and dried to ensure cross contamination did not occur. In addition, any surface that the glassware came into contact with was washed, dried, and covered with clean fresh paper to avoid contamination from previous samples. Samples of the  $x < 250\text{-}\mu\text{m}$ -size fraction analyzed in this study were then run through a Frantz magnetic barrier separator to further separate each sample into a magnetic and non-magnetic fraction. This process was done to rid the samples of magnetic heavy minerals including oxides, olivine, garnet, and altered ferromagnesian minerals to reduce time during the later zircon grain-picking phase. The magnetic pole pieces and other surfaces in and around the magnetic separator were thoroughly wiped down with sterile kimwipes, blown with compressed air, and covered with clean paper before each use.

## **iii. Heavy Liquid Mineral Separation**

The heavy mineral extraction for this study was executed on the non-magnetic  $x < 250\text{-}\mu\text{m}$ -size fraction using methyl iodide (MeI). Methyl iodide is a dense, colorless liquid that darkens when exposed to light with the chemical formula  $\text{CH}_3$ . The methyl iodide used throughout this study maintained a density of 3.325 g/cc to 2.28 g/cc (2.28 g/mL). This density variation occurs after several

---

processes of reclamation are employed on the chemical. The equipment used during the heavy mineral extraction phase include a ring stand and ring stand clamp, separatory funnel and stopcock, two glass funnels with stoppers, a flask for heavy liquid, a flask for heavy liquid and acetone, and a stirring rod. The equipment used throughout the separating process was cleaned thoroughly with acetone and water before each use. Any surface that the glassware came into contact with was washed, dried, and covered with clean fresh paper to avoid contamination from previous samples. When all equipment had been properly sterilized the stopcock was fastened tightly into the separatory funnel and suspended by the ring stand and ring stand clamp above the heavy mineral flask. A glass funnel secured with a stopcock was placed in the opening of the heavy liquid flask and lined with Whatman 5 filter paper labeled with the Sample ID and 'MI Down'. Approximately 150 mL of methyl iodide was then poured into the closed separatory funnel for heavy mineral extraction. Approximately 50 mL of sample was added to the separatory funnel containing methyl iodide and stirred thoroughly to allow heavy minerals to settle. Heavy mineral extraction is executed on 150-200 mL of each sample and requires several rounds of heavy mineral extraction, as the separatory funnel is a more efficient heavy mineral extractor with smaller sample volumes. The settled heavy mineral fraction was released into the filter paper lined glass funnel and heavy mineral flask by fully rotating the stopcock twice. The vacuum line assisted in extracting the majority of pure methyl iodide into the heavy minerals flask to be reused. When most of the methyl iodide had been removed from the collected heavy fraction the filter paper

---

containing the sample was moved to the heavy mineral and acetone flask fastened with a glass funnel and stopcock to be washed thoroughly with acetone. This is done to rid the sample grains of any remaining methyl iodide to be reclaimed at a later time and to help the drying process. Once the sample was completely dry it was transferred immediately to a labeled vial and prepared for the next step in the process.

#### **iv. Heavy Liquid Reclamation**

Heavy liquids can be reclaimed from acetone wash because of its differential solubility in water. Reclamation of the methyl iodide should always be done in areas of adequate ventilation and is achieved by first transferring 1.75 L (0.5 gal) of previously used MI and acetone wash into an empty 4 L (1 gal) amber glass acetone bottle with a narrow mouth or any other similar storage container. From there, an additional 1.25 L (0.3 gal) of fresh water is added to the mixture and the glass container is then tightly sealed. Once properly sealed, the glass container should be shaken vigorously for 1 to 2 minutes and allowed to rest for 4 to 5 minutes. The methyl iodide will visibly settle at the bottom of the bottle and the cloudy acetone-water wash mixture can then be poured off incrementally into a designated hazardous waste receptacle as some methyl iodide could still be in the acetone-water wash. After the first shaking event pour off a maximum of 0.25 L (0.07 gal) and refill the container with fresh water up to the 3 L (0.8 gal) mark. Again, seal the container tightly and shake vigorously for 1 to 2 minutes. Repeat the process of shaking, pouring off, and refilling the container until the acetone-water wash no longer appears cloudy. When the acetone-water wash no longer

---

appears cloudy pour as much of the wash into the designated waste receptacle as possible without discarding any of the newly reclaimed methyl iodide resting at the bottom of the glass container. Transfer the methyl iodide and remaining water into a large 1 L (0.25 gal) separatory funnel with a well-greased, closed stopcock. Open the stopcock and allow only the methyl iodide to filter through a funnel attached to a vacuum line that is double lined with filter paper and into an Erlenmeyer flask. The newly reclaimed methyl iodide should reach a density of approximately 3.2-3.25 g/cm<sup>3</sup>. Once the density has been measured and documented the reclaimed methyl iodide should be stored in a designated dark plastic container in the fume hood.

**v. Hand Picking and Grain Mounting**

The heavy mineral fraction separated from each sample was hand-picked for zircon grains under a binocular Leica EZ4D stereo microscope equipped with 4.4:1 zoom and integrated LED illumination located on the third floor of the SR1 Building in Rm. 319. The heavy fraction was placed in VWR petri dishes of varying sizes (100x10 to 100x20 mm) and saturated with Pharmco-AAPER ethyl alcohol, 95% (CH<sub>3</sub>CH<sub>2</sub>OH). Between 25 and 45 individual zircon grains were selected for analysis from igneous samples and 100 to 200 zircon grains were selected for analysis from detrital samples using SPI anti-magnetic, anti-acid, high precision tweezers. A greater abundance of zircon grains are required for quantitative detrital analysis to provide more meaningful comparisons between the proportions of age components (Gehrels et al., 2008). The selected zircon grains were then mounted within a 1" Buehler Phenolic Ring Forms™ ring mount

---

in an epoxy mixture consisting of 100 parts by weight of Buehler EpoThin® Epoxy Resin to 39 parts by weight Buehler EpoThin® Epoxy Hardener with two zircon standards, Fc5z and Plesovice, of known age and NIST No.613 glass. The grain mount was polished using 600 and 800 grit adhesive-backed paper until the epoxy was void of surficial scratches and the faces of the zircon grains were fully exposed for analysis by LA-ICP-MS.

#### **vi. LA-ICP-MS Analysis and Data Reduction**

The samples were analyzed on the University of Houston's Analyte.193 Ultra-short Pulse Excimer Laser Ablation System. The Analyte.193 Excimer Laser Ablation System is powered by an ATL Ex300si ultra-short pulse length (~4 ns) ArF laser head with a 19.3  $\mu\text{m}$  diameter laser spot, a repetition rate of 10 Hz, and a laser power setting of 3  $\text{J}\cdot\text{cm}^{-2}$  for the duration of this study. The samples were ablated for approximately 20 seconds, and helium (He) was used as the carrier gas that transported ablated particles from the laser to the detector at a flow rate of 600-700  $\text{ml min}^{-1}$  (Shaulis and Lapen, 2010). For the purposes of this study, the Varian 810 Inductively Coupled Plasma-Quadrupole Mass Spectrometer (ICP-MS) was operated in high sensitivity mode for increased sensitivity and lower detection limits for elements including Pb, Th, and U as well as to maximize signal intensities of masses  $^{204}\text{Pb}$  and  $^{207}\text{Pb}$  (Shaulis and Lapen, 2010). The pulse counting detector equipped on the Varian 810 ICP-MS was developed by ETP Electron Multipliers and is an all-digital, extended range, scaling pulse detector that was operated in auto attenuation mode for the duration of this study.

---

The two zircon standards used in this study, Fc5z and Plesovice, have yielded ages of 1096 Ma and 337 Ma respectively. The Fc5z zircon standard is derived from the Duluth Complex, a large suite of intrusive mafic rocks that are associated with the Midcontinental Rift that affected the North American craton over a period of 15 to 22 million years around 1.1 Ga (Heinselman, 1996; Jirsa and Southwick, 2000). The Duluth Complex is comprised of an anorthositic series and troctolitic series (Shaulis and Lapen, 2010). The Fc5z zircon standard having been derived from the anorthositic series (Paces and Miller, 1993; Shaulis and Lapen, 2010) has a reported chemical abrasion ID-TIMS age of  $1096.2 \pm 1.0$  Ma (S.A. Bowring, personal communication, 2008; Shaulis and Lapen, 2010). The Plesovice zircon standard used was extracted from a potassic granulite facies rock collected from the southern portion of the Bohemian Massif in Plesovice, Czech Republic, and has yielded an ID-TIMS age of  $337.13 \pm 0.37$  Ma (all errors  $2\sigma$ ) (Slama *et al.*, 2008).

The raw data consisting of signal intensities of  $^{202}\text{Hg}$ ,  $^{204}\text{Pb}(\text{Hg})$ ,  $^{206}\text{Pb}$ ,  $^{207}\text{Pb}$ ,  $^{208}\text{Pb}$ ,  $^{232}\text{Th}$ , and  $^{238}\text{U}$  were imported into Wavemetrics Igor ProTM (v. 6.12A) software with the add-in Lolite (v. 2.11) (Shaulis and Lapen, 2010; Hellstrom *et al.*, 2008). To avoid biasing of the data, an automated signal selection protocol that neglects the first 2 seconds of the sample signal was used throughout the reduction of the acquired data to avoid surficial Pb contamination. Following the automated signal selection, the sample signals are inspected and modified if necessary to adjust for abnormal  $^{204}\text{Pb}$  spikes obtained during analysis from surficial contamination, inclusions, cracks, or age zoning. The data

---

from each sample was imported into a data reduction spreadsheet where it was corrected for instrumental mass and elemental fractionation. In addition to the internal errors exported from Lolite, random and systematic errors were calculated. The  $^{207}\text{Pb}/^{235}\text{U}$  ratio was calculated from the  $^{206}\text{Pb}/^{238}\text{U}$  ratio on the basis of the constant value of  $^{235}\text{U}/^{238}\text{U}$ . The measured  $^{207}\text{Pb}/^{206}\text{Pb}$  ratio used when plotting the classical concordia diagram varies from an alternative U/Pb presentation method pioneered by Tera and Wasserburg (1973,1974) and was used throughout this study for all igneous samples (Dickin, 2005). The correlation of errors taken into account when fitting discordia regression lines on a classical concordia diagram are largely avoided on the Tera-Wasserburg concordia diagram which plots the  $^{238}\text{U}/^{206}\text{Pb}$  ratio directly against the  $^{207}\text{Pb}/^{206}\text{Pb}$  ratio. The Tera-Wasserburg plot was further developed by Wendt (1984) into a three-dimensional U/Pb diagram with the addition of a  $^{204}\text{Pb}/^{206}\text{Pb}$  that represented the level of common-Pb present in an individual sample. With the addition of the  $^{204}\text{Pb}/^{206}\text{Pb}$  axis the discordia is a plane and ages can be calculated without independent knowledge of the isotopic composition of the common-Pb component (Dickin, 2005). The three-dimensional plot allows for dating of partially open whole-rock U/Pb systems because it allows for a more accurate correction of large common-Pb fractions, which are more common in younger volcanic rocks (Carl *et al.*, 1989).

When analyzing siliciclastic samples as the sample size increases, the Concordia diagrams that convey information about the analytical process such as sample size, accuracy calculated from the standards used, and precision

---

become visually cluttered (Fedo *et al.*, 2003). To adjust for this, the detrital zircon data in this study was displayed on a univariate age-probability distribution plot. Because the ability to display accuracy in terms of concordance is lost, the isotopic data for the detrital samples was filtered during the reduction process. Individual detrital zircon analyses from each sample with a discordance of  $\geq 30\%$  were excluded from the data selection. Ages were then calculated using the in-house DZ Age Pick Program of the University of Arizona LaserChron Center (Gehrels, 2007). A peak is a maximum in age-probability that comprises age-probability contributions (at  $2\sigma$ ) from three or more analyses. For the purposes of this study, the youngest peak consisting of three or more grain analyses was used to determine the max depositional age of the siliciclastic samples.

---

**Chapter 4:**  
**Tertiary Siliciclastic Results and Implications**

**a. Big Bend National Park: Tornillo Flat**

Big Bend National Park (Fig.4.1) spans an area of 3,242 km<sup>2</sup> (801,163 acres) and is located along a 190 km (118 mile) section of the Rio Grande River at the United States-Mexico border, in the southernmost portion of Brewster County, Texas. The geology of the Big Bend National Park region of Trans-Pecos Texas has been affected by several cycles of rifting, mountain building, basin development, volcanism, and plutonism (Gray and Page, 2008). The earliest recorded tectonic episode documented in the park affected this region during the Paleozoic from development of a stable rifted margin at the edge of Laurentia up until the Ouachita-Marathon-Sonora collisional orogeny. Deep-water marine rocks originally deposited off of the southern margin of Laurentia, and south of the present-day park location were thrust northwestward onto the edge of the paleo North American (Laurentian) stable continental margin by the pulsed collision between the Laurentian and South American plates from Middle Mississippian to Early Permian time (Poole *et al.*, 2005). This orogenic event resulted in deformation in the region during the Middle Mississippian to Early Permian (330-285 Ma) and only a small outcrop belt containing Paleozoic rocks and northwest-directed thrust faults are exposed presently in the northeastern portion of the park (Maxwell *et al.*, 1967). The Paleozoic section found in Big Bend National Park includes portions of the previously stable Paleozoic rifted

margin sequences and later orogenic rocks. They include, in ascending order, the Middle Ordovician Marvillas Formation, the Silurian to Mississippian Caballos Novaculite, and the Mississippian to Pennsylvanian Tesnus Formation (Fig.4.2)(Poole *et al.*, 2005).

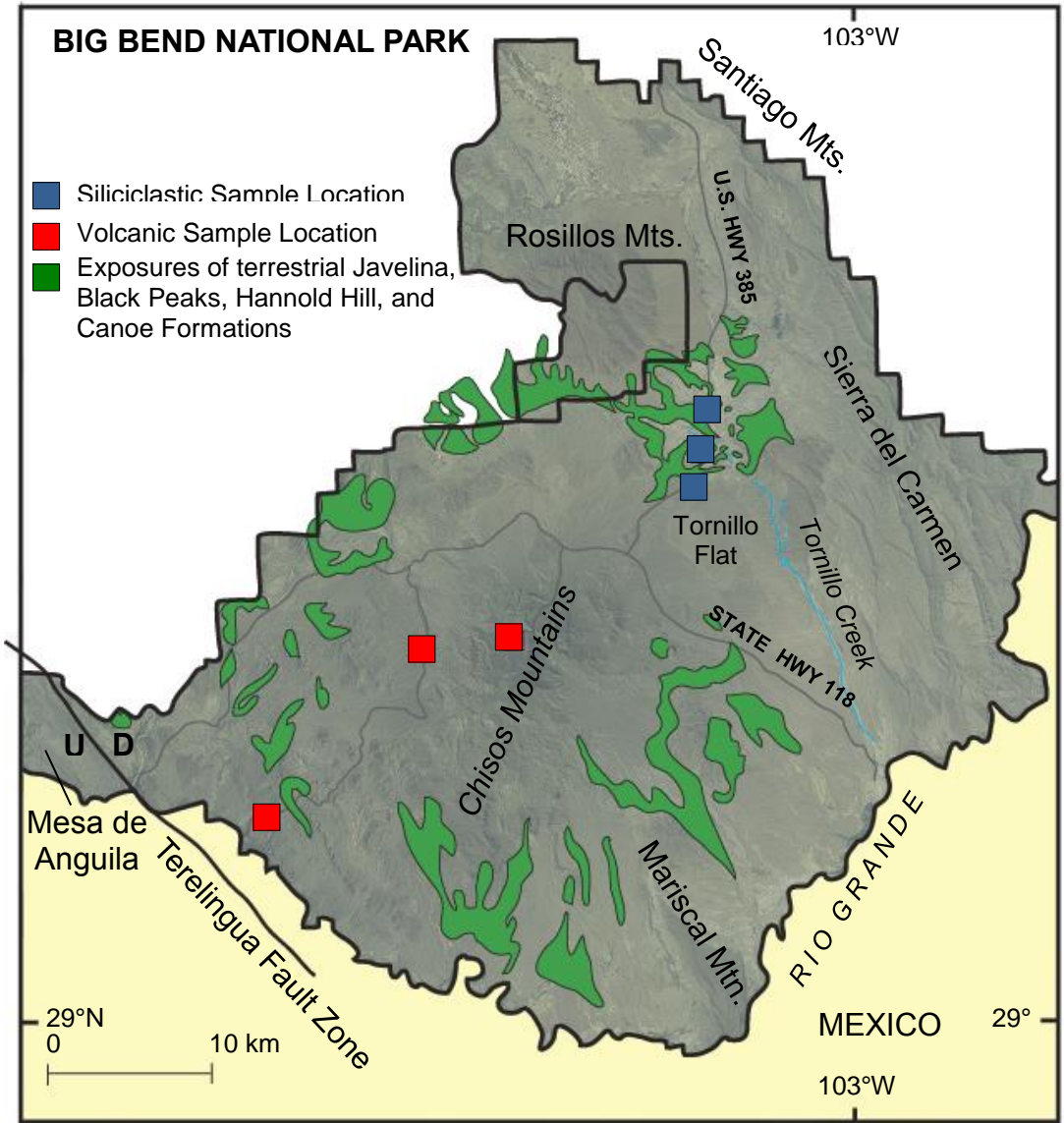


**Fig.4.1:** Generalized map of Big Bend National Park that displays the location of the Chisos Mountains in relation to Laramide-style deformational and exposures of the Javelina, Black Peaks, Hannold Hill, and Canoe Formations. Modified from Schiebout *et al.* (1987).



---

South America-Yucatan terrain from North America began to form the Gulf of Mexico (GOM) (Muehlberger, 1980; Muehlberger and Dickerson, 1989; Lehman and Busbey, 2007). Following the Late to Middle Jurassic rifting event, the Big Bend region was considered part of the Diablo Platform, an expansive shallow-water carbonate platform that was the depositional site for Early to Late Cretaceous limestone and shale units in a shallow, open-marine environment (Page *et al.*, 2007). These units include, in ascending order, the Glen Rose Limestone, Del Carmen Limestone, Sue Peaks Formation, Santa Elena Limestone, Del Rio Clay, Buda Limestone, and Boquillas Formation. They are widely preserved and exposed in the Sierra del Carmen-Santiago Mountains, Nine Point Mesa, Marsical Mountain Anticline, and Mesa de Anguila areas (Fig.4.1; Fig.4.2) (Page *et al.*, 2007). A shift from marine to continental deposition is recorded in the overlying Upper Cretaceous Aguja and Maastrichtian Javelina Formations (Fig.4.2).

The Laramide orogeny affected the entire western margin of North America as far inboard as 1,000 km throughout Late Cretaceous to Early Tertiary time (~88-32 Ma). It had a significant impact on the tectonic evolution of the Big Bend region when the advancing magmatic arc and associated compressional deformation reached the present-day western margin of Trans-Pecos Texas at ~47 Ma (Page *et al.*, 2007). Northeast-directed compressional deformation associated with this orogenic event was responsible for major uplifts, thrust faults, and folds in the park that affected Paleozoic, Late to Early Cretaceous, and Paleocene sections; including the Oligocene aged volcanic Chisos

---

Formation. Late-Cretaceous to Early-Tertiary aged morphological and structural features exposed in the Big Bend National Park region include the Mesa de Anguila, a northeast-facing, uplifted monocline located on the southwestern margin of the Park, and the southwest-facing Sierra del Carmen-Santiago Mountains, an uplifted thrust-faulted monocline that bounds the Park to the east and are attributed to the development of Laramide folds and thrusts that affected this region in the Early Tertiary (Fig.4.1) (Lehman, 1991; Lehman and Busbey, 2007).

The Late Cretaceous to Late Eocene terrestrial formations of Big Bend National Park are well exposed on the Tornillo Flat that is bounded on the east and west by the Mesa de Anguila and Sierra del Carmen-Santiago Mountains (Fig.4.1)(Schiebout *et al.*, 1987). The Tornillo Group is well exposed on the Tornillo Flat and includes, in ascending order, the Javelina, Black Peaks, and Hannold Hill Formations. The Cretaceous-Tertiary boundary falls within the Javelina Formation that is comprised of clay-rich fluvial and alluvial deposits and records a northwest to southeast paleoflow direction and sedimentation pattern on a low-relief alluvial plain throughout the Latest Cretaceous in Big Bend National Park (Lehman, 1986; Schiebout *et al.*, 1987). A single distally derived tuff unit within the formation contains monzanite and has yielded a U-Pb isochron age of  $69.0 \pm 0.9$  Ma (Lehman *et al.*, 2006). The alluvial plain was a largely flat landform created by the deposition of sediment by one or multiple fluvial-deltaic systems being sourced from uplifts associated with the eastward migrating magmatic arc to the northwest. The paleoflow directions recorded in the Javelina

---

Formation and other terrestrial formations exposed on the Tornillo Flat are from the northwest to the southeast, and are important because they document the progression of distal to proximal uplift related to the eastward advancing orogenic front throughout the Cretaceous and Early Tertiary.

For each individual detrital sample between 100 and 125 zircon grains were separated and analyzed on the University of Houston's LA-ICP-QMS. Two grains from the Fc5z (S.A. Bowring personal communication to Dr. Lapen, 2008) and Plesovice (Slama *et al.*, 2008) zircon standards were analyzed between every five sample zircon grains to monitor and correct for instrumental drift. Individual analyses displaying a discordance of  $\geq 30\%$  were discarded from the age calculation. The age was calculated by uploading individual zircon  $^{206}\text{Pb}/^{238}\text{U}$  age data for each sample at  $1\sigma$  into the DZ Age Pick Program from the University of Arizona LaserChron Center (Gehrels, 2007). This chapter reports the results and summarizes the implications of detrital zircon analyses from the siliciclastic Black Peaks, Hannold Hill, and Canoe Formations. The data used for age calculations can be found in the Appendices starting on p.184 of this manuscript.

---

i. **Black Peaks Formation**

The Black Peaks Formation rests conformably on the Javelina Formation and consists of nearly 180 m (540 ft) of gray, maroon, and black fluvial mudstones, siltstones, and gray buff to yellow sandstones (Maxwell, 1967; Rapp *et al.*, 1983). Fining-upward tabular sand bodies that display sedimentary structures indicative of high sinuosity meandering streams are a defining characteristic of the Black Peaks Formation (Schiebout, 1970, 1974; Rapp, 1983). It is the only Paleocene sedimentary unit found in the Trans-Pecos Texas region and contains the southernmost occurrence of large Paleocene mammalian faunas in North America (Rapp *et al.*, 1983). The faunal succession of the unit indicates an age ranging from Torrejonian to early Clarkforkian (63.3-57 Ma) with a mean sedimentation rate of about 1.8 cm/1000 yrs (Rapp *et al.*, 1983). This rate is thought to have remained relatively constant throughout the formation's depositional history (Rapp *et al.*, 1983). Sediments of the Black Peaks Formation accumulated in fluvial channel, floodplain, and lacustrine environments with a stream flow direction of northwest to southeast (Lehman, 1985; Beatty, 1992; Hartnell, 1980). In this study, a sample of the Black Peaks Formation was collected from an exposure south-southeast of the Rosillo Mountains just north of Tornillo Creek along U.S. Route 385 about 20 km (11.4 mi) north of Panther Junction (GPS Location: 29.43258, -103.13862) (Fig.4.3; Fig.4.4). This sample was analyzed to determine the provenance of detrital zircons and to refine the maximum age of deposition of the Black Peaks Formation.

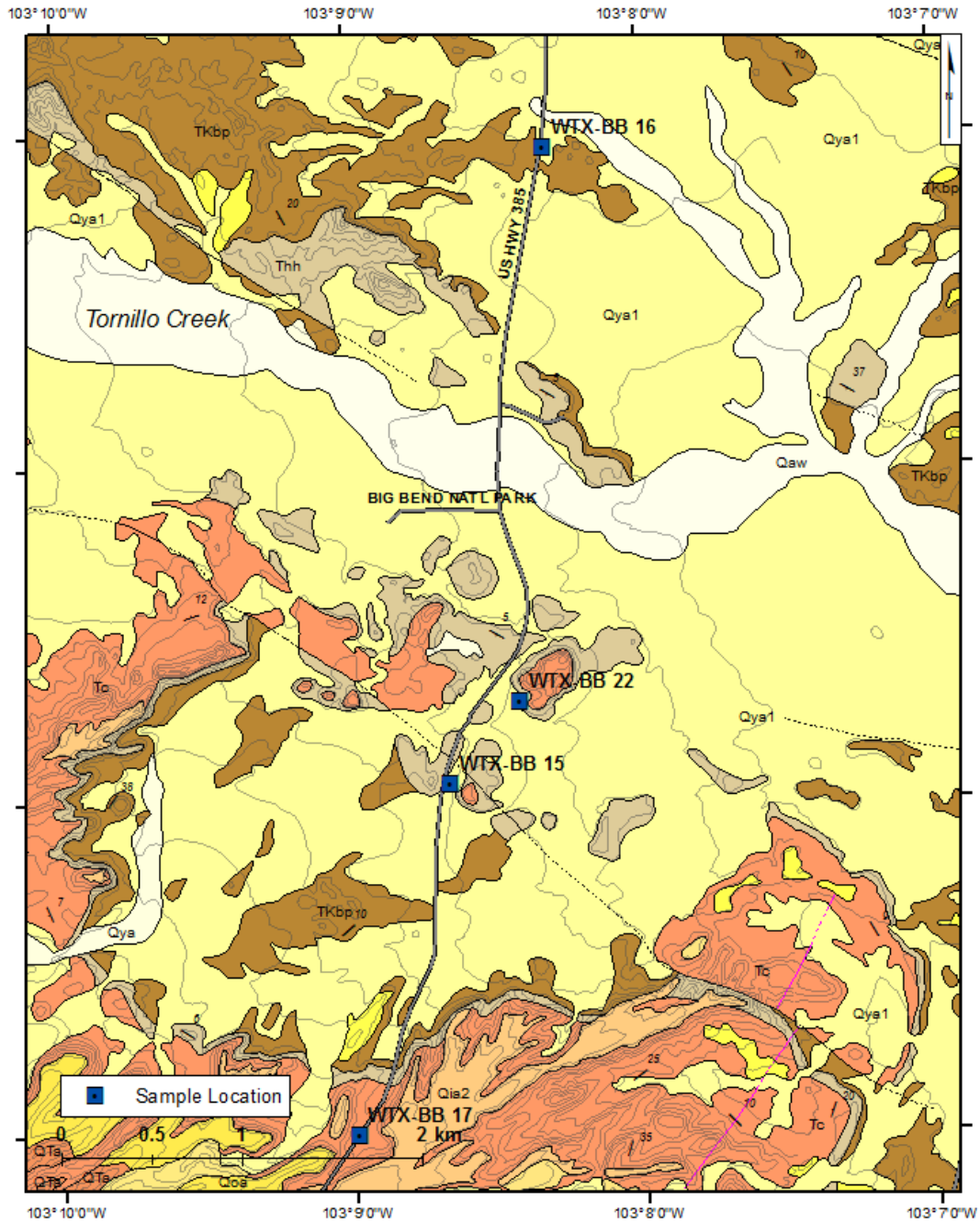


**Fig.4.3:** Map displaying the sample sites of the Black Peaks Formation (WTX-BB 16), Hannold Hill Formation (WTX-BB 15), and the Canoe Formation detrital sample (WTX-BB 17) and basalt sample (WTX-BB 22) shown in relation to one another along US HWY 385 Bend National Park south of Tornillo Creek on the Tornillo Flat. Map modified from Turner et al. (2011).



**Fig.4.4:** Field-photograph displaying sample site of the Black Peaks Formation located on the Tornillo Flat of Big Bend National Park.

One hundred zircon grains were separated from the Black Peaks Formation sample and analyzed. Detrital ages from 67 ( $n=67$ ) of the 100 grains analyzed were uploaded into the DZ Age Pick Program from the University of Arizona LaserChron Center (Gehrels, 2007). The maximum age of deposition is reported in this study as 58 Ma ( $1\sigma$ ) from the youngest age-probability peak that consisted of contributions (at  $2\sigma$ ) from three analyses (Fig.4.5). This age lies directly in the middle of the reported stratigraphic age for this formation of Torrejonian to Clarkforkian (63.3-55.4 Ma). The age-peak spectra from the Black

---

Peaks Formation plot within six major provenance groups classified in studies done by Lakowski and others (2013): (1) Mesozoic eolianites of the western United States, (2) Paleozoic passive margin strata of the western United States, (3) Paleozoic passive margin strata of western Canada, (4) the Mogollon Highlands, (5) the Cordilleran Magmatic arc, or (6) the Yavapai-Mazatzal Province crystalline basement rocks (Fig.4.13). Age-peaks that did not plot within the provenance groups classified by Lakowski and others (2013) were tentatively identified based on inferred regional tectonic events and nearby or distal age provinces. The largest age-peak populations plot within the Triassic and Cretaceous periods and represent detritus that were likely derived from the Cordilleran magmatic arc active throughout the Sevier and Laramide orogenic events (Fig.4.5). The lack of Sevier and documented Laramide zircon peaks from provinces proximal to the Black Peaks Formation at the time of deposition suggests that detritus is unlikely to represent locally derived volcanic/plutonic sources. Implications of the age-peak spectra are expanded on in the discussion of this chapter.

### Black Peaks Formation: WTX-BB 16 Analyses

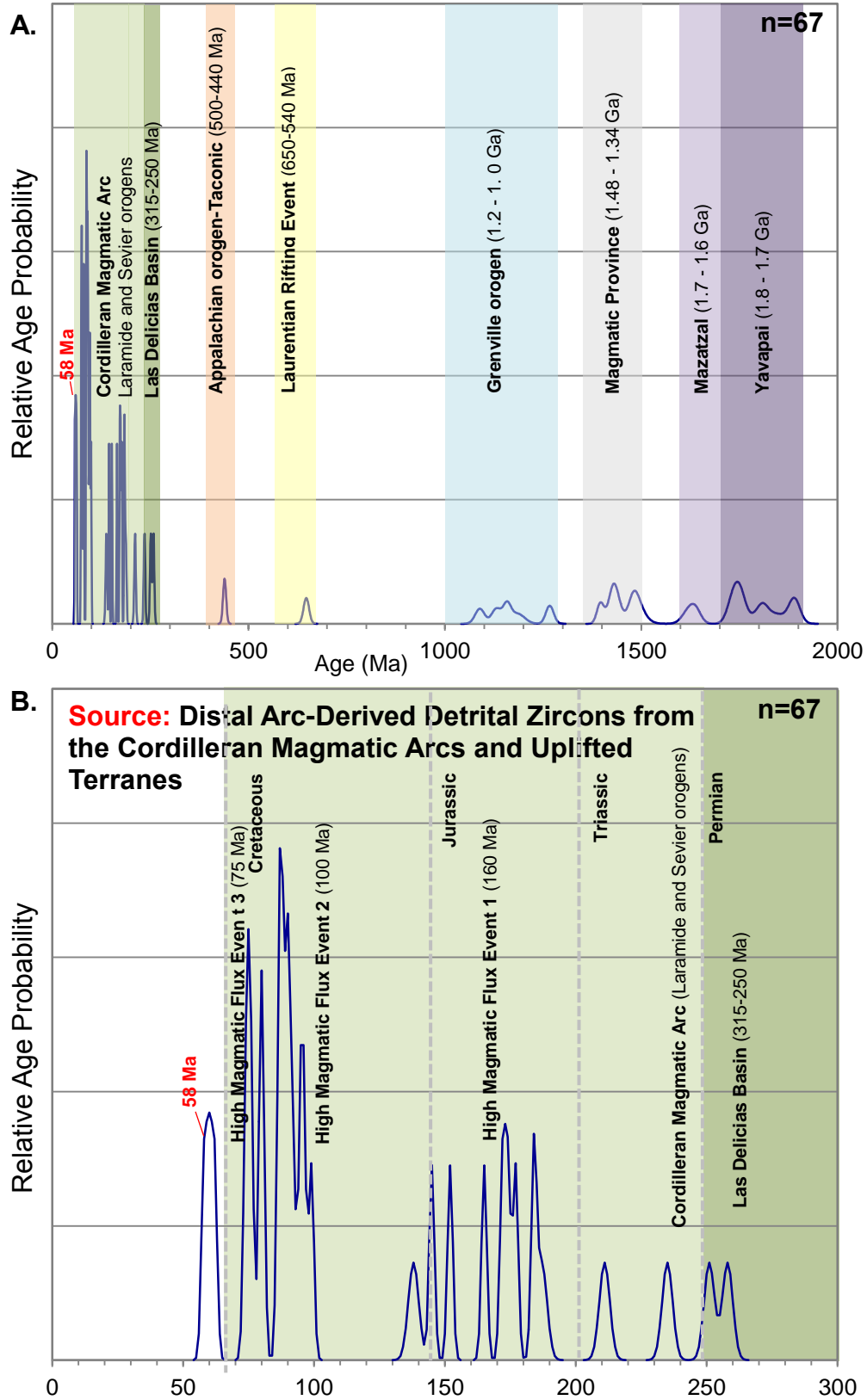


**Fig.4.5:** The maximum age of deposition is reported in this study as 58 Ma ( $1\sigma$ ) **A.** Displays all age-peak contributions from analyses with suggested provenance, and **B.** Displays age-peak contributions from Triassic to Tertiary aged detritus. High magmatic flux events are expanded on in chapter discussion.

---

## ii. Hannold Hill Formation

The Hannold Hill Formation rests conformably on the Black Peaks Formation and is categorized as the middle upper of the Tornillo Group (Fig.4.2) (White *et al.*, 2002). Similar to the Black Peaks Formation, the Hannold Hill was deposited in fluvial channel, floodplain, and lacustrine environments with a stream flow direction of northwest to southeast that likely records the uplift of the incoming Laramide orogenic front to the northwest (Hartnell, 1980; Lehman, 1985; Beatty, 1992). The formation consists of a basal conglomeratic sandstone (Exhibit Sandstone Member), a lower mudstone, a conglomeratic sandstone, and an upper mudstone with some lignite beds and calcareous nodules (Lehman and Busbey, 2007; Busbey and Lehman, 1989; Hartnell, 1980; Maxwell *et al.*, 1967). The Hannold Hill Formation has a maximum thickness of 260 m (780 ft) and is described as mostly gray and maroon clay with a higher proportion of lenticular sand bodies than the Black Peaks Formation (Hartnell, 1980). This is interpreted as a decrease in sinuosity of the meandering streams and viewed as a response to a steepening gradient related to more proximal uplift associated with the inboard advance of the magmatic arc and Laramide orogenic front.

At the time of deposition of the Hannold Hill Formation, the Laramide orogenic front and associated uplift had reached present-day New Mexico and adjacent Mexico (Liu *et al.*, 2010). The Hannold Hill mudstones lack the distinctive black lignite beds that are found in the Black Peaks Formation, which is another indicator of uplift and lowering of the water table (Schiebout *et al.*,

---

1987). The Hannold Hill Formation contains fossil mammal assemblages of Wasatchian age (55.4-50.3 Ma) (Schiebout, 1995; Schiebout *et al.*, 1987).

A sample of the Hannold Hill Formation was collected about 15 km (8.5 mi) north of Panther Junction along U.S. Route 385 (GPS Location: 29.40085, -103.14441). The exposure was located off the west side of the road and the sample was taken from a prominent channel sand within the formation (Fig.4.3; Fig 4.6).

One hundred and twenty five zircon grains were collected from the Hannold Hill Formation sample and analyzed on the University of Houston's LA-ICP-MS. The age of the formation was calculated from 45 analyses (n=45) using the DZ Age Pick Program from the University of Arizona LaserChron Center (Gehrels, 2007). The maximum age of deposition is reported in this study as 60 Ma (at  $1\sigma$ ) from the youngest age-probability peak that consisted of contributions (at  $2\sigma$ ) from three analyses (Fig.4.7). This age is slightly older than the estimated Wasatchian stratigraphic age range (55.4-50.3 Ma), which is common in detrital zircon analyses. Similar to the Black Peaks Formations analysis, the majority of age-peak spectra from the Hannold Hill Formation analysis plotted within the six major provenance groups classified by studies done by Lakowski and others (2013) (Fig.4.13).



**Fig.4.6:** Field-photograph displaying sample site of the Hannold Hill Formation located on the Tornillo Flat of Big Bend National Park.

Age-peaks that did not plot within the provenance groups classified by Lakowski and others (2013) were tentatively identified based on inferred regional tectonic events and potential nearby igneous zircon provinces. The largest age-peak populations plot within the Triassic and Cretaceous periods and are most

---

pronounced in the Middle Cretaceous. This age-peak spectra is thought to be detritus derived from the Cordilleran Magmatic Arc active throughout the Sevier and Laramide orogenic events with an increased proximal source as Permian-aged detritus is included in the analysis (Fig.4.7). This suggests that detritus is unlikely to represent a locally derived volcanic/plutonic source, but it has more input from proximal sources than the Black Peaks Formation as there is a new Permian detritus source component. Implications of these age-peaks are expanded on in the discussion of this chapter.

## Hannold Hill Formation: WTX-BB 15 Detrital Zircon Analyses

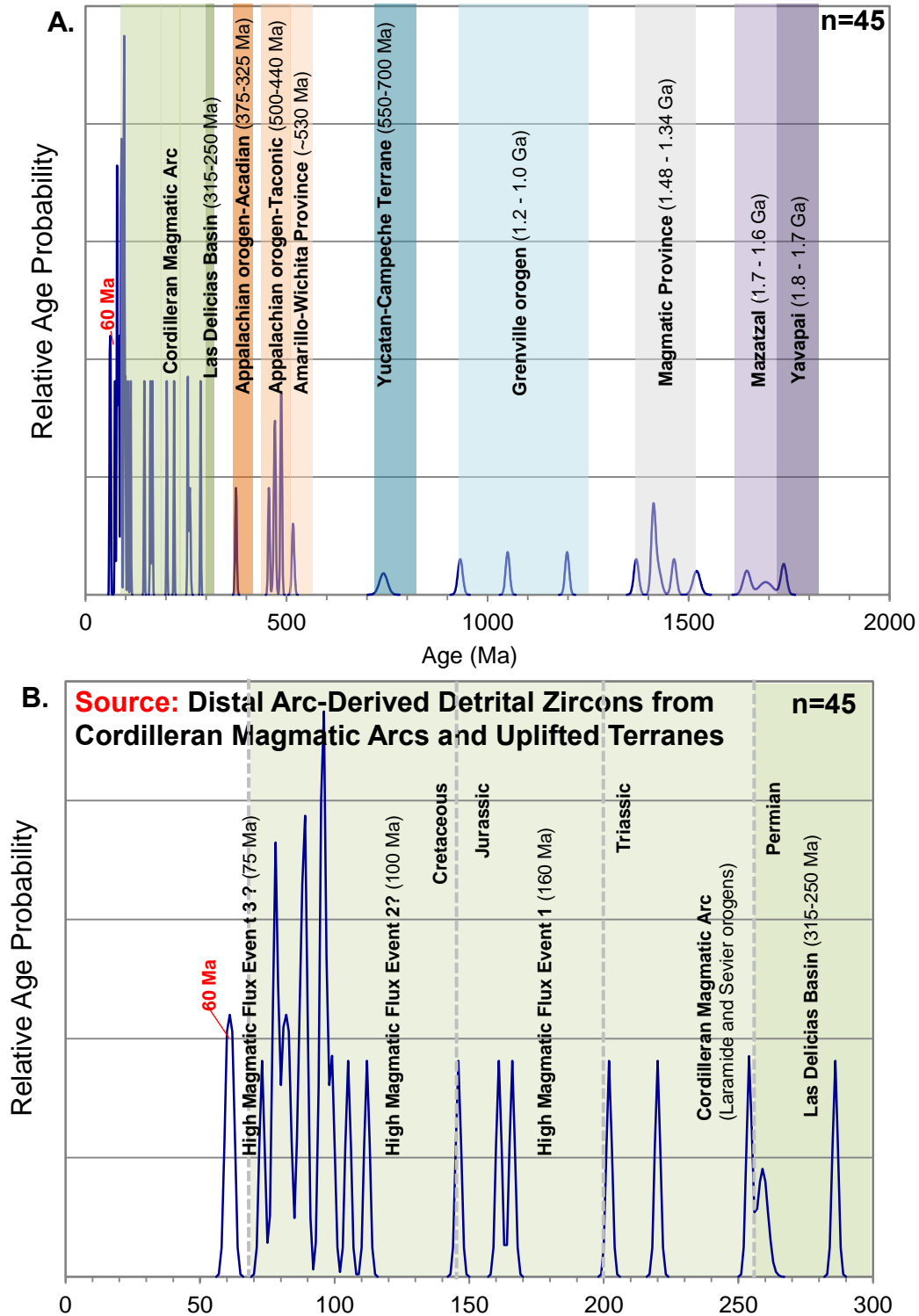


**Fig.4.7:** The maximum age of deposition is reported in this study as 60 Ma (at  $1\sigma$ ). **A.** Displays all age-peak contributions from sample analyses with suggested provenance, and **B.** Displays age-peak contributions from Triassic through Tertiary aged detritus. High magmatic flux events are expanded on in chapter discussion.

---

### iii. Canoe Formation

The Canoe Formation is classified as the basal unit of the Big Bend Park Group that contains all of the Tertiary volcanic rocks in Big Bend National Park consisting of, from base to top, the Canoe, Chisos, and South Rim Formations (Fig.4.2) (Maxwell *et al.*, 1967; Schiebout *et al.*, 1987). The formation consists of a basal massive yellow sandstone unit (the Big Yellow Sandstone Member) that consists of fine- to coarse- grained sandstone with a conglomeratic base that is 10-17 m thick (30-50 ft), purple and gray tuffaceous mudstone and claystone, gray- to whitish-gray nodular tuff, and a capping basaltic lava with a maximum thickness of about 350 m (1,050 ft) (Maxwell *et al.*, 1967; Lehman and Busbey, 2007). It has been noted by Maxwell *et al.* (1967) that "...there is some indication that the basal [Alamo Creek Basalt] of the western Chisos Formation may actually correlate with the uppermost Canoe Formation on the southwestern Tornillo Flat. If future geochronologic work reveals that, this contact should be revised, the Chisos-Canoe Formational contact will probably be placed at the base of the lowest basalt [member previously classified as the uppermost Canoe Formation]".

Although significant uncertainty persists, this study tentatively proposes that the capping basalt of the Canoe Formation be placed into the Alamo Creek Basalt Member of the Chisos Formation based on structural and stratigraphic field relations, as noted by Maxwell *et al.* (1967). This is a tentative proposition as no detailed petrographic, geochemical, or geochronological analysis and

---

comparison with the Alamo Creek Basalt flows has been implemented on the uppermost basalt unit in the Canoe Formation as of yet.



**Fig.4.8: A)** Field-photograph displaying sample locality of the capping basalt of the Canoe Formation (WTX-BB 22), and **B)** the detrital sample collected and analyzed from the Canoe Formation (WTX-BB 17).

Maxwell et al. (1967) previously documented the Canoe Formation to be resting unconformably on the Hannold Hill Formation despite its now known Bridgerian

---

stratigraphic age (50.3-46.2 Ma) as more recently determined by detailed paleontological work done initially by Wilson and Schiebout (1984).

The Canoe-Hannold Hill contact is interpreted here to be conformable based upon this stratigraphic age and the work of Schiebout (1970), Hartnell (1980), Rigsby (1982, 1986), Rapp (1983), and Schiebout et al. (1987) that indicate the basal Big Yellow Sandstone Member of the Canoe Formation is not demarcating an angular unconformity as Maxwell et al. (1967) has previously interpreted. These authors indicate the basal Big Yellow Sandstone Member is a channel in a fluvial system that displays discordancy typical of channels where observed by Maxwell and that his observation is related to incision of the channel in continuation of the fluvial environment represented in units below. Maxwell et al. (1967) in turn suggested that the boundary was associated with the cessation of compression related to the Laramide orogeny between the Hannold Hill Formation below and formations above, but the boundary rather represents a large braided stream deposit with a sheet-like geometry in the Tornillo Flat area. Paleocurrent indicators of the Lower Canoe Formation are exactly the same as the Black Peaks and Hannold Hill Formations, also indicating a similar fluvial source area (Schiebout *et al.*, 1987). The proposed small local erosional boundaries at the bases of the Black Peaks, Hannold Hill, and Canoe Formations are considered in this study as they were by Schiebout et al. (1987) to be part of the generally conformable fluvial system sequence with minor erosional surfaces typical of fluvial deposits that extends from the Cretaceous to Early Eocene.

---

The channel cut associated with the Big Yellow Sandstone Member is regarded in work done by Schiebout et al. (1987) and this study to be a local erosional scour surface associated with the braided-stream channel and not a regional feature representing the 'Laramide' angular unconformity. The paleocurrent indicators show a constant general flow direction from northwest to southeast throughout the Tertiary sections and the lithology changes within the formations represent a transition from high sinuosity stream systems to braided stream systems as the advancing magmatic arc and orogenic front caused uplift to occur at more proximal locations to the present-day Park. The volcanic sediment apron of the upper Canoe Formation defined by Rigsby (1982) reaches thicknesses of 344 m (1129 ft) and consists predominantly of tuffaceous beds, clay, tuffaceous clay, and sandstone with a transport direction toward the north to northeast that is interpreted to be a result of the Chisos Mountains in their early stages of uplift to the southwest (Rigsby, 1982; Schiebout et al., 1987).

A detrital (WTX-BB 17) and uppermost basaltic (WTX-BB 22) sample from the unit mapped as the Canoe Formation have been collected and analyzed from the Tornillo Flat in Big Bend National Park just south of Tornillo Creek along U.S. Route 385 (29.38329, -103.14992; 29.40491, -103.14036 respectively) (Fig.4.9; Fig.4.10). One hundred and ten zircon grains were separated from the detrital sample of the Canoe Formation and analyzed on the University of Houston's LA-ICP-MS. The age of the formation of detrital zircons was calculated from 50 analyses (n=50) using the DZ Age Pick Program from the University of Arizona LaserChron Center (Gehrels, 2007). The maximum age of deposition is reported

---

in this study as 47 Ma (at  $1\sigma$ ) from the youngest age-probability peak that consisted of contributions (at  $2\sigma$ ) from three analyses (Fig.4.10). This youngest age-probability peak plots toward the end of the reported Bridgerian (50.3-46.2 Ma) stratigraphic age for the Canoe Formation. The youngest single zircon age recorded at 2-sigma for the Canoe Formation is 47 Ma. The basal Alamo Creek Basalt of the Chisos Formation that rests directly on top of the Canoe Formation in some areas of the park is suggested to have been emplaced contemporaneously with the Canoe and has a groundmass concentrate  $^{40}\text{Ar}/^{39}\text{Ar}$  age of  $46.62 \pm 0.07$  (Miggins *et al.*, 2007). Based upon the work of Miggins *et al.* (2007) and ages of the Chisos Formation reported in subsequent chapters, it is suggested that the Chisos Formation must be younger than 46.6 Ma and that the upper Canoe Formation that did not span the entire Bridgerian was receiving detritus from more proximal volcanic sources at this time (47-46.6 Ma).

Similar to the Black Peaks and Hannold Hill Formations analyses, the majority of age-peak spectra from the detrital Canoe Formation analysis plotted within the six major provenance groups classified in a study done by Lakowski and others (Fig.4.13) (2013). Age-peaks that did not plot within the provenance groups classified by Lakowski and others (2013) were tentatively identified based on inferred regional tectonic events. The largest age-peak populations plot within the Triassic and Cretaceous periods and are most pronounced in the Late Cretaceous (Fig.4.10). The age-peaks from the Canoe Formation analysis document a more dominant proximal source of detritus that is also reflected in the facies change from braided stream channel sands in the Lower Canoe to

volcaniclastic fan sediments of the Upper Canoe. There is a higher population of peaks centered in the Permian suggesting a larger input from the Las Delicias arc and basin near Coahuila in northeastern Mexico (McKee and Anderson, 1988). The increased population of Permian aged detritus in the Canoe age-peak plot coincides with Liu and others (2010) paleoreconstruction indicating that the eastward migrating volcanic arc had reached the Trans-Pecos margin around ~47 Ma. This uplift and subsequent erosion associated with the migrating magmatic arc resulted in more proximal detritus sourcing.

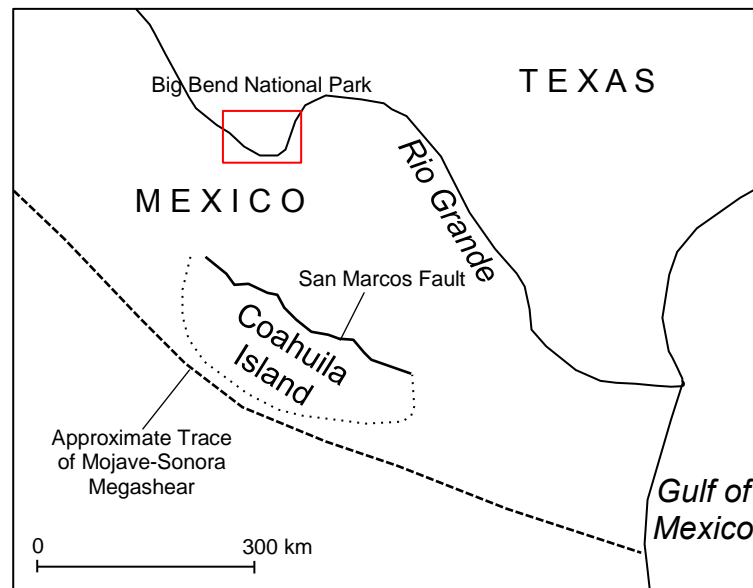


**Fig.4.9:** Location map displaying the location of Coahuila Island that contains exposures of the Las Delicias basin and arc terrane in relation to the West Texas margin. Modified from McKee and Anderson (1988).

Marine sedimentary rocks and mass-gravity flow deposits of Middle Pennsylvanian through Permian age accumulated in a basin adjacent to active arc volcanoes (McKee and Anderson, 1988) in northeastern Mexico. The basin is referred to as the Las Delicias basin and the volcanic arc that flanked it is known as the Las Delicias arc (McKee and Anderson, 1988). Exposures of the Las

---

Delicias basin are restricted to Coahuila island, a geographic feature comprised of Permian aged sediments of the basin bounded to the north by the San Marcos fault (Mckee *et al.*, 1984) and to the south by the Mojave-Sonora megashear (Anderson and Schmidt, 1983) that was uplifted in the Late Jurassic to Early Cretaceous time (McKee and Anderson, 1988). This study suggests that the initial uplift of the Las Delicias basin was associated with the eastward migrating Laramide deformation and magmatic arc during Laramide time. As the orogenic front advances toward the Trans-Pecos Texas margin, more proximal Permian detritus was shed off the uplifted Las Delicias basin and arc. This increased input is reflected in the younger Hannold Hill and Canoe Formations and serves as a record for the paleoposition of the deformation and uplifted orogenic front from nearby delivering Permian zircon from proximal sources in Mexico. The Alamo Creek Basalt ( $^{40}\text{Ar}/^{39}\text{Ar}$  age of  $46.62 \pm 0.07$  Ma) that rests directly on top of the Canoe Formation in some areas of the park is suggested to have been deposited contemporaneously with the Canoe and is thought to be a potential proximal source for the zircon grains found in the detritus in addition to distal volcanism associated with the incoming arc (Miggins *et al.*, 2007).

A doubly-plunging syncline axis referred to as the Tornillo Flat Syncline in this study not previously documented on the northeastern Tornillo Flat just north of Tornillo Creek involves folding of Black Peaks, Hannold Hill, and Canoe Formations. The fold axial trend is oriented in the same overall trend as the Mariscal Mountain Anticline, ascribed to as a major Laramide-style deformational feature (Fig.4.10,4.11) (Muehlberger, 1989; Lehman *et al.*, 1991; Harlan *et al.*,

---

1995). This provides evidence of compression related to the Laramide orogenic forces actively affecting the Eocene and Early Oligocene formations in the Big Bend National Park region following the deposition of the Black Peaks, Hannold Hill, Canoe, and Chisos Formations. The western limb of the fold strikes N 45°W and N 42°W and dips to the northeast at an angle that varied along the fold axis from 8-11°. The eastern limb of the fold is striking N 62°W and N 60°W and dips to the southwest at a slightly higher angle that varied from 10-14° with decreasing proximity to the fold axis. These measurements are plotted on a stereonet in Figure 4.11.

The fold axis of the Tornillo Flat Syncline may have experienced minor affects associated with Basin and Range extensional and intrusion reorientation, but trends at N 34°W and varies within 16° degrees of the Mariscal Mountain Anticline which trends at N18°W as documented by Harlan et al. (1995) and Turner et al. (2011). This indicates that they are likely correlative Laramide compressional fold structures with deformation dates as Oligocene in age based on folding of the youngest strata reported in this Chapter. Tilting of the strata is also present at the edge of igneous intrusions in the area, but axis of tilting conforms to the edge of the intrusion and varies around the intrusion contacts. The conformance of fold trends with known Laramide fold structures in the area indicates that the fold documented here is a Laramide-style compressional feature that formed coevally with the Mariscal Mountain Anticline.

## Canoe Formation: WTX-BB 17 Detrital Zircon Analyses

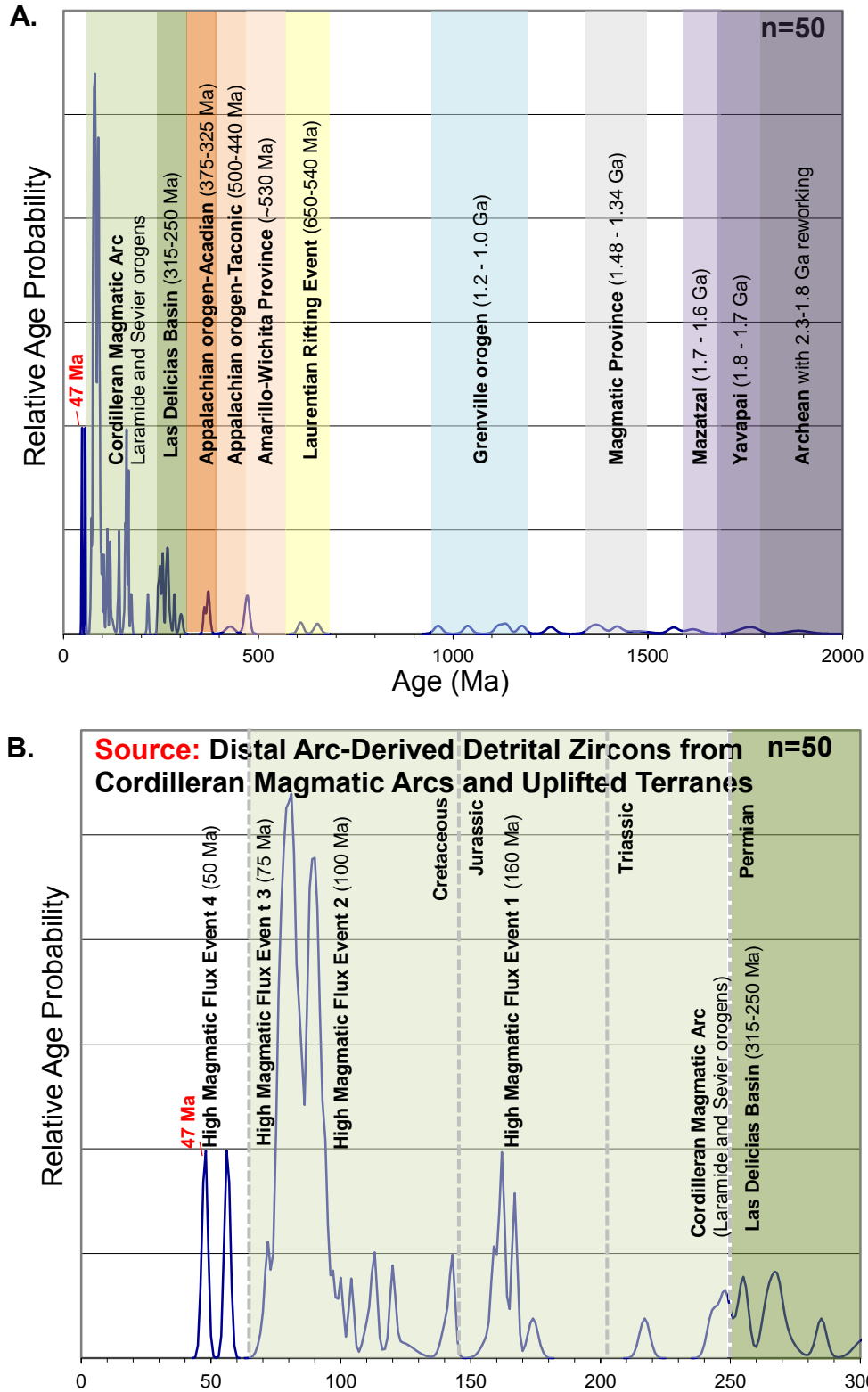


**Fig.4.10:** The maximum age of deposition is reported in this study as 47 Ma ( $1\sigma$ ) **A.** Displays all age-peak contributions from sample analyses with suggested provenance, and **B.** Displays age-peak contributions from Triassic through Tertiary aged detritus. High Magmatic Flux Events are expanded on in discussion.

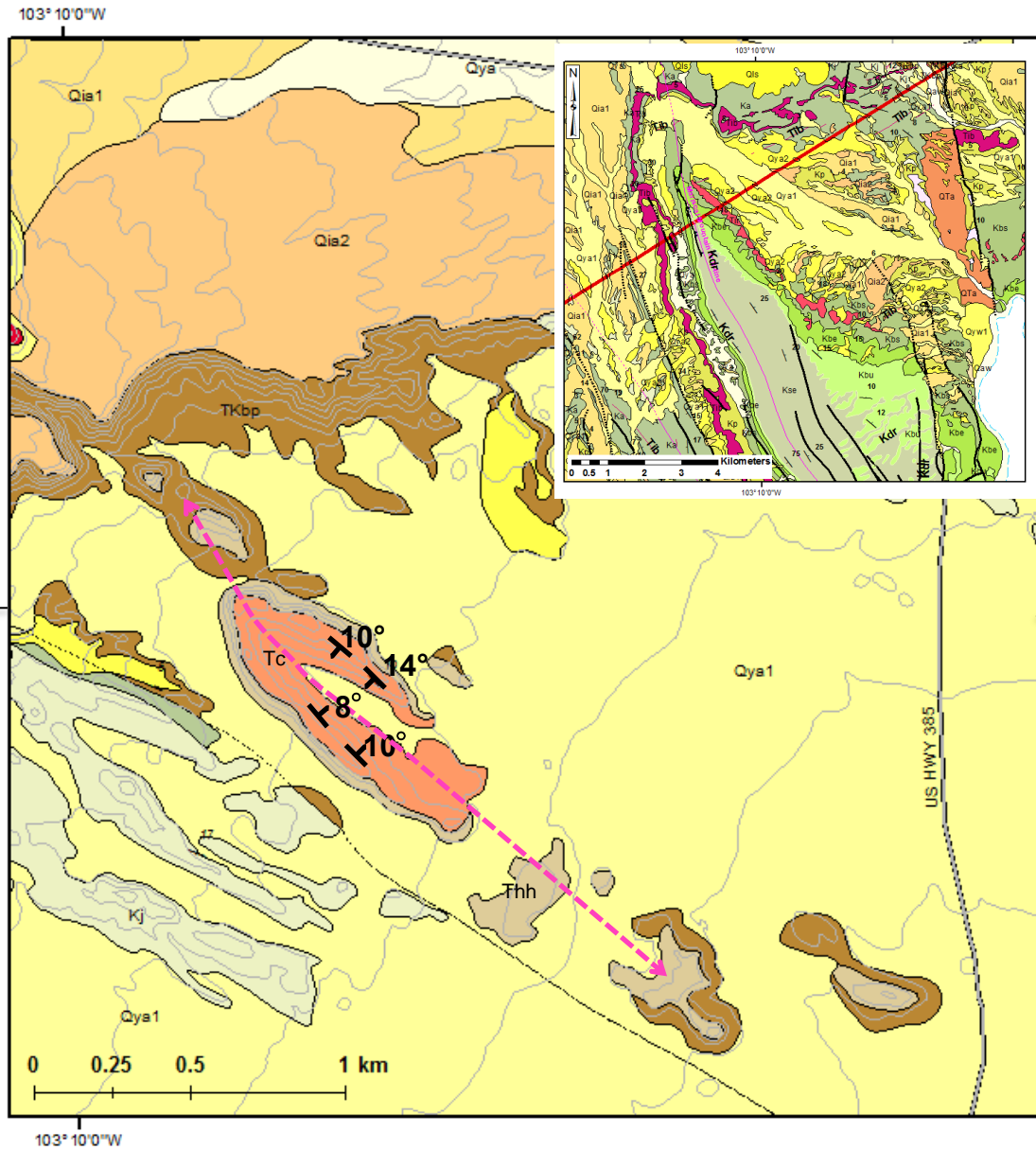
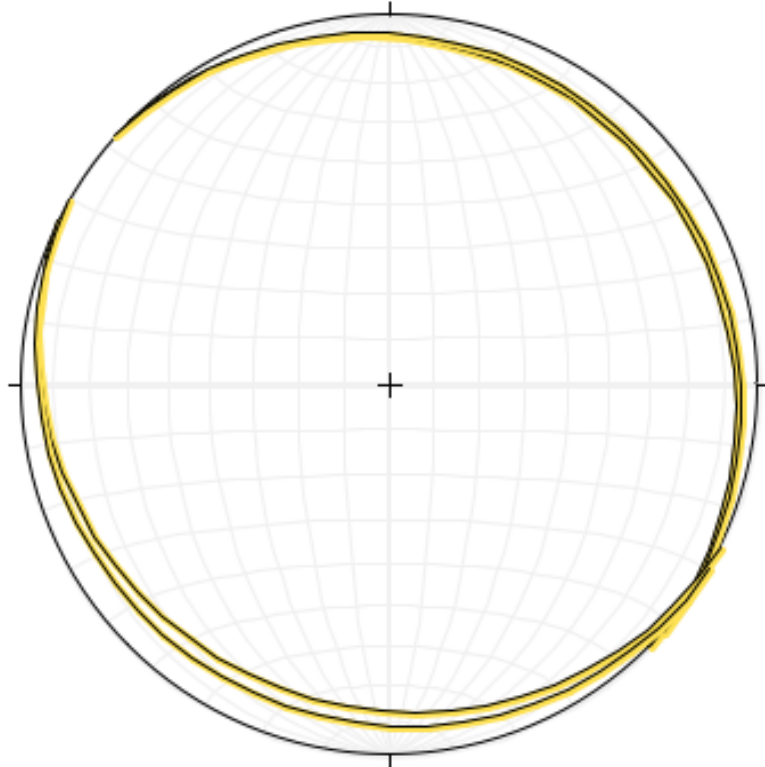


**Fig.4.11:** Map displaying the location of the double-plunging syncline affecting the Hannold Hill (Thh) and Canoe (Tc) Formations on the Tornillo Flat in Big Bend National Park in relation to U.S. State Highway 385. Figure 4.3 serves as another reference map as it displays the syncline in relation to the Black Peaks Formation (WTX-BB 15) sample location. The hinge line has been marked on this map as a dashed pink line with arrows indicating its NW-SE plunging geometry. Strike and dip measurements recorded in this study have been added to each limb of the fold to better demonstrate the geometry of the fold. Inlay of the Mariscal Mountain Fold has been provided to show similarities in fold trend axes. Modified from Turner et al. (2011).

---

### Stereonet of the Tornillo Flat Syncline Measurements



Beta Axis of Tornillo Flat Syncline  $326^\circ$ , Plunge:  $2^\circ$   
**vs.** Trend of Mariscal Mountain Anticline  $342^\circ$ , Plunge:  $11^\circ$   
**Trend Variation:  $16^\circ$**

**Fig.4.12:** Stereonet displaying the measurements taken on the west and east limbs of the syncline discussed in the text versus the measurements for the Mariscal Mountain Anticline made by Harlan et al. (1995).

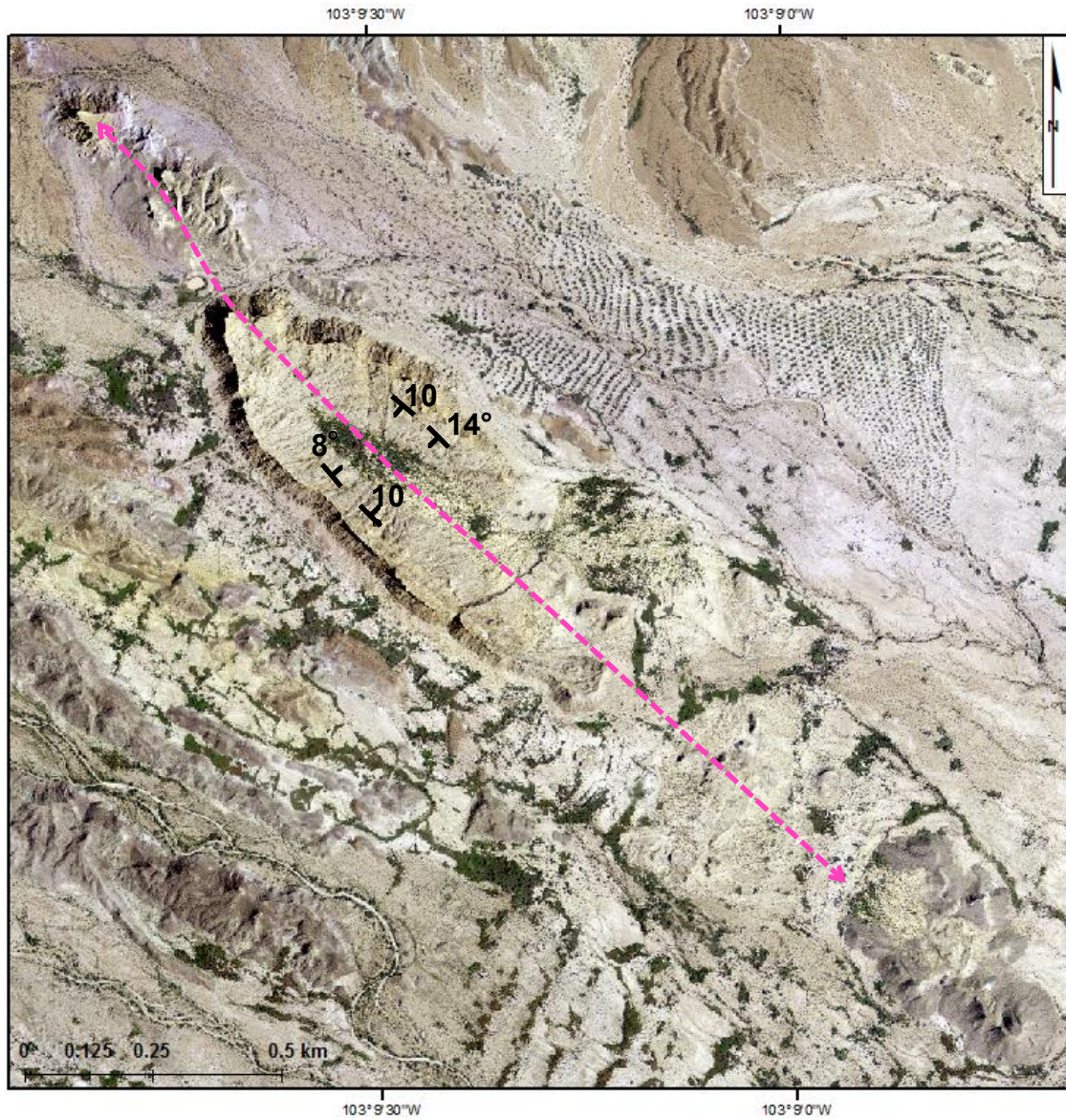


**Fig.4.13:** High resolution aerial image displaying the location of the doubly-plunging syncline affecting the Hannold Hill and Canoe Formations on the Tornillo Flat in Big Bend National Park. The hinge line has been marked on this map as a dashed pink line with arrows indicating its NW-SE plunging geometry . Strike and dip measurements recorded in this study have been added to each limb to better demonstrate the geometry of the fold. Orthoimagery data collected from USGS:The National Map Viewer .

---

#### iv. Discussion

Condie and Aster (2009) state that the relative abundance of specific ages within sufficiently populated detrital zircon data sets can be used to identify the timing of magmatic and accretionary processes. This approach is particularly relevant in understanding ancient supercontinent cycles at the continental scale (Lakowski *et al.*, 2013). Numerous studies executed by Rainbird and others (1992), Dickinson and Gehrels (2003, 2009), Stern and Dickinson (2010), Lier and Gehrels (2011), and LaMaskin (2012) have shown that variations in detrital zircon age spectra track the long-term distribution of orogenic belts, Andean-type magmatic arcs, and sediment dispersal systems. These studies have indicated that detrital zircons can resolve crustal recycling within individual orogenic systems, and have successfully linked synorogenic strata to specific orogenic clastic wedge structures in the North American Cordillera (Lakowski *et al.*, 2013). Lakowski *et al.* compiled 8,717 U-Pb analyses from 95 detrital zircon samples of Jurassic-Eocene North American Cordillera foreland basin strata that record erosion or recycling of basement and cover rocks within the Cordilleran orogenic wedge. Variation in the detrital zircon age spectra from samples compiled by Lakowski *et al.* (2013) is similar to the Black Peaks, Hannold Hill, and Canoe Formations analyses, with some exceptions in detailed distribution and age provinces.

Laurentian craton is comprised of accretionary Archean (>1.8 Ga) continents and continental fragments that came together during the Trans-

Hudson orogeny in the Paleoproterozoic (2.0-1.8 Ga) (Hoffman, 1988).

Throughout the Proterozoic multiple collisional events (1.7-1.30 Ga) accreted

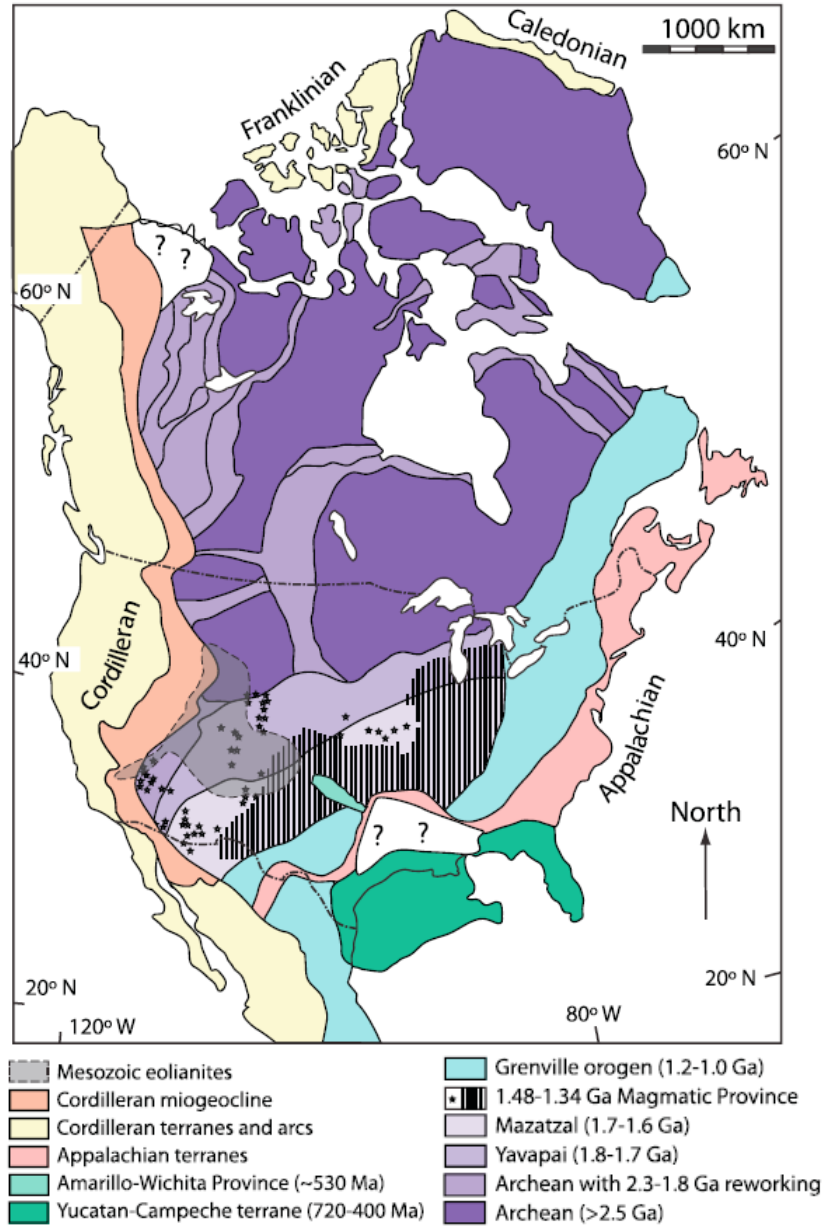


**Fig.4.14:** Location of North American crustal provinces delineated by Lakowski and others (2013) that may have supplied detrital zircons to the Cordilleran retroarc foreland basin system that served as provenance sources for the Black Peaks, Hannold Hill, and Canoe Formations analyzed in this study.

juvenile terranes to the cratonal core that are comprised mostly of Yavapai (1.8-1.7 Ga), Mazatzal (1.7-1.65 Ga), and Grenville (1.2-1.0 Ga) rock (Fig.4.13). The

---

Yavapai and Mazatzal provinces were later intruded by plutons associated with an A-type magmatic event following their accretion between 1.48 and 1.34 Ga (Van Schmus *et al.*, 1996). These processes and assemblage events created a stable Laurentian craton and platform composed of distinct crustal age provinces (Fig.4.14). Late Jurassic provenance was dominated by recycling of volcanic rock associated with the incoming magmatic arc and orogenic front in addition to Mesozoic eolianites from sources in the Sevier fore deep and Colorado Plateau (Stern and Dickinson, 2010). Late Cretaceous to Eocene provenance was dominated by recycling of the Sevier fore deep, Black Mesa Basin, San Juan Basin, Mogollon Highlands, Cordilleran magmatic arc, and Yavapai-Mazatzal, which were locally exposed in the Sevier belt and newly formed Laramide intraforeland province near the Four Corners (~85 Ma) (Decelles, 2004; Stern and Dickinson, 2010; Fuentes *et al.*, 2012). These age signatures are reflected and subsequently classified in the Black Peaks, Hannold Hill, and Canoe Formation analyses (Fig.5A, 8A, 12A).

The transitions in provenance record a basin-wide uplift and compressional deformation sequence that is suggested to have occurred in response to periodic high-flux magmatism in the Cordilleran arc as progressive inboard migration occurred (Lakowski *et al.*, 2013). The oldest Cordilleran magmatism along the western margin of North America initiated with subduction beneath the truncated margin during Middle to Early Triassic time (Dickinson, 2000). The majority of Cordilleran magmatism intruded elongate zones located 100-250 km inboard of the arc-trench system, characterized today by a

---

discontinuous belt of deeply exhumed granitic batholiths of Middle Jurassic to Early Eocene age (Dickinson, 2000; Lakowski, 2013). The timing of emplacement of the Idaho, Montana, Sierra Nevada, Coast Mountains, and Cascade Batholiths coincide with what Lakowski *et al.* (2013) interpret as four cyclic high magmatic flux events (HFEs) in the Cordilleran magmatic arc responsible for marked uplift and increased erosion throughout the Middle Jurassic to Early Eocene (Lakowski *et al.*, 2013). According to Lakowski *et al.* (2013), these HFE peaks occur at ~160, ~100, ~75, and ~50 Ma. The HFE peaks occurring at ~160, ~100, and ~50 Ma are reflected in the detrital analyses reported in this study and have been identified in the Black Peaks, Hannold Hill, and Canoe Formation plots (Fig.5A, 8A, 12A).

High-flux magmatism varies according to changes in the convergence rate between two interacting plates (Fig.4.15) (Decelles *et al.*, 2009). Periods of high convergence correlate with increased activity in the Cordilleran magmatic arc and are reflected in the relative abundance of detrital zircon in the retro arc region (Lakowski *et al.*, 2013). The convergence rate between the Farallon and North American plate remained fairly slow and constant between ~160-100 Ma at between 20 and 75 km/my, resulting in a ~60 Ma recurrence interval between the first two prominent HFEs at ~160 and ~100 Ma (Engebretson, 1984; Ducea and Barton, 2007; Decelles *et al.*, 2009). Lakowski *et al.*'s (2013) data indicates there is a reduction of the HFE recurrence interval from ~60 to ~25 my after ~100 Ma as a result of an increase in overall magmatic flux coinciding with increased

convergence rates of  $\sim 100$  km/my in the Cretaceous (Fig.2.1, Fig.4.15) (Engelbreton, 1984).

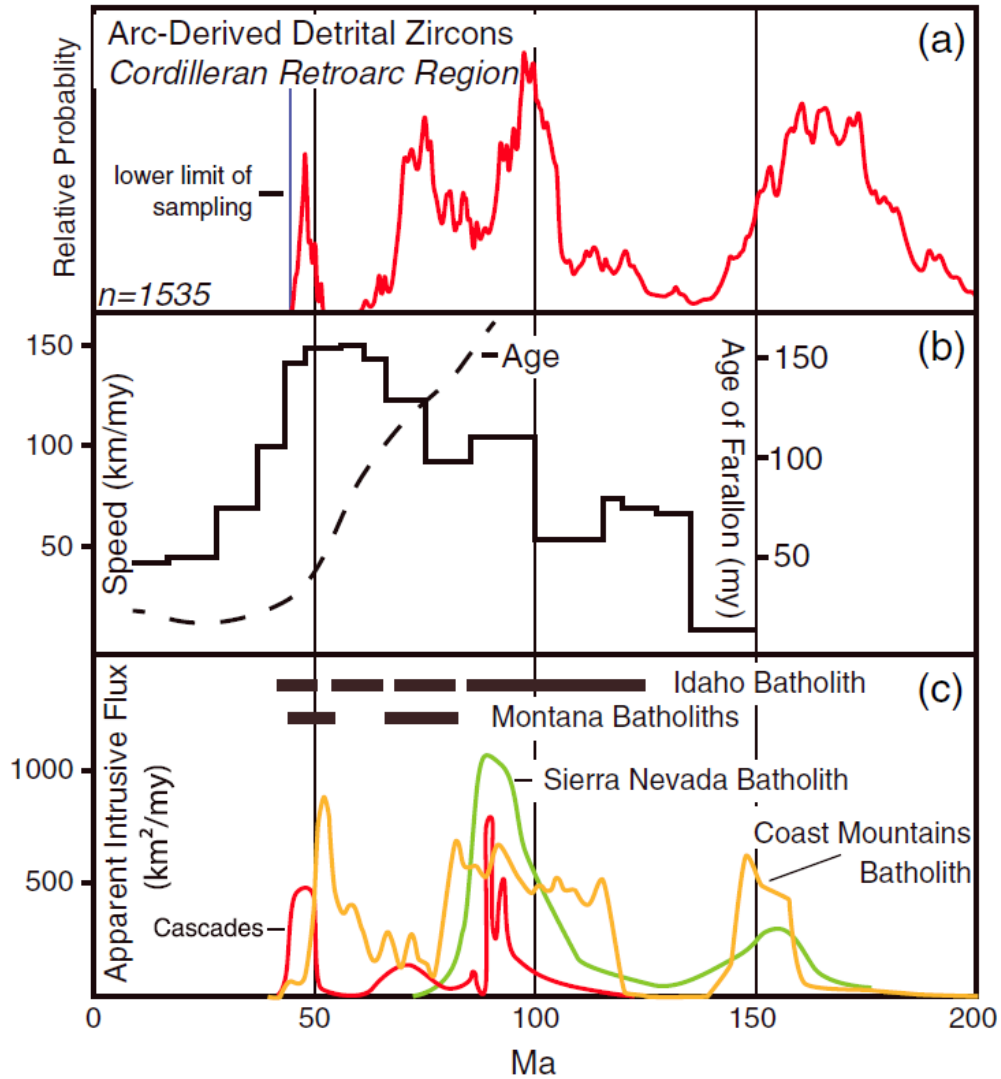


**Fig.4.15:** A. Probability distribution function of arc-derived detrital zircons in Lakowski *et al.* study (2013). B. Velocity and age of the Farallon plate at the subduction interface from Engelbreton (1984). C. Relative magmatic flux curves from exposures of igneous rock along the Cordilleran magmatic arc including the Coast Mountains Batholith (yellow) (Gehrels *et al.*, 2009), Sierra Nevada (green) and Cascades Batholith (red) (Patterson *et al.*, 2011). Lakowski *et al.*, 2013

The compiled analyses of the Jurassic-Eocene North American Cordillera foreland basin strata were plotted against the Farallon-North American plate velocity of the Farallon oceanic lithosphere at the subduction interface (Engelbreton, 1984), and flux curves of the batholiths (Lakowski *et al.*, 2013).

---

Detritus age peaks, increased convergence, and the relative flux curves of batholiths display strong covariance with one another (Fig.4.15) (Lakowski *et al.*, 2013). When the age-peak data of the three analyses from this study were combined they displayed a similar trend to Lakowski *et al.*'s (2013) compiled arc-derived detrital zircons with one marked difference (Fig.4.17). The data obtained in this study appears to fill a pronounced gap between Lakowski *et al.*'s (2013) proposed HFEs occurring at ~100 and ~75 Ma. This indicates that there was likely no lull between high frequency magmatism events at 100 and 75 Ma, and that high frequency magmatism was nearly constant throughout the Cretaceous interval (~100-75 Ma). This study interprets the lull in magmatic activity between ~100 and ~75 Ma in Lakowski *et al.*'s data to be a result of an inboard shift in the focus of volcanism that surpassed the westward extent of Lakowski *et al.*'s samples which span from Canada to the northwestern portion of New Mexico near the Four Corners region (Fig.4.16).

This indicates that the high magmatic flux events, associated uplifts, and subsequent North American Cordillera foreland basin strata sampled in their study may only reflect detritus associated with the incoming Shatsky Rise conjugate plateau that is estimated to have entered the trench at ~88 Ma with a northeast trajectory (Liu *et al.*, 2010). The foreland basin depocenters spanning from Canada to the Four Corners region during the Cretaceous, while still serving as potential sources for detritus in age peak spectra in this study, were more than likely restricted in part by the southwardly advancing Cretaceous Seaway and cutoff from detritus associated with the incoming Hess Rise conjugate plateau

---

that entered into the trench south of Shatsky at ~65 Ma with a more eastward trajectory (Liu *et al.*, 2010).

The results in this study indicate that only three magmatic flux events are reflected in a full compilation of arc-derived detrital zircons from Canada to southern Texas as opposed to four high magmatic flux events identified by Lakowski *et al.* (2013) (Fig.4.17). The age-peaks of the detrital zircons found in the Black Peaks, Hannold Hill, and Canoe Formations record the progression of the incoming magmatic arc associated with the southern eastward advancing Hess Rise conjugate plateau during the Laramide orogeny. In addition to providing a maximum depositional age that coincides with stratigraphic and chronostratigraphic age correlations, variations in distal to more proximal Permian detritus from the Las Delicias basin in northeastern Mexico are present and more pronounced in each progressively younging formation. In addition, the zircon age-peak spectra becomes closer to the maximum depositional ages of the progressively younger formations suggesting volcanic sources are getting closer to the basin and contributing more directly to the detritus.

Further support for this interpretation, and evidence for continuous high magmatic flux throughout the Cretaceous is documented in a U-Pb detrital zircon study from the Paleocene-Eocene Wilcox Group in south Texas (Mackey *et al.*, 2012) that reveals a complex grain assemblage with major populations identical to the age-peak spectra from the composite Black Peaks, Hannold Hill, and Canoe Formations in this study (Fig.4.17). A composite normalized U-Pb diagram of the 10 samples analyzed from the fluvial-deltaic Wilcox Group reveals

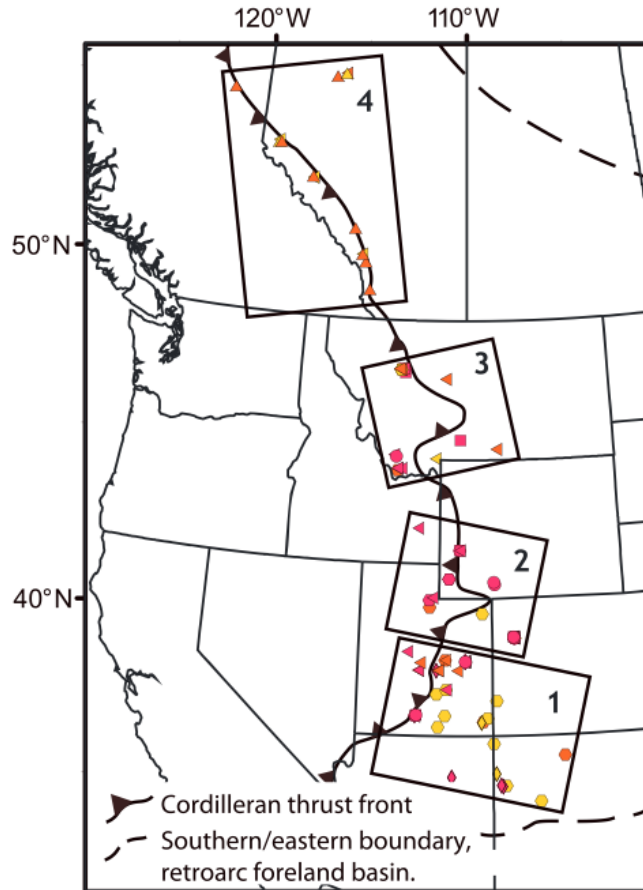


**Fig.4.16:** Location of detrital zircon samples and boundaries of the four sampling regions, including the Four Corners, Uinta, Montana, and Canada in Lakowski *et al.*'s study.

an identical trend of provenance detritus as the age equivalent samples analyzed in this study (Mackey *et al.*, 2012). This suggests that the same diverse provenance assemblage from the southern United States Cordilleran magmatic arc and proximal Permian detritus sources from northern Mexico including the Las Delicias Basin and Late Cretaceous Difunta Group were being transferred from the northwest and west to the southeast via fluvial systems throughout the Cretaceous during Laramide compressional deformation and uplift (Fig.18).

## Compiled Detrital Data: Black Peaks, Hannold Hill, and Canoe Formations

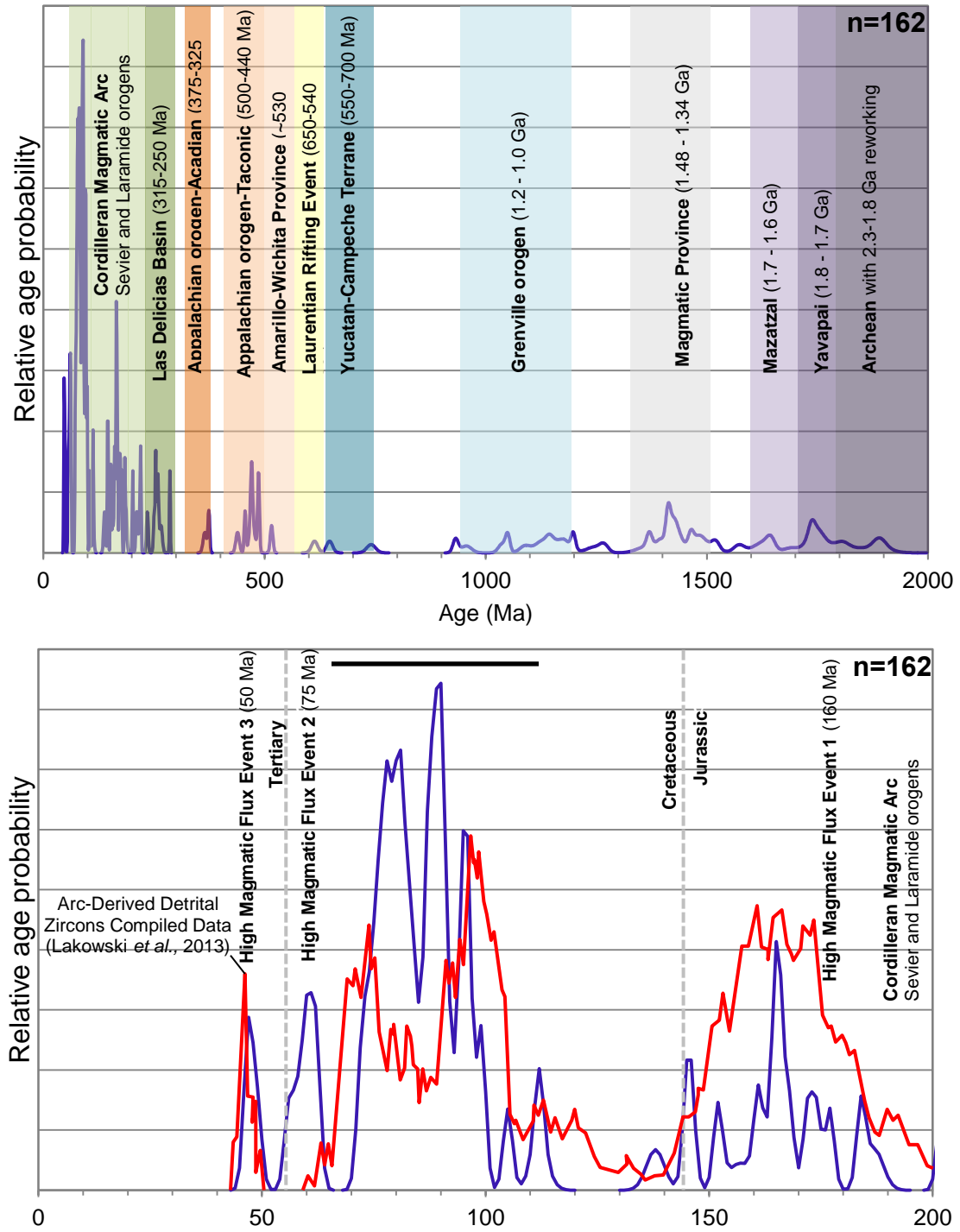


**Fig.4.17:** Combined detrital analyses from the Black Peaks, Hannold Hill, and Canoe Formations **A.** Displays all age-peak contributions from sample analyses with suggested provenance, and **B.** Displays age-peak contributions from Jurassic through Tertiary aged detritus analyzed in this study (Blue) in relation to those provided by Lakowski *et al.*'s (2013) detrital analyses for outcrops in northeastern New Mexico and further west (Red). The addition of data from this study occupies a pronounced gap between ~100 Ma and ~75 Ma previously expressed as two high magmatic flux events. This suggest that high magmatic flux was constant throughout the Cretaceous period during the Laramide orogeny, but likely shifted eastward in focus and did not contribute to the more western basins sampled by Lakowski *et al.* (See map of sample localities from Lakowski *et al.*, 2013 (Fig.17))

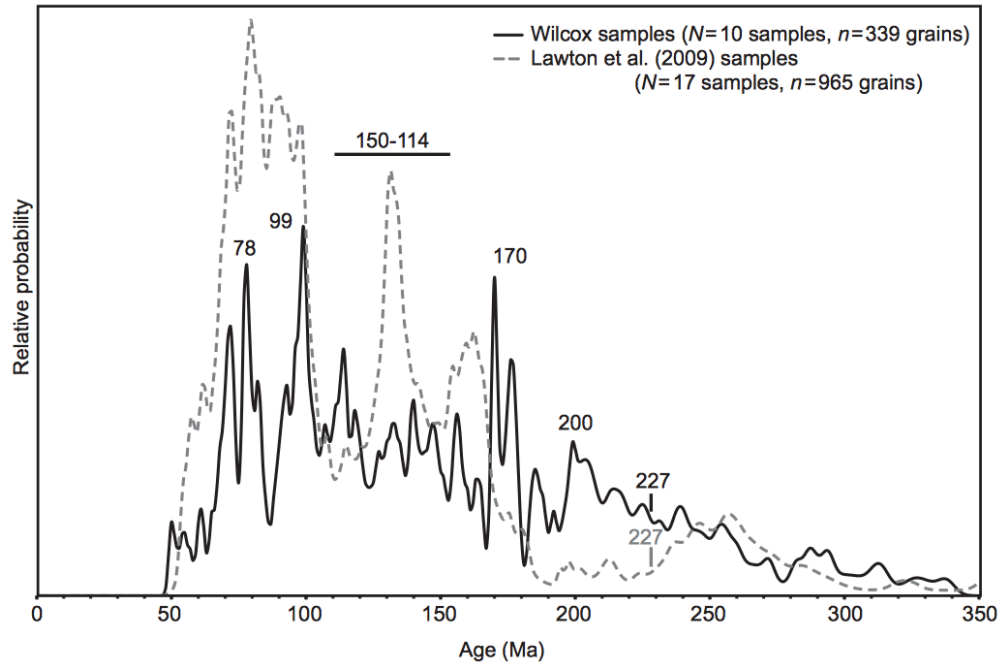


**Fig.4.18:** Composite normalized U-Pb age probability plot for the Wilcox Group (Mackey *et al.*, 2012) plotted against samples of the Sierra Madre Oriental foreland basin strata (Lawton *et al.*, 2009) parallel the compiled analyses from this study. The Sierra Madre Oriental foreland basin strata of the Di Funta Group from Mexico analyzed by Lawton *et al.* (2009) has a similar age-peak spectra trend to the data in this study, whereas the Wilcox samples analyzed by Lackey *et al.* (2012) display a more similar analysis trend to Lakowski *et al.* (2013). These variations in age-peak spectra reflect active source areas from north to south into Central America throughout the Laramide orogeny.

---

**Chapter 5:**  
**Volcanic Results and Implications****a. Introduction**

This chapter describes the geology of the Tertiary volcanic rocks above and below the 'Laramide' angular unconformity exposed in the Trans-Pecos Texas igneous province. Geochronologic data, geochemical data, and details of structural relationships and the nature of angular unconformities at each site documented in this study and previous studies are reported and compared in this chapter. The basal flat-lying volcanic deposits above the angular unconformity, unaffected by thrust faults and folds that are interpreted to be the result of Laramide compression in West Texas provide an upper limit for the age of cessation of Laramide-style compressional deformation. In addition, the basal flat-lying volcanic units record the initiation of emplacement of ignimbrite flare-ups following the flat-slab orogenic period and the associated transition to steep slab roll-back or detachment of the subducted Farallon slab.

If accessible, a sample from the highest volcanic unit in each regions stratigraphy was collected in addition to the basal flat-lying volcanic deposits and analyzed to assess the age of duration of the entire volcanic sequence in West Texas. At one site in the Indio Mountains, the age of the entire sequence of ignimbrite flare-up deposits was measured and established marked regional variations when compiled with other ages collected in this study. GPS locations of each sample site are provided in the sections below

---

within  $\pm 11$ -15 meters. Successful U-Pb zircon ages obtained in this study are reported here. The Square Peak Group volcanic rocks of the Quitman Mountains, Star Mountain Rhyolite of the Davis Mountains, and Burro Mesa Formation of the Chisos Mountains were analyzed in this study but failed to meet criteria and discordance limits for successful age dating due to Pb-204 contamination and abundant Proterozoic aged inherited cores.

Geochemical and geochronologic data from previous studies for these formations have provided age constraints that are utilized in this study to better assess the timing of emplacement of the volcanic rocks and duration of post-unconformity subduction-related volcanism. Unlike detrital zircon geochronology, only 15-25 individual zircon analyses are necessary to obtain a reliable formation age. Zircon grains separated and collected from each volcanic sample were analyzed on the University of Houston's Varian 810 LA-ICP-MS. Two grains of the Fc5z and Plesovice zircon standards were analyzed between every five sample zircon grains to monitor and correct for instrumental drift. Ages were calculated from the  $^{206}\text{Pb}/^{238}\text{U}$  and  $^{207}\text{Pb}/^{235}\text{U}$  ratios and their uncertainties (at  $2\sigma$ ). The data used for age calculations can be found in the Appendices starting on p.184 of this manuscript.

---

## **b. Eagle Mountains**

The Eagle Mountains are a northwest-trending block fault range approximately 27 km (16.7 mi) long and 10 km (6.2 mi) wide located 27 km (16.7 mi) southwest of Van Horn, Texas in Hudspeth County (Fig.5.1) (Underwood, 1980; Zamzow, 1983). The summit of the Eagle Mountains is Eagle Peak, and at 2,285 m (7,500 ft) above sea level it is the highest elevation in Hudspeth County (Underwood, 1962). Exposures in the Eagle Mountains range from Precambrian to Recent, including a 1,525 m (5,000 ft) section of low- grade metamorphosed Precambrian rock of the Carrizo Mountain Formation (King and Flawn, 1953). King and Flawn (1953) mapped five unnamed units of the Carrizo Mountain Formation that are exposed in the Eagle Mountains that consist of a meta-arkose, metaquartzite, schist, phyllite, and limestone. The Hueco Limestone is Permian in age and rests unconformably on the Precambrian Carrizo Mountain Formation (Underwood, 1980).

The exposed basal Powwow Conglomerate and overlying Hueco Limestone reach a maximum thickness in this region of approximately 300 m (900 ft). The conglomerate and limestone record the transgression of the Permian sea onto the Diablo Platform to the northeast during the Wolfcampian Epoch (299-280 Ma) (Henry and Price, 1986). Nearly 2,135 m (7,000 ft) of Cretaceous marine strata that range in age from Late Aptian to Middle Turonian (112-91 Ma) disconformably overlie the Permian Hueco Limestone including, in ascending order, the Yucca Formation, Bluff

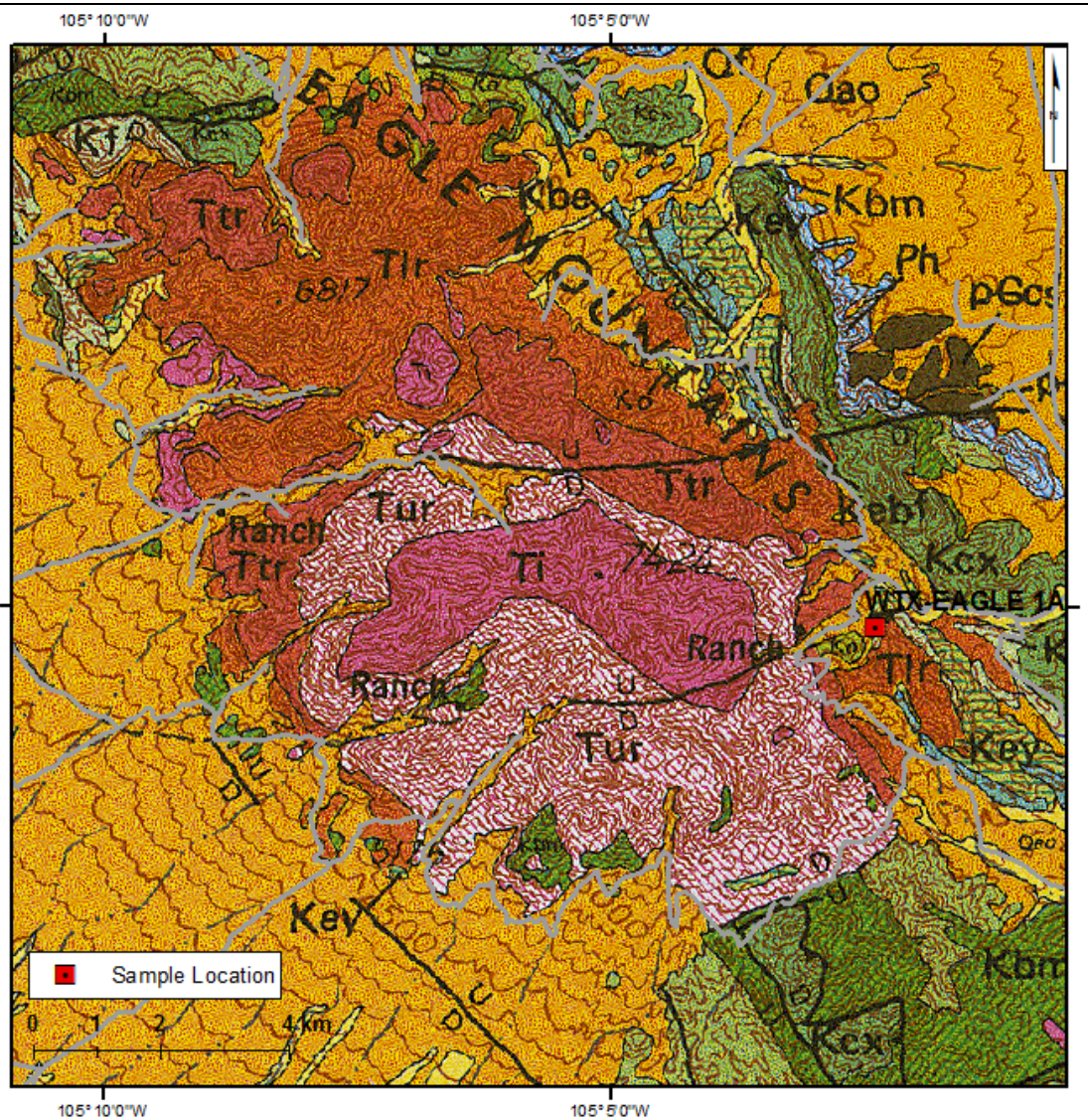


**Fig.5.1:** The Eagle Mountains located in Hudspeth County and sample location of the Lower Rhyolite (Tlr) (WTX-EAGLE 1A) on the southeastern flank of the mountain. Other volcanic units include the Trachyte Porphyry (Ttr) and Upper Rhyolite (Tur) in addition to the Tertiary intrusive rock (Ti) exposed higher in the stratigraphy near Eagle Peak. Modified from Barnes et al. (1979).

Formation, Cox Sandstone, Finlay Limestone, Benevides Formation, Espy Limestone, Eagle Mountains Sandstone, Buda Limestone, and Chispa Summit Formation (Fig.5.2) (Underwood, 1962). The Cretaceous stratigraphy was controlled by a fluctuating shoreline during the general advance of the Cretaceous sea northeastward from the Chihuahua Trough in Mexico onto the Diablo Platform and North American continental margin (Underwood,

1980).

TOP NOT EXPOSED					
CRETACEOUS	Upper Cretaceous	Cenomanian	Tur.		
			Chispa Summit Formation	Thickness (m)	
			305		
	Lower Cretaceous	Upper	Albian	Buda Limestone	66
				Eagle Mts. Sandstone	24
		Middle	Albian	Espy Limestone	333
				Benevides Formation	37
				Finlay Limestone	122
		Lower	Albian	Cox Sandstone	386
				Bluff Formation	243
Aptian		Yucca Formation	616		
BASE NOT EXPOSED (FAULTED)					

**Fig.5.2:** Stratigraphic column displaying the Cretaceous geologic formations exposed in the Eagle Mountains. Modified from Underwood (1980).

The Cretaceous and Permian aged formations exposed in the Eagle Mountains and vicinity contains abundant thrust faults and folds that record intense deformation that occurred throughout the Laramide orogeny.

The Late Cenomanian to Turonian aged Chispa Summit Formation is the youngest exposed formation to display Laramide-style deformation in the Eagle Mountains and vicinity (Twiss, 1959b; Underwood, 1962).

The deformation and uplift resulting from the Laramide orogeny accelerated erosional rates throughout the Cenozoic as a result of the incoming buoyant Hess plateau reaching the present-day border. This tectonic activity

is estimated by Underwood (1980) to have maintained a relief of less than 300 m (900

ft) in this area with a relief of no more than 150 m when the volcanic rock was erupted. The dominant north-northwest structural trend of Laramide-style folds and thrust most likely controlled the topography of the erosional surface on which the volcanic rock was deposited. The irregular distribution of volcanic rock in the Eagle Mountains reflects this uneven erosional surface at

the time of emplacement (Underwood, 1980).

The flat-lying eruptive rocks of the Eagle Mountains lie above an angular unconformity and therefore are deposited after the cessation of contraction and the Laramide orogeny in the area. They are sodic rhyolitic and trachytic rocks including, in ascending order, the Lower Rhyolite/ Carpenter Canyon Tuff, Trachyte Porphyry/ Frenchman Canyon Trachyte, and Upper Rhyolite/ High Mill Tuff (Table 5.1) (Hoffer *et al.*, 1980; Underwood, 1980). The volcanic rocks of the Eagle Mountains are an intra-caldera facies of two eruptive cycles with each cycle producing rhyolitic ash-flow tuffs followed by trachytic volcanism (Zamzow, 1983). The Lower Rhyolite and Trachyte Porphyry represent the first eruptive cycle and the

Formation Name		Thickness (m)	Lithologic Description
Upper Rhyolite	High Mill Tuff	265 to 600	
	- Eagle Bluff Member	0 to 200	Lithic welded tuff
	- Cottonwood Canyon Member		
	Cottonwood Canyon Tuff	265 to 400	Densley welded tuff
	Silver Eagle Tuff	10 to 15	Moderately welded tuff
	Epicastic Unit	0 to 13	Crystal ash-fall tuff
Trachyte Porphyry	Frenchman Canyon Trachyte	0 to 500	Welded tuffs and lava flows
	- Upper Unit	130 to 400	Devitrified trachyte lava flows
	- Lower Unit	0 to 130 m	Densley welded tuff
Lower Rhyolite	Carpenter Canyon Tuff	25 to 330	
	- Panther Peak Member	10 to 330	Welded tuff with well-developed eutaxitic texture
	- Indian Springs Member	25 to 135	Poorly welded ash-flow and air-fall tuffs with locally abundant lithic fragments

**Table 5.1:** Volcanic stratigraphy of the western Eagle Mountains; Table modified from Gillerman (1953), Leggett (1979), Verrillo (1979), and Hoffer and others (1980). Formation names in the far left column reflect those of Gillerman (1953) and the formation names in the right column were later classified by Leggett (1979) and Veal (1979).

Upper Rhyolite and intrusive Eagle Peak Syenite (Gillerman, 1953) represent the second (Zamzow, 1983). A vent or vents have not been identified, however the volcanic rocks of the Eagle Mountains are suggested to be from a local source and a caldera is believed to have formed during each eruptive

---

cycle with subsidence occurring during both periods of eruptive activity (Underwood, 1980; Zamzow, 1983). The basal Lower Rhyolite (rhyolitic ash-flow tuff), informally known as the Carpenter Canyon Tuff, was analyzed in this study and is composed primarily of rhyolitic ash-flow tuffs with minor components of air fall tuffs and tuffaceous sandstones (Zamzow, 1983).

### **i. Lower Rhyolite**

The Lower Rhyolite was first identified by Gillerman (1953) and later reclassified as the Carpenter Canyon Tuff by Legett (1979) and Verrillo (1979). It consists of a sedimentary rock sequence, extrusive and intrusive rhyolite, volcanic breccia, flow breccia, and tuff (Underwood, 1980). The Lower Rhyolite or Carpenter Canyon Tuff has been classified into two distinct members, the Indian Springs Member and Panther Peak Member by Legett (1979) and Verrillo (1979). The Indian Springs Member is comprised of 25-135 m (82-443 ft) of lithic rhyolitic ash-flow tuff and minor ash-fall and tuffaceous sandstone (Hoffer *et al.*, 1980). Located to the north at Indian Springs the Indian Springs member is made up of six ash-flow units that rest disconformably on one another with an average unit thickness of 20 m (65 ft) (Hoffer *et al.*, 1980). The units can be distinguished based upon the quantity of lithic fragments and Verrillo (1979) was able to map two separate units to the south within the member based upon lithic fragment abundance. Petrographic analysis by Hoffer (1980) revealed the tuffs are composed of 70-90% devitrified shards matrix, 5-15% quartz crystals, 5-40% lithic fragments, and sanidine with accessory minerals augite, sphene, and fluorite.



**Fig.5.3:** Field-photograph displaying sample locality of the Lower Rhyolite/ Carpenter Canyon Tuff located on the southeastern flank of the Eagle Mountains. Lower Rhyolite (Tlr) is shown unconformably resting on uneven topography of the Cretaceous Finlay Formation (Kf).

The flat-lying Panther Peak Member that rests disconformably on the flat-lying Indian Springs member was named for exposures at Panther Peak located in the northeastern part of the Eagle Mountains and is composed predominantly of densely welded rhyolitic ash-flow tuff (Hoffer *et al.*, 1980). The Panther Peak member ranges in thickness from 25 to 300 m (82-984 ft)

---

and forms resistant cliffs in exposures (Legett, 1979). The member was mapped by Legett (1979) into four ash-flow tuffs that are generally free of lithic fragments at Indian Springs that have average unit thickness of 27 m (88 ft) and are characterized by dark, densely welded basal zones that grade up into a lighter, less densely welded zone (Hoffer *et al.*, 1980). Petrographic analysis of the four ash-flow tuffs of the member reveal that it is composed of a 70-95% matrix of devitrified shards and pumice which displays strong eutaxitic textures, 10-15% sanidine and quartz crystals, and accessory minerals augite and sphene (Hoffer *et al.*, 1980).

A sample of the Lower Rhyolite or basal member of the Carpenter Canyon Tuff resting unconformably (angular unconformity) on heavily deformed Late Cretaceous Finlay Limestone was collected on the southeastern flank of the Eagle Mountains just south of Radar Road about 1 km (0.62 mi) from the intersection of Radar Road, and the Guest Ranch Road (30.91382, -105.03985)(Fig.5.3). The contact is a marked angular unconformity separating heavily folded and thrust rocks below from relatively undeformed volcanic rocks above. Approximately 20 zircon grains were collected from a sample of the Lower Rhyolite and 19 analyses were included in the age calculation with exclusions due to Pb-204 contamination. This study reports with 95% confidence an age of 35.32 Ma  $\pm$ 0.39 (all uncertainties  $2\sigma$ ) with an MSWD= 1.5 (Fig.5.4).

## Lower Rhyolite/ Carpenter Canyon Tuff: WTX-EAGLE 1A

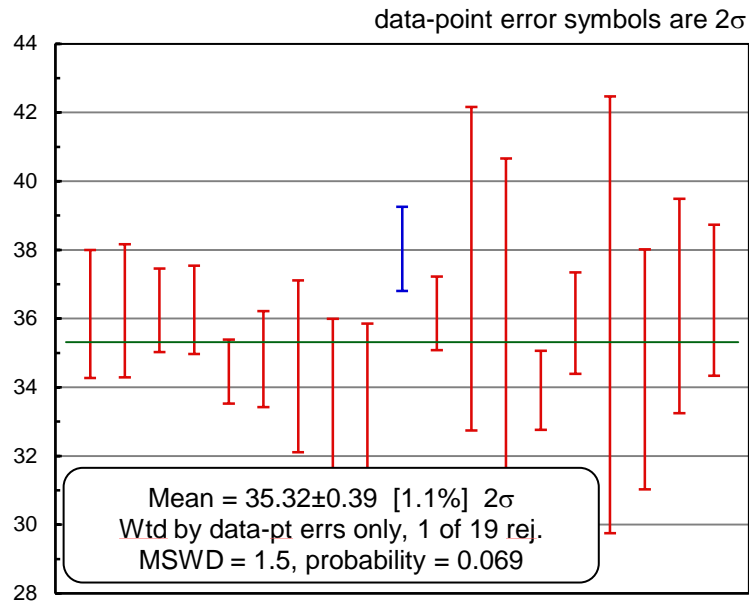


**Fig.5.4:** Nineteen analyses were included in the age calculation and we report with 95% confidence an age of  $35.32 \text{ Ma} \pm 0.39$  (all errors  $2\sigma$ ) with an MSWD= 1.5.

---

### **c. Indio and Van Horn Mountains**

The Indio Mountains are located southwest of Van Horn, Texas in the southeastern portion of Hudspeth County about 120 miles east-southeast of El Paso, Texas (Fig.5.5). This mountain range extends southward from the Eagle Mountains to the Rio Grande and is composed of nearly 7,000 feet of Late Cretaceous regressive sequences of marine limestone that are interbedded with organic-rich shales and terrigenous sandstones (Maxwell *et al.*, 1967). Cretaceous marine strata that range in age from Late Aptian to the Middle Turonian are exposed in the Indio Mountains including, in ascending order, the Yucca Formation, Bluff Formation, Cox Sandstone, Finlay Limestone, Benevides Formation, Espy Limestone, Eagle Mountains Sandstone, Buda Limestone, and Chispa Summit Formation (Fig.5.6) (Underwood, 1962).

As in the Eagle Mountains (Fig.5.2), the Cretaceous stratigraphy was controlled by a fluctuating shoreline during the general advance of the Cretaceous sea northeastward from the Chihuahua Trough onto the Diablo Platform and North American continental margin (Underwood, 1980). The Indio Mountains and vicinity contain abundant thrust faults and folds that record intense deformation having occurred throughout the Laramide orogeny. The Late Cenomanian to Turonian aged Chispa Summit Formation is the youngest exposed formation to display Laramide-style thrusting and folding in the Indio Mountains and Eagle Mountains area (Twiss, 1959b; Underwood, 1962). Flat-lying Tertiary volcanic rocks rest with a pronounced

angular unconformably on the Turonian aged Chispa Summit Formation  
(Table 5.2) (Underwood, 1962).

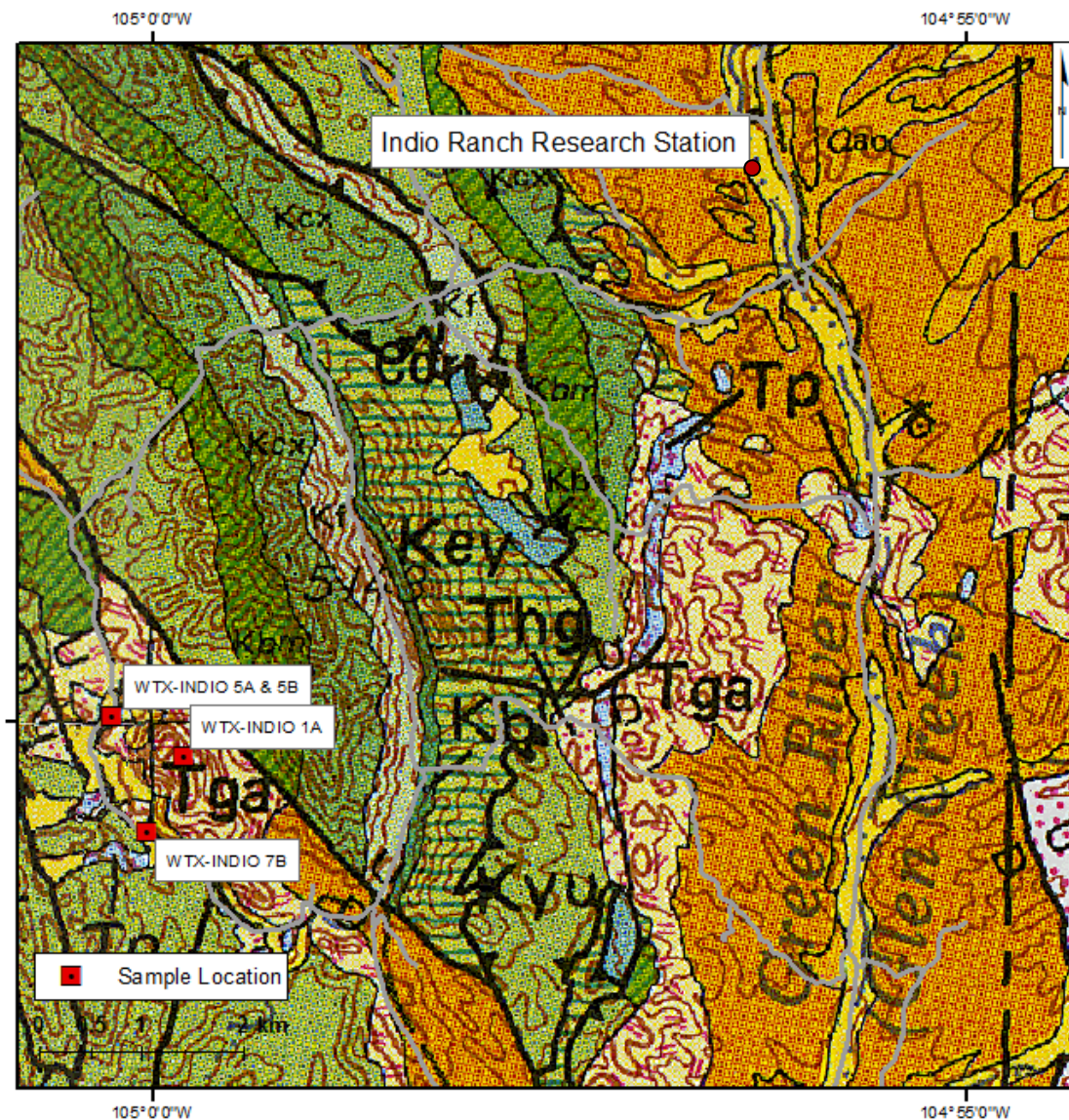


**Fig.5.5:** The Indio Mountains are located south of the Eagle Mountains in Hudspeth County. Samples from the Garren Group (Tga) (WTX- INDIO 1A, 5A, 5B, and 7B) were collected southwest of the UTEP Indio Ranch Research Station from Flat Top Mountain. Modified from Barnes and others (1979).

Tertiary volcanic rocks of the Indio Mountains flank the volcanoclastic fan of the Eagle Mountains but are compositionally correlative to the volcanic deposits of the Van Horn Mountains and Van Horn Mountains Caldera (Henry and Price, 1986). The Van Horn Mountains caldera is a small igneous center

(10 km<sup>2</sup>) located within the Van Horn Mountains in the northwestern part of the Trans-Pecos igneous province just 30 km (19 miles) east of the Indio Mountains in Hudspeth County (Henry and Price, 1986). The Van Horn Mountains caldera is located at the northern end of the Van Horn Mountains, which are bounded by major normal faults with basins that contain up to one kilometer of upper Tertiary sediments (Henry and Price, 1986). Tertiary large-scale calc-alkaline ignimbritic and subsidiary alkaline mafic volcanic deposits in the Indio Mountains region are devoid of thrust faults and folds associated

Garren Group Units (Teal, 1979)	Thickness (m)	Lithologic Description
Bell Valley Andesite	155-186	Andesite porphyry lava
Fairbury Tuff	36-38	Porly to non-welded crystal-lithic, water laid rhyolitic tuff
Bonito Trachyte	35-53	Trachyte lava composed of microcrystalline laths of K-feldspar and oligoclase with minor quartz and hornblende
Crosby Tuff	32-43	Moderately welded lithic-crystal-vitric rhyolitic tuff
Means Trachyte	161	Vesicular trachyte flow compsed of K-feldspar, oligoclase, interstitial actinolite
Water Tuff	36	Densley welded tuff, rhyolite, and vitric-crystal tuff
Buck Mountain	48-119	Densley welded vitric-crystal rhyolite ruff
Garren Mountain Tuff Breccia	33-132	Angular to rounded fragments of scoria and lithic material set in a microcrystalline pyroclatic matrix
Pantera Ignimbrite	27-91	Densley welded tuff with basal vitrophyre
Hogeye Tuff	46-64	Crystal-lithic welded andesite tuff

**Table 5.2:** Summary of the volcanic stratigraphy of the Garren Group in the Chispa Mountain Quadrangle. The Hogeye Tuff and Bell Valley Andesite were sampled and analyzed in this study. Modified after Teal (1979).

with the compressive stress regime of the Laramide orogeny, suggesting emplacement towards or at the end of contraction. However, these volcanic units are displaced by the Indio Normal Fault and rotated with the unconformity from the horizontal as the fault is approached. In addition to other normal faults that control present-day topography in the Indio Mountains, the Indio Fault is a major northwest trending feature associated

---

with Basin and Range faulting in the area (Smith and Julian, 1991). This provides support of the ignimbritic episode's pre-Basin and Range extensional origin, sometime during a rapid transition from Laramide compression. Dikes and sills of Tertiary rhyolite intruding into Cretaceous sediment are commonly found throughout the northern Indio Mountains on the flank of the Eagle Mountains, whereas the Cretaceous units in the southern Indio Mountains lack abundant intrusions and are believed to have been completely covered by Tertiary welded tuff, tuff, rhyolite, basalt, sandstone, and conglomerate at one time (Underwood, 1962). These intrusive bodies in the northernmost Indio Mountains are clearly linked to the Lower Rhyolite of the Eagle Mountains, and were emplaced at the same time that the Lower Rhyolite was extruded (Underwood, 1980)

Tertiary volcanic rocks in the southern Indio Mountains and neighboring Van Horn Mountains have an aggregate thickness of over 900 m (2,950 ft) and are categorized in the Garren Group (Table 5.6) (Hay-Roe, 1957a, 1957b; Twiss, 1959a, 1959b; Underwood, 1962; Hoffer *et al.*, 1980b). The Garren Group was first defined and categorized into seven major volcanic units that occur predominantly in the Chispa Mountain Quadrangle by Hay-Roe (1957a). Teal (1979) reclassified the seven units into ten formations and indicated that the units are lithologically distinct and mappable in the field. The Garren Group of Hay-Roe (1957, 1958) and Twiss (1959a, 1959b) that was later revised by Teal (1979) consists of lava flows, welded tuffs, and breccias that range in composition from andesite to rhyolite (Hoffer

---

*et al.*, 1980). The ten formations of the Garren Group are listed in the table below and include, in ascending stratigraphic order, the Hogeye Tuff, Pantera Ignimbrite, Garren Mountain Tuff Breccia, Buck Mountain, Water Tuff, Means Trachyte, Crosby Tuff, Bonito Trachyte, Fairbury Tuff, and Bell Valley Andesite. Samples analyzed in this study have been collected from the Hogeye Tuff and Bell Valley Andesite.

**i. Hogeye Tuff**

The Hogeye Tuff is a regional unit that was derived in part from tuffs erupted from the Van Horn Mountains caldera and has a thickness of 46-64 m in the Van Horn and Indio Mountains region (150-177 ft) (Henry and Price, 1986). It is comprised of a whitish-gray crystal-lithic welded andesite tuff that is densely welded at the base and grades upward into moderately to poorly welded tuff (Hoffer *et al.*, 1980). The Hogeye Tuff contains phenocrysts of potassium feldspar (5%), oligoclase (3-5%), hornblende (2%), and lithic and pumice fragments (10%) in a microcrystalline devitrified matrix (Hoffer *et al.*, 1980). This is the basal flat-lying volcanic unit of the Garren Group that forms an angular unconformity between the heavily deformed Cretaceous formations below. A sample of the Hogeye Tuff was collected for analysis from an exposure near an arroyo off of a ranch road about 4.8 km (3.0 mi) south of the UTEP Indio Ranch Research Station just east of Flat Top Mountain (GPS Location: 30.74028, -105.00056) (Fig.5.5; Fig.5.6). Forty-five



**Fig.5.6: A)** An exposure of the Hogeye Tuff that was analyzed in this study (WTX-INDIO 5A, 5B, and 7B) and **B)** a field-photograph displaying sample locality of the Bell Valley Andesite of Flat Top Mountain (WTX-INDIO 1A)

zircon grains were separated three samples of the Hogeye Tuff (5A, 5B, and 7B) and analyzed. Thirteen analyses were included in the age calculation for sample 5A and an age of 37.34 Ma  $\pm$ 0.96 (all errors  $2\sigma$ ) is reported in this study with 95% confidence and an MSWD= 1.9 (Fig.5.8). Nine analyses were included in the age calculation for sample 5B, and an age of 37.65 Ma  $\pm$ 0.75 with 95% confidence and an MSWD= 3.7 (Fig.5.9). Lastly, fifteen analyses

---

were included in the age calculation for sample 7B and an age of 38.02 Ma  $\pm 0.99$  is reported in this study with 95% confidence and an MSWD= 2.9 (Fig.5.10). These ages are significant as they help to constrain the timing of cessation of Laramide folding and thrusting in the Indio region to 38.02 Ma.

The Hogeye Tuff is also observed in the Van Horn Mountains unconformably overlying Permian and Precambrian aged strata. This is the only mountain range in West Texas where an angular unconformity between Permian and Precambrian strata and flat-lying Tertiary volcanics exist (Fig.5.7). The Van Horn Mountains area is a major structural high, and because of this, meta-quartzite, meta-arkose, muscovite and biotite schist, amphibolite, and pegmatites of the Precambrian Carrizo Mountain Group, the oldest rocks exposed in Trans-Pecos Texas, crop out in these mountains (Denison, 1980; Flawn, 1951; King and Flawn, 1953). As mapped by Barnes (1979), the Hogeye Tuff rests unconformably on the Laramide-thrust-faulted and folded Permian Hueco Limestone and Precambrian Carrizo Mountain Group just north and east of the Van Horn Caldera complex and east of the Indio Mountains where the Hogeye Tuff was sampled and analyzed in this study. It has been suggested that the Carrizo Mountain Group represents an originally bimodal volcanic assemblage of rhyolitic ash-flow tuffs that resulted from subduction and continental accretion during the Proterozoic (2,500-541 Ma) that were affected by almadine-amphibolite facies metamorphism at approximately 1,000 Ma (Condie, 1982; Denison, 1980).

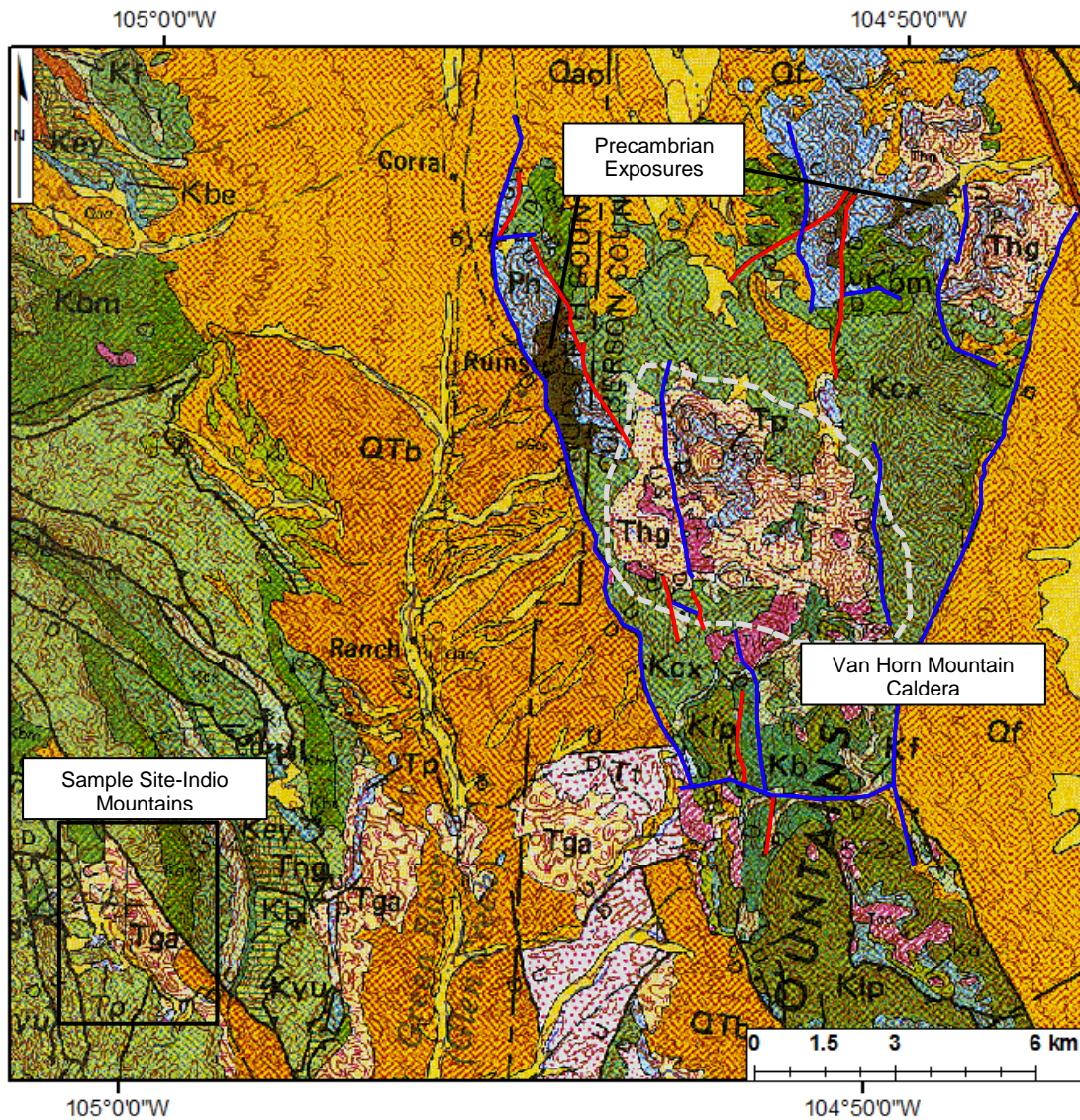


**Fig.5.7:** Map displaying the Van Horn Mountains Caldera Complex located in the Van Horn Mountains in relation to the Indio Mountains and the sample site locality of the Hogeeye Tuff and Bell Valley Andesite analyzed in this study. The Garren Group volcanic units of the Indio Mountains were erupted from the Van Horn Mountains Caldera from 38 to 36.5 Ma. The basal unit of the Garren Group (Hogeeye Tuff: Thg on map) is unconformably overlying the Permian Hueco Limestone (Ph on map) and Precambrian units of the Carrizo Mountains Group (pCc on map). Modified from Barnes (1979).

The Allamore Formation of the Carrizo Mountain Group, consisting of predominantly talc-rich phyllites and 25-30% rhyolitic and basaltic tuffs with limestones, is the youngest Precambrian unit exposed in the Van Horn Mountains and has a U-Pb, zircon age of  $1256 \pm 5$  Ma (Roths, 1993; Bickford et al., 2000). The Laramide thrust faulted and folded Permian aged Hueco

---

Formation (299-280 Ma) sits unconformably on the heavily metamorphosed rocks of the Carrizo Mountain Group (Twiss 1959a, 1959b). Precambrian exposures are limited to the northern portion of Trans-Pecos Texas region indicating higher uplift in the north throughout the Laramide orogeny.

## ii. **Bell Valley Andesite**

The Bell Valley Andesite is the capping unit of Flat Top Mountain in the Indio Mountains and has a thickness of 155-186 m (508-610 m) (Fig.5.5; 5.6). The unit is comprised of andesite porphyry lava that consists of andesine plagioclase (60-67%), hypersthene (5-10% altered to iron oxides), augite (10-15%), biotite (2-5%), and hornblende (1%) (Hoffer *et al.*, 1980). A sample of the Bell Valley Tuff was collected for analysis at the top of Flat Top Mountain about 3.8 km (3.0 mi) southeast of the UTEP Indio Ranch Research Station (Fig.5.6). Ten zircon grains were separated from one sample of the Bell Valley Andesite and analyzed. Twelve analyses are included in the age calculation and an age of 36.57 Ma  $\pm$ 0.80 is reported in this study with 95% confidence with an MSWD= 2.8 (GPS Location: 30.74690, -104.99679) (Fig.5.11). As this is the highest unit of the Garren Group, the age is significant because it constrains the age of volcanism and ignimbrite flare-ups in the Van Horn and Indio Mountains and presumably the age of westward migration and roll-back of the slab and volcanic arc from the Indio Mountain region, or asthenospheric upwelling if the slab has foundered from its former flat slab position in the Tertiary.

### Hogeye Tuff: WTX-INDIO 5A

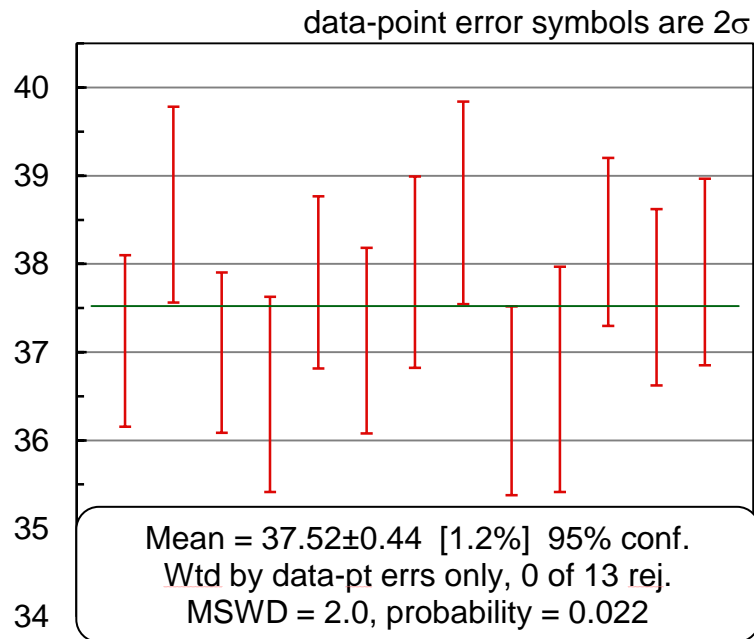
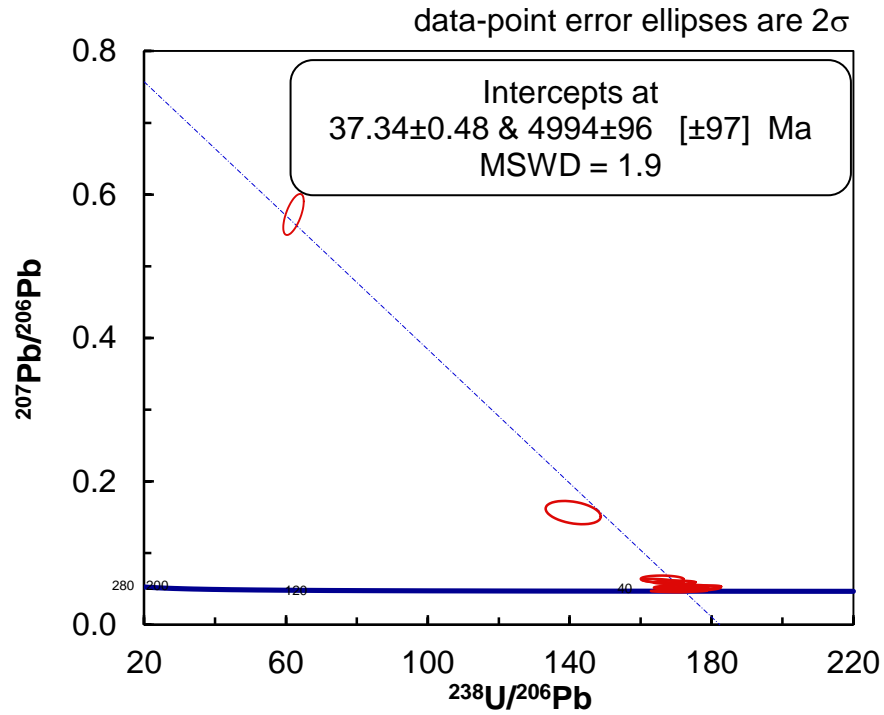


**Fig.5.8:** Thirteen analyses were included in the age calculation and an age of  $37.34\text{Ma} \pm 0.48$  (all errors  $2\sigma$ ) with an MSWD= 1.9 is reported in this study. The Tera-Wasserburg plot for this sample is shown above and the Normalized Age Distribution plot is displayed below.

### Hogeye Tuff: WTX-INDIO 5B

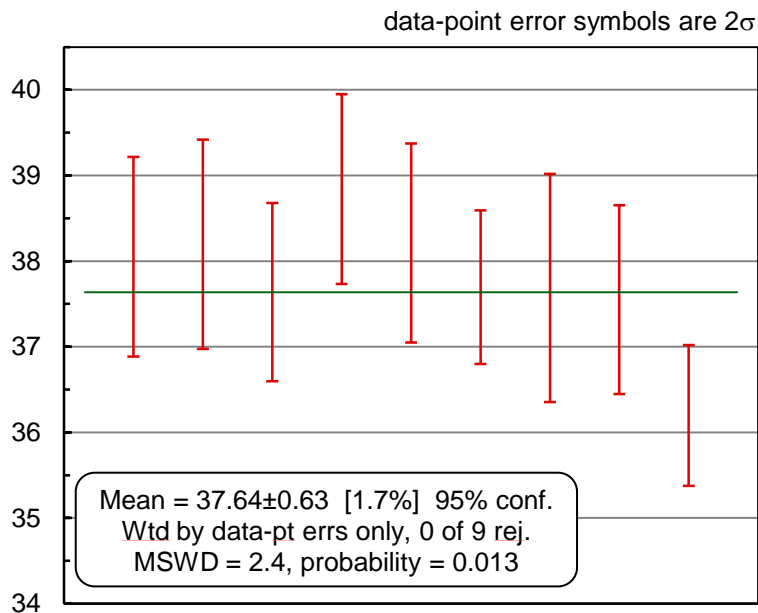
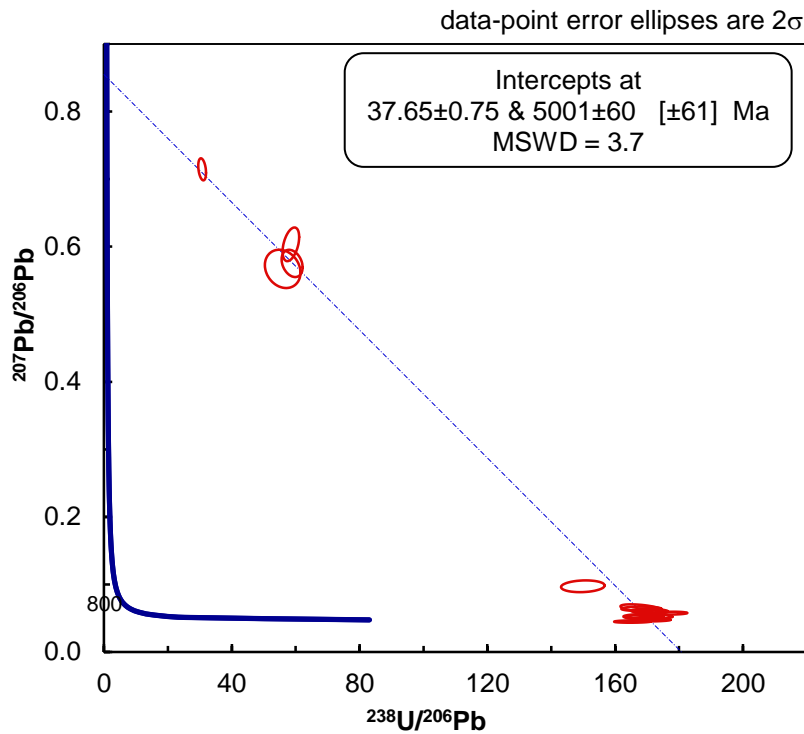


**Fig.5.9:** Approximately 9 analyses were included in the age calculation and an age of  $37.64 \text{ Ma} \pm 0.63$  (all errors  $2\sigma$ ) with an MSWD= 2.4 is reported in this study. The Tera-Wasserburg plot for this sample is shown above and the Weighted Mean Average plot is displayed below.

### Hogeye Tuff: WTX-INDIO 7B

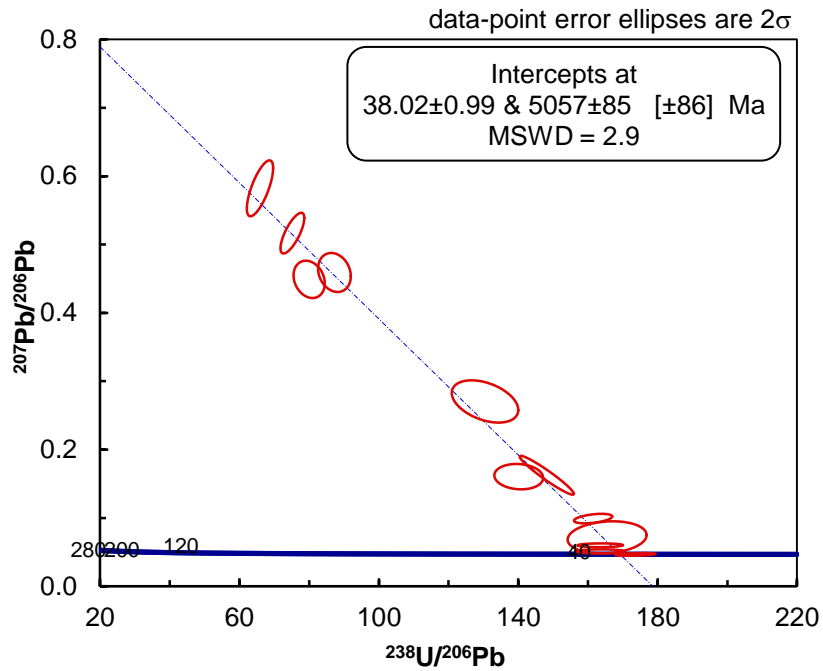


**Fig.5.10:** Approximately 12 analyses were included in the age calculation and an age of 38.02 Ma  $\pm 0.99$  (all errors  $2\sigma$ ) with an MSWD= 2.9 is reported in this study.

### Bell Valley Andesite: WTX-INDIO 1A

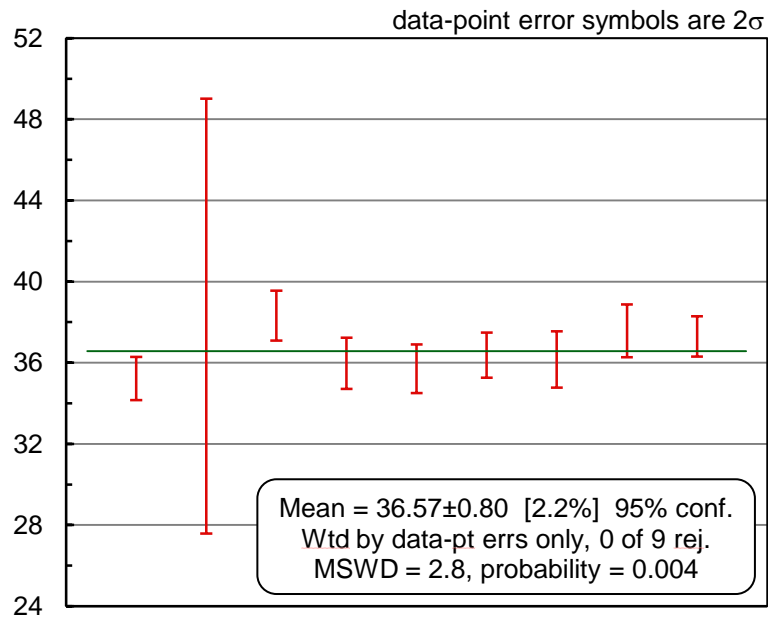


**Fig.5.11:** Approximately 9 analyses were included in the age calculation and an age of 36.57 Ma  $\pm 0.80$  (all errors  $2\sigma$ ) with an MSWD= 2.8 is reported in this study.

---

#### **d. Davis Mountains**

The Davis Mountains are the second highest range in Texas, and the largest volcanic center of the Trans-Pecos igneous province with its highest peak, Mount Livermore, reaching approximately 2,553 m (8,378 ft) above sea level (Henry *et al.*, 1994). This range delineates the easternmost portion of the Trans-Pecos magmatic field, and therefore the easternmost in the southern Cordillera. The Davis Mountains extend sixty miles from north to southwest in central Jeff Davis County with the center of the range lying approximately ten miles northwest of Fort Davis (Henry *et al.*, 1994). K-Ar and  $^{40}\text{Ar}/^{39}\text{Ar}$  data from studies employed by Parker and McDowell (1979) and Henry *et al.* (1994) indicate that volcanic activity in the Davis Mountains occurred in six episodes between 38 and 35 Ma, and at 0.3 my intervals between 36.8 and 35.3 Ma (Henry *et al.*, 1994).

The Tertiary volcanic rocks of the Davis Mountains vary from most continental arc silicic volcanic fields as intermediate volcanism did not precede silicic volcanism and occurred only in lulls between silicic activity in the Davis Mountains. The Tertiary volcanic rocks exposed in the Davis Mountains and throughout the Trans-Pecos igneous province are dominantly alkalic in composition, and are classified as the largest alkalic province in North America (Henry *et al.*, 1994; Cameron *et al.*, 1996). The most striking variation from the Davis Mountains and other silicic volcanic fields is that the majority of major volcanic units were emplaced as extensive, large-volume, silicic flood rhyolites (Henry *et al.*, 1989). Identified calderas in the volcanic

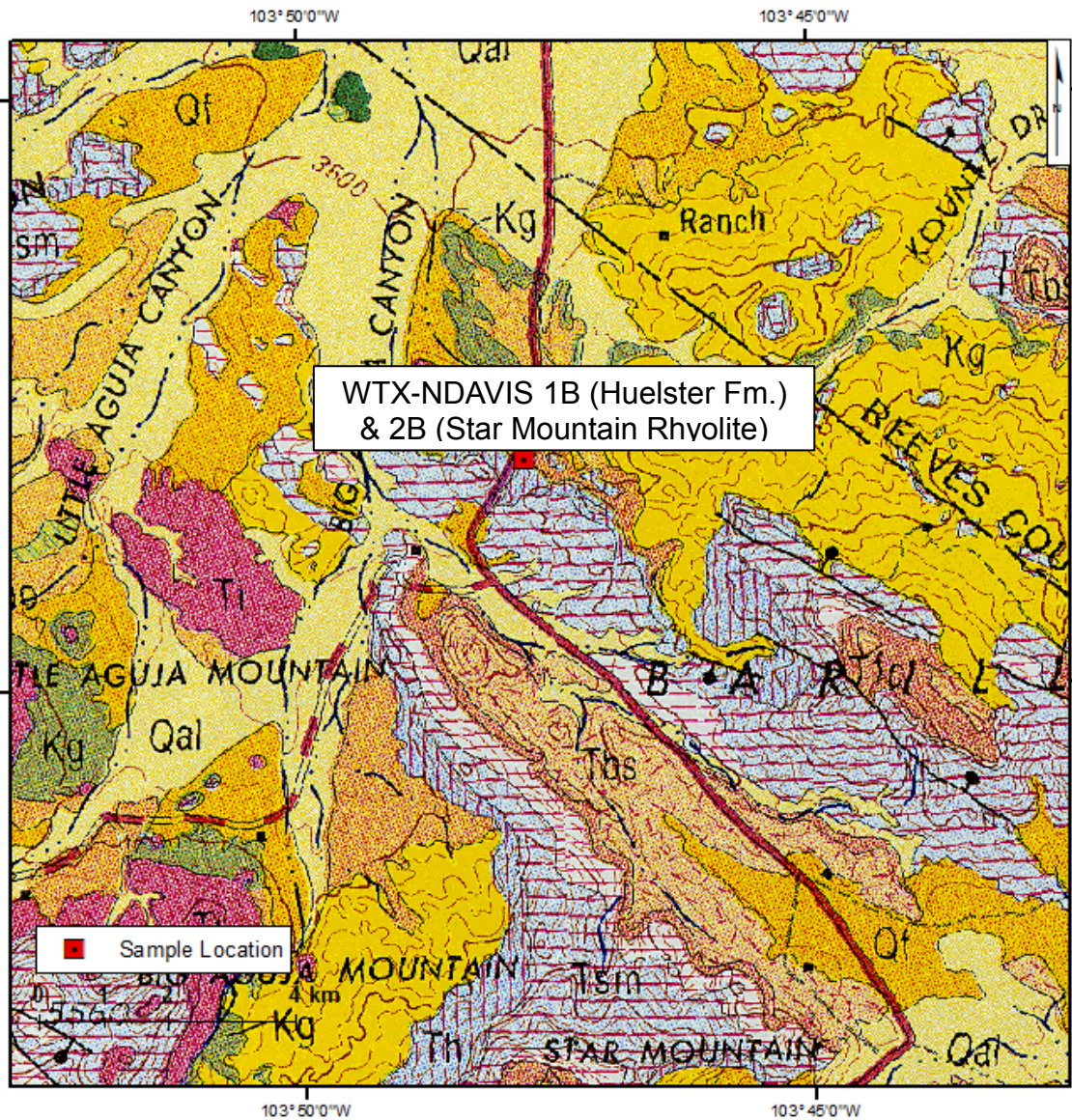


**Fig.5.12:** Sample location of WTX-NDAVIS 1B (Huelster Fm.) and WTX-NDAVIS 2B (Star Mountain Rhyolite) located in the Davis Mountains in Reeves County. The Huelster Formation is labeled Th on the above map and the Star Mountain Rhyolite is labeled Tsm.; Tertiary intrusives (Ti), Cretaceous undivided Gulfian strata (Kg). Modified from Barnes and others (1979).

field include the Buckhorn (36.8 Ma), El Muerto (36.0 Ma), Paradise Mountain (35.3 Ma), and Paisano Calderas (Henry *et al.*, 1994). Ash-flow tuffs in the Davis Mountains are rare and were commonly involved in secondary flow, but clear evidence of pyroclastic origin is maintained in most exposures.

The stratigraphically lowest volcanic unit in the Davis Mountains is comprised of volcanoclastic sediments of the stratigraphically equivalent

---

Huelster and Pruett Formations (Fig.12). The Huelster Formation consists predominantly of reworked tuffs and some minor mafic lava flows, but is believed to have accumulated before silicic volcanism occurred in the Davis Mountains from sources outside of the range (Parker, 1986; Eifler, 1951). It rests with an angular unconformity upon heavily faulted undivided Gulfian aged rocks that are correlative with the Taylor Marl, Austin Chalk, and upper portion of the Eagleford in Central Texas (145-66 Ma) (Eifler, 1951; Barnes *et al.*, 1979). The deformation documented in the Gulfian aged strata consist of predominantly normal faults that strike in a northwest-southeast direction that are thought to be reactivated thrust faults during Basin and Range extension. These northwest-southeast striking reactivated normal faults record compressional deformation that occurred throughout the Laramide orogeny when the advancing orogenic front reached the present-day Texas border. The relatively flat-lying Huelster Formation directly above the unconformity was analyzed in this study to gain a better understanding of the age of emplacement of flat-lying volcanic rock unaffected by Laramide-style compressional deformation in the region (Fig.5.12, Fig.5.13).

The oldest volcanic unit derived locally within the Davis Mountains analyzed in this study is the flat-lying Star Rhyolite that was deposited coevally with the Crossen Trachyte and Bracks Rhyolite and rests conformably on top of the Huelster Formation (Henry *et al.*, 1994). The formations consist of rhyolite to quartz trachyte lavas that form a regional unit that encompasses and extends well beyond the Davis Mountains (Henry *et*

*al.*, 1994). The flood rhyolites of the Star Mountain Rhyolite, Crossen Trachyte, and Bracks Rhyolite display overlap in composition and are nearly indistinguishable in outcrop characteristics, petrography, and age (Henry *et al.*, 1989). The Star Mountain Formation has a cumulative volume of 240 km<sup>3</sup> (58 mi<sup>3</sup>) and is thought to consist of a large but unknown amount of individual flows (Henry *et al.*, 1994). At least eight flows have been identified from field, petrographic, chemical age, and paleomagnetic data with individual flows ranging in thickness from 40-120 km (25-75 mi) (Henry *et al.*, 1989; Henry *et al.*, 1990). The silicic magmatism shifted from north to south in the Davis Mountains through time with the 36.8 Ma and 36.5 Ma episodes that are distinguishable within error occurring in the north and east, the 36.3 Ma episode in the south (Henry *et al.*, 1994)

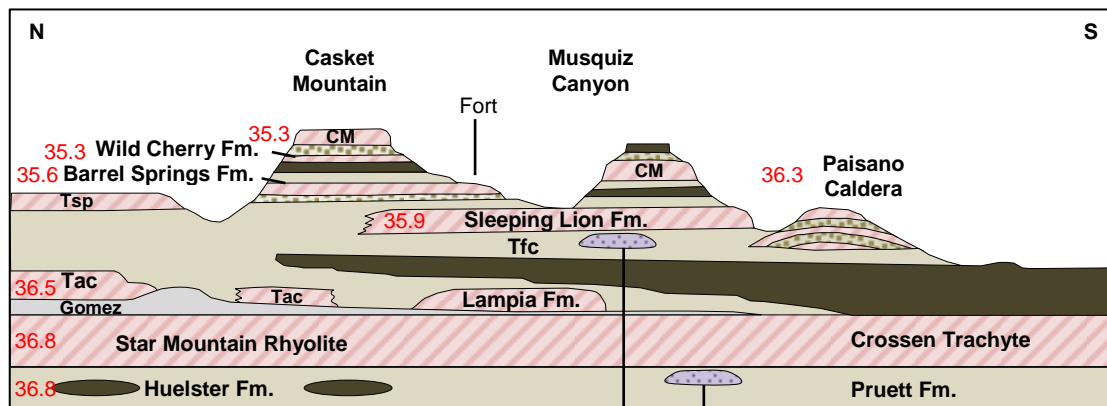


**Fig.5.13:** N-S diagrammatic stratigraphic sections and average <sup>40</sup>Ar/<sup>39</sup>Ar ages (Ma) from Henry and Price's study (1994) of the Davis Mountains volcanic field. Cross section line transects the Davis Mountains in a N-S direction from the Buckhorn Caldera to the Paisano Caldera. Modified from Henry and Price (1994).

The 35.9 Ma and 35.6 Ma episodes that are distinguishable within error are suggested to have been emplaced in the central Davis Mountains, and the 35.3 Ma and younger undated events in the southwest and west including late intrusions (Henry *et al.*, 1994). The 36.8 Ma volcanic episode

---

that occurred in the northern Davis Mountains was a regional eruptive event responsible for the emplacement of the Star Mountain Rhyolite, Crossen Trachyte, and Bracks Rhyolite and extends well beyond the Davis Mountains (Henry *et al.*, 1994). The 35.3 Ma volcanic episode includes the ash-flow tuff of the Wild Cherry Formation that is suggested to have erupted from the Paradise Mountain Caldera, and the lava flows of Casket Mountain thought to have erupted and dispersed from several vents throughout the central, eastern, and southern Davis Mountains (Fig.5.13) (Henderson, 1989; Henry *et al.*, 1994). All volcanic units of the Davis Mountains rest unconformably on undivided Gulfian sediments (145-66 Ma).

#### **i. Huelster Formation**

The Huelster Formation, correlative with the Pruett Formation of the southern Davis Mountains is the lowest flat-lying volcanic unit exposed throughout the Davis Mountains in Jeff Davis County. The Huelster Formation has been described by Barnes (1979) as predominantly tuff with thin layers of sandstone and conglomerate, lenses of fresh-water limestone, and trachydoleritic lava that reaches a thickness of up to 150 m (490 ft) in the Madera Canyon area (McAnulty, 1955; Smith, 1975; Barnes *et al.*, 1979). The Huelster Formation is overlain by the Star Mountain Rhyolite or the Gomez Tuff where the Star Mountain Rhyolite is stratigraphically absent in the southeast and is divisible into the Jeff Conglomerate Member at the base (Eifler, 1951; Parker, 1986). The Jeff Conglomerate is a sandstone conglomeratic unit that constitutes the lowest beds of the Huelster Formation

---

with an average thickness of 38 m (125 ft)(Eifler, 1951). Henry and others (1986) obtained a K/Ar age of 39.3 Ma  $\pm$ 0.9 for a trachyandesite clast sampled from the conglomeratic unit which coincides with earlier K/Ar ages obtained by Goldrich and Elms (1949), and Eifler (1951) that were reported at <38.34 Ma  $\pm$ 0.7.



**Fig.5.14:** Field photograph displaying the sample location of the Huelster Formation and overlying Star Mountain Rhyolite just east of the Davis Mountains in Reeves County.

A sample of the upper-most tuffaceous bed in the Huelster Formation that was in direct contact with the Star Mountain Rhyolite above was collected and analyzed in this study. The sample was taken 2.5 km (1.5 mi) east of Big Aguja Canyon off of Texas State Highway 17 about 9 km (5.6 mi) south of the Farm to Market Road 3078 and Texas State Highway 17 junction (Fig.5.12; Fig.5.14) (GPS Location: 30.86547, -103.79678). Ninety-five zircon grains were separated from the Huelster Formation sample and analyzed on the

University of Houston's LA-ICP-MS. The Huelster Formation was treated as a detrital sample because it is a reworked tuff deposit. Zircon analyses with a discordance of less than 30% and similar or identical Pb206-U238 and Pb207-U235 ages were selected for the age calculation. The analyses were plotted on a Tera-Wasserburg plot and yielded an age of  $36.8 \pm 1.5$  Ma and is indistinguishable from the alkali feldspar phenocryst  $^{40}\text{Ar}/^{39}\text{Ar}$  age of  $36.8 \pm 0.13$  Ma obtained by Henry et al. (1994) for the Star Mountain Rhyolite that rests directly above the formation indicating conformability (Fig.5.15).

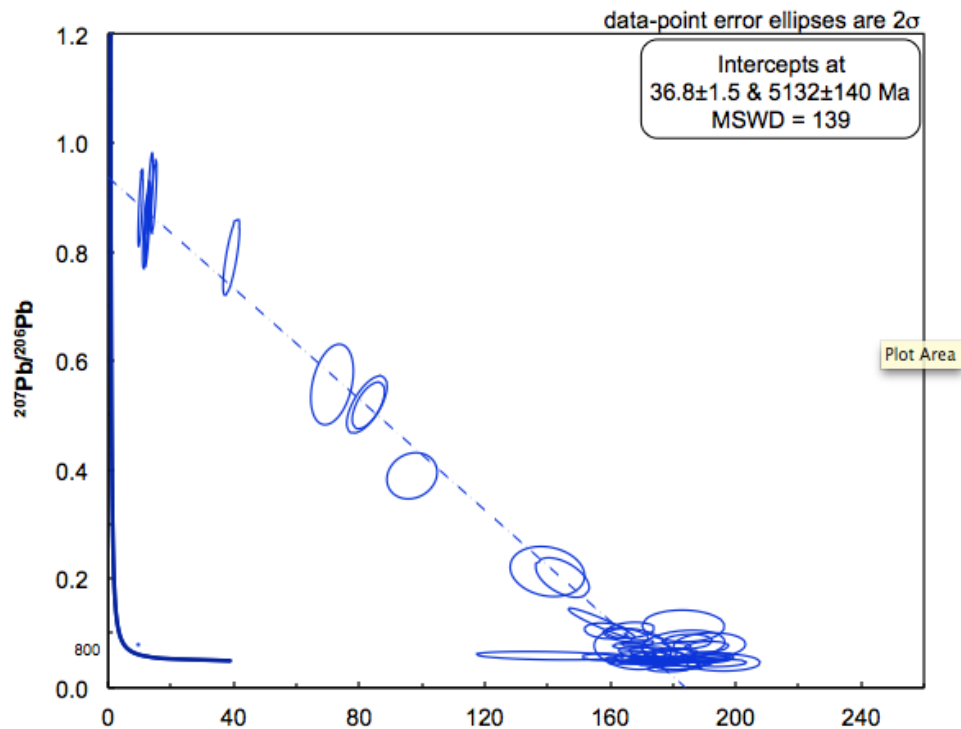


**Fig.5.15:** Tera-Wasserburg plot containing analyses of the Huelster Formation that has yielded an age of  $36.8 \pm 1.5$  Ma

---

## ii. Star Rhyolite

The Star Mountain Rhyolite is regarded as the oldest volcanic flow unit present in the Davis Mountains from a local source and is one of the most extensive volcanic units in the Trans-Pecos igneous field (Henry *et al.*, 1988). The formation consists of an unknown number of expansive individual flows with a volume exceeding 240 km<sup>3</sup> (58 mi<sup>3</sup>) (Fig.5.13; Fig.5.14) (Henry *et al.*, 1994). Field, petrographic, chemical, paleomagnetic, and age data from studies done by Henry and others (1989) have distinguished at least eight flows in the Star Mountain Rhyolite with as many as three flows occurring at any one location throughout the Davis Mountains. Individual flows vary in thickness from 40-120 m (131-393 ft), and flow fronts or margins where flows terminate abruptly form thicknesses of up to 100 m (328 ft) indicating that they were more than likely emplaced as lava (Henry *et al.*, 1994). Compositionally, the Star Mountain Rhyolite is holocrystalline glomeroporphyritic rhyolite and trachyte that contains variable amounts (5-13% by volume) of subhedral anorthoclase phenocrysts that vary in size from 1 to 3 mm in diameter (Parker and McDowell, 1979) Most flows range from 66% to 72% SiO<sub>2</sub> with the exception of one flow that contains 76% SiO<sub>2</sub> (Henry *et al.*, 1994).

A sample of the lowest rhyolite flow unit of the Star Mountain Rhyolite that was in direct contact with the Huelster Formation below was collected and analyzed in this study (Fig.5.12). The sample was taken 2.5 km (1.5 mi) east of Big Aguja Canyon off of Texas State Highway 17 about 9 km (5.6 mi)

---

south of the Farm to Market Road 3078 and Texas State Highway 17 junction (30.86547, -103.79678). An age was not obtained for the Star Mountain Rhyolite from this study's analysis due to abundant inclusions and inherited Proterozoic aged zircon cores. Henry et al. (1994) obtained six alkali feldspar phenocryst  $^{40}\text{Ar}/^{39}\text{Ar}$  ages that vary from 36.9-36.7  $\pm$ 0.13 Ma ( $1\sigma$ ) for the Star Mountain Rhyolite that are used in this study to analyze age progression of the emplacement of volcanic rocks in Trans-Pecos Texas.

**e. Rio Grande River Area**

**i. Vieja Group: Buckshot Ignimbrite**

The Vieja Group is comprised of 760 m (2,550 ft) of interbedded conglomerate, sandstone, water-laid tuff, ash-flow tuff (ignimbrite), and lava rock found throughout the Sierra Vieja Mountains with the first exposures appearing about 30 km (18.6 mi) south of the Van Horn and Indio Mountains in Presidio County (Wilson *et al.*, 1968; Testarmata and Gose, 1980). The northern Garren Group of Hay-Roe (1957a, 1957b) and Twiss (1959a, 1959b) exposed predominantly in the Van Horn and Indio Mountains interfingers southward with the Vieja Group (Wilson *et al.*, 1968). The Vieja Group, first defined by DeFord (1958) and later refined by Barnes and others (1979) consists of seven formations including, in ascending order, the Gill Breccia, Colmena Tuff, Buckshot Ignimbrite, Chambers Tuff, Bracks rhyolite, Capote Mountain Tuff, and Brite Ignimbrite (Table 5.3).

<b>Vieja Group Units</b>	<b>Thickness (m)</b>	<b>Lithologic Description</b>
Brite Ignimbrite	0-78 (Avg. 14)	Light brownish-gray, slightly porphyritic, vitric ignimbrite that contains up to 25% quartz and chatoyant sanidine phenocrysts; microeutaxitic
Capote Mountain Tuff	183-640	Fine-grained, vitric, tuffaceous sandstone and siltstone with a few interbeds of conglomerate containing pebble-sized limestone, sandstone, and igneous rock clasts.
Bracks Rhyolite	0-110	Dark reddish-brown to grayish-olive, slightly porphyritic quartz pantellerite with rhombic anorthoclase phenocrysts in matrix of alkalic feldspar, quartz, and mafic minerals.
Chambers Tuff	32-230	Varicolored, fine-grained, crystal-vitric tuff that contains white, pale red, grayish-pink, grayish-green, pale purple, and grayish-orange to pink beds with abundant crystal and vitric fragments
Buckshot Ignimbrite	Avg. 14	Grayish-red, slightly porphyritic, vitric, rhyolitic ignimbrite that contains dark red spheres (2-10 mm in diameter); blishter cones that reach up to 6 ft high and 45 ft in diameter; sharp contact
Comena Tuff	0-137	pale red to white fine-grained, thin-bedded tuffaceous sandstone and pebble-to-boulder sized limestone and sandstone clasts in conglomeratic facies; discordantly overlies Gill Breccia
Gill Breccia	0-110	Grayish-red, porphyritic, trachybasalt breccia

**Table 5.3:** Summary of the volcanic stratigraphy of the Sierra Vieja Group in the Rim Rock Country along the Rio Grande River. Modified from Wilson and others (1968).

---

Although some individual beds of water-laid tuffs documented in the Vieja Group cannot be traced for more than a few hundred feet, the Buckshot Ignimbrite and Chambers Tuff extend northward and interfinger with the Hogeye Tuff and Pantera Trachyte of the Garren Group. The Hogeye Tuff that has been analyzed in this study in from the Van Horn and Indio Mountains extends to the south and interfingers with the Buckshot Ignimbrite.

The Buckshot Ignimbrite overlies and occupies the same valley as the Colmena Formation and is considered the oldest volcanic unit in this area of the Trans-Pecos igneous field from a local source (Henry and Price, 1986). The Buckshot Ignimbrite was erupted from the Infiernito Caldera Complex and is regarded to have been emplaced coevally with the Morita Ranch Formation (Duex and Henry, 1981; Henry and Price, 1984; Henry and McDowell, 1986). The formation is composed of predominantly peralkaline, rhyolitic ash-flow tuff and contains minor amounts of alkali feldspar phenocrysts and green clinopyroxene (Henry and Price, 1984). Remnants of fumaroles that are commonly referred to as blister cones are a defining feature of the Buckshot Ignimbrite and developed on the upper surfaces of the ash-flow tuff during the early stages of cooling and devitrification (Henry and Price, 1984). A sample of the Buckshot Ignimbrite sample was collected about 30 km (18.6 mi) southeast of Marfa on Ruidosa Marfa Road/State Highway 2810 just off the north side of the road near Fletcher Ranch (Fig.5.16) (GPS Location: 30.19257, -104.26791). Fifteen zircon grains were separated from the Buckshot Ignimbrite (WTX-SEAST 2) analyzed in this

study.

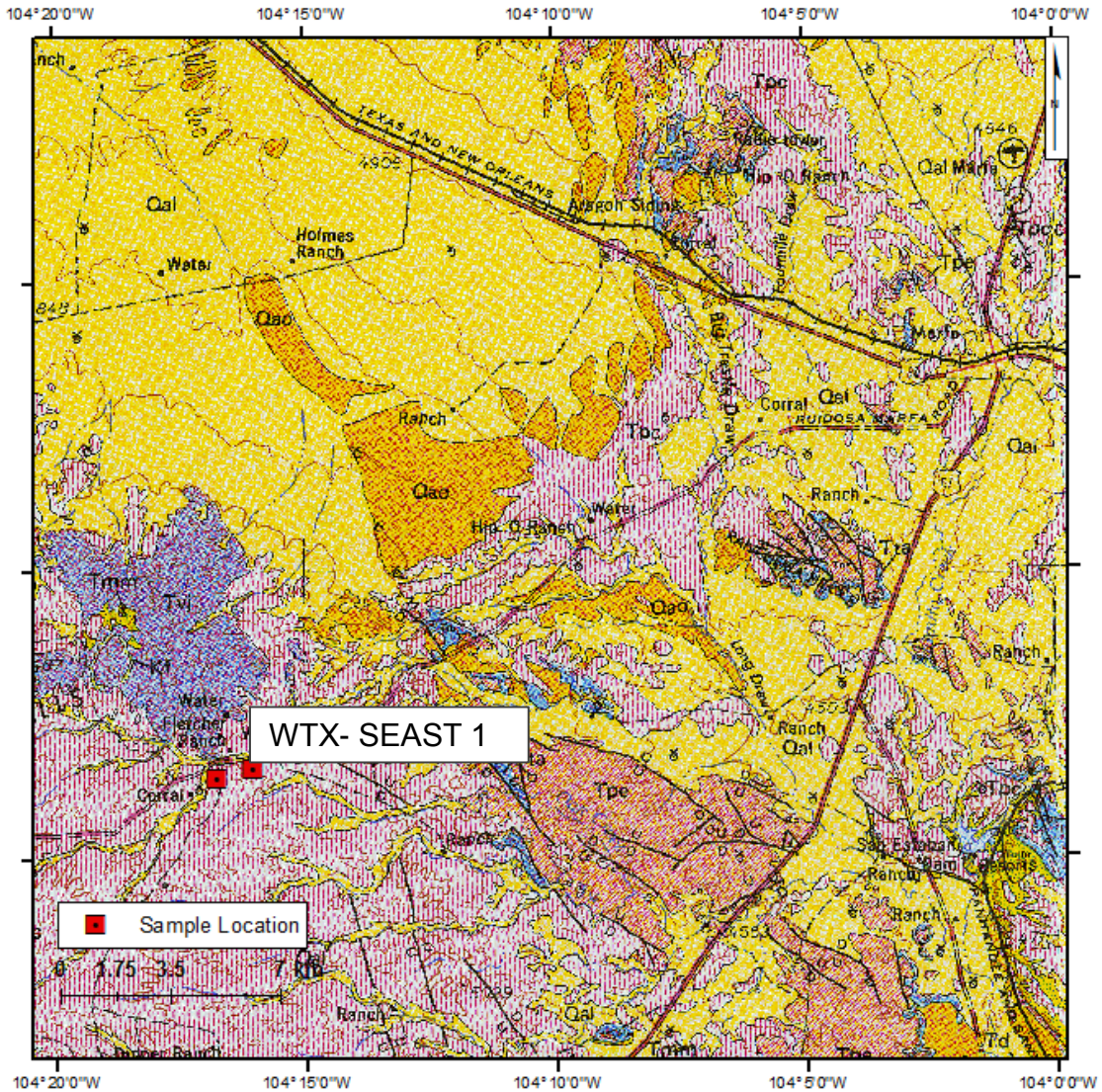


**Fig.5.16:** Sample location of WTX-SEAST 1(Buckshot Ignimbrite of the Sierra Vieja Group (Tvj)) located on Ruidosa Marfa Road/State Highway 2810 just off the north side of the road near Fletcher Ranch. Modified from Barnes and others (1979).

Eleven analyses were included in the age calculation for sample WTX-SEAST 2 that is reported in this study with 95% confidence as 36.73 Ma  $\pm$ 0.57 (all errors  $2\sigma$ ) with an MSWD= 1.9 (Fig.5.17).

### Buckshot Ignimbrite: WTX-SEAST 2

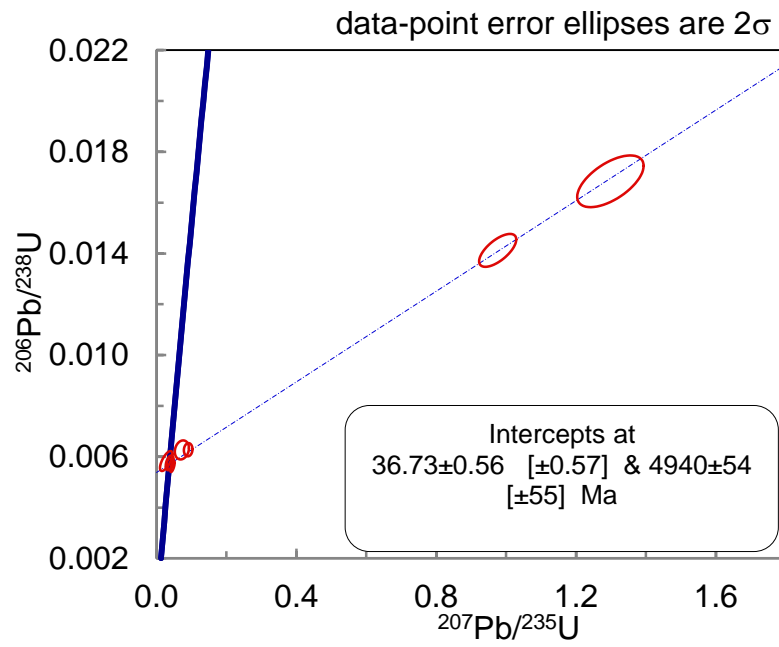


**Fig.5.17:** Approximately 11 analyses were included in the age calculation for sample WTX-SEAST 2 that is reported in this study with 95% confidence as  $36.73 \text{ Ma} \pm 0.57$  (all errors  $2\sigma$ ) with an MSWD= 1.9

---

**f. Alamito Creek and Green Valley Area**

**i. Tascotal Formation**

The Tascotal Formation is a volcanic sedimentary unit of the Buck Hill Group exposed in the south-central portion of the Trans-Pecos igneous province in the Alamito Creek Valley and along the northeast escarpment of the Tascotal Mesa (Walton, 1979). The volcanic series of the Buck Hill Group was first defined by Goldich and Elms (1949), with later studies focusing predominantly on the interval equivalent of the Tascotal Formation by Erickson (1953), Dietrich (1966), and McKnight (1970). The formation's type section is exposed at Wire Gap and can be divided into four members that reach a thickness of up to 250 m (820 ft) (Watson, 1979). The four members have been categorized lithologically and include, in ascending order, 150 m (492 ft) of volcanic clastic apron deposits that total over half of the formation's exposed thickness; a sequence of eolian sands; fan gravel; interbedded sandstones and conglomerates that correlate with the Perdiz Conglomerate that is widespread but not formally defined; and pumice-rich sandstones and mudrocks that contain some conglomerate (Fig. 5.18) (Ramsey, 1961; Dietrich, 1966; Walton, 1979).

The volcanic clastic apron of the Tascotal Formation consists of interbedded sandstone, mudrock, and minor amounts of pebble to boulder sized conglomerate rock, but the constituent particles are predominantly from volcanic derivation (Watson, 1979). The volcanic derived particles are comprised of volcanic glass shards that have mostly been dissolved and



**Fig.5.18: A)** A field-photograph displaying the Tascotal Mesa and Tascotal Formation that was analyzed in this study (WTX-SEAST 4) and **B)** a field-photograph displaying sample locality of the Tascotal Formation 3 mi north of Singleton Ranch.

replaced by clinoptilolite, pumice fragments, sanidine, zoned and twinned plagioclase, and fragments of lavas and welded ash-flow tuffs (Walton, 1977; Walton 1979). The basal volcanoclastic apron facies of the Tascotal Formation resembles a sediment wedge that thickens toward the east from its pinch-out on the lower slopes of the Chinati Mountains Caldera Complex (Walton, 1977). A sample of the basal member of the Tascotal Formation was collected along Ranch Road 169 about 20 km (12.42 mi) south of the intersection of U.S. Highway 67 and Ranch Road 169 southeast of Marfa in

Presidio County (Fig.5.19) (GPS Location: 30.19019, -104.27943). The flat-lying Tascotal Formation was analyzed in this study in an attempt to constrain the entire volcanic sequence in the Chinati Mountains region of Trans-Pecos Texas because it is the highest formation in this regions stratigraphy that contains volcanic derived tuffaceous sediments. A U-Pb zircon age of a tuffaceous bed in this unit will better limit the timing of cessation of volcanic ignimbrite flare-ups in the Trans-Pecos Texas region.

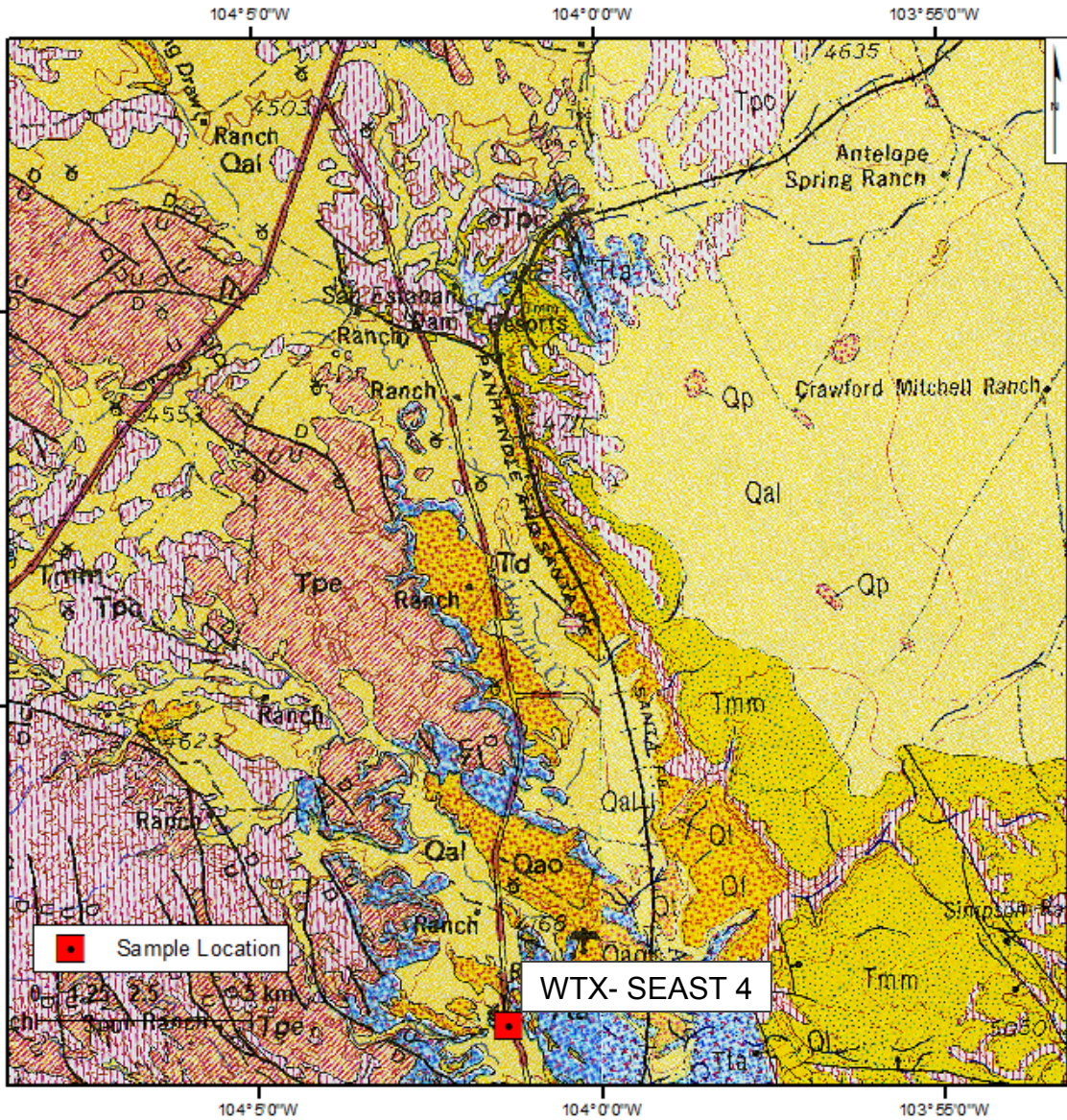


**Fig.5.19:** Sample location of WTX-SEAST 4 (Tascotal Formation (Ta)) collected along Ranch Road 169 about 20 km (12.42 mi) south of the intersection of U.S. Highway 67 and Ranch Road 169 southeast of Marfa in Presidio County. Modified from Barnes and others (1979).

---

Ninety zircon grains were separated from a sample of the basal volcanic sediment apron of the Tascotal Formation and analyzed on the University of Houston's LA-ICP-MS. Individual analyses displaying a discordance of  $\geq 30\%$  were discarded and the age of the tuffaceous member was calculated from 26 analyses on a Tera-Wasserburg plot. In addition, only zircon grains analyses that displayed similar or identical  $^{208}\text{Pb}/^{238}\text{U}$  and  $^{207}\text{Pb}/^{235}\text{U}$  ages were included in the age calculation. This study reports with 95% confidence an age of 32.72 Ma  $\pm 0.84$  with an MSWD= 6.2. This age provides support that ignimbrite flare-ups and local volcanism in the central Trans-Pecos igneous province had ceased by 32.72 Ma (Fig.5.20).

### Tascotal Formation: WTX-SEAST 4

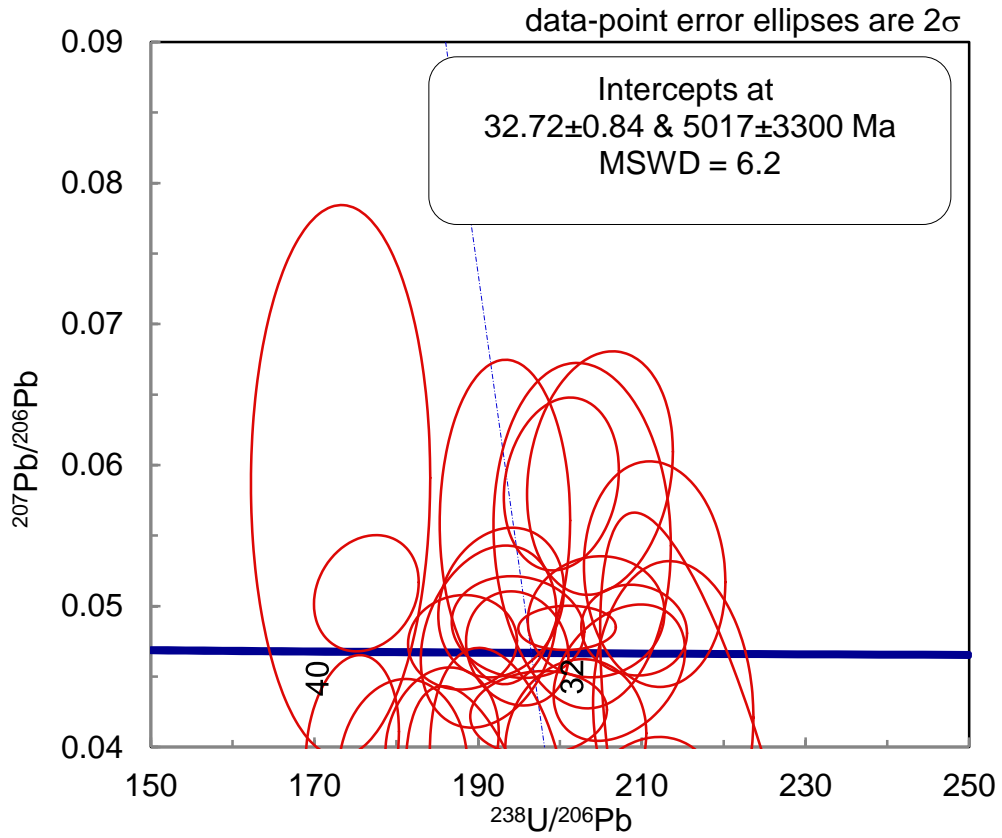


**Fig.5. 20:** This study reports with 95% confidence an age of  $32.72 \text{ Ma} \pm 0.84$  (all errors  $2\sigma$ ) with an MSWD= 6.2.

---

### **g. Chinati Mountains**

The Chinati Mountains caldera complex, more commonly referred to as the Chinati Mountains, is located about 45 km (25 mi) southwest of Marfa, Texas in Presidio County and lies in the southern Basin and Range Province (Duex and Henry, 1981). The Chinati Mountains include two eruptive centers responsible for thick accumulations of volcanic strata, the Infiernito caldera and the younger Chinati Mountain caldera which truncates the southwestern portion of the Infiernito. Upper Pennsylvanian and Permian carbonates that crop out along the northern, eastern, and southern edges of the Chinati Mountain caldera are the oldest pre-volcanic strata exposed in the Chinati Mountains affected by Laramide-style compressional deformation (Duex and Henry, 1981; Amsbury, 1958; Rix, 1953; Rigby, 1953; Skinner, 1940). In the northern portion of the range the carbonates have been described as silty and sandy having a lower detrital influence toward the south (Duex and Henry, 1981). Broadly folded and thrust faulted marine carbonates and terrigenous siliciclastics of Early to Middle Cretaceous age overlie the Permian rocks found along the border of the Chinati Mountains caldera with the thickest accumulations being documented in the Loma Plata anticline. The Loma Plata Formation is Early Cretaceous (127-99.6 Ma) in age and comprised predominantly of limestone and interbedded marl with some bulk shales and nodular limestones with thicknesses exceeding 730 m (2,200 ft) in some areas (Barnes *et al.*, 1992).

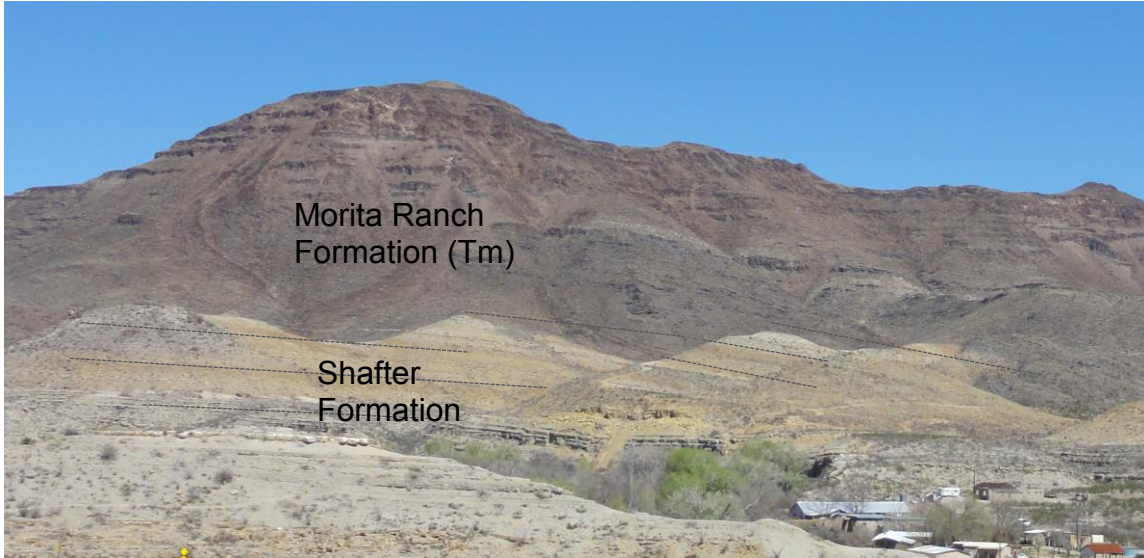


**Fig.5.21:** Field-photograph displaying relationship of the flat-lying Morita Ranch Formation above and underlying Cretaceous Shafter Formation. Sample location of WTX-BB 10 (Morita Ranch Formation) is located about 1 km (0.6 mi) north of Shafter along U.S. Route 67 where the Morita Ranch Formation rests unconformably on the Shafter Formation.

The relatively flat-lying Morita Ranch formation rests with a marked angular unconformity on the broadly folded and thrust faulted Early to Late Cretaceous strata and was analyzed in this study to refine the cessation of Laramide-style compression in this region (Fig.5.21). The Morita Ranch Formation and the rocks of the Infiernito caldera are the oldest rocks in the Chinati Mountains volcanic sequence and are postulated to have occurred coevally (Duex and Henry, 1981). The sequences are adjacent to the Chinati Mountains caldera and disconformably overlie Early to Late Cretaceous sediments; the youngest formation in this area is documented as the Cenomanian aged Buda Limestone (Bedinger *et al.*, 1989). In 1966, Dietrich redefined the Morita Ranch Formation in the Presidio area to include all volcanic and sedimentary rocks that crop out between pre-Tertiary strata and the Perdiz Conglomerate. The Perdiz Conglomerate and similar gravel

deposits are Late Tertiary to Quaternary aged fanglomerate of highly variable composition with thicknesses that exceed 500 ft in the Marfa-Presidio County area that unconformably overlie the Chinati Mountains Tertiary volcanic sequence.

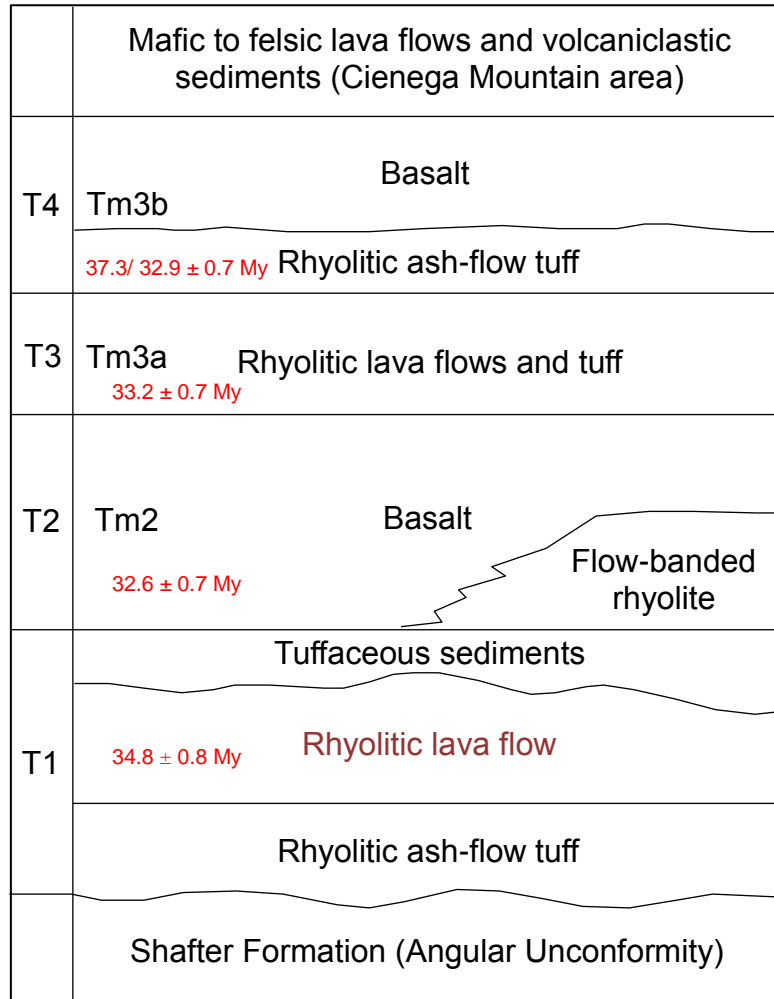


**Fig.5.22:** The Morita Ranch Formation includes informal members 1 through 4 (ascending), and has been previously dated by K-Ar methods:(1) "Member 4" sample of rhyolite dated at 34.8 ±0.8 m.y.; correlated with member 6 of Shely Group, but stratigraphic position relative to member 3 not established; (2) "Member 3", sample of rhyolite dated at 32.6 ±0.7 m.y.; (3) "Member 2", sample of rhyolite dated at 33.2 ±0.5 m.y.; and (4) "Member 1" rhyolite flow two samples dated at 37.3 +/-0.7 and 32.9 +/-0.7 m.y. (Henry *et al.*, 1986).

Four members of the Morita Ranch Formation were described from exposures found southeast of Shafter, TX including, from base to top: Tm2 (unit T2 of Rix), Tm3a (unit T3 of Rix), Tm3b (lower part of unit T4 of Rix), and

---

Tm4 (upper part of T4 unit of Rix) (Fig.5.22)(Duex and Henry, 1981). The basal volcanic layer of the Morita Ranch Formation (Tm2) that was sampled and analyzed in this study is a lithic, moderately welded, rhyolitic ash-flow tuff that is flat-lying and contains some normal faults from Basin and Range extension (Duex and Henry, 1981). Directly overlying this basal ash-flow tuff is a thick, but laterally discontinuous porphyritic rhyolite flow that has an autobreccia zone at its base, which has been interpreted by Duex and Henry to be parts of a single flow (Rix, 1953). At the top of the Tm2 member is a thin porphyritic rhyolite and a poorly exposed sequence of bedded tuffs with interbedded minor mudflows (Duex and Henry, 1983). The presence of biotite in several of the Morita Ranch Formation members and the rocks of the Infiernito caldera not only suggest their correlation, but distinguish them from the Chinati Mountains Group and more alkaline igneous rocks in the Trans-Pecos Texas regions that are devoid of the mineral. The previously published K-Ar ages for the members of the Morita Ranch Formation provide partial constraint, but display inaccuracies; i.e. younger ages for older members.

The Infiernito caldera rocks have been grouped into four genetic sequences to better explain the geologic history including, from base to top, precollapse volcanic strata, ash-flow tuffs of the main eruptive event, postcollapse volcanic units, and intrusion of the Ojo Bonito resurgent dome (Henry and Price, 1984). The precollapse volcanic strata and ash-flow tuffs of the main eruptive event that occurred around 37 Ma have been tilted to the north by the intrusion of the resurgent dome (Henry and Price, 1984; Duex

---

and Henry, 1983). Postcollapse units have been observed symmetrically dipping away from the main ash-flow tuff to the east, west, and north (Duex and Henry, 1981). The southern portion of the Infiernio caldera is truncated and presumably covered by the collapse of the Chinati Mountain caldera.

The Chinati Mountains caldera is the best-exposed resurgent caldera of the Chinati caldera complex. The exposed extrusive products show a systematic whole-rock and trace-element chemical variation that can be attributed to fractional crystallization of parent magma (Duex and Henry, 1981). Flows and tuffs of more than 1,000 m (3,300 ft) comprise the Chinati Mountains Group, erupted from the Chinati Mountains caldera following the volcanic activity of the Infiernio caldera. The Chinati Mountain caldera complex Rix (1953), Amsbury (1958), and Cepeda (1977) have noted the stratigraphic nomenclature of the flows and tuffs in the Chinati Mountain Group, the most geologically notable being the eruption of the Mitchell Mesa Rhyolite ash-flow tuff, which is the most extensive ash-flow tuff of the Trans-Pecos volcanic field (Duex and Henry, 1981). The Mitchell Mesa Rhyolite ash-flow tuff covered an area of over 1,000 km<sup>3</sup> (240 mi<sup>3</sup>) and was responsible for the formation of the Chinati Mountains caldera (Duex and Henry, 1981). The Tm2 member of the Morita Ranch Formation collected for analysis was the stratigraphically lowest flat-lying volcanic member in this range unaffected by compressional deformation collected for analysis in this study.

---

### **i. Morita Ranch Formation**

The Morita Ranch Formation, initially assigned to the Buck Hill volcanic series by Rix (1952, 1953) was later remapped and given its name by Dieterich (1966). Dieterich (1966) described four members of the formation (Tm2, Tm3a, Tm3b, and Tm4) from exposures located southeast of Shafter based upon initial observations and classified members (T1, T2, T3, and T4) of Rix (1952, 1953) (Fig.5.21). The four members include, in ascending order, Tm2, Tm3a, Tm3b, and Tm4. Tm2 correlative to the T2 member of Rix (1952,1953) is composed of predominantly black porphyritic basalt with abundant large feldspar phenocrysts; Tm3a coincides to unit T3 of Rix (1952,1953) and consists of thick sequences of rhyolitic flows and tuffs; Tm3b is equivalent to the lower portion of T4 from Rix (1952, 1953) and is composed of rhyolitic ash-flow tuff with abundant feldspar and minor quartz phenocrysts; and lastly Tm4 which is the upper portion of the T4 unit of Rix (1952, 1953) has been classified as medium- to fine- grained basalt (Duex and Henry, 1981). Rix (1952, 1953) documented tuff and olivine basalt below the Tm2 unit of Dieterich (1966) which he labeled T1 that pinch out both north and south of Shafter that were not recognized by Dieterich (1966) in the Presidio area. Reconnaissance field work done by Duex and Henry (1981) have indicated that there is a sequence of rock just east of the Chinati Mountains Caldera complex boundary and north of Shafter that is in part correlative with what Rix described and mapped as T1.

The lowest volcanic layer observed was defined in a study by Duex and Henry (1981) and is more than likely what Rix (1952,1953) refers to as the basal tuff and described as a lithic, moderately welded, rhyolitic ash-flow tuff that has been faulted and possibly folded with underlying Permian and

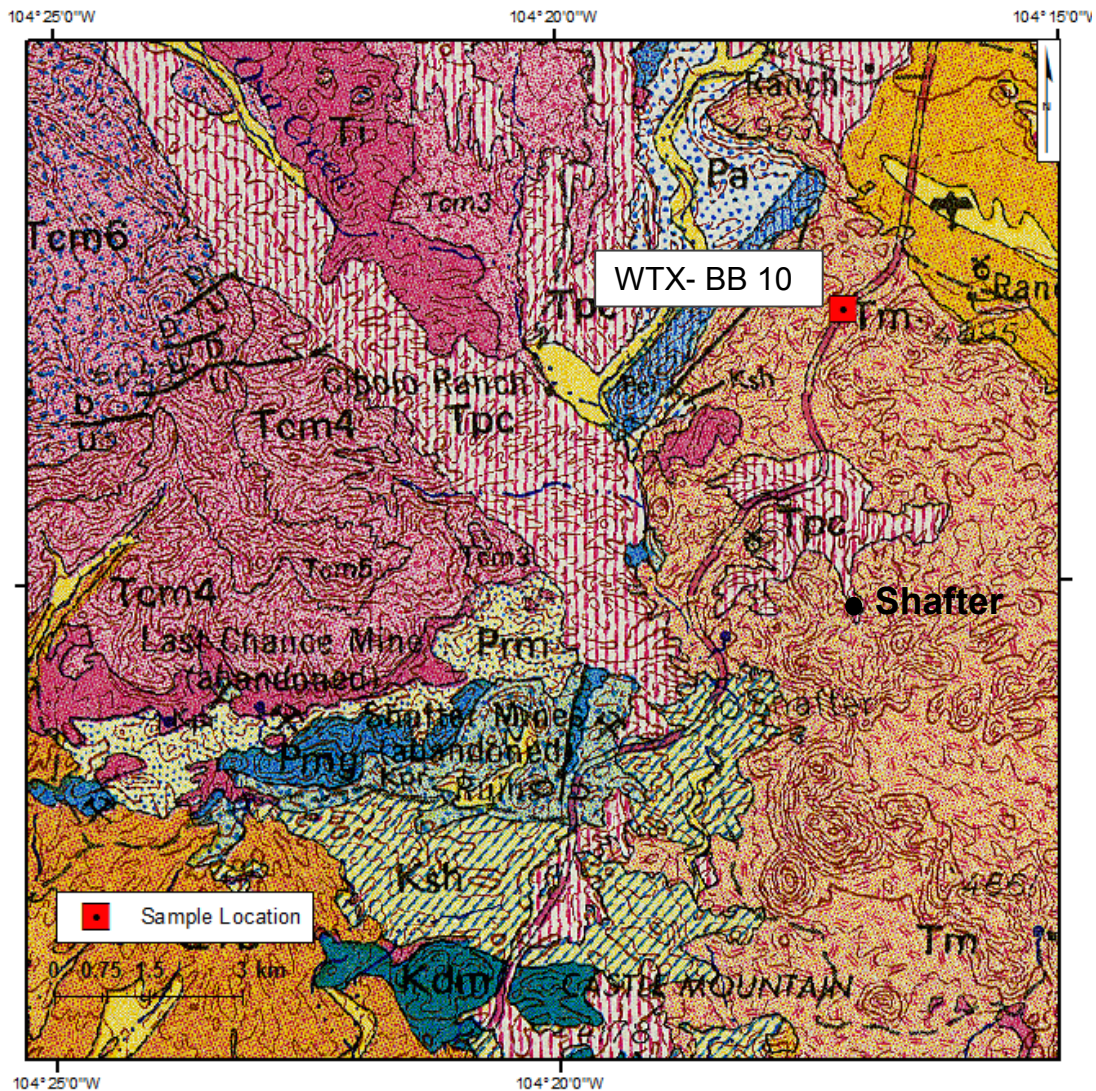


**Fig.5.23:** Sample location of WTX-BB 10 (Morita Ranch Formation) collected about 1 km (0.6 mi) north of Shafter along U.S. Route 67 where the Morita Ranch Formation rests unconformably on the Shafter Formation.

Cretaceous sedimentary rocks. Resting unconformably on top of the faulted ash-flow tuff is a flat-lying, thick but laterally discontinuous porphyritic rhyolite flow unaffected by thrust faults or folds with zones of thick autobreccia at the

---

base (Duex and Henry, 1981). the porphyritic rhyolite is a series of thinly bedded and poorly exposed tuffs and minor mudflows that were not documented by Rix in his description of T1 (Duex and Henry, 1981). The presence of biotite in the Morita Ranch Formation also occurs in the rocks of the Infiernito Caldera and distinguishes it from the younger Chinati Mountains Group and from other more alkaline igneous rocks of the Trans-Pecos igneous province (Duex and Henry, 1981).

The sample analyzed in this study was collected from the flat-lying, thick but laterally discontinuous porphyritic rhyolite flow categorized into T1 unaffected by thrust faults or folds that overlies with a potential unconformity the basal ash-flow tuff. The basal ash-flow tuff was not chosen for analysis based on the field observations made by Henry and Duex (1981) that this unit was thrust faulted and broadly folded along with the underlying Cretaceous and Permian strata. Thus, the limit of Laramide compressional deformation has been placed at the top of this basal ash-flow tuff. The rhyolite flow of member T1 was collected about 1 km (0.6 mi) north of Shafter along U.S. Route 67 where the Morita Ranch Formation is observed resting with a marked angular unconformity atop the Cretaceous aged Shafter Formation (Fig.5.23) (GPS Location: 29.87272, -104.28577). Fifteen zircon grains were separated and collected from the rhyolitic lava flow of the T1 member from Rix (1952, 1953) Twelve analyses were included in the age calculation with multiple exclusions due to Pb-204 contamination and an age of 36.57 Ma

$\pm 0.80$  is reported in this study with 95% confidence and an MSWD= 2.8

(Fig.5.24).

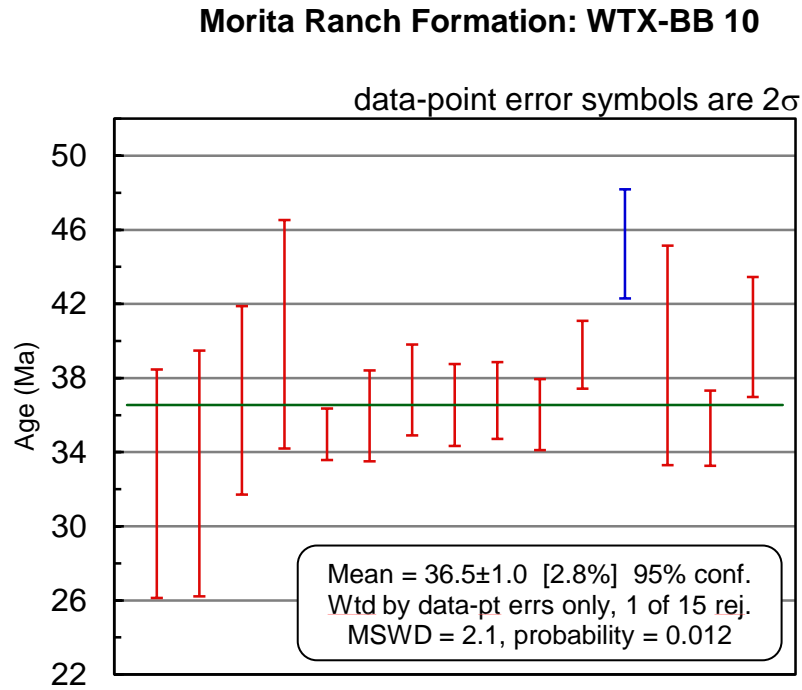


**Fig.5.24:** Approximately 12 analyses were included in the Normalized Age-Probability Distribution Chart calculation with multiple exclusions due to Pb-contamination and with 95% confidence a mean age of 36.57 Ma  $\pm 0.80$  (all errors  $2\sigma$ ) with an MSWD= 2.8.

---

#### **h. Big Bend National Park: Chisos Mountains**

Middle-Tertiary volcanism and plutonism is estimated to have occurred in the park from 47-28 Ma and is regarded as a result of incoming arc magmatism/plutonism and slab removal processes upon the cessation of the Laramide orogeny (Page *et al.*, 2007). The earliest volcanism to occur in Big Bend National Park consisted of lavas and tuffs from the Chisos Group. The Chisos Group erupted between 47 and 33 Ma from poorly known sources in southwestern Big Bend National Park and neighboring areas in Mexico and are exposed south and west of the Pine Canyon Caldera and extend into Mexico (Maxwell *et al.*, 1967; Henry and McDowell, 1986; Henry and Davis 1996). These rocks include the basal mafic lava flows of the Alamo Creek Basalt (TABC) that we have interpreted to be associated with the incoming arc arriving at the present-day Texas-New Mexico border (47 Ma), and later silicic ash-fall, and ash-flow tuffs (47-32 Ma) that are interpreted in this study to have been emplaced prior to folding and tilting related to compression (Davidson *et al.*, 2012; Davidson *et al.*, 2013)

Major volcanic ignimbrite flare-ups and plutonism occurred in the park from 31-28 Ma of which the principal features include numerous flat-lying volcanic flows extruded from a complex system of volcanic vents and lava domes in the western part of the park and the Pine Canyon Caldera Complex, which comprises the peaks of the Chisos Mountains (White *et al.*, 2006). Major laccolithic complexes developed in response to the compressional deformation associated with the migrating orogenic front and intruded

---

Cretaceous and Early Tertiary carbonate and siliciclastic rock (Page *et al.*, 2007). Timing of the emplacement of the Dagger Flats sills is closely contemporaneous with the eruption of large-volume ignimbrites having occurred slightly before at about  $32.47 \pm 0.41$  Ma and are thought to be related to other alkali gabbroic to monzonite intrusive bodies in the northeast quadrant of the park such as the McKinney Hills, Rosillos Mountains, and Grapevine Hills (Carman, 1994; Morgan *et al.*, 2006). The flat-lying South Rim Formation sitting with a pronounced angular unconformity above the volcanic sequence of the Chisos Formation erupted from the Pine Canyon caldera complex around 32 Ma and is interpreted in this study to be the first ignimbritic flare-up unaffected by compressional deformation in this area (Miggins *et al.*, 2007).

The Pine Canyon caldera complex formed originally as a volcano that elevated topography throughout the Chisos Mountains (Ogley, 1978; Barker *et al.*, 1986). The Burro Mesa Formation is the youngest major volcanic and intrusive episode in the park and has been previously mapped as the Burro Mesa Member of the South Rim Formation includes the Wasp Spring Member and the Burro Mesa Rhyolite Member (Benker, 2005; White *et al.*, 2006). The Burro Mesa Formation is comprised predominantly of ash-flow tuffs that erupted from small localized vents and lava domes in the southwestern region of the park (Holt, 1998; Parker, 2002). There are many large intrusive bodies including Grapevine Hills, McKinney Hills, and Rosillos Mountains throughout Big Bend National Park that were emplaced around the same time as the

---

Pine Canyon caldera (reported  $^{40}\text{Ar}/^{39}\text{Ar}$  ages of 33-32 Ma), but the events are not thought to be related (Miggins et al., 2007). Alkali basalt and hawaiite diatreme root zones collected from the Pitcock Rosillos Ranch have yielded groundmass K-Ar ages of  $46.12 \pm 0.36$  and  $46.78 \pm 0.14$ , but have been interpreted by Befus *et al.* (2009) to be derived from the Christmas Mountains to the west (Befus, 2008). This study makes an effort to better understand the geologic and chronologic history of structural development before, during, and after the Tertiary siliciclastic and volcanic deposits in this area were deposited and emplaced in an attempt to refine the cessation of compressional deformation related to the Laramide orogeny. Critical field observations and geochronologic analysis of the volcanic stratigraphy below and above the Laramide unconformity in this area have been made and are reported below in this chapter.

#### **i. Chisos Formation**

The Chisos Formation was originally defined by Maxwell and others (1967) to include, from base to top, the Alamo Creek Basalt, Ash Spring Basalt, Bee Mountain Basalt, Mule Ear Spring Tuff, and Tule Mountain Trachyandesite (Fig.5.25). These distinct members are separated by undifferentiated tuffaceous sedimentary rock including conglomerate, sandstone, mudstone, tuff, tuffaceous sandstone and clay, and minor occurrences of lacustrine limestone (Miggins *et al.*, 2011). Henry and Davis (1996) renamed this formation the Chisos Group as they felt the volcanic flows were widespread and identifiable features of the Trans-Pecos region.

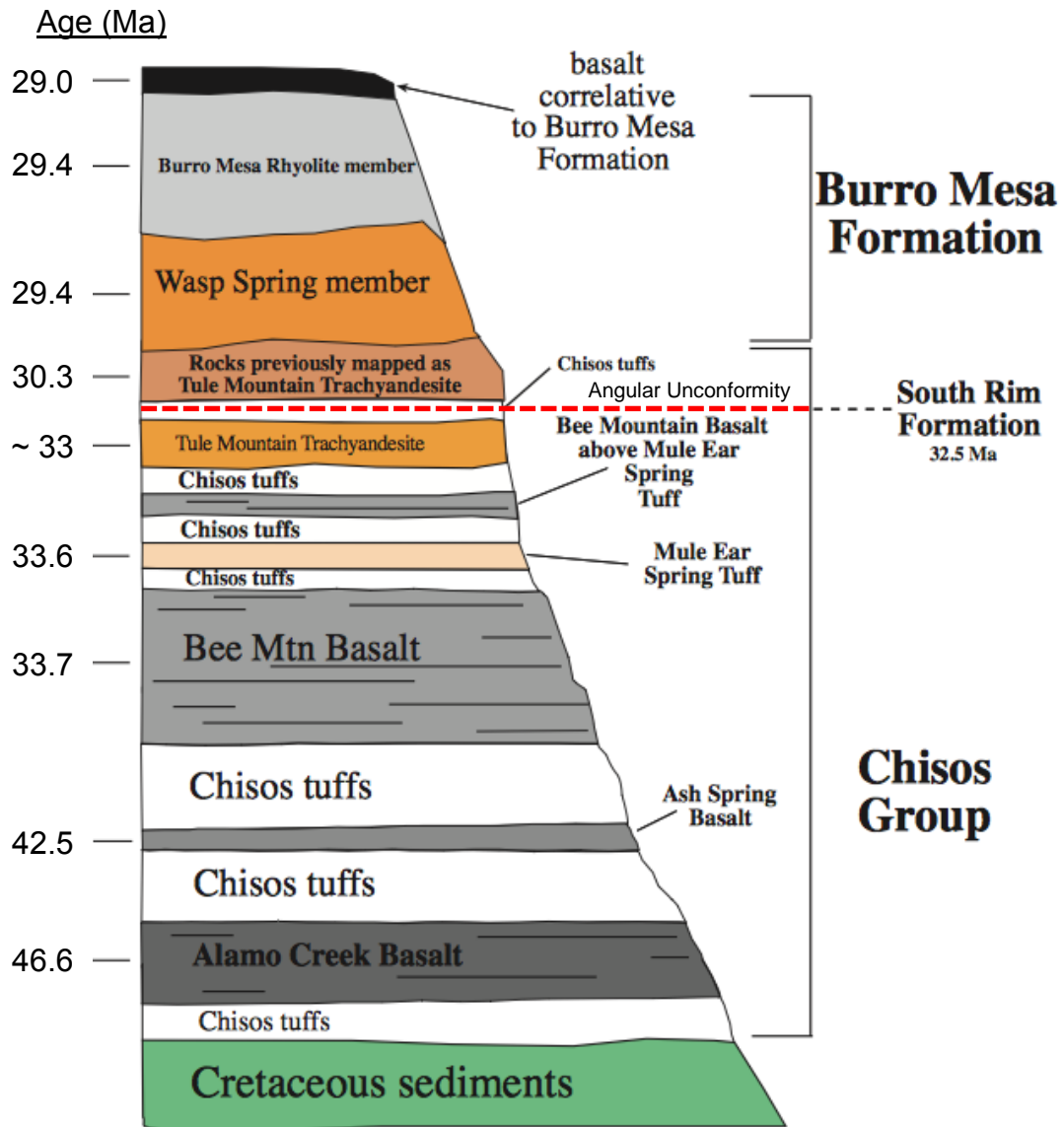


**Fig.5.25:** Generalized volcanic stratigraphy of the Big Bend National Park Group modified from Miggins and others (2011).

Bee Mountain Basalt, Mule Ear Spring Tuff, and Tule Mountain Trachyandesite) were reclassified as formations. The Ash Spring Basalt is not found outside the confines of the park and therefore was not recognized as a formation in the Chisos Group which are mafic and felsic rocks exposed predominantly on the western side of the park by Henry and Davis (1996).

---

The Alamo Creek Basalt has been reported to consist of up to eight individual flows with the oldest flow having yielded an  $^{40}\text{Ar}/^{39}\text{Ar}$  age of  $46.62 \pm 0.07$  my from plagioclase that range in composition from basalt, through trachybasalt and basaltic trachyandesite, to trachyandesite (Henry and Davis 1996; Carman *et al.*, 2003; Miggins *et al.*, 2006). Exposures of the Alamo Creek Basalt are limited to the western side of the park where they unconformably overlie Upper Cretaceous and Lower Tertiary (Black Peaks Fm., Hannold Hill Fm., and Canoe Fm.) sedimentary rocks with the thickest sections found west of the Mule Ear Peaks and Punta de la Sierra (Miggins *et al.*, 2011). The Alamo Creek Basalt is overlain by thick sections of air-fall tuffs and the following member comprised of two or more lava flows of the Ash Spring Basalt that are petrographically and geochemically similar to the Alamo Creek Basalt (Maxwell *et al.*, 1967; Miggins *et al.*, 2011).

The Ash Spring Basalt consists of porphyritic basalt with abundant plagioclase phenocrysts and yielded an  $^{40}\text{Ar}/^{39}\text{Ar}$  age of 42.5 Ma that is consistent with reported ages from Henry and Davis (1996) (Miggins *et al.*, 2011). The thickest member of the Chisos Formation is the Bee Mountain Basalt which follows the Ash Spring Basalt and is thought to consist of at least five lava flows below the Mule Ear Spring Tuff and three to four flows above the Mule Ear Spring Tuff. The Bee Mountain Basalt ranges in composition from trachybasalt to basalt with abundant plagioclase and ranges and has yielded an  $^{40}\text{Ar}/^{39}\text{Ar}$  age of  $33.74 \pm 0.09$  Ma for the lower portion of the member below the Mule Ear Spring Tuff (Miggins *et al.*, 2006).

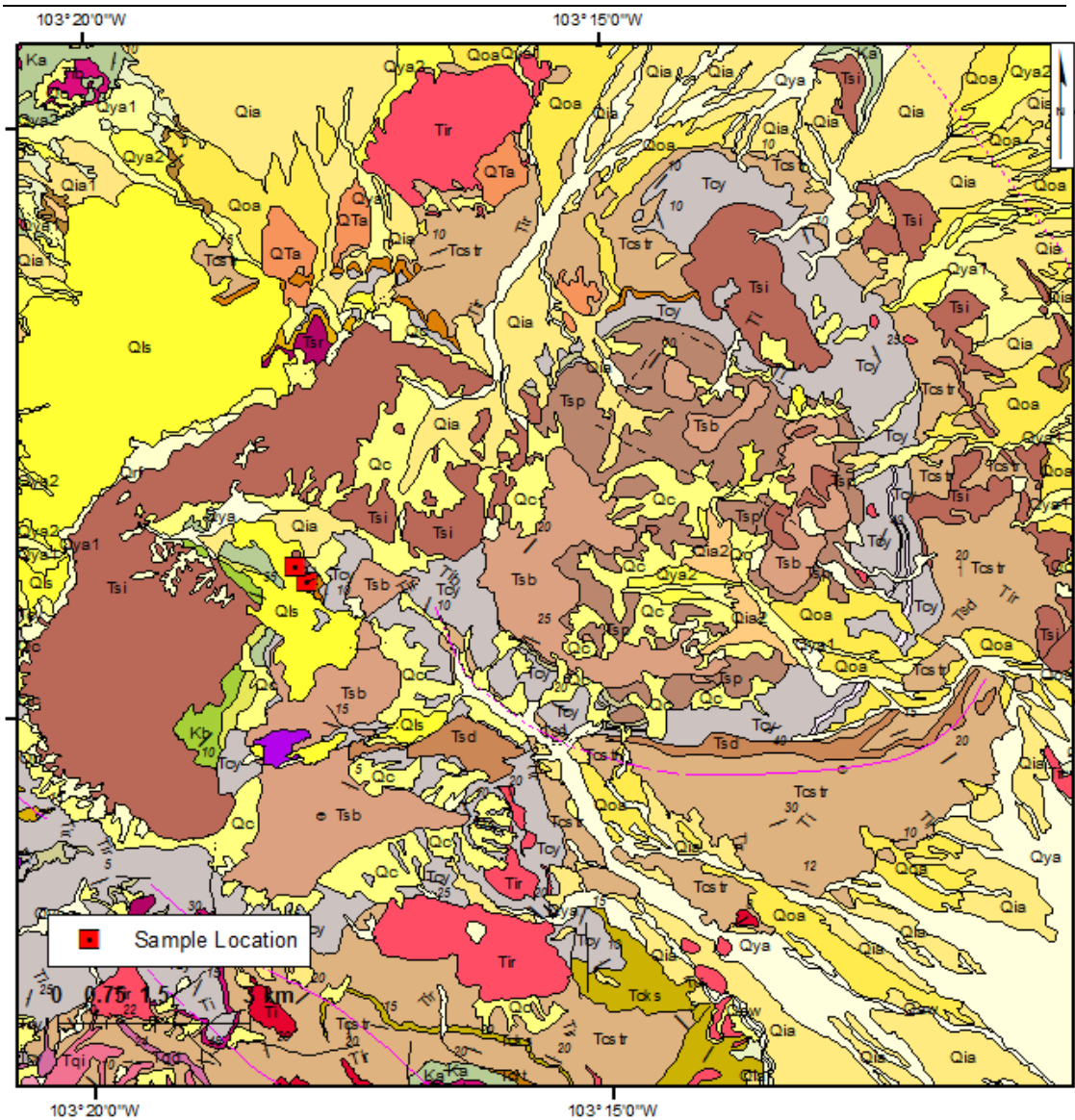


**Fig.5.26:** Map displaying sample locations of the Chisos Group (WTX-BB 19) and South Rim Formation (WTX-BB 18) within the collapsed Pine Canyon Caldera Complex in Big Bend National Park. Tcy on the map represents the Chisos Formation and Tsb, Tsp, and Tsd represent the South Rim Formation.

The Mule Ear Spring Tuff is considered to be the only regional ash-flow tuff that occurs in the park has yielded an  $^{40}\text{Ar}/^{39}\text{Ar}$  age of  $33.5 \pm 0.21$  Ma from plagioclase (Miggins *et al.*, 2006). The Mule Ear Spring Tuff varies in composition from non-welded to moderately-welded tuff with lithic clasts and pumice and maintains a nearly uniform thickness that ranges from 6-8 m (18-

---

24 ft) (Henry and Davis, 1996). The Tule Mountain Trachyandesite is the stratigraphically highest distinguishable member exposed on the western side of the park in the Chisos Formation and has been described by Henry and Price (1996) to consist of a single flow that is intermediate to moderately silicic in composition with an  $^{40}\text{Ar}/^{39}\text{Ar}$  of approximately 33 Ma. The uppermost portion of the Tule Mountain Trachyandesite exposed southwest of Tule Mountain to Sierra del Chino previously identified by Maxwell (1967) have been reclassified as rocks of the Burro Mesa Formation as they are compositionally distinct and vary in age ( $^{40}\text{Ar}/^{39}\text{Ar}$  of 30.3 Ma) from rocks of Burro Mesa, Tule Mountain, and Sierra Aguja rocks (Turner *et al.*, 2011; Miggins *et al.*, 2011).

The undifferentiated tuffaceous sedimentary deposited between the major lava flows of the Chisos Formation range in thickness from tens to hundreds of meters and represent a significant portion of its stratigraphy (Miggins *et al.*, 2011). Exposures are found predominantly throughout the western portion of the park and include air-fall deposits, tuffaceous sediments, conglomerates, and reworked ponded tuffs such as those found at Cerro Castellan and west of Mule Ear Peaks (Miggins *et al.*, 2011).

All units of the Chisos Formation are heavily folded and thrust faulted. Intrusions are speculated to have facilitated some of the deformation of the Chisos Formation, but extensive folds and thrust faults within the formation are trending northwest-southeast indicating that they were most likely deformed along with the Tertiary and Cretaceous strata below by Laramide

compressional deformation as the advancing orogenic front reached present-day Big Bend National Park.

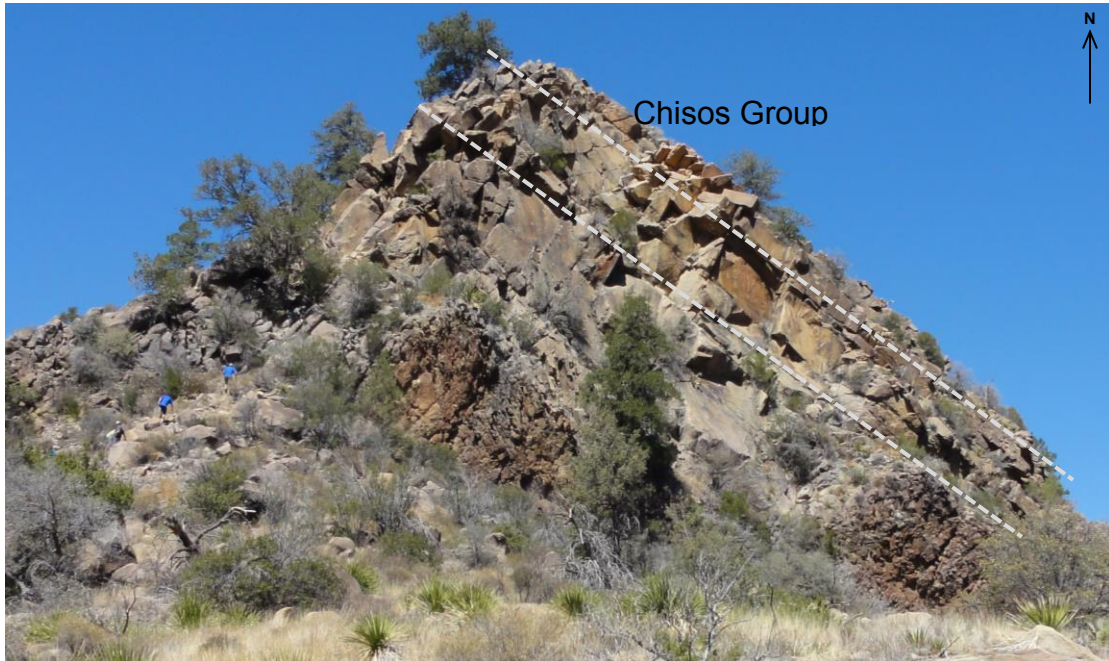


**Fig.5.27:** Field-photograph displaying the sample location of the Tule Mountain Trachyandesite (WTX-BB 19).

A sample of the Tule Mountain Trachyandesite was collected near the Chisos Mountain Lodge from the top of the Chisos Formation exposed northwest of Casa Grande at the end of Chisos Basin Road about 10 km (6 mi) from the junction of Chisos Basin Road and U.S. State Highway 118/ Texas State Highway 170 (Fig.5.26; Fig.5.27) (GPS Location: 29.27095, -103.30025). Twenty zircon grains were separated from a sample of the Tule Mountain Trachyandesite and analyzed on the University of Houston's LA-ICP-MS. Twelve analyses were included in the age calculation with exclusions due to Pb-204 contamination and an age of 31.73 Ma  $\pm$ 0.56 with 95% confidence is reported in this study with an MSWD= 2.2. The Trachyandesite of the Chisos Formation is considered in this study to be the

stratigraphically highest unit in the Big Bend National Park region to be affected by Laramide compressional deformation (Fig.5.29).

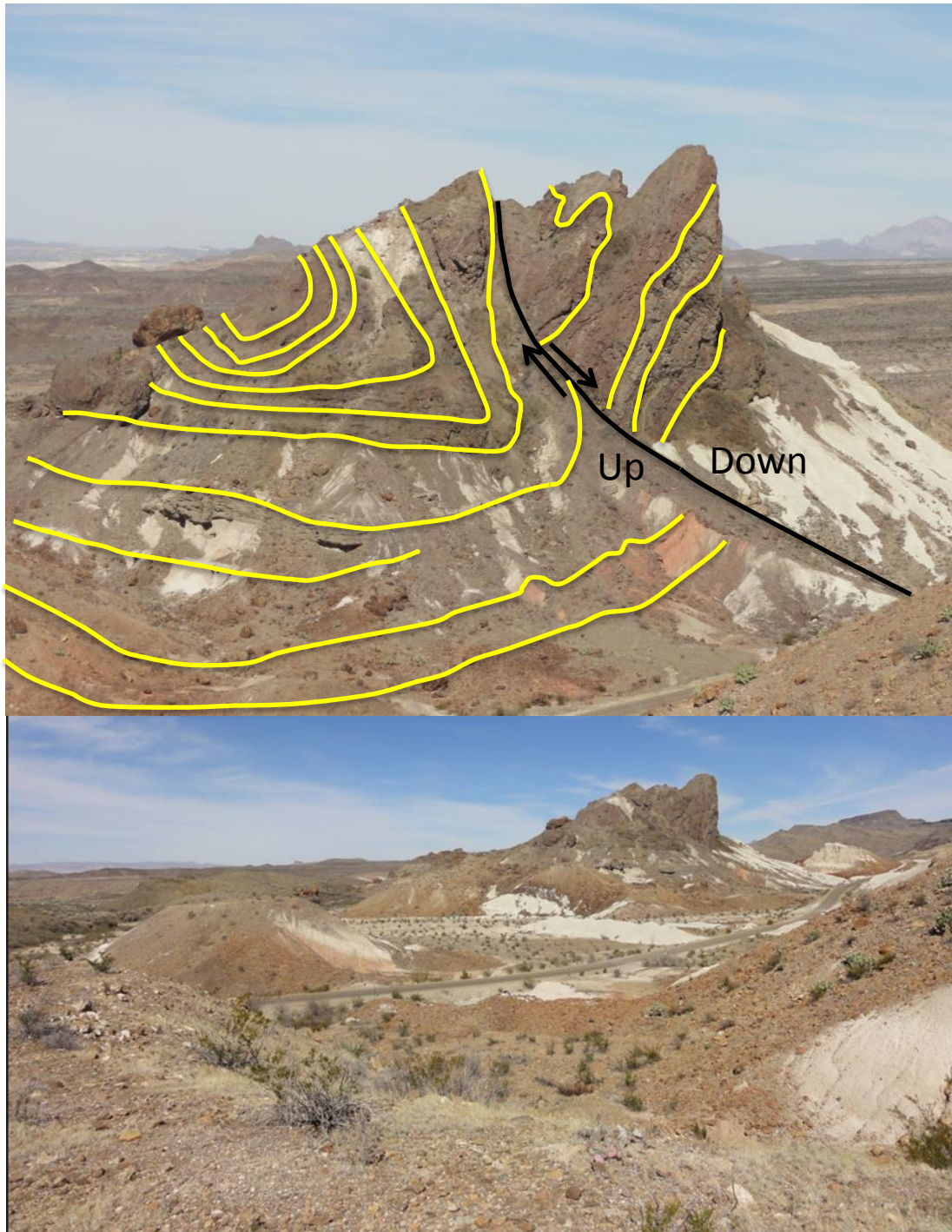


**Fig.5.28:** Field-photograph displaying compressional deformation in the Chisos Formation Bee Mountain Basalt Unit just east of Cerro Castellan in the southwestern portion of the park, **A.** Annotated , **B.** Unannotated

### Chisos Formation: WTX-BB 19

data-point error ellipses are  $2\sigma$

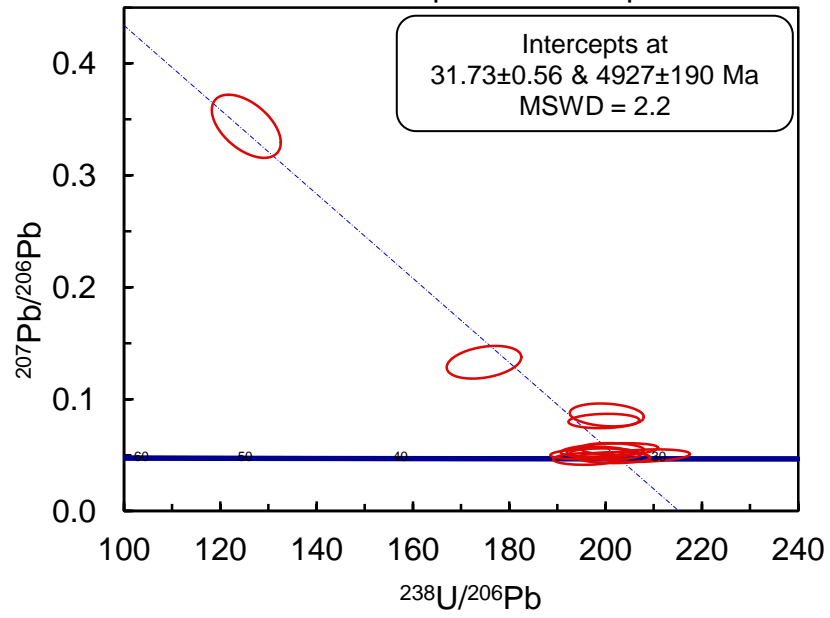


**Fig.5.29:** Approximately 12 analyses in the age calculation with exclusions due to Pb contamination and report with 95% confidence an age of  $31.73 \text{ Ma} \pm 0.56$  (all errors  $2\sigma$ ) with an MSWD= 2.2.

---

## ii. South Rim Formation

The flat-lying South Rim Formation has recently been revised based upon petrologic, geochemical, and petrographic studies implemented by Benker (2005) and White (2006) and geochronologic analysis completed by Turner and others (2011) that has refined the original work of Maxwell and others (1967). Originally suggested by Benker (2005) and White (2006), the new data has allowed for the removal of rocks equivalent to the Burro Mesa Riebeckite Rhyolite and Wasp Spring Flow Breccia from the South Rim Formation initially described by Maxwell and others (1967) and reclassified as the Burro Mesa Formation (Turner *et al.*, 2011). Fundamental reasoning behind the exclusion of the Burro Mesa Formation from the South Rim Formation includes a 3 my age difference between the formations, restriction of the Burro Mesa Formation to the western portion of the park, and differences in petrographic and trace element composition (Benker, 2005; Miggins, 2004, 2007, and 2008; Turner *et al.*, 2011).

The members of the South Rim Formation are restricted to eruptive rocks of the Pine Canyon Caldera magmatic system that developed originally as a large volcano responsible for elevated topography throughout the Chisos Mountains prior to caldera formation (Ogley, 1978; Barker *et al.*, 1986). The South Rim Formation originally described by Maxwell (1967) has been revised by Turner and others (2011) to include these informal members, in ascending order, the Pine Canyon Rhyolite Member, Boot Rock Member, and Emory Peak Rhyolite Member. The Pine Canyon Rhyolite Member is

---

distributed within the caldera boundary and is the primary fill of the Pine Canyon Caldera complex (Ogley, 1978; Barker *et al.*, 1986; Turner *et al.*, 2011). The member ranges in thickness from 400 to over 1,000 m (1,200-3,000 ft) with a minimum thickness of 300 m (900 ft) reported by Ogley (1978) and is predominantly peralkaline rhyolite composed of several cooling units of heavily welded vitrophyre to welded ash-flow tuff (Drenth and Finn, 2007; Turner *et al.*, 2011).

The Boot Rock Member is exposed in the Pine Canyon Caldera and South Rim area and is composed of quartz trachyte and rhyolite lava, tuff, and maar-surge deposits that erupted from vents surrounding the caldera post-collapse (Barker *et al.*, 1986; Urbanczyk and White, 2000; Turner *et al.*, 2011). The Pine Canyon Rhyolite and the boot Rock Members share a common magma source that has been interpreted to have evolved predominantly through crystal fractionation of a mafic melt with an alkali basalt composition (Benker, 2005; White *et al.*, 2006; Turner *et al.*, 2011). The Emory Peak Rhyolite Member erupted from intracaldera and extracaldera vents and consists of lava, rheomorphic tuff, and vitrophyre (Turner *et al.*, 2011). The unit is exposed at Emory Peak and the blue Creek Ranch area and is the same age as the rocks found at Emory Peak (Turner *et al.*, 2011). Parental magmas of the Emory Peak Rhyolite Member are speculated to have likely developed contemporaneously from partial melting of a lower crustal source (Benker, 2005; White *et al.*, 2006).

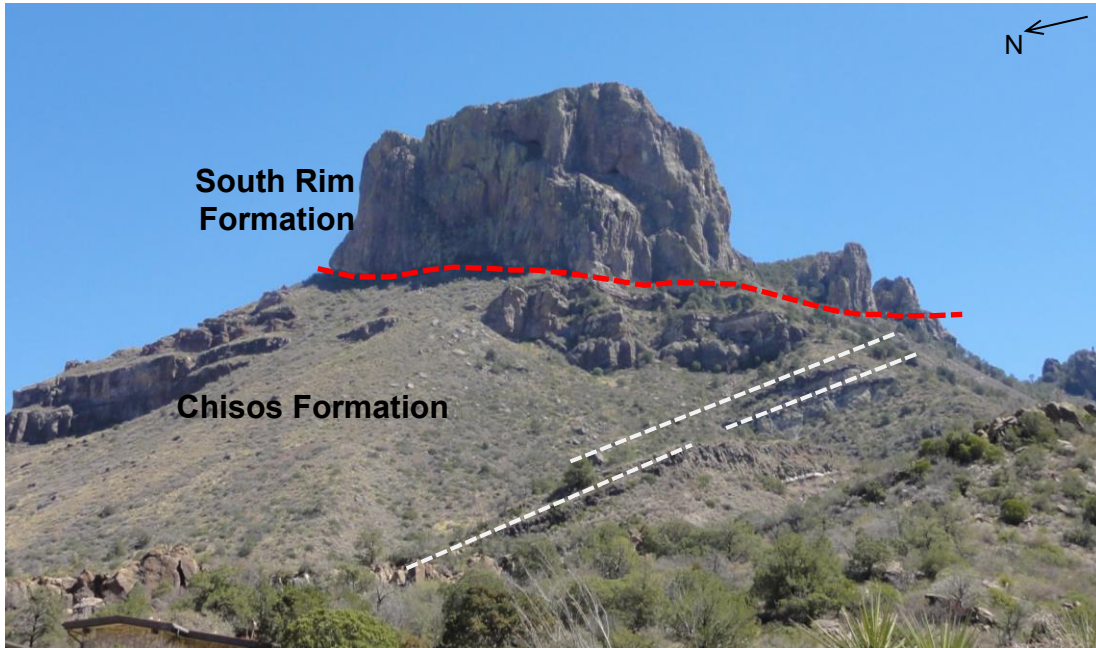


**Fig.5.30:** Field-photograph displaying relationship of the flat-lying South Rim Formation above and underlying tilted Chisos Group.

All members of the South Rim Formation are relatively flat-lying, relatively undeformed, and rest with a marked angular unconformity atop the volcanic units of the Chisos Formation. The sample analyzed in this study was collected from the Pine Canyon Rhyolite/Boot Canyon contact exposed on Casa Grande at the end of Chisos Basin Road about 10 km (6 mi) from the junction of Chisos Basin Road and U.S. State Highway 118/ Texas State Highway 170 near Chisos Mountain Lodge (GPS Location: 29.26879, -103.29823) (Fig.5.26; Fig.5.30). Twenty zircon grains were collected from a sample of the Tule Mountain Trachyandesite and analyzed. Eleven analyses were included in the age calculation with multiple exclusions due to Pb-204 contamination and an age of 31.21 Ma  $\pm$ 0.56 is reported in this study with 95% confidence and an MSWD= 2.7.

### South Rim Formation: WTX-BB 18

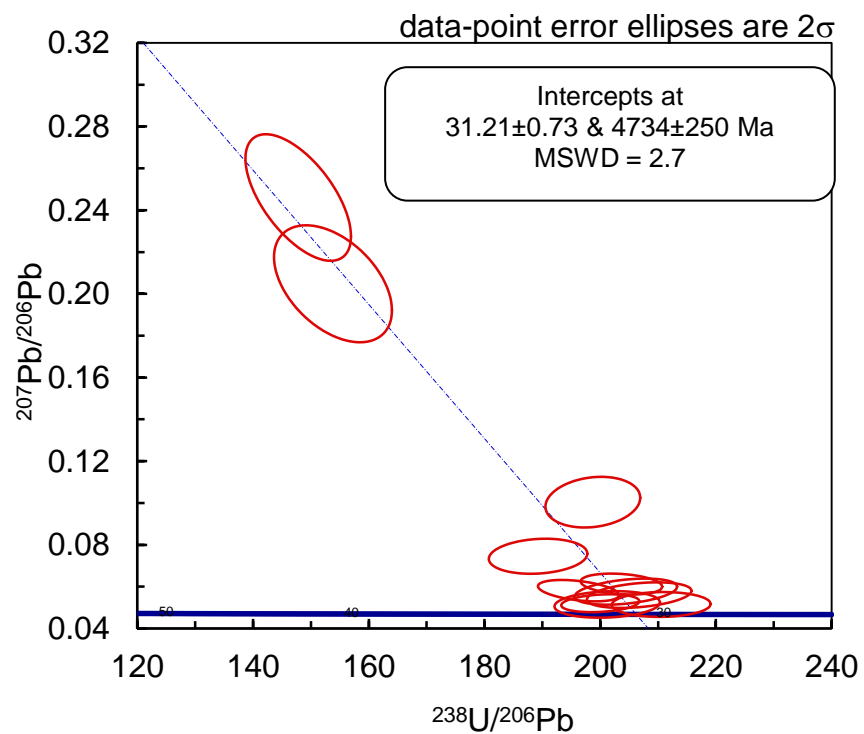


**Fig.5.31:** An age of  $31.21 \text{ Ma} \pm 0.56$  is reported in this study with 95% confidence and an MSWD= 2.7 for the Boot Rock Member of the South Rim Formation

---

### iii. Burro Mesa Formation

The Burro Mesa Formation, initially included in the South Rim Formation by Maxwell and others (1967) has been reclassified as a separate formation based upon a marked difference in age (Miggins *et al.*, 2004, 2007, and 2008) and petrographic variations described by Benker (2005) and White (2006). The Burro Mesa Formation unconformably overlies undifferentiated tuffs of the Chisos Formation and is comprised of the Wasp Spring Member and the Burro Mesa Rhyolite Member that have yielded  $^{40}\text{Ar}/^{39}\text{Ar}$  ages ranging from 29.48 to 29.25 Ma. The Wasp Spring Member reaches thicknesses of over 200 m (600 ft) with typical exposures consisting of ignimbrites containing 5-60 percent lithic clasts that vary in color from bright orange, to gray, to cream, and in some instances white (Miggins *et al.*, 2011). The units of the Burro Mesa Formation erupted from multiple vents on the western side of the park unlike the South Rim Formation which is restricted to eruptive rocks of the Pine Canyon Caldera magmatic system (Ogley, 1978; Barker *et al.*, 1986; Holt, 1998; Parker, 2002; Benker, 2005; White *et al.*, 2006; Turner *et al.*, 2011) Similar to the Emory Peak Rhyolite Member of the South Rim Formation the Burro Mesa Rhyolite Member has an  $\text{SiO}_2$  content of greater than 72%, but is more strongly enriched in FeO,  $\text{K}_2\text{O}$ , Rb, Y, Zr, Nb, and Th than the Emory Peak Rhyolite and show light REE enrichment and depletion of Ba, Sr, Ti, and K relative to the South Rim Formation (Benker *et al.*, 2005).

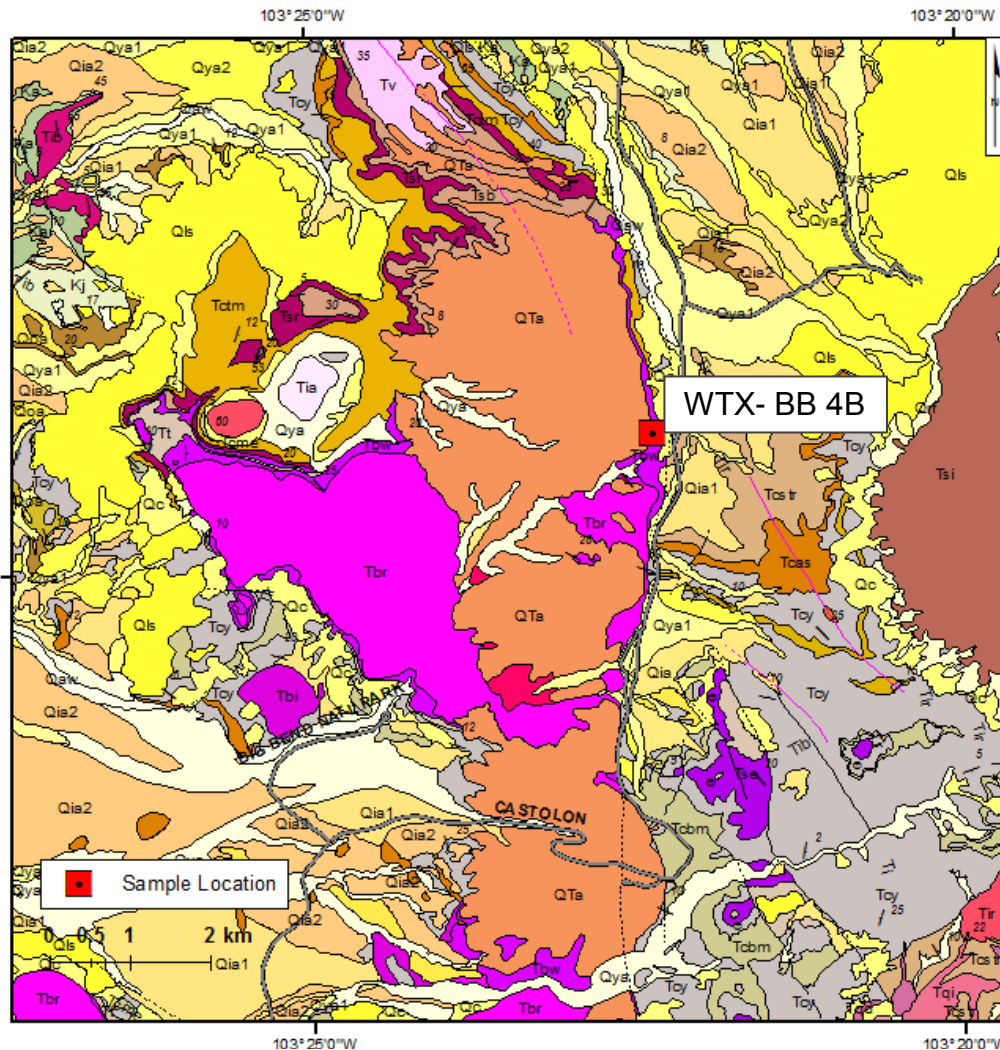


**Fig.5.32:** Map displaying sample location of the Wasp Spring Member of the Burro Mesa Formation (WTX-BB 4B) west of the Pine Canyon Caldera Complex in Big Bend National Park. Tbw represents the Wasp Spring Member of the Burro Mesa Formation and Tbr represents the Burro Mesa Rhyolite Member; Tcy, Tcbm, Tcas, and Tcs tr all represent units within the Chisos Formation. Complete legend located in Appendix A for reference.

The two members of the Burro Mesa Formation are exposed at Burro Mesa, Goat and Kit Mountains, and in various outcrops scattered between Castolon and the Chisos Mountains. The Wasp Spring Member is the basal unit of the formation and is composed of surge deposits and air-fall and ash-flow tuffs with abundant lithic fragments and fiamme (Turner *et al.*, 2011). The Wasp Spring Member is fairly recognizable throughout the park because it forms brightly colored orange to yellow cliffs near Burro Mesa Pouroff and at



**Fig.5.33:** Map displaying sample location of the Wasp Spring Member of the Burro Mesa Formation (WTX-BB 4B) west of the Pine Canyon Caldera Complex in Big Bend National Park.

Cerro Castellan along Ross Maxwell Scenic Drive. One sample collected from a butte located along Ross Maxwell Scenic Drive about 8 km (5 mi) south of the junction between U.S. State Highway 118 and Ross Maxwell Scenic Drive and another moderately welded tuff collected from the base of the member at Cerro Castellan have been analyzed in this study. An age was not obtained in this study's analysis for the Burro Mesa Formation due to abundant inclusions and inherited Proterozoic aged zircon cores. A single plagioclase crystal  $^{40}\text{Ar}/^{39}\text{Ar}$  age obtained by Miggins *et al.* (2006) of  $29.4 \pm 0.17$  Ma (Fig.5.32, Fig. 33) (29.14520, -103.49918) is used in this study to analyze the north to south age progression of the emplacement of volcanics in Trans-Pecos Texas.

---

## **i. Discussion**

In this chapter, descriptions and ages for the stratigraphically lowest flat-lying or only slightly rotated volcanic units that mark a pronounced angular unconformity with heavily thrust faulted and folded Tertiary, Cretaceous, Permian, and Precambrian aged strata and volcanics below are reported. Some rotation of the flat-lying volcanic units occurred locally in the Indio and Van Horn Mountains along normal faults related to the more recent Basin and Range extensional deformation emplaced around 24-17 Ma when extension is thought to have affected this region based on igneous ages obtained from sills and dikes (Price and Henry, 1984; Smith and Julian 1991). The reported ages in this study for the basal flat-lying volcanic units above the angular unconformity, and deformed volcanic units below the angular unconformity associated with Laramide compression in Trans-Pecos Texas help to refine the age of rocks affected by Laramide compressional deformation structures throughout the West Texas, regional uplift prior to ignimbrite flare-up, and erosional trends along this unconformity from north to south.

In addition, the relationship between the age of volcanism and definition to the cessation of Laramide-style compressional deformation is established from north to south. Sample ages obtained in this study from various regions of Trans-Pecos Texas include, from north to south, 1) the Lower Rhyolite from the Eagle Mountains; 2) the Hogeye Tuff and Bell Valley Andesite from the Indio and Van Horn Mountains; 3) the Huelster Formation

and Star Mountain Rhyolite\* from the Davis Mountains; 4) the Buckshot Ignimbrite of the southwestern Rio Grande River area; 5) the Tascotal Formation from the Alamito Creek and Green Valley area; 6) the Morita Ranch Formation from the Chinati Mountains; and 7) the Black Peaks, Hannold Hill, Canoe, Chisos, South Rim, and Burro Mesa\* Formations of the Chisos Mountains located in Big Bend National Park. These sample sites and ages listed in Table 5.4 were added to a base-map of Trans-Pecos Texas (Fig.5.31). A general younging trend from north to south of the basal flat-lying volcanic rock samples situated directly above the Laramide angular unconformity defined in Texas by relatively flat-lying, undeformed Tertiary volcanic ignimbrite deposits resting on Laramide thrust faulted and folded Tertiary-, Cretaceous-, and Permian-aged strata can be observed (Fig.5.34). Geochemical and geochronologic data from previous studies for these formations have provided age constraints that are utilized in this study to

Sample Site	Formation	Age (Ma)	Error (2 $\sigma$ )	Latitude	Longitude
Quitman Mountains	Square Peaks Volcanic Gp.	36* (K-Ar)	$\pm 0.6$	31.15051	-105.49786
Eagle Mountains	Lower Rhyolite	35.2	$\pm 0.39$	30.91382	-105.03985
Indio Mountains	Hogeye Tuff	37.34	$\pm 0.48$	30.75056	-105.00417
	Hogeye Tuff	37.65	$\pm 0.75$	30.75056	-105.00417
	Hogeye Tuff	38.02	$\pm 0.99$	30.74028	-105.00056
	Bell Valley Andesite	36.57	$\pm 0.80$	30.74690	-104.99679
Davis Mountains	Star Mountain Rhyolite	36.81* (Ar-Ar)	$\pm 0.13^*$	30.86547	-103.79678
	Huelster Fm.	36.8	$\pm 1.5$	30.86547	-103.79678
Rio Grande River Area	Buckshot Ignimbrite	36.73	$\pm 0.84$	30.19257	-104.26791
Alamito Creek and Green Valley Area	Tascotal Fm.	32.72	$\pm 0.57$	30.19019	-104.27943
Chinati Mountains	Morita Ranch Fm.	36.5	$\pm 1.0$	29.87272	-104.28577
Big Bend National Park	Black Peaks Fm.	58	1 $\sigma$	29.43258	-103.13862
	Hannold Hill Fm.	60	1 $\sigma$	29.40085	-103.14441
	Canoe Fm.	47	1 $\sigma$	29.38329	-103.14992
Chisos Mountains	Chisos Fm.	31.2	$\pm 0.73$	29.27095	-103.30025
	South Rim Fm.	31.2	$\pm 0.73$	29.26879	-103.29823
	Burro Mesa Fm.	29.4* (Ar-Ar)	$\pm 0.17^*$	29.14520	-103.49918

**Table 5.4:** Displays the age and error of formations analyzed in this study in relation to their sample site and GPS coordinate locations. The formations marked in red represent flat-lying basal volcanic units that unconformably overlie heavily deformed Cretaceous to Oligocene aged strata. The formations marked in blue represent the Paleocene-Eocene aged siliciclastic samples discussed in Chapter 4 that are below the unconformity in Big Bend National Park.

(\*) - Age data not collected in this study (McDowell, 1979; Henry *et al.*, 1986; Henry *et al.*, 1994; Miggins *et al.*, 2006).

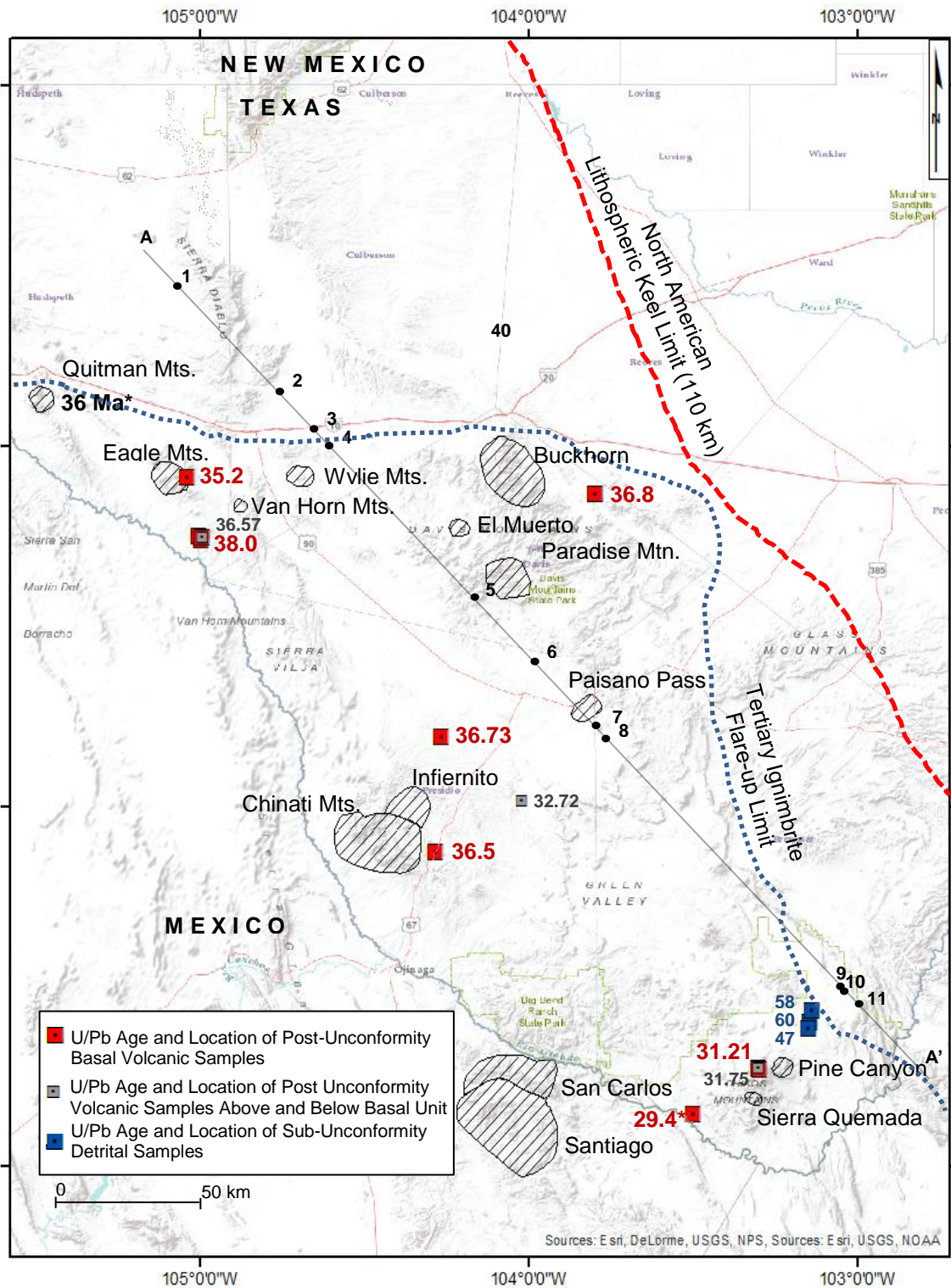


**Fig.5.34:** Regional map displaying sample location and U/Pb age of analyzed volcanic samples collected from directly above and below the unconformity. The known calderas in Texas and Mexico have been labeled and given a hatched pattern. Two plots (Fig.5.36, Fig.5.37) have been constructed from the A-A' line drawn perpendicular to the Hess conjugate trajectory projection that assess north-south erosional trends observed in West Texas and variation in basal flat-lying volcanic ignimbrite age from north to south. The dashed red line displays the western limit of cratonic lithospheric keel in Texas inferred from anisotropic shear wave velocity imaging (Nettles and Dziewonski, 2008). The blue dotted line represents the eastward extent of ignimbrite flare-ups exposed in the Trans-Pecos.

---

better assess the timing of emplacement of the volcanic rocks.

Northern Trans-Pecos Texas records an erosional vacuity of up to 60 my of stratigraphic section between Early to Middle Cretaceous strata that varies in age from 100 to 85 Ma and the Tertiary basal flat lying ignimbritic volcanic rock determined here to be 38 and 36.5 Ma in the Quitman, Eagle, Indio, and Davis Mountains (Fig.5.34). The Van Horn Mountains area discussed previously in this chapter is a major structural high, and exposes the Precambrian aged Carrizo Mountain Group, the oldest rocks exposed in Trans-Pecos Texas (Denison, 1980; Flawn, 1951; King and Flawn, 1953). Precambrian exposures are also found in the Eagle Mountains, but do not make a contact between the Tertiary flat-lying volcanics assessed in this study. As mapped by Barnes (1979), the Hogeye Tuff rests unconformably on the Laramide thrust faulted and folded Permian Hueco Limestone and Precambrian Carrizo Mountain Group just north and east of the Van Horn Caldera complex and east of the Indio Mountains where the Hogeye Tuff (38.02 Ma) was sampled and analyzed in this study.

The Permian and Precambrian exposures are located on a massive upthrown fault block and could reflect, in part, local abrupt uplift and erosion of over 1,100 m (3,300 ft) of Cretaceous section in the Van Horn Mountains; however, the Precambrian exposures just east of the northeastern flank of the Eagle Mountains to the west are not situated on a fault block and could indicate that deeper seated erosion into the Permian and Precambrian sections occurred locally in northern Trans-Pecos region (Twiss, 1959a,

---

1959b). This uplift and accelerated erosion is associated with the incoming subducting flat-slab deformation and partial magmatic arc/ plutonism that occurred in the northern Trans-Pecos region between 47-40 Ma (Fig.5.34).

As there are major pre-Laramide unconformities between the Cretaceous and Permian strata and Permian and Precambrian units we report the vacuity between flat-lying ignimbrites in the north and deformed Cretaceous stratigraphic section as a minimum vacuity. Fault bounded blocks of Permian and Precambrian aged formations in contact with Cretaceous strata just below the angular unconformity demonstrates that the faults truncate at the Laramide unconformity (see Indio and Van Horn Mountains map- Fig.5.7) and that the deformation and uplift of these blocks along faults at the level of Cretaceous strata was likely Laramide in age during flat-slab compression. However, because each site examined in this study retains a Cretaceous contact with the Laramide unconformity flat-lying and we have not measured or evaluated local stratigraphic thicknesses lost regionally during these various episodes prior to the Laramide orogenic event each sites erosional profile was evaluated in relation to the unconformable contact between the Tertiary ignimbrite deposits and heavily deformed Cretaceous strata.

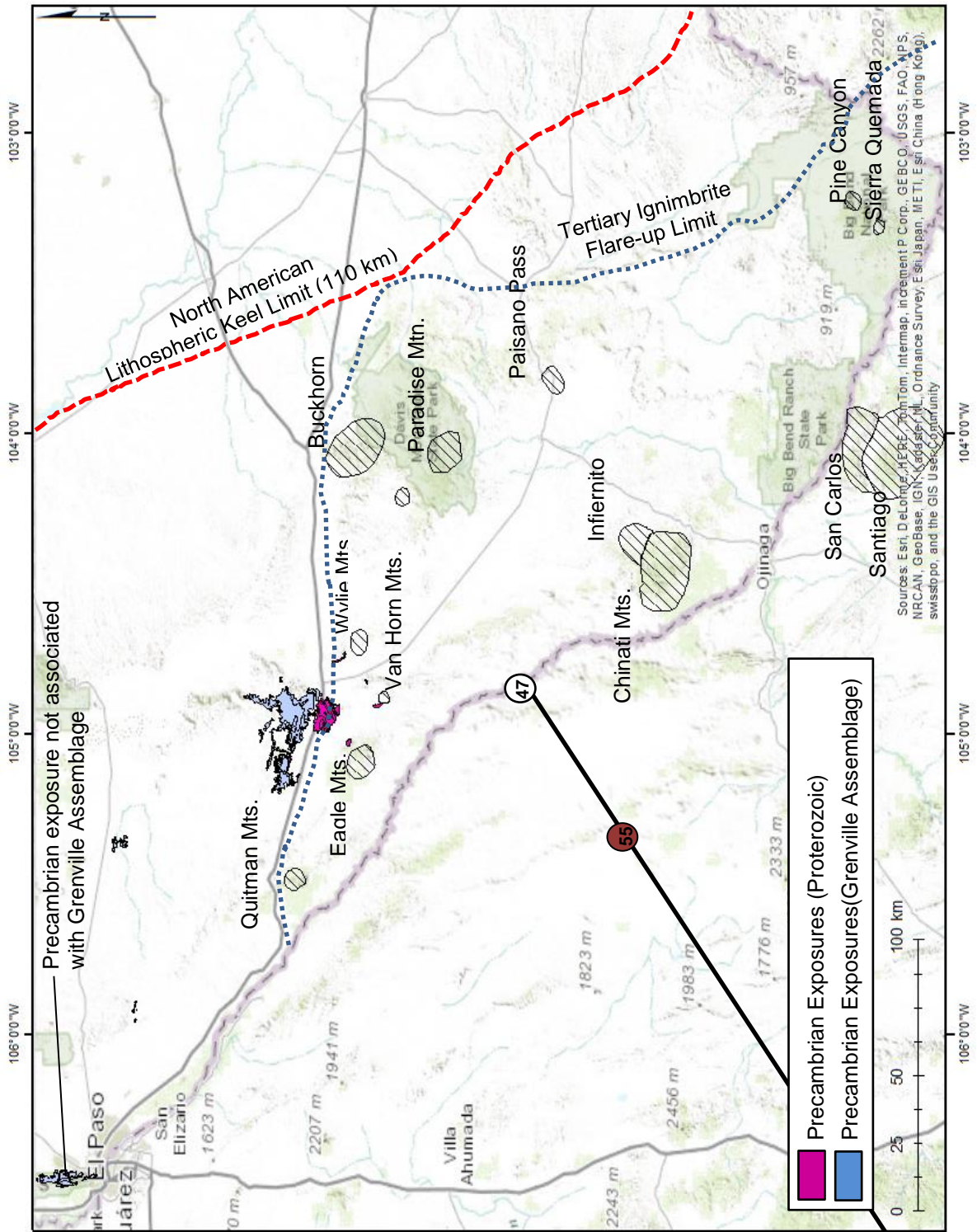


**Fig.5.35:** Regional map displaying Precambrian exposures associated with the Grenville orogeny and other Proterozoic aged uplifts of the Carrizo Mountain Group found in the Van Horn Mountains and neighboring areas. The trajectory of the Hess Rise plateau modeled from Liu *et al.* (2010) has been extended to the Texas border and added to this map to provide an idea of its incoming trajectory.

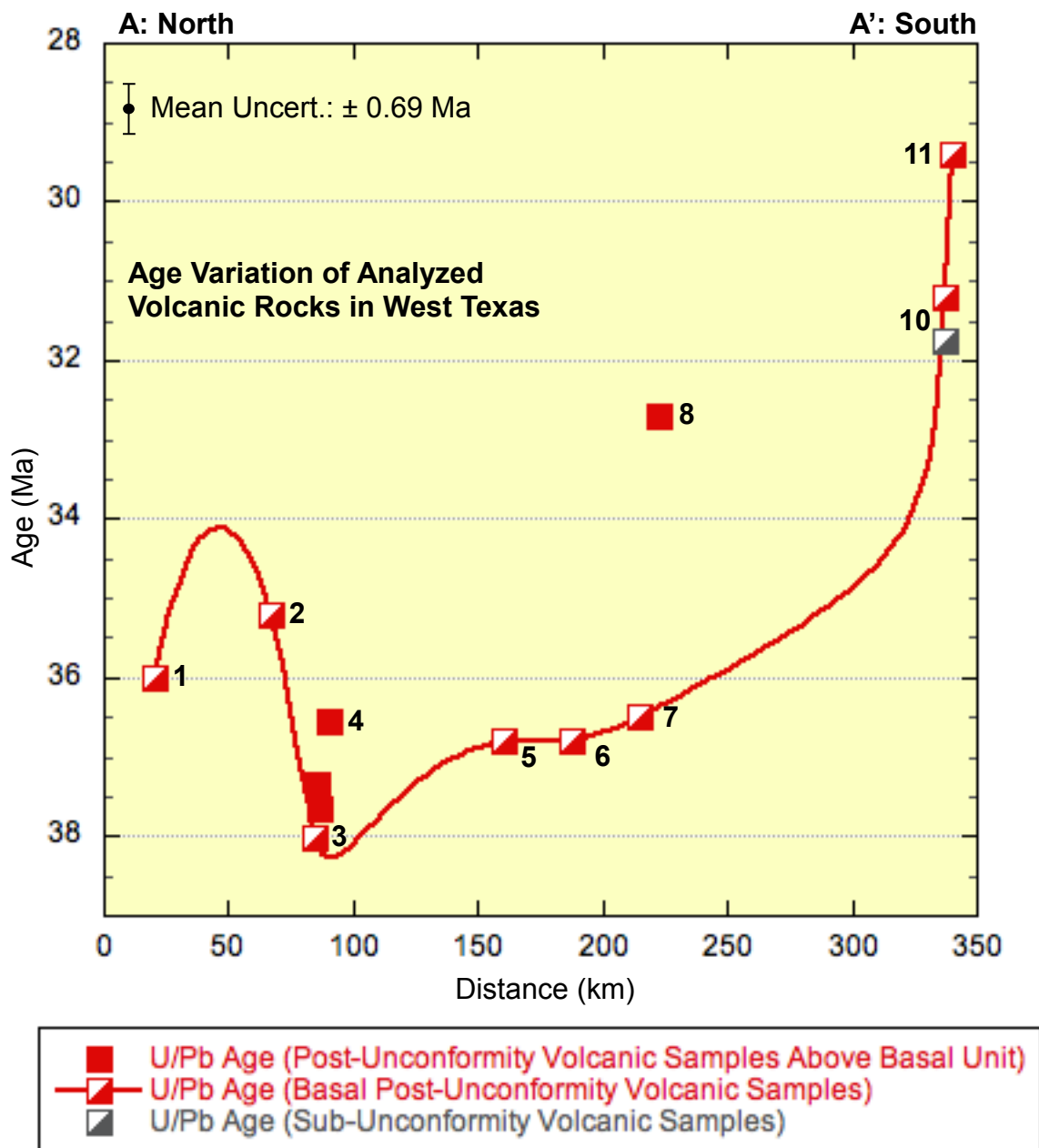


**Fig.5.36:** Plot emphasizing the age variation of all volcanic rocks analyzed in this study from northwest to southeast along the section line A-A' drawn on Fig.5.31. Most notable on this plot are the basal post-unconformity volcanic samples that are 38 Ma in the north in the Van Horn and Indio Mountains and 31-28 Ma in the south in the Chisos Mountains.

Field observations made in this study document abundant Laramide-style thrust faults and folds throughout the Chisos Formation that is unconformably overlain by flat-lying volcanic rocks of the South Rim Formation; marking a major angular unconformity in the southern Trans-

---

Pecos region between the two volcanic units. Volcanic units of the Chisos Formation in present-day Big Bend National Park record a nearly continuous volcanic sequence ranging from 47 to 32 Ma that are folded and thrust faulted in Laramide structural orientation. Folding of the Tertiary siliciclastic formations below the Chisos Formation in Big Bend National Park documented in Chapter Four do have typical Laramide fold trends also supports the timing of this Tertiary folding which affected the Chisos Formation. The volcanic units of the Chisos Formation are interpreted in this study to have deformed shortly after their deposition from far-field Laramide-compressional deformation that had not fully ceased in southern Trans-Pecos Texas by 31 Ma. The erosional vacuity between the tilted strata affected by Laramide compressional deformation below the unconformity in Big Bend National Park and the flat-lying ignimbrites, rhyolites, and tuffs of the South Rim Formation (31.2 Ma) above the unconformity represents a much smaller interval of time (0.5 Ma) than the erosional vacuity observed in the northern Trans-Pecos region.

This is reflected locally by significantly less uplift and erosion in southern Trans-Pecos Texas and indicates a markedly abrupt cessation of compressional deformation in the Big Bend region. In addition to variations in the erosional profile from north to south in the Trans-Pecos Texas region, the younging trend reflected in the basal flat-lying ignimbrite deposits unaffected by Laramide compressional deformation suggests cessation of major compressional deformation to have occurred initially in northern Trans-Pecos

Texas at 38 to 36.5 Ma and occurred later in Big Bend National Park from 31.75 to 31.2 Ma (Fig.5.36; Fig.5.37).

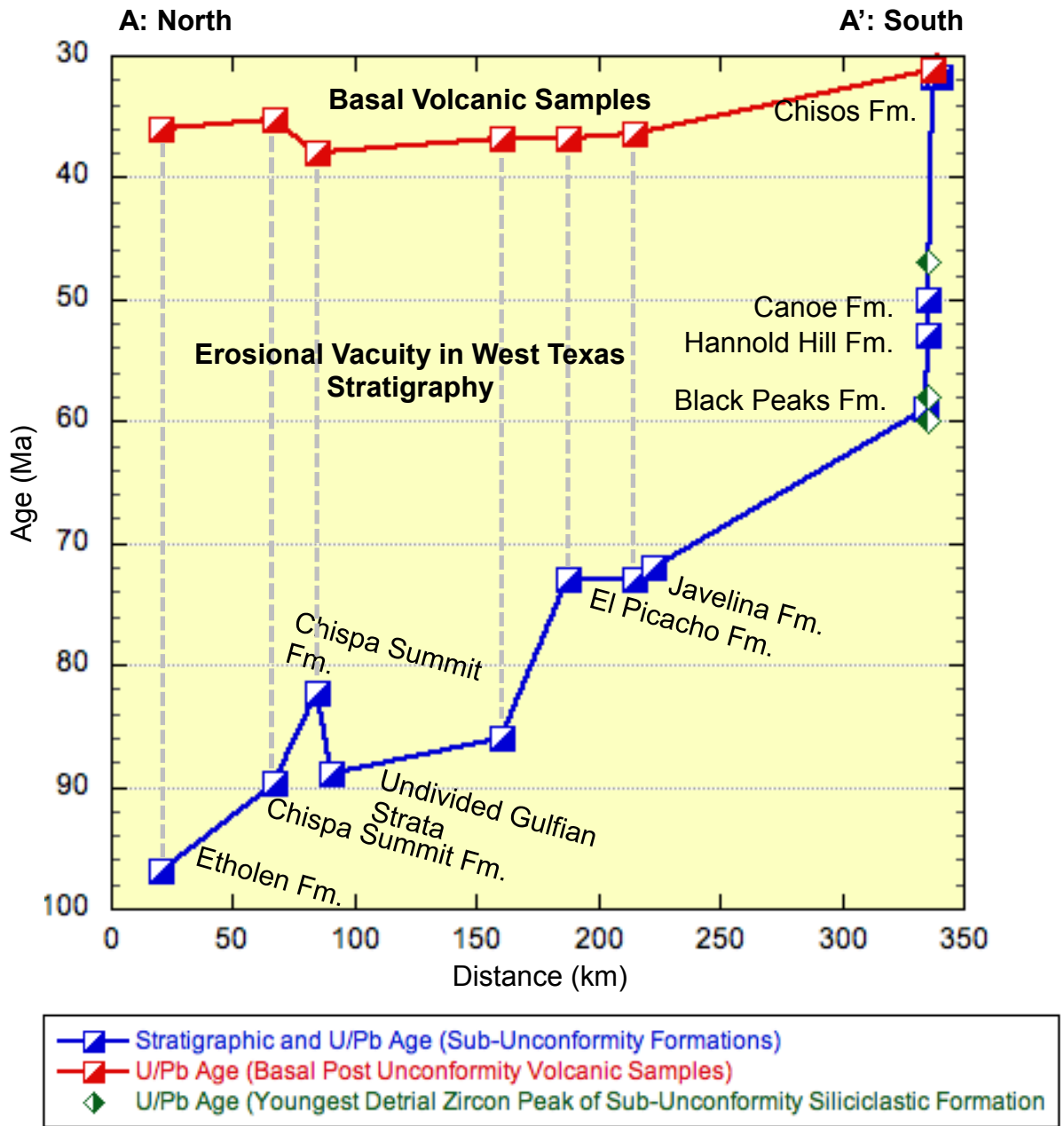


**Fig.5.37:** Displays the varying erosional level or vacuity based on the age of sub-unconformity rocks and the age of each basal volcanic unit in several localities listed on the A-A' section line in Fig.5.31 from northwest to southeast in Trans-Pecos Texas. The erosional vacuity and age of basal volcanic unit decreases from north to south in West Texas.

---

The structural observations documented in the Late Cretaceous to Eocene aged Javelina, Black Peaks, Hannold Hill, and Canoe Formations discussed in Chapter Four indicate that they are conformable and folded into a broad syncline about an axis interpreted in this study to be consistent with Laramide folding trends and fold scales in southern Big Bend National Park (e.g. Mariscal Mountain Anticline). Turner et al. (2011) has previously documented numerous thrust faults in the Dagger Flat and Tornillo Flat areas of Big Bend National Park in the same area that the broad synclinal fold in the this study was observed. This data consistently shows that intense compressional deformation associated with the Laramide orogeny initiated and ceased in southern Trans-Pecos Texas within a narrow window of time (31.75-31.21 Ma) and was immediately followed by the deposition of ignimbrite flare ups between 31.21 and 28 Ma in southern Trans-Pecos Texas.

The ages of cessation of Laramide compression and post-unconformity ignimbrite flare-ups lead to specific conclusions regarding compressional deformation and the transition to a later steeper slab slab breakway period that will be addressed in Chapter Six. However, the arrival of the arc volcanism to Texas the flat-slab subduction drives the magmatic arc westward is also of interest in this study. Much of the evidence is contained in igneous rocks of the Big Bend National Park area, but there are other intrusive events documented in Texas that provide relevance to the transition from steep-slab to flat-slab subduction and magmatic arc arrival in Texas. The

---

Campus Andesite Pluton located at UTEP in El Paso has an absolute K-Ar age of  $47.1 \pm 2.3$  Ma and is interpreted in this study to reflect the arrival of the magmatic arc across the present-day Texas-New Mexico border (Hoffer, 1980).

Similar to the Campus Andesite Pluton in El Paso, the dikes and sills of the Finlay Mountains located 32 km northwest of Sierra Blanca, Texas have yielded a K-Ar, amphibole age of  $47.5 \pm 1.2$  Ma (Matthews and Adams, 1986) indicating that arc magmatism and associated plutonism had reached the present-day Texas border at  $\sim 47$  Ma. Furthermore, the Round Top rhyolite and rhyolite porphyry intrusion north of the Quitman Mountains has yielded an age of  $41.6 \pm 0.4$  Ma (Barker, 1980, James and Henry, 1993; Rubin *et al.*, 1987; Rubin *et al.*, 1990) providing indisputable evidence that magmatic arc plutonism was active in the northern and southern Trans-Pecos Texas region between 47-40 Ma. The oldest flow of the Alamo Creek Basalt has yielded a slightly younger  $^{40}\text{Ar}/^{39}\text{Ar}$  age of  $46.62 \pm 0.07$  Ma and is considered in this study to represent the first southernmost Trans-Pecos Texas bimodal volcanism associated with the incoming Farallon slab and the arrival of the magmatic arc in present-day Big Bend National Park (Henry and Davis 1996; Carman *et al.*, 2003; Miggins *et al.*, 2006).

The nearly identical ages of the Campus Andesite Pluton in El Paso and the slightly younger Alamo Creek Basalt located in Big Bend National Park provide a north-south age constraint indicating the subducting Hess Rise conjugate plateau drove the Farallon slab to reach the present-day Texas

---

border at ~47 Ma. These synchronous volcanic and plutonic events indicate that volcanism and plutonism related to the Laramide orogeny began nearly simultaneously throughout the Trans-Pecos region. Earlier porphyry deposits, such as the Red Hills Porphyry in northern Trans-Pecos Texas, preceded these magmatic events.

Porphyry deposits (75-65 Ma) such as those found throughout New Mexico and Texas are thought to be a signature record of the transition between steep and flat-slab subduction and represent a precursor to abundant inboard arc volcanism in modern-day analogs of flat-slab subduction (Dickinson and Snyder, 1978; Jordan and Allmendinger, 1986; Humphreys *et al.*, 2003; McLemore, 2008). The Trans-Pecos igneous province of Texas and adjacent New Mexico region are comprised of more than 200 intrusive bodies with exposures that generally exceed 1 km<sup>2</sup> in size (Barker, 1977, 1979, 1987) of which many are associated with porphyry deposits. The Red Hills Porphyry in Texas, is a brecciated quartz monzonite exposed 1 km from the southern margin of the Chinati Mountains caldera is the oldest known Cenozoic igneous rock in the Trans-Pecos region with a zircon U-Pb age of 64.2 ±0.2 Ma, and is considered the easternmost recognized Laramide related porphyry deposit (Gilmer, 2001; Gilmer 2003).

In conclusion, West Texas documents 1) clear signs of the western North American margins transition from steep to flat-slab subduction in early precursor porphyry deposits in the earliest Tertiary; 2) the later arrival of the steep-slab (in advance of flat-slab) magmatic arc rocks at 47 to 46 Ma; 3) flat-

---

slab compressional fold and thrust structures, uplift, and erosion prior to 38 to 36.5 Ma in the northern Trans Pecos region (with a period of magmatic quiescence or gap) and prior to 31.2 Ma in the southern Trans Pecos region (without volcanic quiescence or gap); and 4) a period of ignimbrite flare-up signifying the transition to steep-slab subduction, the rise of hot asthenospheric mantle to the base of the continental lithosphere, and likely slab roll-back or breakaway.

---

**Chapter 6:****Evolution of the Laramide Orogen to West Texas****i. The Cretaceous-Tertiary Laramide Orogen**

Hypothesized mechanisms thought to contribute to the Laramide orogeny include: 1) collision with an exotic terrane (Silver and Smith, 1983; Maxson and Tikoff, 1996; Hilderbrand, 2009); 2) collapse of the Sevier orogeny hinterland (Livaccari, 1991); and (3) shallowing in the angle of subduction of oceanic lithosphere (Coney and Reynolds, 1977; Dickinson and Snyder, 1978; Bird, 1984). Hildebrand (2009) suggests that magmatic arcs of western North America were allochthonous and sutured to the continent directly before the Laramide orogeny; viewing the Sevier orogeny as the culmination of collision and the Laramide orogeny as the manifestation of east-dipping subduction beneath the North American plate. Unless focused, collision of an exotic terrane requires that stresses be greater at the margin than the continental interior. However, only minor amounts of compressional deformation were produced in the Great Valley-Sierra Nevada-Southern Nevada region throughout the Laramide orogeny (Burchfiel and Davis, 1977; Barth *et al.*, 2004; Unruh *et al.*, 2007).

This absence of compressional deformation would require greater lithospheric strength at the western margin than the continental interior, or increased gravitational potential energy to divert compressional stresses; neither of which have been demonstrated to occur across the entire distance from trench to foreland in western North America, rendering the 'collision with an exotic terrane' hypothesis improbable (Livaccari, 1991; Wells and Hoisch, 2008; Jones

---

*et al.*, 2011). The 'Sevier orogen hinterland collapse' process of Livaccari (1991) requires the Colorado Plateau to be stronger than the Wyoming craton, and fails to explain the shutdown of frontal thrusts in southern Nevada where the greatest increase in compressional stresses is presumed to occur (Jones *et al.*, 2011). In addition, this mechanism does not associate Laramide shortening with the inboard migration of arc magmatism and views the shift in volcanic activity as a coincidental occurrence, further marginalizing this hypothesis. The 'oceanic lithosphere shallowing' hypothesis is the preferred mechanism for the Laramide orogeny at this time because the Colorado Plateau is widely considered to be strong, and the absence of prolific arc-magmatism in the western United States is thought to be caused by an unknown difficulty in penetration of the lithosphere more steeply into the mantle (Spencer, 1996; Schmidt *et al.*, 2002; English *et al.*, 2003; Humphreys *et al.*, 2003; Humphreys, 2009).

The 'flat-slab subduction' hypothesis is supported by modern analog comparison of basement cored uplifts from the Sierra Pampeans in Argentina, which are inboard of a magma quiescent segment of the Andean arc and above a shallowly dipping segment of the subducting Nazca plate (Dickinson and Snyder, 1978; Jordan and Allmendinger, 1986; Humphreys *et al.*, 2003). The mechanical evidence for flat-slab subduction comes from the notion that balance of basal shear tractions occurs by compressional stresses increasing with distance from the trench and driving crustal contraction and thickening (Dickinson and Snyder, 1978; Bird, 1984, 1988). Thus, most investigators attribute the

---

Cretaceous-Tertiary Laramide orogeny to rapid flat-slab subduction of the Farallon plate beneath North America beginning at about 88 Ma.

## **ii. Evidence of Buoyant Farallon Slab Segments**

The flat-slab subduction is interpreted to be caused by the subduction of two buoyant plateaux and associated thicker crustal plume tracks situated on the Farallon plate; i.e., the conjugate plateaux of the Shatsky and Hess Rises on the present-day Pacific Plate, both of which formed along the Pacific-Farallon ridge axis indicating a split twin must exist for both on the Farallon plate (Liu *et al.*, 2010). Plate reconstructions and models predict that the Shatsky and Hess conjugates entered the western North American trench at 88 and 65 Ma respectively (Liu *et al.*, 2010) causing the top of the Farallon lithosphere to be in contact with the base of the North American lithosphere beneath a progressively broader area of the western United States throughout Laramide orogenic development (Lipman *et al.*, 1971; Snyder *et al.*, 1976; Coney and Reynolds, 1977). Thicknesses of the Shatsky and Hess Rises crustal sections are heterogeneous and vary along strike, therefore the thicknesses of the conjugate plateau discussed in this study are likely to have varied between 15-30 km respectively based on the seismic refraction research of the current rises (Neprochnov, 1989; Rudnik, 1981; Rudnik and Melankholina, 1984) and paleoreconstructions (Liu *et al.*, 2010).

Thicker crust associated with an oceanic plateau and their connected aseismic ridges increases the average buoyancy of the lithospheric plate. This increase in thickness may the oceanic plate to become lighter than the

---

asthenosphere, which is dependent on the age of the plate and the thickness of the crustal layer (Molnar and Gray, 1979; Cloos, 1993). The Hess Rise formed between 116 and 95 Ma (Vallier *et al.*, 1980) indicating that at the time of subduction into the trench at 65 Ma it was ~50 m.y. in age or younger. Modeling the subduction of 80 km-thick lithosphere (~50 m.y.-old oceanic plate) with a 'normal' oceanic crustal thickness (~7 km) will result in negative buoyancy with respect to the asthenosphere with an average buoyancy ( $\Delta\rho L$ ) Nature =  $-35 \text{ kg/m}^3$  (Cloos, 1993; Gutscher *et al.*, 2000). The same plate will act neutrally buoyant if the thickness of the basaltic crust increases to 14 km (Martinod *et al.*, 2010; Gerya *et al.*, 2002). When the oceanic crustal thickness of a plate reaches 17 km the section would have a buoyancy of  $16 \text{ kg/m}^3$ . A plate with an oceanic crustal thickness of 17 km would have a neutral buoyancy of  $\sim +16 \text{ kg/m}^3$ .

Local isostatic equilibrium implies that such a plateau corresponds to 1,250 meters of local relief above an oceanic floor with 'normal' crustal thicknesses. Higher plateaus and ridges above 50 my-old oceanic plates correspond to positively buoyant lithospheric segments. The Hess rise has a broad width of 150-250 km standing more than 1,500 meters above normal adjacent crust, and reaching more than 2,000 meters of local relief in some areas (Vallier *et al.*, 1980). Based on these facts, measured crustal thicknesses reported above, and its age at subduction, the lithosphere of the Hess conjugate would have significant buoyancy. The trajectory of the Hess Rise conjugate in the plate reconstruction model of Liu *et al.* (2010) is projected to advance directly towards West Texas upon flat-slab subduction. It is interpreted that this

---

subducted plateau and adjacent track would have more than sufficient positive buoyancy to initiate flat-slab subduction at 65 Ma and subsequently affect the Trans-Pecos region of Texas (Vallier *et al.*, 1980; Cloos, 1993; Gutscher *et al.*, 2000; Gerya *et al.*, 2002; Martinod *et al.*, 2010; Liu *et al.*, 2010). If the thickened crustal segment of the slab remains at depths shallower than 150 km, it would continue to have significant positive buoyancy throughout the duration of flat-slab subduction. Implications of descent below 150 km and its affect on buoyancy will be discussed further below.

Subduction of aseismic ridges transitions from deep to shallow seismic activity (Vogt *et al.*, 1976; Kelleher and McCann, 1977; Nur and Ben Avraham, 1983; McCann and Sykes, 1984; Adameck *et al.*, 1987; Gutscher *et al.*, 2000), volcanic-arc segmentation and/or inhibition of arc volcanism (Nur and Ben Avraham, 1983; McGaery *et al.*, 1985), and coastal geomorphic modifications characterized by a rapid crustal uplift of the overriding plate (Chung and Kanamori, 1978; Gardner *et al.*, 1992; Machare and Ortlieb, 1992; Taylor *et al.*, 1995). The buoyant Farallon-North American lithospheric contact throughout the Laramide orogeny facilitated increased thick-skinned inboard crustal contraction and thickening, causing steady eastward advancing regional uplift that followed in the wake an eastward migrating magmatic arc (Snyder *et al.*, 1976; Coney and Reynolds, 1977; Dickinson and Snyder, 1978; Humphreys *et al.*, 2003). Limited slab-dewatering under the increasingly cool conditions of slab contact with the North American mantle lithosphere hydrated the western-most basal continental

lithosphere, possibly contributing to uplift across California during initial flat-slab subduction around 65 Ma (Humphreys *et al.*, 2003).

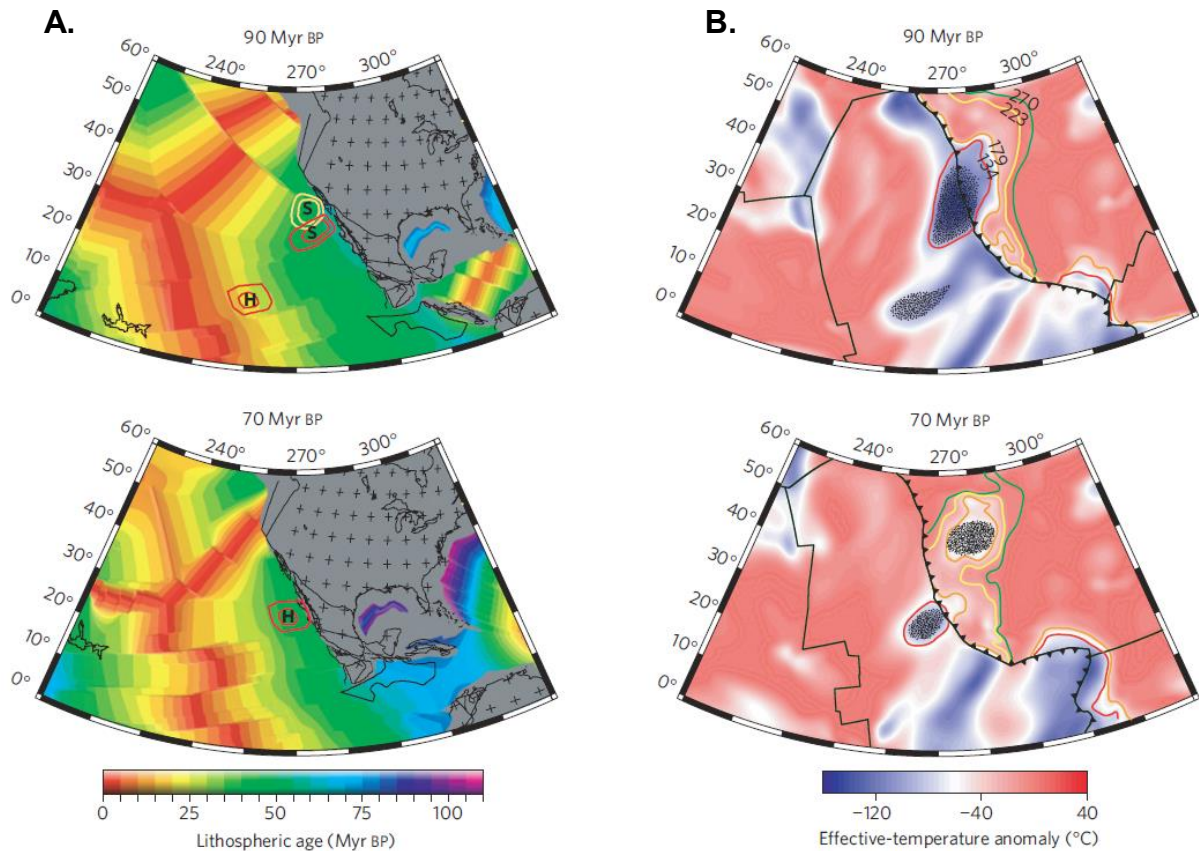


**Fig.6.1:** **A.** Plate reconstruction compiled by Liu *et al.* (2010) of the Shatsky (S) and Hess (H) conjugate plateaus denoted by red and yellow contours forming along the paleo Pacific-Farallon (Farallon-Izanagi) ridges ; the contours represent their maximum/ minimum extents overlying the age of the sea floor. **B.** Inverse model tracers compiled by Liu *et al.* (2010) that delineate the thickest part of the recovered lithosphere above 179 km depth from inverse convection models in black (starting with seismic tomography); background effective temperature is color-coded. Colored contours (red, orange, yellow, green) show isotherms at various depths (km) of effective temperature anomalies 40°C lower than the ambient mantle.

Laramide volcanism associated with the steeper ‘pre-shallowing’ portion of the slab in advance of the flat-slab that was in contact with the asthenosphere migrated eastward through time as the flat-slab contact between the Farallon and North American plates became more extensive and expansive inboard of the trench across Western North America (Fig.6.2). This resulted in the eastward migration of the magmatic arc across the western United States, and a lack of

---

deep, high temperature slab dehydration occurring to the west leaving the Sierra Nevada arc quiescent.

### **iii. Magmatism and its Migration through Time**

The emplacement of the  $64.2 \pm 0.2$  Ma Red Hills Porphyry in northern Trans-Pecos discussed in Chapter Five is important in developing the tectonic history of Texas in relation to the Hess Rise conjugate because porphyry copper deposits are regarded to form in environments where the magmatic arc is in a nearly neutral stress regime, usually recording transitions in or out of flat-slab subduction (Gutscher *et al.* 2000; Tisdale and Richards, 2001; Kay and Mpodozis 2001; Beck and Zandt, 2002; Chapin *et al.*, 2004). Volcanism associated with the migrating magmatic-arc reached as far east as western South Dakota in the north and Trans-Pecos Texas in the south (Humphreys *et al.*, 2003; Sigloch *et al.*, 2008). Eastward propagation of the magmatic arc is suggested by Lipman *et al.* (1971), Snyder *et al.* (1976), and Coney and Reynolds (1977) to be the result of a progressive shallowing in the subduction angle of the oceanic lithosphere beneath North America. Extreme shallowing of subduction angle is supported by Farallon subduction rate and younging slab age calculations of Jarrard (1986) and Engebreston *et al.* (1984). Progressive quiescence in volcanism migrated eastward in addition to the migrating magmatic arc associated with the steeper portion of the slab until a volcanic gap in time evolved with the possibility of some extreme eastern portions of the arc remaining active.

Synchronous north to south volcanic and plutonic events observed in Texas document the arrival of the migrating magmatic arc and advance of the

---

flat-slab suggested in this study to have reached the present-day Texas-New Mexico border at ~47 Ma based on the  $47.1 \pm 2.3$  Ma Andesite Pluton in El Paso and the  $46.62 \pm 0.07$  Ma basal flow of the Alamo Creak Basalt in Big Bend National Park discussed previously in Chapter Five (Hoffer, 1980; Henry and Davis 1996; Carman *et al.*, 2003; Miggins *et al.*, 2006). It is important to note that this initial volcanism associated with the arrival of the arc does not represent the time of major compression indicated by pre-angular unconformity folding and thrusting in the area. Dikes and sills of the Finlay Mountains located 32 km northwest of Sierra Blanca, Texas that are  $47.5 \pm 1.2$  Ma (Matthews and Adams, 1986), and the Round Top rhyolite and rhyolite porphyry intrusions north of the Quitman Mountains that are  $41.6 \pm 0.4$  Ma (Barker, 1980, James and Henry, 1993; Rubin *et al.*, 1987; Rubin *et al.*, 1990) indicate that plutonism associated with the eastward migrating magmatic arc was active in the northern and southern Trans-Pecos Texas region between 47-40 Ma.

In addition to volcanism and plutonism, the age-peak spectra of the analyzed siliciclastic samples (Black Peaks, Hannold Hill, and Canoe Formations) in Chapter Four track the incoming magmatic arc throughout the Laramide orogeny with age-peak spectra variation that represents distal to more proximal detritus present in each progressively younger formation. The Canoe Formation was the stratigraphically highest siliciclastic formation in Big Bend National Park having yielded a maximum depositional age of ~47 Ma (at  $1\sigma$ ), and contains a significantly higher population of Permian and Late Cretaceous age-peaks than the Black Peaks or Hannold Hill Formations. This detritus is

---

suggested in this study to be sourced in part from the Permian aged Las Delicias Basin and Late Cretaceous Difunta Group of northern Mexico near Coahuila providing evidence for a more proximal source to Texas and another record of the incoming magmatic arc and uplift approaching Texas.

Based on global plate circuit analysis, an abrupt decrease in Farallon-North American convergence occurred at about 45 Ma from 11-14 cm/yr to 6-9 cm/yr slowing the inboard migration of the magmatic arc (Stock and Molnar, 1988). At 60 Ma the Hess Rise conjugate according to Liu *et al.* (2010) had migrated 183.8 km inboard of the trench along its modeled east-northeast trajectory predominantly affecting northern Mexico, Arizona, and east-central New Mexico. At 55 Ma on the same trajectory model, the Hess conjugate is postulated by Liu *et al.* (2010) to have migrated another 162.2 km inboard affecting northeastern Mexico and west-central New Mexico. Remaining consistent with Liu *et al.*'s (2010) calculations, in an additional 162 km the extent of the trajectory of the Hess conjugate plateau would be positioned just east of Trans-Pecos Texas igneous province at 38 to 37 Ma. The flat-slab appears to steepen again first in northern Trans-Pecos Texas (38-36.5 Ma) and then in the south (31.75-28 Ma), allowing ignimbritic volcanism to occur at the waning stages of the Laramide orogeny representing a change from relatively low mantle heat flow and no evidence for significant magma transfer into the crust, to markedly hot conditions with massive volumes of basalt transferred into the crust (Johnson *et al.*, 1991; Perry *et al.*, 1993; Humphreys, 1995; Humphreys, 2003).

## Shatsky and Hess Rise Conjugate Plateau Trajectories

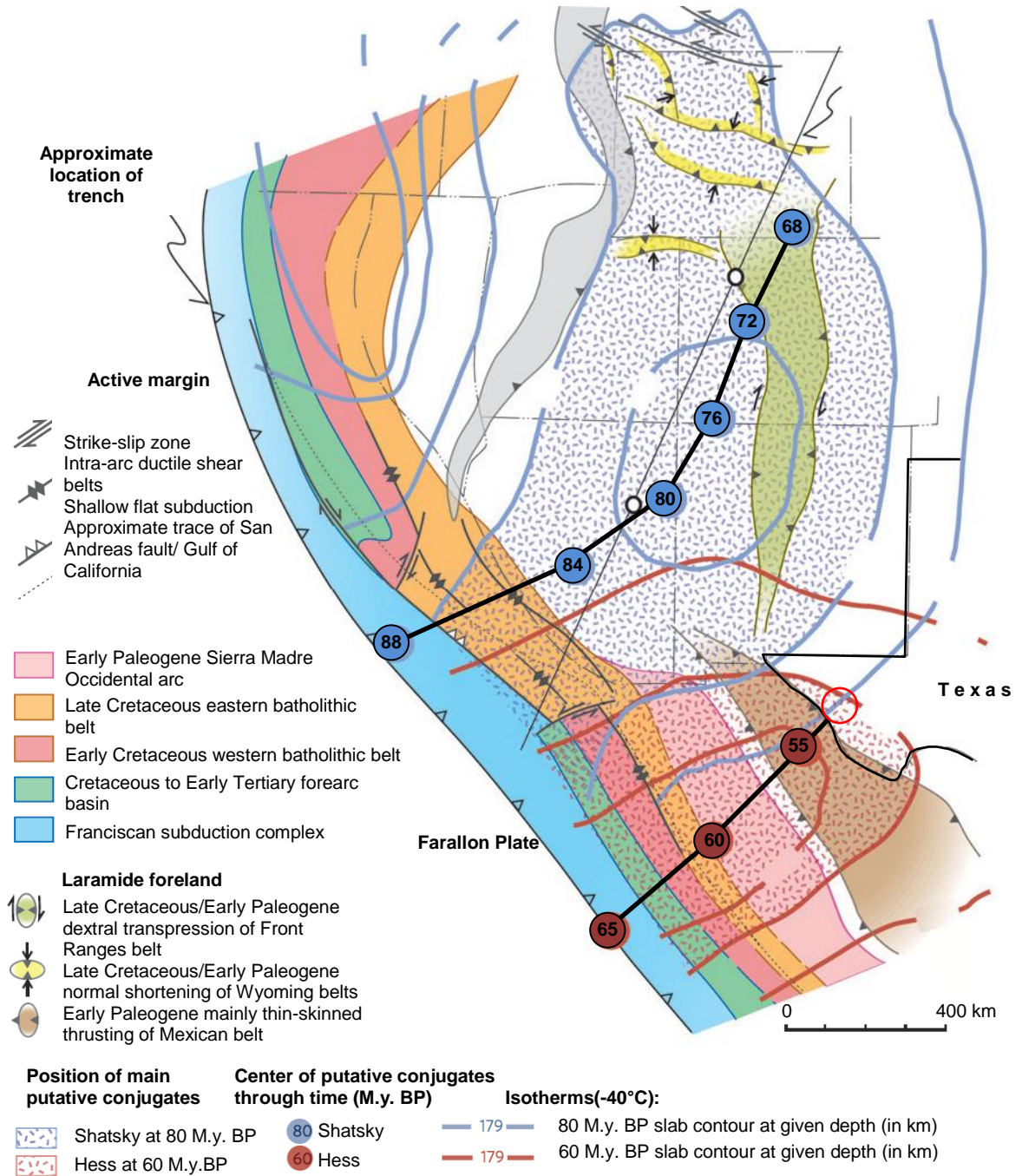


**Fig.6.2:** Palinspastic map displaying the southwest Cordilleran active margin and Laramide foreland during Late Cretaceous time with temperature field overlain. Shatsky and Hess conjugate plateaus initially subducted beneath the North American plate 88 and 65 Ma. The Hess conjugate plateau trajectory has been extended into the West Texas region and the ages of its trajectory path are believed to have errors of  $\pm 5$  My. Modified from Liu and others (2010).

---

#### **iv. Arrival of Flat-Slab to Texas and Collision Against Keel**

In order to explain the mass and thermal budget of ignimbrite flare-ups that initiated in northern Trans-Pecos Texas at 38 to 36.5 Ma, this transition from low mantle heat flow and no evidence for significant magma transfer into the crust to markedly hot conditions with massive volumes of basalt transferred into the crust can be explained by progressive Farallon slab removal and exposure of the basal North American lithosphere to hot upwelling asthenosphere (Johnson *et al.*, 1991; Perry *et al.*, 1993; Humphreys, 1995). It has been suggested by Sigloch *et al.* (2008) that the Laramide period of flat-slab subduction ended across the western North American margin by re-initiating a steeper angle of descent between 50-40 Ma caused by collision of the Farallon slab along the edge of the craton ~1,000-1,200 km inboard of the western margin.

This study suggests that the westward younging ignimbritic volcanism and associated plutonism in the southwestern United States initiated in Trans-Pecos Texas as a result of abutting and steepening of the Farallon slab against stable cratonic crust of the continental interior commonly referred to as the keel that is present and most pronounced just east of the northern Trans-Pecos region of Texas. In continental regions, fast seismic velocities show a clear association with old, tectonically stable cratonic crust and lithosphere, while slow seismic velocities are associated with regions of recent or active tectonism (Nettles and Dziewonski, 2008). Locations of strongest radial anisotropy generally correlate with locations of fastest isotropic velocity. The regional and continental scale dynamics of North America are resolved to a depth of 1450 km using a high-

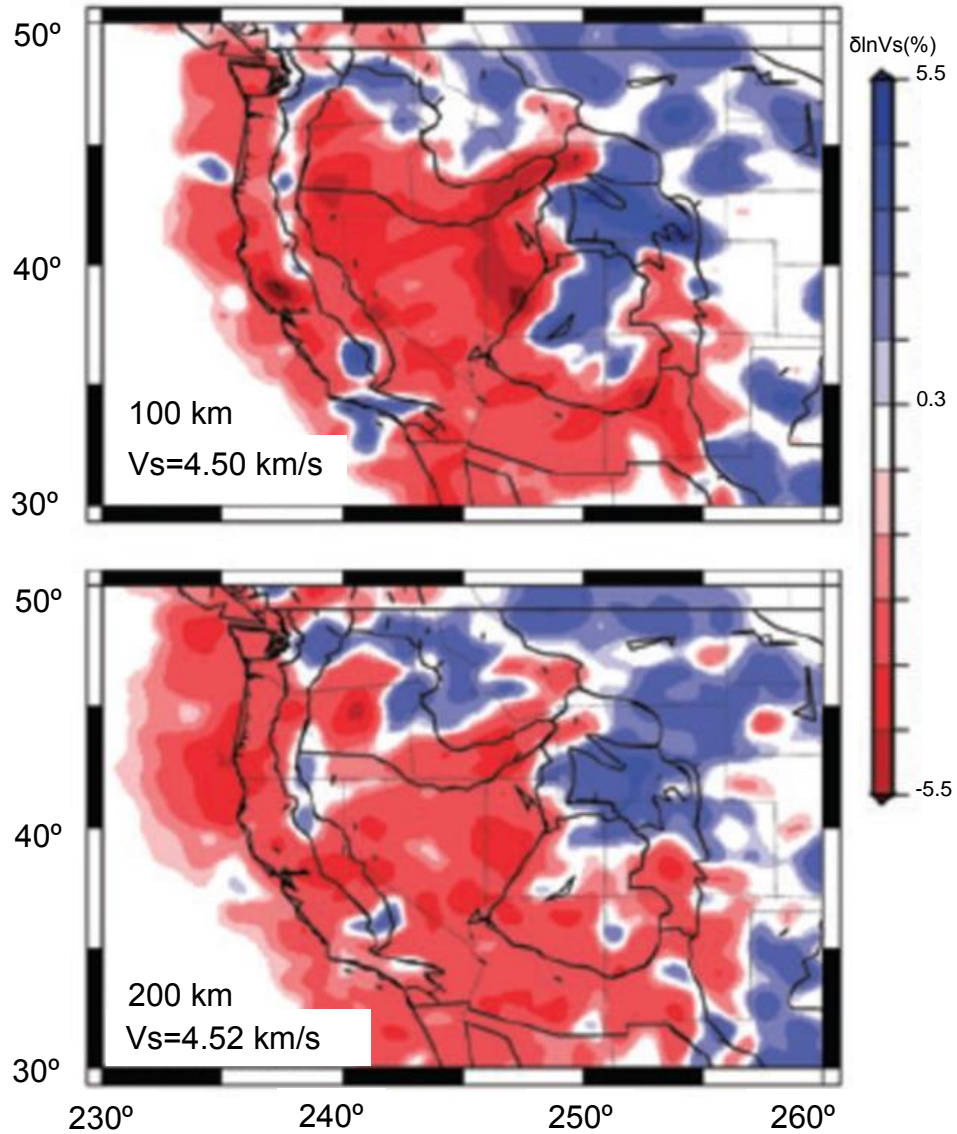


**Fig.6.3:** Joint inversion S- and P- wave velocity models at depths of 100 and 200 km modeled by Sigloch *et al.* (2008) that display stable cratonic lithosphere east of the Trans-Pecos Texas region associated with seismically fast P-wave anomalies (blue).

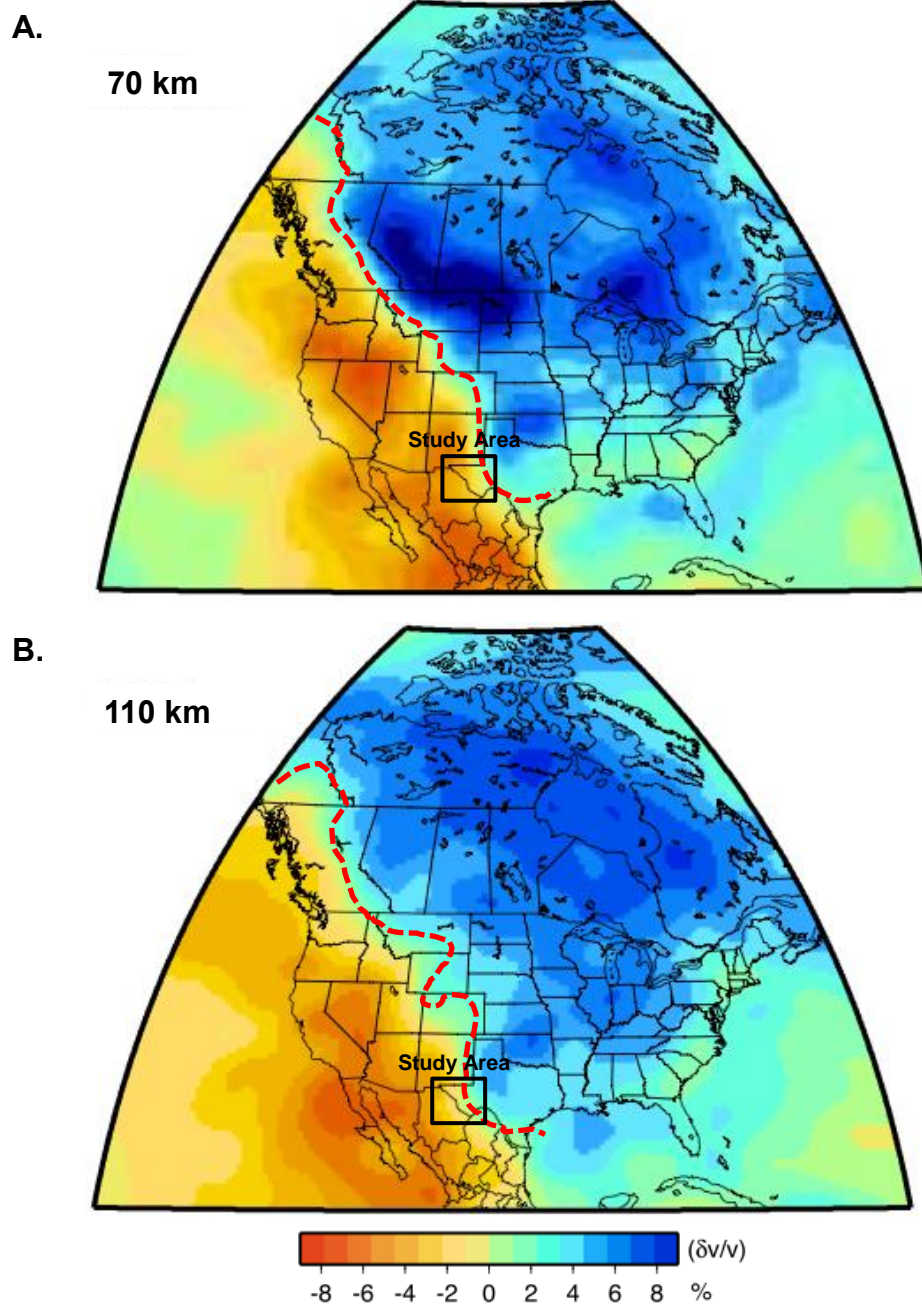


**Fig.6.4:** North American model for vertically polarized shear wave velocity ( $V_{sv}$ ) plotted at depths of 70 and 110 km determined by Nettles and Dziewonski (2008). The average value within each model has been removed. These models clearly identify a cratonic lithospheric keel to the east the Trans-Pecos region of Texas.

---

resolution model of mantle flow in a study done by Forte *et al.* (2010). This model is constrained by inverting global seismic and mantle convection data sets, and explicitly corrects for the positive chemical buoyancy of the continental lithosphere (Forte *et al.*, 2010). The mantle structure below Trans-Pecos Texas, clearly resolved to depths of 350 km in Forte *et al.*'s study, indicates fast seismic shear wave velocities in the upper mantle that support the presence of a stable, cratonic lithospheric keel east of Trans-Pecos Texas that appears to be more pronounced at greater depths in the north than in the south.

In addition, multiple-frequency shear wave tomography of the western United States upper mantle down to 1,000 km from P- and S-wave velocity models by Sigloch *et al.* (2008) indicate seismically coherent fast anomalies east of Trans-Pecos Texas resolved at depths of 225-350 km about 1,150 km inboard of the western margin of North America east of Trans-Pecos Texas (Fig.6.3) (Liu *et al.*, 2010; Sigloch *et al.*, 2008; Nettles and Dziewonski, 2008; Fortes *et al.*, 2010). Furthermore, a variable resolution model of the radially anisotropic shear wave velocity structure of the upper mantle beneath North America constructed by Nettle and Dziewonski (2008) has identified strong radial anisotropy in Trans-Pecos Texas resolved to 70 and 110 km depth. These studies indicate that there is stable, cratonic crust and lithosphere present in the Trans-Pecos Texas region (Fig.6.4).

The North American keel present east of Trans-Pecos Texas acted as a strong mantle lithospheric buttress, halting further progression of the flat-slab. Collision of the Farallon slab against the keel facilitated steepening and forced

---

the buoyant lithosphere to descend into the mantle. This forced descent hastened the basalt to eclogite facies transition of the coarser grained portion of the thickened Farallon oceanic crust that occurs at depths of 150 km (Wylie, 1981). Finer-grained extrusive basalts and sheeted dikes of Layers 1 and 2 of the oceanic crust have an average density of  $2.85 \text{ gm/cm}^3$ , and begin to transition into garnet-granulite and eclogite facies at shallower depths of 60-70 km (Wylie, 1981; Liu *et al.*, 1996; Schmidt and Poli, 1998; Forneris and Holloway, 2004). Coarser-grained gabbroic and ultramafic rock in Layer 3 of the oceanic crust transitions to garnet-granulite and denser eclogite facies ( $3.2\text{-}3.4 \text{ gm/cm}^3$ ) at depths of 150 km (Ahrens and Schubert, 1975; Wylie, 1981). Seismic data obtained from refraction lines by the Shirshov Institute of Oceanology (Neprochnov, 1989) and earlier studies by the Hawaii Institute of Geophysics (HIG) (Rudnik *et al.*, 1981; Rudnik and Melankholina, 1984) indicate that the crustal thicknesses along small segments of the Shatsky and Hess Rises in the western Pacific Ocean near Japan are 16-18 km thick, which is 2-3 times thicker than normal oceanic crustal thicknesses (Hussong *et al.*, 1979).

Thicknesses of the Shatsky and Hess Rises are heterogeneous and will vary along strike, therefore the average thickness of the conjugate plateau discussed in this study is equated to vary between 15-30 km respectively based on the seismic refraction research done by Neprochnov (1989), Rudnik (1981), Rudnik and Melankholina (1984), and paleoreconstructions of Liu *et al.* (2010). As the gabbroic portion of the Hess conjugate plateau is over thickened with respect to normal oceanic crust, gabbroic layer 3B would equate to nearly 75% of

---

the down going oceanic crust, resulting in extreme densification of the descending slab at 150 km as it transitions into eclogite.

#### **v. West Texas Ignimbrite Flare-Ups and Westward Retreat**

Roll-back of a steepened and densified thicker crustal Farallon slab ca. 38 Ma causes northern Trans-Pecos Texas to lose its lithosphere-lithosphere contact and strong compressional component. As this happens, hot asthenosphere rapidly rises to fill the gap and invade the base of the thinner Trans-Pecos continental lithosphere directly west of the stable cratonic keel. Thus leading to the classic post- angular unconformity ignimbrite flare ups associated with the progressive close of the Laramide orogeny found in West Texas. Greater uplift and deeper-seated erosion observed in the north (60 m.y. erosional vacuity between Middle Cretaceous and Tertiary strata) discussed in the summary of Chapter Five can be explained in part by the more intense abutting and steepening of the subducting Farallon flat-slab against a more pronounced lithospheric keel in the north.

The plate reconstructed trajectory of the Hess Rise conjugate (Liu *et al.*, 2010) on the Farallon plate plots in an east-northeastward direction initially colliding more directly with northern Trans-Pecos Texas when it first reaches the present-day Texas-New Mexico border (~47 Ma) providing an explanation for the accelerated erosional rates observed in the north (Fig.6.5). An erosional vacuity of less than 0.5 m.y. marks the angular unconformity between the folded and thrust faulted volcanic units of the Chisos Formation deformed by the Laramide

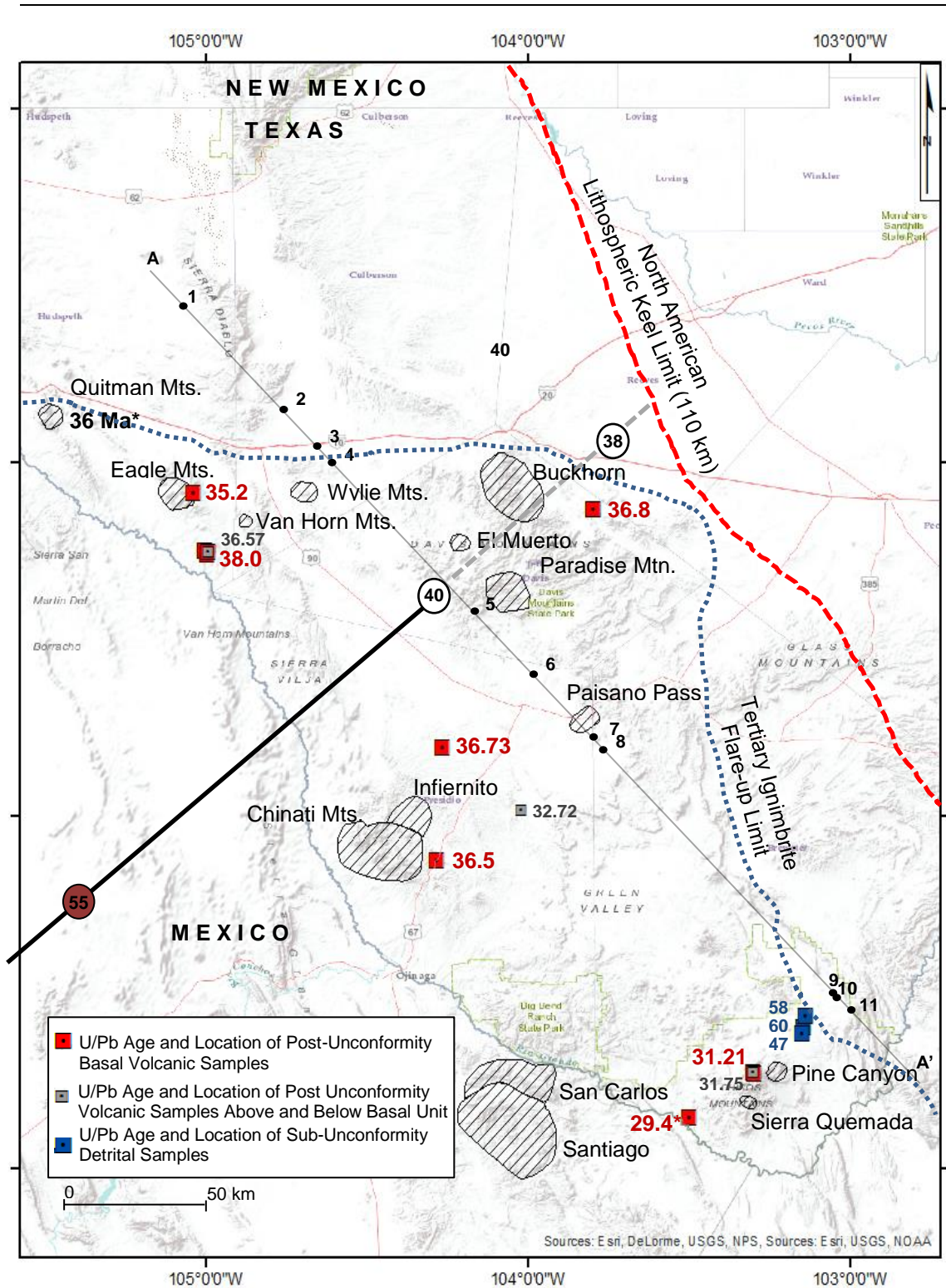


**Fig.6.5:** Regional map displaying sample location and U/Pb age of analyzed volcanic samples collected from directly above and below the unconformity. The trajectory of the Hess Rise conjugate plateau has been projected on to the base map from Liu *et al.* (2010) to indicate where it would have initial and most prolonged impact on West Texas (although uncertainties exist in the age capsules of its projection). The known calderas in Texas and Mexico have been labeled and given a hatched pattern. Two plots (Fig.6.4, Fig.6.5) have been constructed from the A-A' line drawn perpendicular to the Hess twin trajectory projection. The dashed red line displays the western limit of cratonic lithospheric keel in Texas inferred from anisotropic shear wave velocity imaging. The blue dotted line represents the eastward extent of ignimbrite flare-ups exposed in the Trans-Pecos.

---

orogeny and relatively flat-lying South Rim Formation in present-day Big Bend National Park in southern Trans-Pecos Texas discussed previously.

The age of the 'Laramide' unconformity and deformational thrust faults and folds are best constrained in Big Bend where the final deformation and uplift occurs more than 15 Ma after the initial Alamo Creek arc volcanism at 46.6 Ma (Miggins *et al.*, 2009). The volcanic units of the Chisos Formation in Big Bend National Park likely formed from continuous magma production from a magmatic arc that never shut down fully in the south. The magmatic arc is thought to have remained active as a result of a steeper slab and constant lithosphere-asthenosphere contact due to a less pronounced keel to the south and east in Texas. This interaction caused the bimodal volcanic units of the Chisos to become deformed syndepositionally from continued far-field Laramide compressional deformation that had not fully ceased in the south when collision between the Farallon flat-slab and more pronounced lithospheric keel to the north was occurring around 38 Ma. The flat-lying volcanic rocks of the South Rim Formation deposited in Big Bend National Park unaffected by deformation at 31.21 Ma are interpreted in this study to be the result of secondary steepening or slab tear of the southern Farallon-slab from differential stresses caused by collision, steepening, and densification of the slab in the north and no interaction with the slab and keel to the south.

In the south where roll back associated with secondary steepening of the slab or segmenting and tearing where the keel bends north and east of Big Bend National Park, allowed hot asthenosphere pathways from the south(as flat-slab

would be maintained in the north but not in the south) that occurred 5 Ma later than in the north (Fig.6.9). The steepening and roll-back event having initiated at the keel continued and resulted in the onset of rapid westward migrating volcanism first described by Coney and Reynolds (1977). This westward retreat

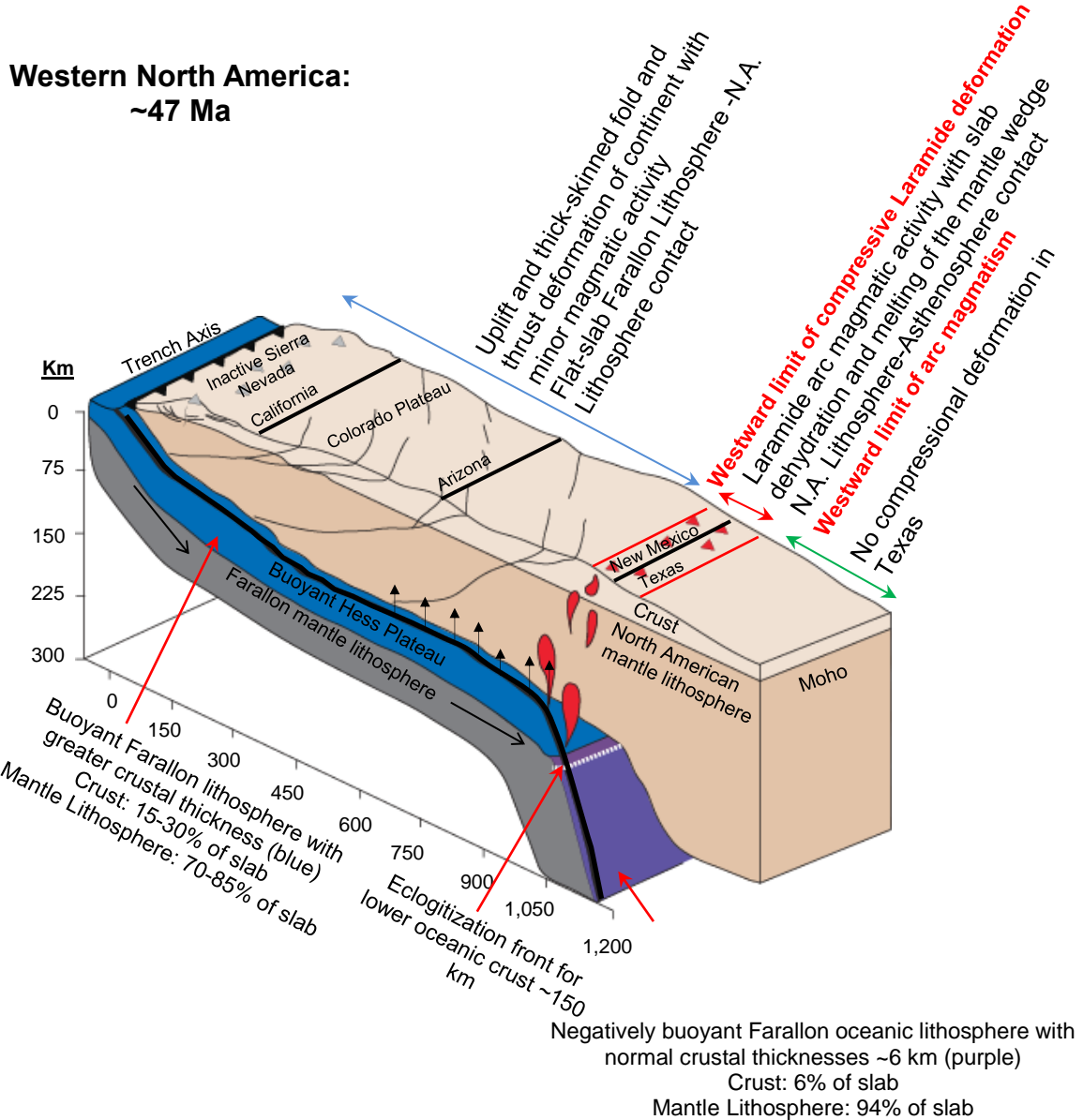


**Fig.6.6:** The Hess conjugate plateau and associated magmatic activity with slab dehydration and melting of the mantle wedge is projected to have reached the present-day Texas-New Mexico border at ~47 Ma. The westward limit of compressive Laramide deformation is directly behind the arc in central New Mexico. No significant compressional deformation related to the orogenic front has occurred in Texas at this time.

**Western North America:  
~40 Ma**

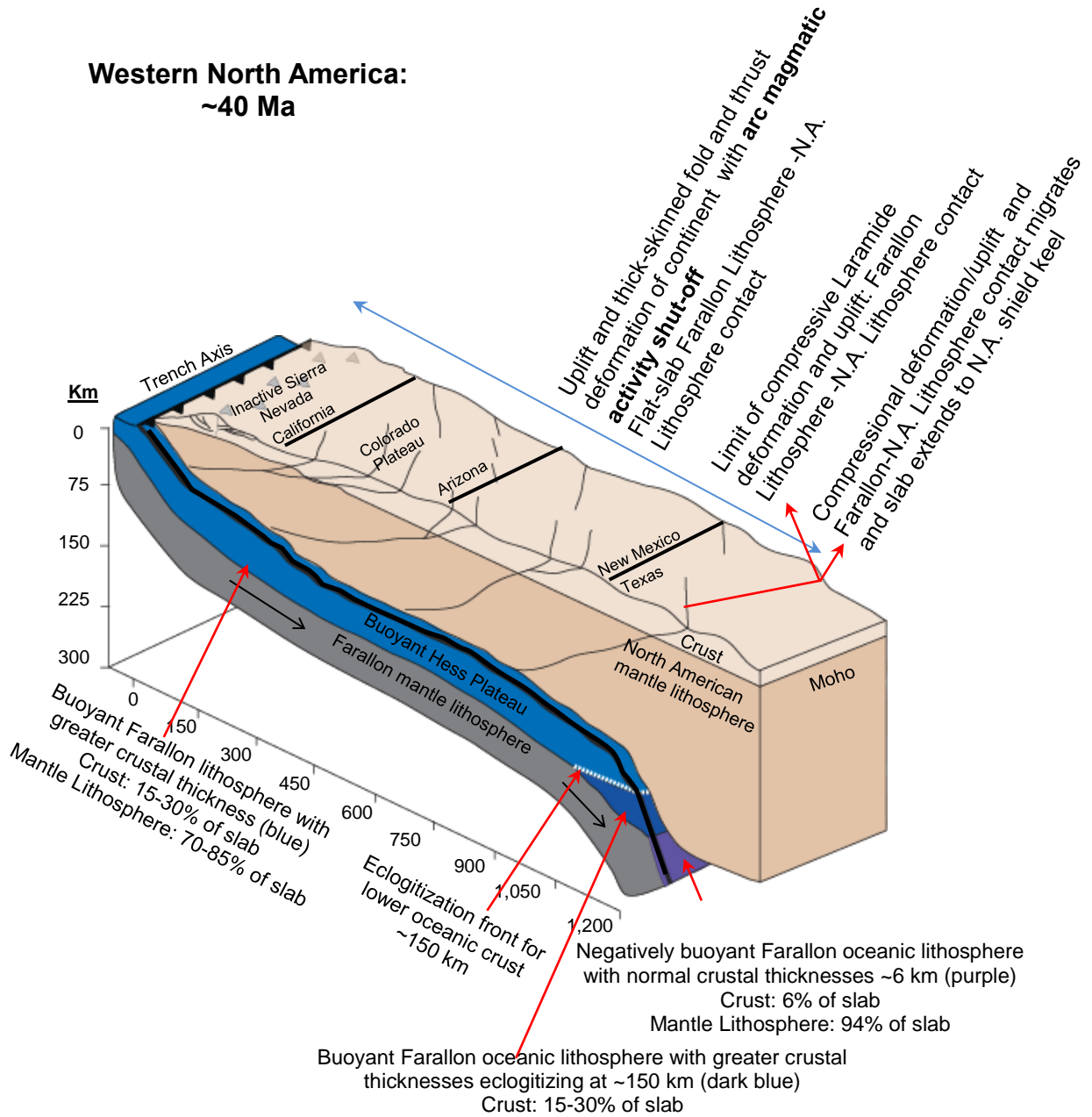


**Fig.6.7:** Arc magmatism shuts off briefly across the western United States around 40 Ma when flat-slab Farallon-North American lithosphere contact extends across the western margin and before collision with the continental interiors stable craton. Thick-skinned deformation, uplift, and subsequent erosion is occurring across Trans-Pecos Texas.

**Western North America:  
~38 Ma**

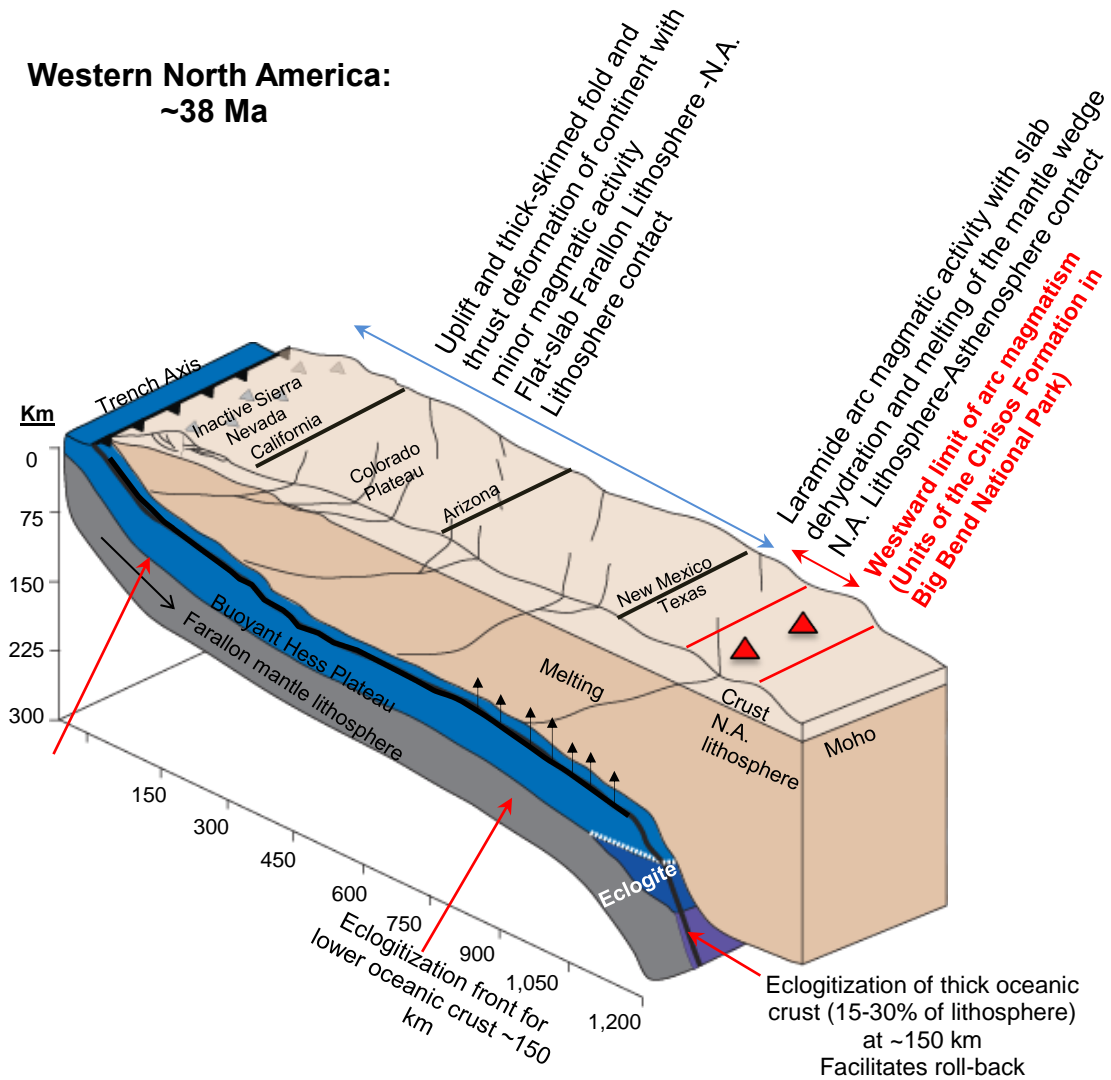


**Fig.6.8:** Diagram displaying the flat-slab and steeper components of the Farallon plate descending beneath North America in the southern Trans-Pecos Texas region near present-day Big Bend National Park. The magmatic arc activity occurred constantly with no shut-off due to constant lithosphere-asthenosphere contact made possible by a less pronounced keel to the east of West Texas. Secondary steepening or slab tear in the south around 31.2 Ma is postulated to be the cause of the flat-lying ignimbrite deposits that make up the South Rim and Burro Mesa Formations.

**Western North American:  
~30 Ma**

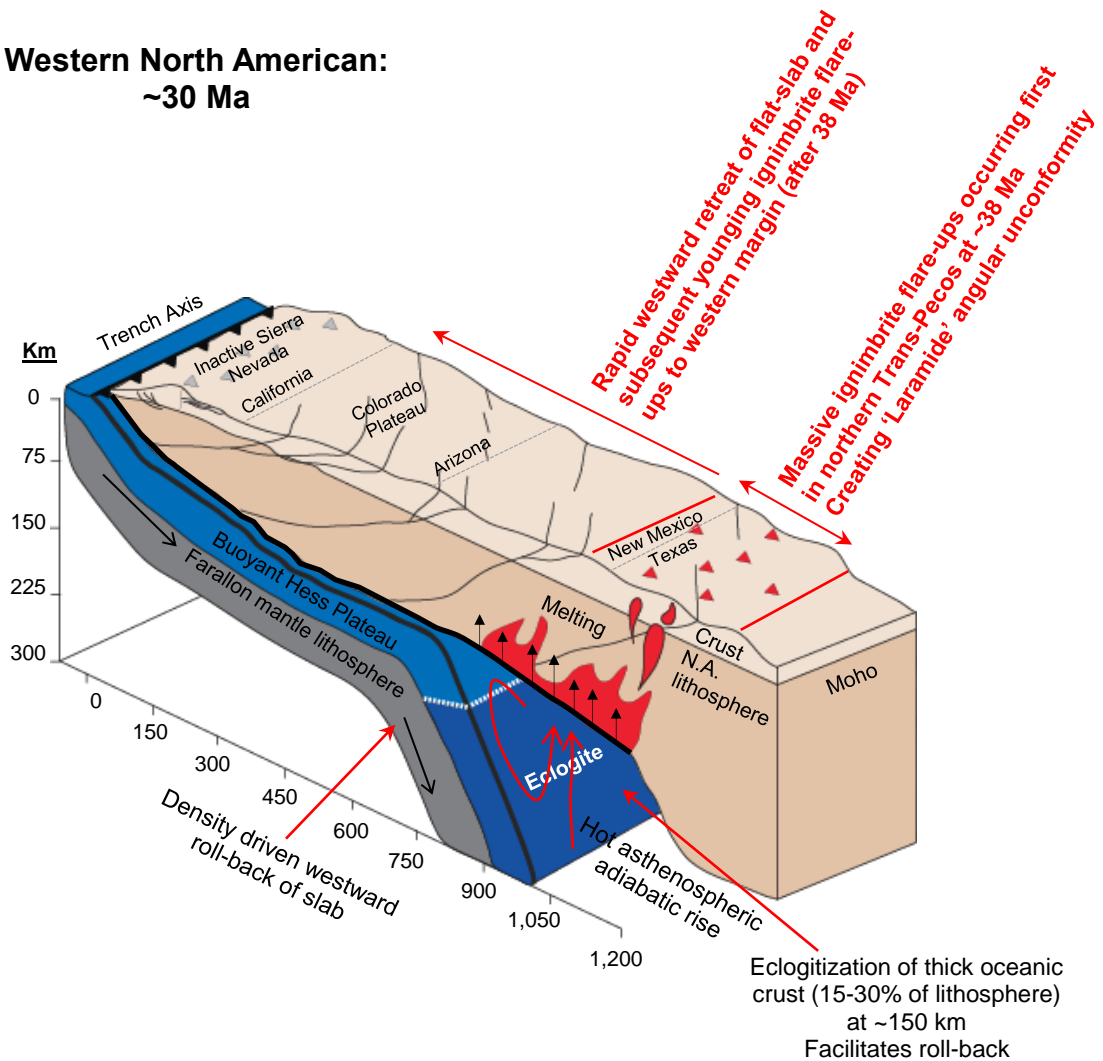


**Fig.6.9:** Collision of the Farallon slab against the keel facilitated steepening and forced the buoyant lithosphere to descend into the mantle. This forced descent hastened the basalt to eclogite facies transition of the coarser grained portion of the thickened Farallon oceanic crust that occurs at depths of 150 km facilitating roll-back. Roll-back of a steepened and densified thicker crustal Farallon slab in the north ca. 38 Ma allowed hot asthenosphere to invade the base of the thinner Trans-Pecos continental lithosphere directly west of the stable cratonic keel.

---

of the arc caused magmatic activity to sweep back across the same terrain in which it had previously advanced, affecting Texas, New Mexico, Arizona, and reaching southern California at 15-20 Ma (Fig.6.10). Tectonic stresses control the ascent of magmas through the crust and therefore play a major role in the style and composition of continental volcanism by affecting the differentiation of the magmas (Chapin *et al.*, 2004). Volcanism of an intermediate composition is favored by a compressional tectonic environment where rising rhyolitic diapirs trap basalt and mix convectively to form hybrid magmas (Eichelberger, 1978). The predominantly alkalic and calc-alkaline ignimbrite deposits in West Texas reflect this convective mixing described by Eichelberger, (1978).

Ignimbrite volcanism in Trans-Pecos Texas and adjacent New Mexico were episodic from north to south, beginning at approximately 38-36 Ma and ending by 26.8 Ma with three last pulses between 25.1 and 23.3 Ma (Chapin *et al.*, 2004). Two regional gaps of 31.4-29.3 Ma and 26.8-25.1 Ma separate these ignimbrite pulses. These brief periods of ignimbrite volcanism suggests a correlation between the ignimbrite flare-ups and a change of regional stress from compression to tension based on work done by Lawton and McMillan (1999) that assessed the creation of passive continental rifts above foundering subducted slabs. Extensional related magmatism at ~25 Ma was intermixed with this retreat in later stage of the evolution. In a period of just over 100 Ma the arc magmatism advanced continuously inboard over 1,000 km and then retreated rapidly back to the western margin where it had originated after collision, steepening, and roll-back of the Farallon slab initiating in Trans-Pecos Texas. The ignimbrite flare-ups

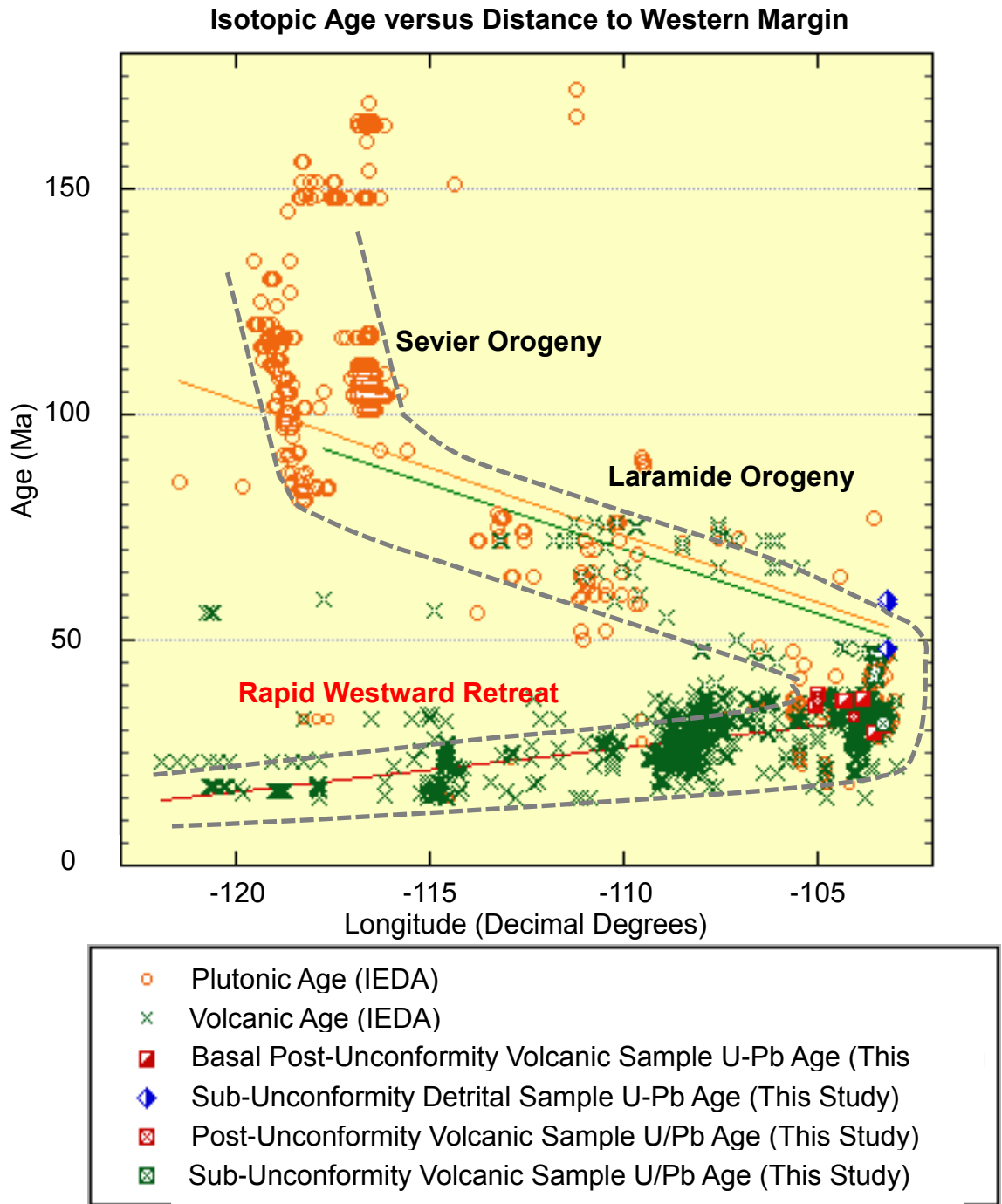


**Figure 6.10:** Displays the distribution of over 3,000 isotopic ages (U/Pb, Ar/Ar, K/Ar, Rb/Sr, Sr/Sr, Sr/Nd, and Nd/Nd) for plutonic and volcanic samples collected from the IEDA-EarthChem Portal plotted with the U/Pb data obtained in this study as a function of time (Modified after Coney and Reynolds, 1977). The dashed line limits the overall trend of magmatism in the northern U.S. Cordillera. Several best-fit lines have been constructed to analyze sloping trends of the incoming and retreating volcanic and plutonic activity. The inlay displays the equations for each best-fit line trend in addition to the relationship between the U/Pb data in this study and the retreating volcanic and plutonic activity trend line.

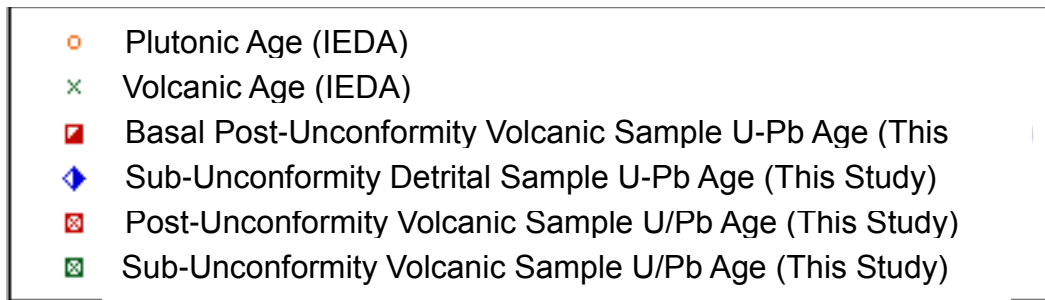
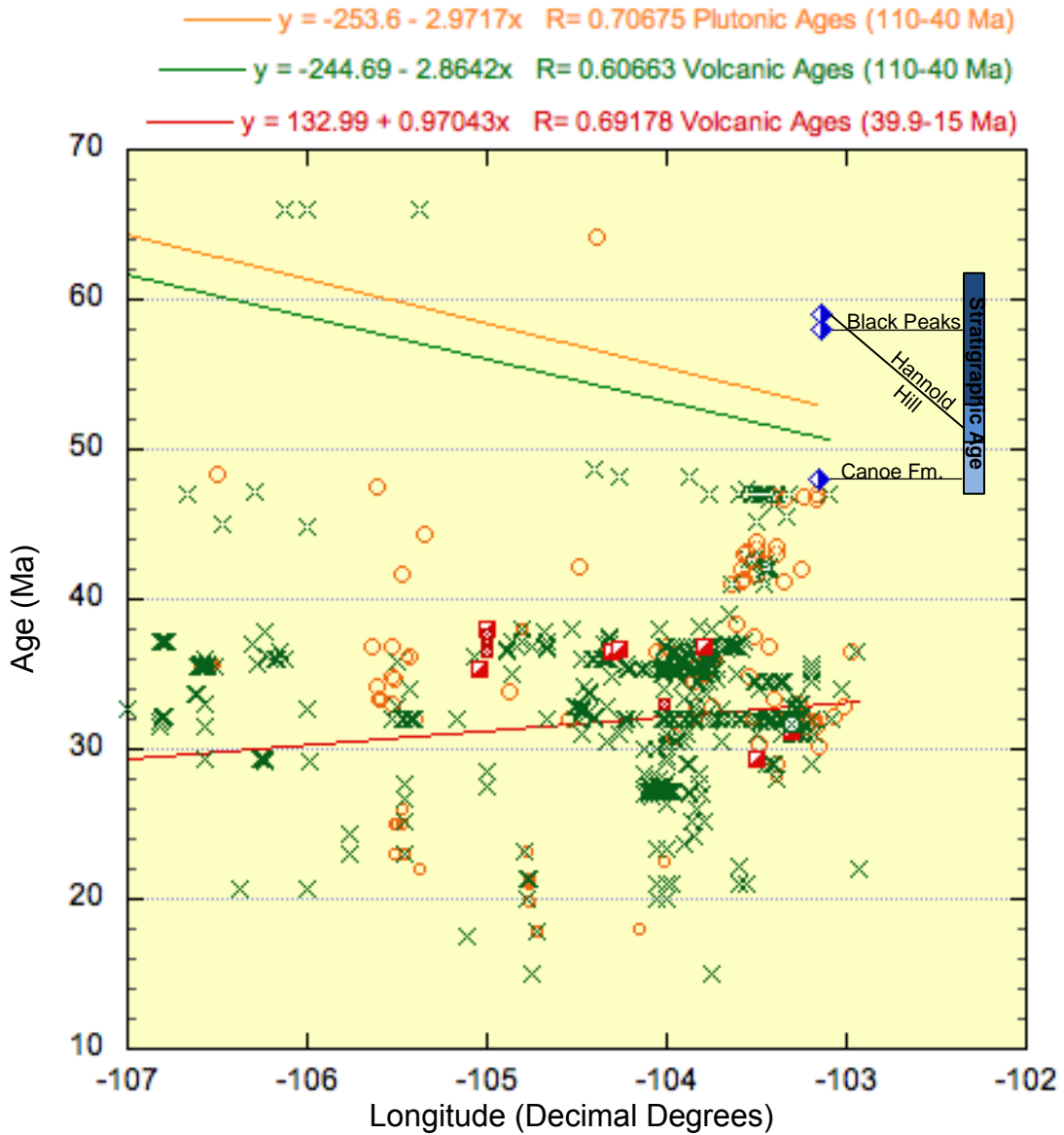


**Figure 6.11:** Inlay of Fig. 6.10 that displays the distribution of over 3,000 isotopic ages (U/Pb, Ar/Ar, K/Ar, Rb/Sr, Sr/Sr, Sr/Nd, and Nd/Nd) for plutonic and volcanic samples collected from the IEDA-EarthChem Portal plotted with the U/Pb data obtained in this study as a function of time (Modified after Coney and Reynolds, 1977). Displays the equations for each best-fit line trend in addition to the relationship between the U/Pb data in this study and the retreating volcanic and plutonic activity trend line.

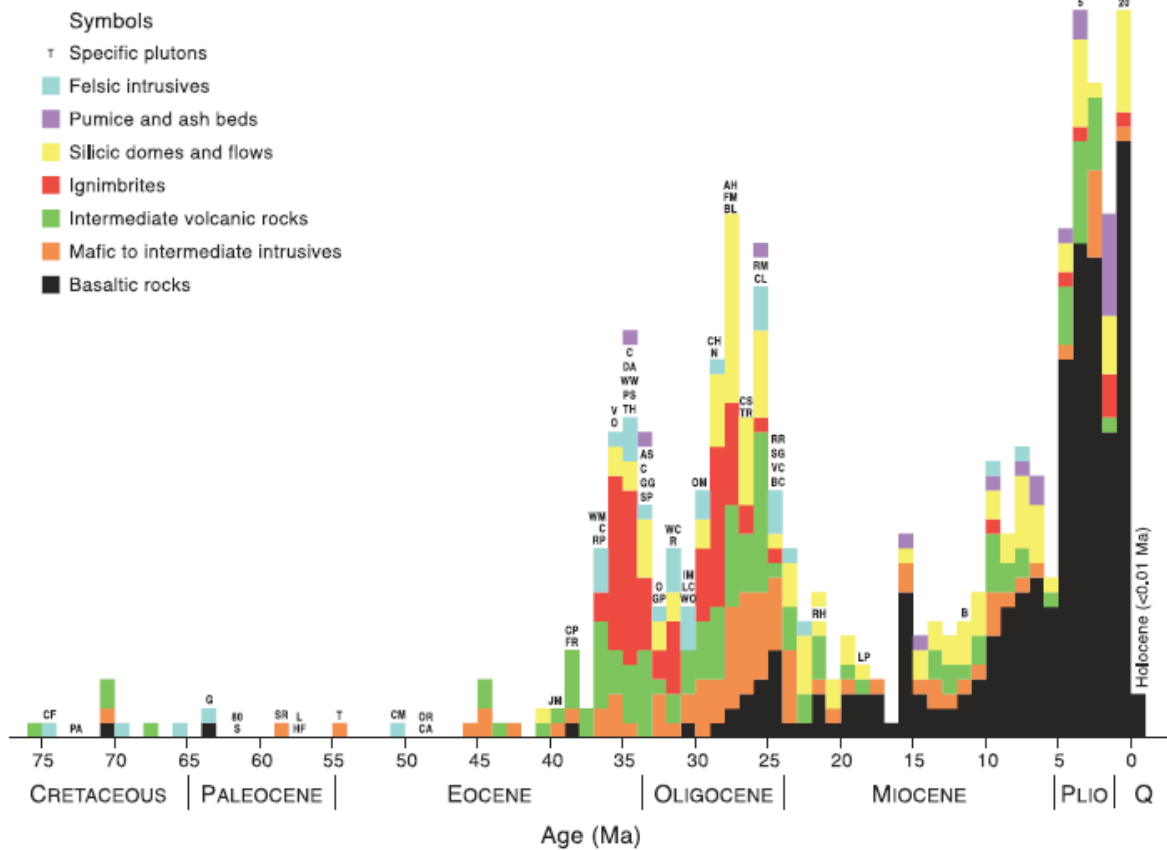


**Fig.6.12:** Histogram of K-Ar and  $^{40}\text{Ar}/^{39}\text{Ar}$  ages of igneous rocks in New Mexico from Late Cretaceous to present-day compiled by Chapin *et al.*(2004) that clearly displays the pulses of ignimbrite volcanism in red in relation to increased bimodal and basaltic volcanism associated with the Basin and Range extensional province that displays a marked increase in volume and distribution around 10-15 Ma

were nearly over before the ‘slab-free’ window began to open coevally with the growth of the transform margin along western California (Dickinson and Snyder, 1979). Over 3,000 isotopic ages (U/Pb, Ar/Ar, K/Ar, Rb/Sr, Sr/Sr, Sr/Nd, and Nd/Nd) for plutonic and volcanic samples in southern California, Arizona, New Mexico, and Texas collected from the IEDA-EarthChem Portal were plotted with the U/Pb data obtained in this study as a function of time in an attempt to recreate Coney and Reynolds’ (1977) diagram displaying radiometric ages in relation to the distance from the western margin to assess if a younging trend still

---

remained. A younging trend can still be observed indicating that steepening and roll-back is the preferred method for slab removal in the southern United States as opposed to slab detachment, sinking, and unloading.

Sigloch *et al.* (2008) utilized finite-frequency travel-time and amplitude measurements of teleseismic P-waves in seven frequency bands to create a high-resolution tomographic image to 1,800 km depth within the mantle beneath present-day North America. Sigloch *et al.* (2008) discovered several large portions of the Farallon plate which displayed two distinct stages of whole-mantle subduction; the currently active one descending from the Pacific Northwest coast to 1,500 km depth beneath the Great Plains, and its stalled predecessor that occupies the transition zone and lower mantle beneath the eastern half of the continent near the Great Lakes that provide evidence for a slab-steepening event based on the geometry of the descending foundered slab (Fig.6.13) (Sigloch *et al.*, 2008; Liu *et al.*, 2010).

Important observations and interpretations surrounding the Laramide orogeny that are crucial to the foundation of this study compiled by Chapin *et al.* (2004) from Gutscher *et al.* (2000), Tosdale and Richards (2001), Kay and Mpodozis (2001), and Beck and Zandt (2002) are: 1) the Andean arc is comprised of alternating segments of flat and normal subduction; 2) volcanism migrates inboard away from the trench as the angle of subduction decreases and ceases when the asthenospheric wedge between the subducting slab and lithospheric mantle becomes too thin or dehydrated; 3) throughout flat-slab

subduction, the slab dips at a normal angle ( $30^\circ$  for Andes) to a depth of around 100 km and then hugs the base of the lithospheric mantle because the slab is

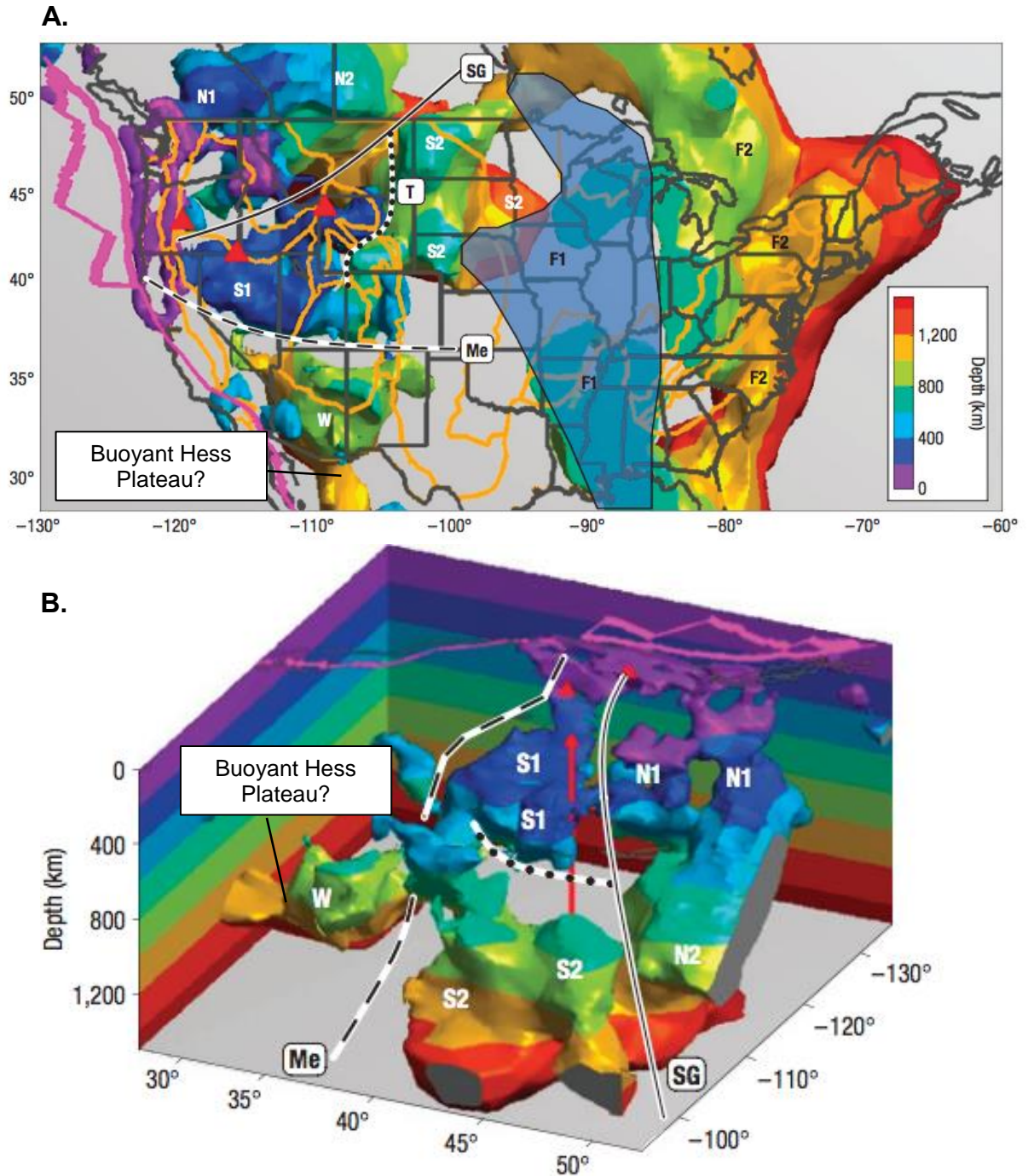


**Fig.6.13:** Three-dimensional views provided by Sigloch *et al.* (2008) of the subducted Farallon plate beneath North America; **A.** Map view of the Cascadia subduction system (S1, S2, N1, N2, W) displays the geometry of the slab, and it's suggested predecessor (F1, F2) to the east. **B.** A bird's eye view of the Cascadia system from the northeast provided by Sigloch *et al.* (2008); portion W of the Cascadia subduction system would must accurately represent the Hess Rise conjugate plateau system now residing under the current day Great Plains region.

---

less dense than the asthenospheric mantle and has not yet gone through the basalt to eclogite phase change; 4) volcanism is episodic with regionally synchronous magmatic activity interspersed with magmatic lulls or quiescence; 5) shortening of the lithosphere thickens the ductile lower crust and produces an uplifted plateau when coupled with tectonic wedging and magmatic activity; 6) dewatering of the subducting slab and hydration of the asthenospheric wedge and overriding plate induces melting and magmatism; 7) fluids for mineralization are released as the crust thickens and hydrous lower crustal amphibole bearing mineral assemblages in the lower crust break down to garnet bearing assemblages; 8) porphyry copper deposits form in environments where the magmatic arc is in a nearly neutral stress regime, usually recording transitions in or out of flat-slab subduction; and 9) extensive melting of lithospheric mantle and crust with subsequent ignimbritic volcanism occurs as asthenospheric mantle intrudes above the slab during a transition from flat-slab subduction to normal subduction. All of which are documented in the migration, arrival, collision, steepening, roll-back and subsequent ignimbrite flare-ups in West Texas.

---

## References

- Adamek, S., Tajima, F., & Wiens, D. A. (1987). Seismic rupture associated with subduction of the Cocos Ridge. *Tectonics*, 6(6), 757-774.
- Ahrens, T. J., & Schubert, G. (1975). Gabbro-eclogite reaction rate and its geophysical significance. *Reviews of Geophysics*, 13(2), 383-400.
- Amsbury, D. L. (1958). Geology of the Pinto Canyon area. Presidio County, Texas: Texas Bureau of Economic Geology, Quadrangle Map, (22).
- Barnes, M. A., Rohs, C. R., Anthony, E. Y., Van Schmus, W. R., & Denison, R. E. (1999). Isotopic and elemental chemistry of subsurface Precambrian igneous rocks, west Texas and eastern New Mexico. *Rocky Mountain Geology*, 34(2), 245-262.
- Barnes, V. E. (1982). Geologic Atlas of Texas, Fort Stockton Sheet. Texas Bureau of Economic Geology.
- Barnes, V. E. (1979). Geologic Atlas of Texas-Marfa Sheet. Bureau of Economic Geology, Austin, scale, 1(250,000), 1.
- Barnes, V. E. (1979). Emory Peak-Presidio sheet The University of Texas at Austin. Bureau of Economic Geology, Geologic Atlas of Texas, scale, 1(250,000).
- Barker, D. S. (1987). Tertiary alkaline magmatism in Trans-Pecos Texas. *Geological Society, London, Special Publications*, 30(1), 415-431.
- Barker, D. S., Henry, C. D., & McDowell, F. W. (1986). Pine Canyon caldera, Big Bend National Park: a mildly peralkaline magmatic system. *Igneous geology of Trans-Pecos Texas, the University of Texas at Austin Bureau of Economic Geology Guidebook*, 23, 266-285.
- Barker, D. S. (1979). Magmatic evolution in the Trans-Pecos province. *Guideb. Univ. Tex. Austin Bur. Econ. Geol.*, 19, 4-9.
- Barker, D. S. (1977). Northern Trans-Pecos magmatic province: Introduction and comparison with the Kenya rift. *Geological Society of America Bulletin*, 88(10), 1421-1427.
- Barth, A. P., Wooden, J. L., Jacobson, C. E., & Probst, K. (2004). U-Pb geochronology and geochemistry of the McCoy Mountains Formation, southeastern California: A Cretaceous retroarc foreland basin. *Geological Society of America Bulletin*, 116(1-2), 142-153.

---

Beatty, H. L. (1992). Fluvial Sedimentology and Sandstone Petrography of the Hannold Hill Formation (Eocene), Bib Bend, Texas (Doctoral dissertation, Texas Tech University).

Beck, S. L., & Zandt, G. (2002). The nature of orogenic crust in the central Andes. *Journal of Geophysical Research: Solid Earth* (1978–2012), 107(B10), ESE-7.

Befus, K. S., Hanson, R. E., Miggins, D. P., Breyer, J. A., & Busbey, A. B. (2009). Nonexplosive and explosive magma/wet-sediment interaction during emplacement of Eocene intrusions into Cretaceous to Eocene strata, Trans-Pecos igneous province, West Texas. *Journal of Volcanology and Geothermal Research*, 181(3), 155-172.

Befus, K. S., Hanson, R. E., Lehman, T. M., & Griffin, W. R. (2008). Cretaceous basaltic phreatomagmatic volcanism in west Texas: maar complex at Pena Mountain, Big Bend National park. *Journal of Volcanology and Geothermal Research*, 173(3), 245-264.

Benker, S.C., 2005, The petrology of the South Rim Formation, Big Bend National Park, Texas: Richmond, Ky., Eastern Kentucky University, M.S. thesis, 104 p.

Bickford, M. E., Soegaard, K., Nielsen, K. C., & McLelland, J. M. (2000). Geology and geochronology of Grenville-age rocks in the Van Horn and Franklin Mountains area, west Texas: Implications for the tectonic evolution of Laurentia during the Grenville. *Geological Society of America Bulletin*, 112(7), 1134-1148.

Bird, P. (1998). Kinematic history of the Laramide orogeny in latitudes 35–49 N, western United States. *Tectonics*, 17(5), 780-801.

Bird, P. (1988). Formation of the Rocky Mountains, western United States: A continuum computer model. *Science*, 239(4847), 1501-1507.

Bird, P. (1984). Laramide crustal thickening event in the Rocky Mountain foreland and Great Plains. *Tectonics*, 3(7), 741-758.

Burchfiel, B. C., & Davis, G. A. (1977). Geology of the Sagamore Canyon–Slaughterhouse Spring area, New York Mountains, California. *Geological Society of America Bulletin*, 88(11), 1623-1640.

Busbey, A.B., and Lehman, T. (eds.), (1989). *Vertebrate Paleontology, Stratigraphy, and Sedimentology of Big Bend National Park: Society of Vertebrate Paleontology Field Guide*, 100 p.

---

Cameron, K. L., Parker, D. F., & Sampson, D. E. (1996). Testing crustal melting models for the origin of flood rhyolites: A Nd-Pb-Sr isotopic study of the Tertiary Davis Mountains volcanic field, west Texas. *Journal of Geophysical Research: Solid Earth* (1978–2012), 101(B9), 20407-20422.

Carl, C., Wendt, I. and Wendt, J. I. (1989). U/Pb whole-rock and mineral dating of the Falkenburg granite in northeast Bavaria. *Earth Planet. Sci. Lett.* **94**, 236-244.

Carman, M.F., Stewart, R.M., Jr., and Casey, J.F., 2003, Characterization of the Alamo Creek Basalt, Big Bend National Park, Texas: *Texas Journal of Science*, v. 55, no. 2, p. 99–128.

Carman Jr, M. F. (1994). Mechanisms of differentiation in shallow mafic alkaline intrusions, as illustrated in the Big Bend area, western Texas. *Journal of volcanology and geothermal research*, 61(1), 1-44.

Cepeda, J. C. (1977). Geology and geochemistry of the igneous rocks of the Chinati Mountains, Presidio County, Texas: The University of Texas at Austin (Doctoral dissertation, Ph. D. dissertation).

Chapin, C. E., McIntosh, W.C., & Chamberlin, R. M. (2004). The late Eocene-Oligocene peak of Cenozoic volcanism in southwestern New Mexico. *The Geology of New Mexico—A geologic history*, 11, 271-294.

Chung, W. Y., & Kanamori, H. (1978). Subduction process of a fracture zone and aseismic ridges—the focal mechanism and source characteristics of the New Hebrides earthquake of 1969 January 19 and some related events. *Geophysical Journal International*, 54(1), 221-240.

Cloos, M. (1993). Lithospheric buoyancy and collisional orogenesis: Subduction of oceanic plateaus, continental margins, island arcs, spreading ridges, and seamounts. *Geological Society of America Bulletin*, 105(6), 715-737.

Condie, K. C., & Aster, R. C. (2009). Zircon age episodicity and growth of continental crust. *Eos, Transactions American Geophysical Union*, 90(41), 364-364.

Coney, P. J., & Reynolds, S. J. (1977). Cordilleran benioff zones. *Nature*, 270, 403-406.

DeCelles, P. G., Ducea, M. N., Kapp, P., & Zandt, G. (2009). Cyclicity in Cordilleran orogenic systems. *Nature Geoscience*, 2(4), 251-257.

DeCelles, P. G. (2004). Late Jurassic to Eocene evolution of the Cordilleran thrust belt and foreland basin system, western USA. *American Journal of Science*, 304(2), 105-168.

---

DeFord, R. K. (1958). Tertiary formations of Rim Rock country, Presidio County, Trans-Pecos, Texas. Bureau of Economic Geology, University of Texas.

Denison, R. E. (1980). Pre-Bliss (PC) rocks in the Van Horn region, Trans-Pecos, Texas. Trans-Pecos Region, southeastern New Mexico and West Texas: New Mexico Geological Society, Guidebook, (31,155-158).

Dietrich, J.W., Owen, D.E., Shelby, C.A., (1983).Geologic Atlas of Texas, Van Horn-El Paso Sheet. University of Texas at Austin, Bureau of Economic Geology, 1983.

Dickerson, P.W., 1980, Structural zones transecting the southern Rio Grande rift—Preliminary observations, in Trans-Pecos Region (West Texas): New Mexico Geological Society Fall Field Conference Guidebook 31, p. 63–70.

Dietrich, J. W. (1966). Geology of Presidio Area, Presidio County, Texas.

Dickin, A. P. (2005). Radiogenic isotope geology. Cambridge University Press.

Dickerson, P. W. (2003). Intraplate mountain building in response to continent–continent collision—the Ancestral Rocky Mountains (North America) and inferences drawn from the Tien Shan (Central Asia). *Tectonophysics*, 365(1), 129-142.

Dickinson, W. R., & Gehrels, G. E. (2009). Use of U–Pb ages of detrital zircons to infer maximum depositional ages of strata: a test against a Colorado Plateau Mesozoic database. *Earth and Planetary Science Letters*, 288(1), 115-125.

Dickinson, W. R., & Gehrels, G. E. (2003). U–Pb ages of detrital zircons from Permian and Jurassic eolian sandstones of the Colorado Plateau, USA: paleogeographic implications. *Sedimentary Geology*, 163(1), 29-66.

Dickinson, W. R. (2000). Geodynamic interpretation of Paleozoic tectonic trends oriented oblique to the Mesozoic Klamath-Sierran continental margin in California. *SPECIAL PAPERS-GEOLOGICAL SOCIETY OF AMERICA*, 209-246.

Dickinson, W. R., Snyder, W. S. (1978). Plate tectonics of the Laramide orogeny. *Geological Society of America Memoir*, 151, 355-366.

Drenth, B. J., & Finn, C. A. (2007). Aeromagnetic mapping of the structure of Pine Canyon caldera and Chisos mountains intrusion, Big Bend National Park, Texas. *Geological Society of America Bulletin*, 119(11-12), 1521-1534.

Ducea, M. N., & Barton, M. D. (2007). Igniting flare-up events in Cordilleran arcs. *Geology*, 35(11), 1047-1050.

- 
- Duex, T. W., & Henry, C. D. (1981). Calderas and mineralization: Volcanic geology and mineralization in the Chianti caldera complex, Trans-Pecos Texas. Unknown, 1.
- Eichelberger, J. C. (1978). Andesitic volcanism and crustal evolution. *Nature*, 275, 21-27.
- Engebretson, D. C. (1985). Relative motions between oceanic and continental plates in the Pacific basin (Vol. 206). Geological society of America.
- Engebretson, D. C., Cox, A., & Thompson, G. A. (1984). Correlation of plate motions with continental tectonics: Laramide to basin-range. *Tectonics*, 3(2), 115-119.
- English, J. M., Johnston, S. T., & Wang, K. (2003). Thermal modelling of the Laramide orogeny: testing the flat-slab subduction hypothesis. *Earth and Planetary Science Letters*, 214(3), 619-632.
- Eifler, G. K. (1951). Geology of the Barrilla Mountains, Texas. *Geological Society of America Bulletin*, 62(4), 339-353.
- Erickson, R. L. (1953). Stratigraphy and petrology of the Tascotal Mesa quadrangle, Texas. *Geological Society of America Bulletin*, 64(12), 1353-1386.
- Fedo, C. M., Sircombe, K. N., & Rainbird, R. H. (2003). Detrital zircon analysis of the sedimentary record. *Reviews in Mineralogy and Geochemistry*, 53(1), 277-303.
- Flawn, P. T. (1951). Pegmatites of the Van Horn Mountains, Texas. *Economic Geology*, 46(2), 163-192.
- Forneris, J. F., & Holloway, J. R. (2004). Evolution of mineral compositions during eclogitization of subducting basaltic crust. *American Mineralogist*, 89(10), 1516-1524.
- Forte, A. M., Moucha, R., Simmons, N. A., Grand, S. P., & Mitrovica, J. X. (2010). Deep-mantle contributions to the surface dynamics of the North American continent. *Tectonophysics*, 481(1), 3-15.
- Gardner, T. W., Verdonck, D., Pinter, N. M., Slingerland, R., Furlong, K. P., Bullard, T. F., & Wells, S. G. (1992). Quaternary uplift astride the aseismic Cocos ridge, Pacific coast, Costa Rica. *Geological Society of America Bulletin*, 104(2), 219-232.
- Gehrels, G. E., Valencia, V.A., and Ruiz, J., (2008). "Enhanced precision, accuracy, efficiency, and spatial resolution of U-Pb ages by laser ablation—

---

multicollector–inductively coupled plasma–mass spectrometry." *Geochemistry, Geophysics, Geosystems* 9, no. 3.

Gehrels, G.E., 2007, AgePick,  
<https://sites.google.com/a/laserchron.org/laserchron/home/>.

Gehrels, G., et al. (2006), Detrital zircon geochronology by laser-ablation multicollector ICPMS at the Arizona Laserchron Center, in *Geochronology: Emerging Opportunities*, Paleontological Society Short Course, October 21, 2006, Philadelphia, PA. Paleontological Society Papers, edited by T. Olszewski, pp. 67–76, Paleontol. Soc., Lawrence, Kans.

Gerya, T. V., Stöckhert, B., & Perchuk, A. L. (2002). Exhumation of high-pressure metamorphic rocks in a subduction channel: A numerical simulation. *Tectonics*, 21(6), 6-1.

Gillerman, E. (1953). Fluorspar deposits of the Eagle Mountains, Trans-Pecos Texas, p.45.

Gilmer, A. K., Kyle, J. R., Connelly, J. N., Mathur, R. D., & Henry, C. D. (2003). Extension of Laramide magmatism in southwestern North America into Trans-Pecos Texas. *Geology*, 31(5), 447-450.

Gilmer, A. (2001, November). The Red Hills Intrusive System, Presidio County, Texas: The Easternmost Laramide Porphyry-Molybdenum Deposit in Southwestern North America. In GSA Annual Meeting, November 5-8, 2001.

Gray, J.E., and Page, W.R., eds., 2008, Geological, geochemical, and geophysical studies by the U.S. Geological Survey in Big Bend National Park, Texas: U.S. Geological Survey Circular 1327, 93 p.

Goldrich, S. S., and Elms, M. A., (1949). Stratigraphy and petrology of the Buck Hill Quadrangle, Texas: *Geological Society of America Bulletin*, v. 60, no. 7, p. 1133-1182.

Gutscher, M. A., Spakman, W., Bijwaard, H., & Engdahl, E. R. (2000). Geodynamics of flat subduction: Seismicity and tomographic constraints from the Andean margin. *Tectonics*, 19(5), 814-833.

Gutscher, M. A., Maury, R., Eissen, J. P., & Bourdon, E. (2000). Can slab melting be caused by flat subduction?. *Geology*, 28(6), 535-538.

Harlan, S. S., Geissman, J. W., Henry, C. D., & Onstott, T. C. (1995). Paleomagnetism and <sup>40</sup>Ar/<sup>39</sup>Ar geochronology of gabbro sills at Mariscal Mountain anticline, southern Big Bend National Park, Texas: Implications for the

---

timing of Laramide tectonism and vertical axis rotations in the southern Cordilleran orogenic belt. *Tectonics*, 14(2), 307-321.

Hartnell, J. A. (1980). The vertebrate paleontology, depositional environment and sandstone provenance of early eocene rocks on Tonillo Flat, Big Bend National Park, Brewster County, Texas (Doctoral dissertation, Louisiana State University, Baton Rouge).

Hay-Roe, H. (1957). Geology of Wylie Mountains and Vicinity, Culberson and Jeff Davis Counties, Texas. The University of Texas, Bureau of Economic Geology, Geologic Quadrangle, Map, 21.

Hay-Roe, H. (1957). Geology of Wylie Mountains and vicinity. Culberson and Jeff Davis Counties, Texas. University of Texas, Bureau of Economic Geology.

Heinselman and Miron, (1996). The boundary waters wilderness ecosystem: Minneapolis and London, University of Minnesota Press, 334 p.

Hellstrom, J., Paton, C., Woodhead, J., & Hergt, J. (2008). Lolite: software for spatially resolved LA-(quad and MC) ICPMS analysis. Mineralogical Association of Canada short course series, 40, 343-348.

Henderson, G. D., 1989, Geology of the Medley kaolin deposits and associated volcanic rocks, Jeff Davis County, Texas [Master's thesis]: Waco, Texas, Baylor University, 186 p.

Henry, C.D., and Davis, L.L., 1996, Tertiary volcanic, volcanoclastic, and intrusive rocks adjacent to the Solitario, in Henry, C.D., and Muehlberger, W.R., eds., Geology of the Solitario Dome, Trans-Pecos Texas—Paleozoic, Mesozoic, and Cenozoic sedimentation, tectonism, and magmatism: University of Texas at Austin, Bureau of Economic Geology Reports of Investigations 240, p. 81–108.

Henry, C. D., Kunk, M. J., & McIntosh, W. C. (1994).  $^{40}\text{Ar}/^{39}\text{Ar}$  chronology and volcanology of silicic volcanism in the Davis Mountains, Trans-Pecos Texas. *Geological Society of America Bulletin*, 106(11), 1359-1376.

Henry, C. D., Price, J. G., Rubin, J. N., & Laubach, S. E. (1990). Case study of an extensive silicic lava: the Bracks Rhyolite, Trans-Pecos Texas. *Journal of Volcanology and Geothermal Research*, 43(1), 113-132.

Henry, C. D. (1989). Late Cenozoic Basin and Range structure in western Mexico adjacent to the Gulf of California. *Geological Society of America Bulletin*, 101(9), 1147-1156.

---

Henry, C. D., Price, J. G., Rubin, J. N., Parker, D. F., Wolff, J. A., Self, S., ... & Barker, D. S. (1988). Widespread, lavalike silicic volcanic rocks of Trans-Pecos Texas. *Geology*, 16(6), 509-512.

Henry, C. D., & McDowell, F. W. (1986). Geochronology of magmatism in the Tertiary volcanic field, Trans-Pecos Texas. *Igneous geology of Trans-Pecos Texas. Bureau of Economic Geology Guidebook*, 23, 99-122.

Henry, C. D., & Price, J. G. (1986). Early basin and range development in Trans-Pecos Texas and adjacent Chihuahua: Magmatism and orientation, timing, and style of extension. *Journal of Geophysical Research: Solid Earth* (1978–2012), 91(B6), 6213-6224.

Henry, C. D., & Price, J. G. (1984). Variations in caldera development in the Tertiary volcanic field of Trans-Pecos Texas. *Journal of Geophysical Research: Solid Earth* (1978–2012), 89(B10), 8765-8786.

Hildebrand, R. S. (2009). Did westward subduction cause Cretaceous-Tertiary orogeny in the North American Cordillera? (Vol. 457). *Geological Society of America*.

Hoffer, J. M., Leggett, B. D., & Verrillo, D. E. (1980). Tertiary volcanics of the western Eagle Mountains, Hudspeth County, Texas. In *Field Conf. Guideb. NM Geol. Soc* (Vol. 31, pp. 237-240).

Hoffer, J. M. (1970). Petrology and Mineralogy of the Campus Andesite Pluton, El Paso, Texas. *Geological Society of America Bulletin*, 81(7), 2129-2136.

Hoffman, P. F. (1988). United Plates of America, the birth of a craton-Early Proterozoic assembly and growth of Laurentia. *Annual Review of Earth and Planetary Sciences*, 16, 543-603.

Holt, G.S. (1998) Trace element partitioning of alkali feldspar in Burro Mesa Rhyolite and other units of the Trans-Pecos Magmatic Province. Unpublished M.S.thesis, 190 p. Baylor University, Waco, Texas.

Humphreys, E. (2009). Relation of flat subduction to magmatism and deformation in the western United States. *Backbone of the Americas: Shallow subduction, plateau uplift, and ridge and terrane collision*, 204, p. 85.

Humphreys, E., Hessler, E., Dueker, K., Farmer, G. L., Erslev, E., & Atwater, T. (2003). How Laramide-age hydration of North American lithosphere by the Farallon slab controlled subsequent activity in the western United States. *International Geology Review*, 45(7), 575-595.

---

Humphreys, E. D. (1995). Post-Laramide removal of the Farallon slab, western United States. *Geology*, 23(11), 987-990.

James, E. W., & Henry, C. D. (1993). Pb isotopes of ore deposits in Trans-Pecos Texas and northeastern Chihuahua, Mexico; basement, igneous, and sedimentary sources of metals. *Economic Geology*, 88(4), 934-947.

Hussong, D. M., Wipperman, L. K., & Kroenke, L. W. (1979). The crustal structure of the Ontong Java and Manihiki oceanic plateaus. *Journal of Geophysical Research: Solid Earth (1978–2012)*, 84(B11), 6003-6010.

Jarrard, R. D. (1986). Relations among subduction parameters. *Reviews of Geophysics*, 24(2), 217-284.

Jirsa, M. A., Miller Jr, J. D., Severson, M. J., & Chandler, V. W. (2006). Final Report on the Geology, Geochemistry, Geophysical Attributes, and Platinum Group Element Potential of Mafic to Ultramafic Intrusions in Minnesota, Excluding the Duluth Complex.

Johnson, K., & Dick, H. J. (1992). Open system melting and temporal and spatial variation of peridotite and basalt at the Atlantis II fracture zone. *Journal of Geophysical Research: Solid Earth (1978–2012)*, 97(B6), 9219-9241.

Jones, C. H., Farmer, G. L., Sageman, B., & Zhong, S. (2011). Hydrodynamic mechanism for the Laramide orogeny. *Geosphere*, 7(1), 183-201.

Jordan, T. E., & Allmendinger, R. W. (1986). The Sierras Pampeanas of Argentina: A modern analogue of Rocky Mountain foreland deformation. *American Journal of Science*, 286(10), 737-764.

Kay, S. M., & Mpodozis, C. (2001). Central Andean ore deposits linked to evolving shallow subduction systems and thickening crust. *GSA TODAY*, 11(3), 4-9.

Kelleher, J., & McCann, W. (1977). Bathymetric highs and the development of convergent plate boundaries. *Maurice Ewing Series*, 1, 115-122.

King, P. B., & Flawn, P. T. (1953). *Geology and mineral deposits of pre-Cambrian rocks of the Van Horn area, Texas (No. 5301)*. Bureau of Economic Geology, University of Texas.

LaMaskin, T. A. (2012). Detrital zircon facies of Cordilleran terranes in western North America. *GSA Today*, 22(3), 4-11.

- 
- Laskowski, A. K., DeCelles, P. G., & Gehrels, G. E. (2013). Detrital zircon geochronology of Cordilleran retroarc foreland basin strata, western North America. *Tectonics*, 32(5), 1027-1048.
- Lawton, T. F., & McMillan, N. J. (1999). Arc abandonment as a cause for passive continental rifting: Comparison of the Jurassic Mexican Borderland rift and the Cenozoic Rio Grande rift. *Geology*, 27(9), 779-782.
- Legett, B. D. (1979). Tertiary volcanics of the northwest Eagle Mountains, Hudspeth County, Texas.
- Lehman, T. M., & Busbey, A. B. (2007, October). Big Bend field trip guidebook. In Society of Vertebrate Paleontology, 67th Annual Meeting (Austin, TX).
- Lehman, T. M., Mcdowell, F. W., & Connelly, J. N. (2006). First isotopic (U-Pb) age for the Late Cretaceous Alamosaurus vertebrate fauna of West Texas, and its significance as a link between two faunal provinces. *Journal of Vertebrate Paleontology*, 26(4), 922-928.
- Lehman, T. M. (1991). Sedimentation and tectonism in the Laramide Tornillo Basin of west Texas. *Sedimentary Geology*, 75(1), 9-28.
- Lehman, T. M. (1990). Paleosols and the Cretaceous/Tertiary transition in the Big Bend region of Texas. *Geology*, 18(4), 362-364.
- Lehman, T. M. (1989). Upper Cretaceous (Maastrichtian) paleosols in Trans-Pecos Texas. *Geological Society of America Bulletin*, 101(2), 188-203.
- Lehman, T. M. (1988). Stratigraphy of the Cretaceous-Tertiary and Paleocene-Eocene transition rocks of Big Bend National Park, Texas: A discussion. *The Journal of Geology*, 627-631.
- Lehman, T. M. (1986). Late Cretaceous sedimentation in Trans-Pecos Texas. *Geology of the Big Bend Area and Solitario Dome, Texas: West Texas Geological Society, Fieldtrip Guidebook*, (86-82), 105-110.
- Lehman, T. M. (1985). Transgressive-regressive cycles and environments of coal deposition in Upper Cretaceous strata of the Trans-Pecos Texas: Gulf Coast Association of Geological Societies. *Transactions*, 35, 431-438.
- Lipman, P. W., Prostka, H. J., & Christiansen, R. L. (1971). Evolving subduction zones in the western United States, as interpreted from igneous rocks. *Science*, 174(4011), 821-825.

---

Liu, L., Gurnis, M., Seton, M., Saleeby, J., Müller, R. D., & Jackson, J. M. (2010). The role of oceanic plateau subduction in the Laramide orogeny. *Nature Geoscience*, 3(5), 353-357.

Liu, J.P., You, Z.D., Zhong, Z.Q., (1996). Eclogites from the middle and north of Dabie mountain in southern Henan and northern Hubei. *Sci. China (Ser. D)* 39, 293–300.

Livaccari, R. F. (1991). Role of crustal thickening and extensional collapse in the tectonic evolution of the Sevier-Laramide orogeny, western United States. *Geology*, 19(11), 1104-1107.

Mackey, G. N., Horton, B. K., & Milliken, K. L. (2012). Provenance of the Paleocene–Eocene Wilcox Group, western Gulf of Mexico basin: Evidence for integrated drainage of the southern Laramide Rocky Mountains and Cordilleran arc. *Geological Society of America Bulletin*, 124(5-6), 1007-1024.

Martinod, J., Husson, L., Roperch, P., Guillaume, B., & Espurt, N. (2010). Horizontal subduction zones, convergence velocity and the building of the Andes. *Earth and Planetary Science Letters*, 299(3), 299-309.

Macharé, J., & Ortlieb, L. (1992). Plio-Quaternary vertical motions and the subduction of the Nazca Ridge, central coast of Peru. *Tectonophysics*, 205(1), 97-108.

Matthews III, W. K., & Adams, J. A. S. (1986). Geochemistry, age, and structure of the Sierra Blanca and Finlay Mountain intrusions, Hudspeth County, Texas. *Igneous Geology of TransPecos Texas, Field Trip Guides and Research Articles*, University of Texas at Austin Bureau of Economic Geology, Guidebook, 23, 207-224.

Maxson, J., & Tikoff, B. (1996). Hit-and-run collision model for the Laramide orogeny, western United States. *Geology*, 24(11), 968-972.

Maxwell, R.A., Lonsdale, J.T., Hazzard, R.T., and Wilson, J.A., 1967, *Geology of Big Bend National Park, Brewster County, Texas*: University of Texas at Austin, Bureau of Economic Geologic Publication no. 6711, 320 p.

McAnulty, W. N. (1955). *Geology of Cathedral Mountain Quadrangle, Brewster County, Texas*. *Geological Society of America Bulletin*, 66(5), 531-578.

McBride, E.F., (1989), Stratigraphy and sedimentary history of pre-Permian Paleozoic rocks in the Marathon uplift, in Hatcher, R.D., Jr., Thomas, W.A., and Viele, G.W., eds., *The Appalachian-Ouachita orogen in the United States*. *The Geology of North America*, v. F2, chapter 20: Geological Society of America, p. 603–620.

---

McCann, W. R., & Sykes, L. R. (1984). Subduction of aseismic ridges beneath the Caribbean plate: Implications for the tectonics and seismic potential of the northeastern Caribbean. *Journal of Geophysical Research: Solid Earth* (1978–2012), 89(B6), 4493-4519.

McGEARY, S. U. S. A. N., Nur, A., & Ben-Avraham, Z. (1985). Spatial gaps in arc volcanism: The effect of collision or subduction of oceanic plateaus. *Tectonophysics*, 119(1), 195-221.

McKee, J. W., Jones, N. W., & Anderson, T. H. (1988). Las Delicias. Previous Hit basin Next Hit, 37-40.

McKee, J. W., Jones, N. W., & Anderson, T. H. (1988). Las Delicias basin: A record of late Paleozoic arc volcanism in northeastern Mexico. *Geology*, 16(1), 37-40.

McKee, J. W., Jones, N. W., & Long, L. E. (1984). History of recurrent activity along a major fault in northeastern Mexico. *Geology*, 12(2), 103-107.

McKnight, J. F. (1970). *Geologic Map of Bofecillos Mountains Area, Trans-Pecos, Texas*. Bureau of Economic Geology, University of Texas.

Miggins, D., Ren, M., Anthony, E. (2011). Volcanic Geology of Several Prominent outcrops in the Western Part of Big Bend National Park: U.S. Geological Survey Circular 1327, 29 p.

Miggins, D., Anthony, E., Ren, M., and Wache, K., (2007), New  $^{40}\text{Ar}/^{39}\text{Ar}$  ages, geochemistry, and stratigraphy for mafic and rhyolitic volcanic units from Big Bend National Park, Texas [abs.]: *Geological Society of America Abstracts with Programs*, v. 39, no, 6, p. 635.

Miggins, D.P., Ren, M., Anthony, E., Iriondo, A., and Wooden, J.L., 2006, New constraints on the timing of volcanism and associated intrusive rocks in Big Bend National Park using  $^{40}\text{Ar}/^{39}\text{Ar}$  and U-Pb geochronology [abs.]: *Geological Society of America Abstracts with Programs*, v. 38, no. 7, p. 156.

Miggins, D., Scott, R.B., Snee, L.W., 2004, New  $^{40}\text{Ar}/^{39}\text{Ar}$  ages from Big Bend National Park [abs.]: *Geological Society of America Abstracts with Programs*, v. 36, no. 5, p. 128.

Molnar, P., & Gray, D. (1979). Subduction of continental lithosphere: Some constraints and uncertainties. *Geology*, 7(1), 58-62.

Muehlberger, W. R., & Dickerson, P. W. (1989). A tectonic history of Trans-Pecos Texas. *Field Trip Guidebooks*, 317, 35-54.

---

Muehlberger, W. R. (1980). Texas lineament revisited. In New Mexico Geological Society Guidebook, 31st Field Conference, Trans-Pecos Texas: Socorro, New Mexico Geological Society (pp. 113-121).

Neprochnov, Y. P. (1989). Study of the lower crust and upper mantle using ocean bottom seismographs. Geophysical Monograph Series, 51, 159-168.

Nettles, M., & Dziewoński, A. M. (2008). Radially anisotropic shear velocity structure of the upper mantle globally and beneath North America. *Journal of Geophysical Research: Solid Earth* (1978–2012), 113(B2).

Nur, A., & Ben-Avraham, Z. (1983). Break-up and accretion tectonics. *Accretion tectonics in the circum-Pacific Regions*, 3-18.

Ogley, D.S., 1978, Eruptive history of the Pine Canyon Caldera, Big Bend National Park, Texas: Austin, Tex., University of Texas, M.S. thesis, 68 p.

Paces, J. B., & Miller, J. D. (1993). Precise U-Pb ages of Duluth Complex and related mafic intrusions, northeastern Minnesota: Geochronological insights to physical, petrogenetic, paleomagnetic, and tectonomagmatic processes associated with the 1.1 Ga Midcontinent Rift System. *Journal of Geophysical Research: Solid Earth* (1978–2012), 98(B8), 13997-14013.

PAGE, W. R. (2007, October). Late Ordovician Conodonts from the Maravillas Formation near Persimmon Gap, Big Bend National Park, Texas. In 2007 GSA Denver Annual Meeting.

Page, W.R., and Harris, A.G., 2007, Late Ordovician conodonts from the Maravillas Formation near Persimmon Gap, Big Bend National Park, Texas [abs.]: *Geological Society of America Abstracts with Programs*, v. 39, no. 6, p. 635.

Parker, D. F. (2002). *Volcanology and Petrology of Burro Mesa Rhyolite, Southwestern Big Bend Park, Texas.*

Parker, D. F. (1986). Stratigraphic, structural, and petrologic development of the Buckhorn caldera, northern Davis Mountains, Trans-Pecos Texas. *Igneous geology of Trans-Pecos Texas. Univ Texas Austin Bur Econ Geol Guideb*, 23, 286-302.

Parker, D. F., & McDOWELL, F. W. (1979). K-Ar geochronology of Oligocene volcanic rocks, Davis and Barrilla Mountains, Texas. *Geological Society of America Bulletin*, 90(12), 1100-1110.

---

Peacock, M. A. (1931). Classification of igneous rock series. *The Journal of Geology*, 54-67.

Perry, F.V., De Paolo, D.J., and Baldrige, W.S., 1993, Neodymium isotopic evidence for decreasing crustal contributions to Cenozoic ignimbrites of the Western United States: Implications for the thermal evolution of the Cordilleran crust: *Geological Society of America Bulletin*, v. 105, p. 872–882.

Poole, F. G., Perry, W. J., Madrid, R. J., & Amaya-Martínez, R. (2005). Tectonic synthesis of the Ouachita-Marathon-Sonora orogenic margin of southern Laurentia: Stratigraphic and structural implications for timing of deformational events and plate-tectonic model. *Geological Society of America Special Papers*, 393, 543-596.

Price, J. G., & Henry, C. D. (1984). Stress orientations during Oligocene volcanism in Trans-Pecos Texas: Timing the transition from Laramide compression to Basin and Range tension. *Geology*, 12(4), 238-241.

Rainbird, R. H., Hearnan, L. M., & Young, G. (1992). Sampling Laurentia: Detrital zircon geochronology offers evidence for an extensive Neoproterozoic river system originating from the Grenville orogen. *Geology*, 20(4), 351-354.

Ramsey, J. W. (1961). Perdiz conglomerate, Presidio County, Texas: University of Texas, Austin (Doctoral dissertation, MA thesis, 88 p).

Rapp, S. D. (1983). Sedimentology and magnetic polarity stratigraphy of the Black Peaks Formation, Big Bend National Park, Brewster County, Texas: Unpub. Master's thesis, Louisiana State University, Baton Rouge.

Rapp, S. D., MacFadden, B. J., & Schiebout, J. A. (1983). Magnetic polarity stratigraphy of the early Tertiary Black Peaks Formation, Big Bend National Park, Texas. *The Journal of Geology*, 555-572.

Rigby, J. K. (1958). Mass movements in Permian rocks of Trans-Pecos Texas. *Journal of Sedimentary Research*, 28(3).

Rigsby, C. A. (1986). The Big Yellow Sandstone: a sandy braided stream. *Geology of the Big Bend Area and Solitario Dome, Texas, West Texas Geol. Soc. Fieldtrip Guidebook*, Publ, 86-82.

Rigsby, C. A. (1982). Provenance and depositional environments of the Middle Eocene Canoe Formation. Big Bend National Park, Brewster County, Texas [MS Thesis]: Louisiana State University and Agricultural and Mechanical College, 111p.

---

Rix, C. C. (1953). Geology of Chinati Peak Quadrangle, Trans-Pecos Texas (Doctoral dissertation, University of Texas.).

Rix, C. C. (1952). Chinati Peak Quadrangle. Presidio County, Texas: University of Texas, Austin, Bureau of Economic Geology, open-file map, scale, 1(48,000).

Roths, P. J. (1993, March). Geochemical and geochronological studies of the Grenville-age (1250–1000 Ma) Allamoore and Hazel Formations, Hudspeth and Culberson counties, west Texas. In Precambrian Geology of Franklin Mountains and Van Horn Area, Trans-Pecos, Texas: Geological Society of America, South-Central Meeting Guidebook, University of Texas at Dallas (pp. 1-35).

Rubin, C. M., Saleeby, J. B., Cowan, D. S., Brandon, M. T., & McGroder, M. F. (1990). Regionally extensive mid-Cretaceous west-vergent thrust system in the northwestern Cordillera: Implications for continent-margin tectonism. *Geology*, 18(3), 276-280.

Rudnik, G. B., and E. N. Melankholina, Rock composition of the Oceanic crust in the North-West Pacific (according to the data on drilling, dredging and study of deep-seated xenoliths), in *Structure of the North-West Pacific Ocean Floor (Geophysics, Magmatism, Tectonics)*, edited by Yu. M. Pushcharovsky and Yu. P. Neprochnov, pp. 127-157, Nauka, Moscow, 1984 (in Russian)

Rudnik, G. B., Melankholina, E. N., & Kudryavtsev, V. I. (1981). Rocks of the Second Oceanic Layer in the Sections of the Shatsky and Hess Rises (Pacific Ocean). *Izv. Akad. Nauk SSSR, Ser. Geol.*, (11), 21-33.

Schiebout, J. A., Rigsby, C. A., Rapp, S. D., Hartnell, J. A., & Standhardt, B. R. (1987). Stratigraphy of the Cretaceous-Tertiary and Paleocene-Eocene transition rocks of Big Bend National Park, Texas. *The Journal of Geology*, 359-375.

Schiebout, J. A. (1974). Vertebrate paleontology and paleoecology of Paleocene Black Peaks Formation, Big Bend National Park, Texas. Texas Memorial Museum.

Schiebout, J. A. (1970). Sedimentology of Paleocene Black Peaks Formation, western Tornillo Flat, Big Bend National Park, Texas: Unpub. Master's thesis, Univ. of Texas, Austin.

Schmidt, C. J. (1996). Neogene inversion of Cretaceous rift basins and reversion of Carboniferous uplifts in the Pampean Ranges, Argentina, with implications for reactivation in the Laramide Rocky Mountains (abs.): Geological Society of America Annual Meeting Abstracts with Programs, v. 28, no. 7, p. A-112.

---

Shaulis, B., Lapen, T. J., & Toms, A. (2010). Signal linearity of an extended range pulse counting detector: Applications to accurate and precise U-Pb dating of zircon by laser ablation quadrupole ICP-MS. *Geochemistry, Geophysics, Geosystems*, 11(11).

Sigloch, K., McQuarrie, N., & Nolet, G. (2008). Two-stage subduction history under North America inferred from multiple-frequency tomography. *Nature Geoscience*, 1(7), 458-462.

Skinner, J. W. (1940). Upper Paleozoic section of Chinati Mountains, Presidio County, Texas. *AAPG Bulletin*, 24(1), 180-188.

Sláma, J., Košler, J., Condon, D. J., Crowley, J. L., Gerdes, A., Hanchar, J. M., ... & Whitehouse, M. J. (2008). Plešovice zircon—a new natural reference material for U–Pb and Hf isotopic microanalysis. *Chemical Geology*, 249(1), 1-35.

Snyder, W. S., Dickinson, W. R., & Silberman, M. L. (1976). Tectonic implications of space-time patterns of Cenozoic magmatism in the western United States. *Earth and Planetary Science Letters*, 32(1), 91-106.

Silver, E. A., & Smith, R. B. (1983). Comparison of terrane accretion in modern Southeast Asia and the Mesozoic North American Cordillera. *Geology*, 11(4), 198-202.

Smith, D. E., & Julian, F. E. (1991). Stratigraphy of the Yucca Formation, Indio Mountains, west Texas. *Geomorphology*, 4.

Schmidt, M. W., & Poli, S. (1998). Experimentally based water budgets for dehydrating slabs and consequences for arc magma generation. *Earth and Planetary Science Letters*, 163(1), 361-379.

Smith, M. C. (1975). The Los Alamos scientific laboratory dry hot rock geothermal project (LASL Group Q-22). *Geothermics*, 4(1), 27-39.

Spencer, J. E. (1996). Uplift of the Colorado Plateau due to lithosphere attenuation during Laramide low-angle subduction. *Journal of Geophysical Research: Solid Earth* (1978–2012), 101(B6), 13595-13609.

Stern, R. J., & Dickinson, W. R. (2010). The Gulf of Mexico is a Jurassic backarc basin. *Geosphere*, 6(6), 739-754.

Stock, J., & Molnar, P. (1988). Uncertainties and implications of the Late Cretaceous and Tertiary position of North America relative to the Farallon, Kula, and Pacific plates. *Tectonics*, 7(6), 1339-1384.

---

Taylor, F. W., Bevis, M. G., Schutz, B. E., Kuang, D., Recy, J., Calmant, S., ... & Reichenfeld, C. (1995). Geodetic measurements of convergence at the New Hebrides island arc indicate arc fragmentation caused by an impinging aseismic ridge. *Geology*, 23(11), 1011-1014.

Teal, L. W. (1979). Geology and petrology of the Chispa Mountain quadrangle and vicinity, Culberson and Jeff Davis counties, Texas.

Tera, F. O. U. A. D., & Wasserburg, G. J. (1974). U-Th-Pb systematics on lunar rocks and inferences about lunar evolution and the age of the moon. In *Lunar and Planetary Science Conference Proceedings* (Vol. 5, pp. 1571-1599).

Tera, F. and Wasserburg, G. J. (1973). A response to a comment on U/Pb systematics in lunar basalts. *Earth Planet. Sci. Lett.* 19, 213-217.

Testarmata, M. M., & Gose, W. A. (1980). Magnetostratigraphy in the Trans-Pecos volcanic field: Preliminary results from the Eocene-Oligocene Vieja Group. *New Mexico Geol. Soc. Guidebook*, 31, 101-103.

Turner, K. J., James, R. B., & Daniel, P. M. (2008, October). A Reinterpretation of Some Correlations of Chisos Group Mafic Lavas with New Geochemistry and Geochronology, Big Bend National Park, Texas. In 2008 Joint Meeting of The Geological Society of America, Soil Science Society of America, American Society of Agronomy, Crop Science Society of America, Gulf Coast Association of Geological Societies with the Gulf Coast Section of SEPM.

Turner, K.J., Budahn, J.R., and Miggins, D.P., in press, A reinterpretation of some correlations of Chisos Group mafic lavas with new geochemistry and geochronology, Big Bend National Park, Texas [abs.]: Geological Society of America Abstracts with Programs.

Twiss, P.C., (1959a), Geologic Map of the Van Horn Mountains, Texas: Texas Univ. Bur. Econ. Geology Quad. Map 23.

Twiss, Page C, (1959b), Geology of the Van Horn Mountains, Trans-Pecos Texas: Unpub. Ph.D. dissert., Univ. Texas.

Underwood Jr, J. R. (1980). Geology of the Eagle Mountains, Hudspeth County, Texas. In *Trans-Pecos region: New Mexico Geological Society, 31st Field Conference Guidebook* (pp. 183-193).

Underwood Jr, J. R. (1962). Geology of Eagle Mountains and vicinity, Trans-Pecos Texas: University of Texas at Austin (Doctoral dissertation, Ph. D. dissertation 559 p.

---

Unruh, J. R., Dumitru, T. A., & Sawyer, T. L. (2007). Coupling of early Tertiary extension in the Great Valley forearc basin with blueschist exhumation in the underlying Franciscan accretionary wedge at Mount Diablo, California. *Geological Society of America Bulletin*, 119(11-12), 1347-1367.

Urbanczyk, K. M., & White, J. C. (2000). Pine Canyon caldera. Big Bend National Park, Texas: A new interpretation: *Geological Society of America Abstracts with Programs*, 32(3), 43.

Vallier, T. L., Windom, K. E., Seifert, K. E., & Thiede, J. (1980). Volcanic rocks cored on Hess Rise, western Pacific ocean. *Nature*, 286(5768), 48-50.

Van Schmus, W. R., Bickford, M. E., & Turek, A. (1996). Proterozoic geology of the east-central Midcontinent basement. *SPECIAL PAPERS-GEOLOGICAL SOCIETY OF AMERICA*, 7-32.

Verrillo, D. E. (1979). Geology and petrography of the tertiary volcanic rocks in the southwest Eagle Mountains, Hudspeth County, Texas.

Vogt, P.R., Lowrie, A., Bracey, D. and Hey, R., 1976. Subduction of aseismic oceanic ridges: effects on shape, seismicity, and other characteristics of consuming plate boundaries. *Geol. Soc. Am., Spec. Pap.*, 172: 59 pp.

Walton, A. W. (1979). Volcanic sediment apron in the Tascotal Formation (Oligocene?), Trans-Pecos Texas. *Journal of Sedimentary Research*, 49(1).

Wells, M. L., & Hoisch, T. D. (2008). The role of mantle delamination in widespread Late Cretaceous extension and magmatism in the Cordilleran orogen, western United States. *Geological Society of America Bulletin*, 120(5-6), 515-530.

Wendt, I. (1984). A three-dimensional U/Pb discordia plane to evaluate samples with common lead of unknown isotopic composition. *Isot. Geosci.* 2, 1)12.

White, J.C., Benker, C.S., Ren, M., Urbanczyk, K.M., and Corrick, D.W., (2006). Petrogenesis and tectonic setting of the peralkaline Pine Canyon caldera, Trans-Pecos Texas, USA: *Lithos*, v. 91, p. 74–94.

White, J.C. (ed.), Barker, D.S., Duex, T.W., Erdlac, R.J., Kinsland, G.L., Lehman, T.M., Rolfe, M.D., Parker, D.F., Urbanczyk, K.M., (2002). *The Geology of Big Bend National Park: What Have We Learned Since Maxwell and others (1967)?* Geological Society of America, South-Central Section Meeting, Field Trip Guidebook, Sul Ross State University, Alpine, Texas.

---

Wilson, J. A. (1984). Vertebrate faunas 49 to 36 million years ago and additions to the species of *Leptoreodon* (Mammalia: Artiodactyla) found in Texas. *Journal of Vertebrate Paleontology*, 4(2), 199-207.

Wilson and Schiebout, 1984

Wilson, J. A., Twiss, P. C., DeFord, R. K., & Clabaugh, S. E. (1968). Stratigraphic succession, potassium-argon dates, and vertebrate faunas, Vieja Group, Rim Rock country, Trans-Pecos, Texas. *American Journal of Science*, 266(7), 590-604.

Zamzow, C. E. (1983). Tertiary Volcanics of the Eastern Eagle Mountains, Hudspeth County, Texas [Ph.D Dissertation].

# Appendix I

**Table 1: Black Peaks Formation**

Spot	Conc. (ppm)	Ratios				Ages				% Disc.						
		U/Th	<sup>206</sup> Pb/ <sup>238</sup> U ±2σ	<sup>207</sup> Pb/ <sup>235</sup> U ±2σ	<sup>207</sup> Pb/ <sup>206</sup> Pb ±2σ	<sup>206</sup> Pb/ <sup>238</sup> U ±2σ	<sup>207</sup> Pb/ <sup>235</sup> U ±2σ	<sup>207</sup> Pb/ <sup>206</sup> Pb ±2σ								
BB16.1	3143	835	3.76	0.01009	1.98	0.067300	3.71	0.04760	3.57	77.9	1.8	76.92	3.1	45	±88	-42.0
BB16.5	3181	1660	1.92	0.28070	2.32	4.173000	2.20	0.10760	1.12	1880.2	44.0	1811.35	20.5	1733	±26	-7.8
BB16.8	780	715	1.09	0.21820	1.56	2.819000	1.67	0.09310	1.50	1507.2	25.5	1489.00	18.3	1463	±33	-2.9
BB16.9	1173	1189	0.99	0.17060	3.22	2.084000	3.41	0.08910	1.35	1207.2	37.4	1270.49	27.4	1379	±31	14.3
BB16.12	7488	1244	6.02	0.08920	1.91	0.753000	1.73	0.06191	1.15	659.3	14.4	655.19	10.2	641	±32	-2.8
BB16.13	9278	2912	3.19	0.03146	1.78	0.222400	1.98	0.05083	1.34	240.3	5.2	236.67	4.9	201	±38	-16.4
BB16.16	2185	1771	1.23	0.20410	1.37	2.515000	1.55	0.08960	1.12	1419.3	19.6	1407.88	24.0	1391	±32	-2.0
BB16.17	1796	992	1.81	0.01193	1.76	0.080400	4.23	0.04770	4.19	92.1	1.8	90.65	4.6	52	±104	-43.9
BB16.19	1221	562	2.17	0.28760	1.74	4.713000	1.68	0.11880	1.18	1920.1	32.3	1917.00	31.5	1914	±31	-0.3
BB16.22	2493	1141	2.19	0.25960	1.66	3.853000	1.48	0.10770	1.02	1754.7	29.7	1746.18	23.8	1736	±23	-1.1
BB16.24	2931	1410	2.08	0.01064	1.97	0.068200	4.11	0.04740	3.80	82.1	1.8	80.63	3.7	37	±93	-54.7
BB16.26	3136	1177	2.66	0.01923	1.77	0.130200	2.84	0.04950	2.63	147.5	3.1	147.08	5.1	140	±64	-4.9
BB16.29	1082	433	2.50	0.01195	2.18	0.080500	5.96	0.04880	6.15	92.0	2.3	92.55	5.6	107	±146	16.1
BB16.30	1922	754	2.55	0.15510	2.19	1.596000	2.38	0.07530	1.59	1102.5	26.1	1084.88	21.7	1050	±35	-4.8
BB16.31	764	654	1.17	0.00823	3.16	0.055300	9.58	0.04790	9.39	63.4	2.3	63.40	5.9	63	±226	-0.7
BB16.32	5401	1998	2.70	0.21950	2.32	2.749000	2.22	0.09050	1.10	1508.3	42.5	1468.29	20.2	1411	±31	-6.5
BB16.33	494	376	1.31	0.20950	1.67	2.663000	1.84	0.09240	1.62	1446.5	35.2	1448.14	17.6	1451	±38	0.3
BB16.38	2298	889	2.58	0.00987	2.13	0.062700	4.31	0.04560	3.95	75.8	1.9	71.92	3.5	55	±100	-172.6
BB16.39	3728	1148	3.25	0.01162	1.89	0.075400	3.05	0.04760	2.73	89.1	2.0	87.68	3.4	49	±71	-45.5
BB16.44	13254	2500	5.30	0.23980	1.63	3.573000	1.43	0.10890	1.10	1623.3	33.8	1682.84	23.3	1758	±30	8.3
BB16.45	195	73	2.66	0.16120	1.80	1.731000	2.89	0.07810	3.07	1134.6	25.8	1131.05	25.8	1124	±66	-0.9
BB16.52	1367	452	3.02	0.01049	2.29	0.070500	4.96	0.04860	4.94	79.9	2.0	80.53	3.9	100	±117	24.6
BB16.54	1534	476	3.23	0.27160	1.51	4.182000	1.41	0.11100	1.17	1803.0	28.6	1798.63	14.7	1794	±23	-0.5
BB16.55	2833	1894	1.50	0.02337	1.75	0.160700	2.43	0.05070	2.76	176.5	3.5	178.10	4.3	199	±65	12.6
BB16.56	1751	411	4.26	0.02438	1.68	0.170800	3.10	0.05050	2.97	183.8	3.7	184.28	5.5	190	±70	3.3
BB16.58	4059	1939	2.09	0.02273	2.07	0.158600	2.71	0.05080	2.36	171.5	3.8	173.69	4.6	204	±55	18.9
BB16.61	8698	583	14.91	0.26920	3.31	3.800000	3.68	0.10300	1.36	1784.1	53.1	1726.28	32.6	1657	±27	-7.1
BB16.62	2644	1144	2.31	0.02296	1.74	0.159800	2.38	0.05050	2.57	172.9	3.4	174.15	4.6	191	±61	10.2
BB16.63	1960	1429	1.37	0.02006	1.89	0.136700	3.07	0.04900	2.65	151.3	3.2	149.47	4.9	120	±64	-20.7
BB16.67	1817	794	2.29	0.18170	1.71	2.109000	1.52	0.08410	1.31	1255.3	20.3	1261.50	15.3	1272	±33	1.3
BB16.68	13138	5499	2.39	0.02461	2.80	0.167800	2.74	0.04980	1.51	185.0	5.2	183.10	5.2	158	±43	-14.3
BB16.69	2094	665	3.15	0.02791	2.04	0.194500	2.88	0.05040	2.58	209.4	4.3	207.55	6.1	186	±65	-10.9
BB16.72	654	586	1.12	0.20830	1.73	2.655000	1.69	0.09340	1.39	1419.9	24.7	1441.79	18.3	1474	±32	3.8
BB16.73	1445	789	1.83	0.25930	1.97	3.624000	1.88	0.10120	1.09	1724.6	32.6	1680.09	20.6	1625	±27	-5.8
BB16.75	1975	996	1.98	0.05890	1.87	0.455800	2.13	0.05630	1.78	434.2	8.7	434.95	9.6	439	±45	1.1
BB16.76	815	235	3.48	0.25970	1.66	3.714000	1.75	0.10400	1.25	1727.6	28.8	1704.36	18.0	1676	±33	-3.0
BB16.80	1645	548	3.00	0.20670	1.55	2.581000	1.43	0.09070	1.10	1412.0	22.9	1414.79	12.9	1419	±32	0.5
BB16.81	845	391	2.16	0.26100	1.65	3.774000	1.85	0.10510	1.43	1738.1	29.4	1718.98	17.5	1696	±34	-2.4
BB16.82	969	433	2.24	0.16420	1.58	1.765000	1.87	0.07820	1.41	1147.0	21.5	1141.13	15.4	1130	±36	-1.5
BB16.86	419	712	0.59	0.28390	1.48	4.512000	1.57	0.11680	1.46	1874.9	29.5	1881.27	15.4	1888	±33	0.7
BB16.87	1175	1081	1.09	0.03318	1.78	0.242700	2.88	0.05330	3.00	249.5	5.1	256.11	6.9	317	±73	27.1

Table: Black Peaks Formation

Spot	[U]		[Th]		Ratios										% Disc.	
	Conc. (ppm)				U/Th	206Pb/238U	±2σ	207Pb/235U	±2σ	207Pb/206Pb	±2σ	206Pb/238U	±2σ	207Pb/235U		±2σ
BB16.89	1826	881	2.07	0.01132	2.30	0.074300	4.85	0.04800	4.79	86.5	2.2	86.06	4.1	74	±117	-14.5
BB16.91	2772	894	3.10	0.01257	2.15	0.080400	3.61	0.04630	3.46	96.2	2.2	92.15	3.3	-12	±85	-112.6
BB16.93	5451	2212	2.46	0.02168	2.12	0.147000	2.86	0.04940	2.23	165.2	3.9	163.75	4.5	142	±54	-13.9
BB16.94	6345	1283	4.94	0.21600	2.18	2.890000	2.53	0.09650	1.24	1483.8	32.0	1506.19	20.7	1538	±26	3.6
BB16.96	4970	1764	2.82	0.01289	1.94	0.085600	2.80	0.04880	2.46	99.1	2.4	99.72	2.7	114	±59	14.8
BB16.97	1749	548	3.19	0.03406	1.73	0.246100	2.84	0.05240	2.86	258.9	5.3	260.90	6.6	279	±66	7.9
BB16.98	680	456	1.49	0.24060	1.58	3.517000	1.68	0.10510	1.24	1639.6	28.3	1664.96	13.9	1697	±24	3.5

**Table 2: Hannold Hill Formation**

Spot	Conc. (ppm)				Ratios				Ages				% Disc.			
	[U]	[Th]	U/Th	206Pb/238U	±2σ	207Pb/235U	±2σ	207Pb/206Pb	±2σ	206Pb/238U	±2σ	207Pb/235U		±2σ	207Pb/206Pb	±2σ
BB15C.1	3832	956	4.01	0.300361	4.736	5.709829	6.475	0.137873	3.264	1693.1	70.5	1932.86	56.0	2201	±57	30.0
BB15C.2	568	437	1.30	0.247299	2.595	3.010589	3.521	0.088293	3.093	1424.5	33.2	1410.30	26.8	1389	±59	-2.5
BB15C.3	2909	1075	2.71	0.290891	2.508	3.898179	3.427	0.097192	2.716	1646.0	36.4	1613.31	27.7	1571	±51	-4.6
BB15C.4	1229	65	18.85	0.155580	2.775	1.463270	3.648	0.068213	2.906	932.2	24.1	915.36	22.0	875	±60	-6.1
BB15C.5	4753	1031	4.61	0.121823	5.894	1.108646	7.452	0.066003	3.377	741.0	41.3	757.52	39.8	806	±71	8.8
BB15C.6	4420	1714	2.58	0.041110	3.192	0.293447	3.872	0.051770	3.514	259.7	8.1	261.27	8.9	275	±80	6.0
BB15C.7	2304	698	3.30	0.015113	3.381	0.095275	4.956	0.045721	5.175	96.7	3.2	92.41	4.4	-17	±125	-117.7
BB15C.8	2266	1308	1.73	0.034818	2.999	0.243670	3.263	0.050757	3.936	220.6	6.5	221.42	6.5	230	±91	4.2
BB15C.9	1677	800	2.10	0.266003	2.874	3.337900	2.631	0.091009	3.122	1520.5	38.9	1489.96	20.6	1447	±59	-4.8
BB15C.10	4075	1281	3.18	0.012984	3.784	0.085164	4.478	0.047571	4.695	83.2	3.1	82.99	3.6	78	±112	-6.2
BB15C.13	8085	5479	1.48	0.011490	2.091	0.071993	3.110	0.045442	2.962	73.6	1.5	70.59	2.1	-32	±72	-143.3
BB15C.14	2566	1083	2.37	0.013974	2.166	0.092685	4.209	0.048103	4.201	89.5	1.9	90.00	3.6	104	±99	16.7
BB15C.15	2692	1262	2.13	0.012243	2.260	0.079862	4.093	0.047308	4.268	78.4	1.8	78.02	3.1	65	±102	-17.4
BB15C.17	2846	677	4.20	0.014946	2.725	0.096017	4.463	0.046593	3.734	95.6	2.6	93.09	4.0	28	±90	-70.3
BB15C.18	3156	1433	2.20	0.026085	2.383	0.175023	3.585	0.048663	3.005	166.0	3.9	163.77	5.4	132	±71	-20.7
BB15C.19	8466	3262	2.60	0.015498	7.829	0.103557	8.989	0.048463	2.447	98.1	7.7	100.05	8.0	122	±58	23.0
BB15C.21	4920	1881	2.62	0.016486	2.965	0.106112	4.459	0.046681	3.240	105.4	3.1	102.40	4.3	33	±78	-68.7
BB15C.22	2654	1285	2.06	0.023002	1.931	0.155585	4.196	0.049051	3.584	146.6	2.8	146.81	5.7	150	±84	2.5
BB15C.23	1476	1019	1.45	0.015085	2.444	0.096689	6.485	0.046486	6.050	96.5	2.3	93.72	5.8	23	±145	-76.3
BB15C.24	7737	1417	5.46	0.245213	1.797	3.573966	3.324	0.105708	2.334	1413.7	22.8	1543.77	26.4	1727	±43	22.1
BB15C.25	3264	2060	1.58	0.031816	2.551	0.214763	4.405	0.048957	3.097	201.9	5.1	197.54	7.9	146	±73	-27.8
BB15C.26	2452	858	2.86	0.045467	2.601	0.323109	11.263	0.051541	9.875	286.6	7.3	284.29	27.9	265	±227	-7.5
BB15C.30	2439	675	3.61	0.009446	2.362	0.059184	11.658	0.045444	11.333	60.6	1.4	58.38	6.6	-32	±275	-152.5
BB15C.31	446	367	1.22	0.254895	2.006	3.408768	10.891	0.096992	10.253	1463.7	26.3	1506.42	85.7	1567	±192	7.1
BB15C.33	2364	1877	1.26	0.059702	2.263	0.446988	10.969	0.054300	10.252	373.8	8.2	375.17	34.4	384	±230	2.6
BB15C.35	3081	2250	1.37	0.083263	3.073	0.621354	11.107	0.054124	10.181	515.6	15.2	490.70	43.2	376	±229	-27.0
BB15C.36	5914	2687	2.20	0.012658	3.154	0.080221	4.481	0.045966	3.267	81.1	2.5	78.35	3.4	-4	±79	-105.2
BB15C.37	2185	681	3.21	0.012179	2.267	0.076709	5.276	0.045681	4.584	78.0	1.8	75.05	3.8	-19	±111	-124.6
BB15C.38	1610	615	2.62	0.075879	2.254	0.571380	2.621	0.054614	2.236	471.5	10.2	458.91	9.7	396	±50	-15.9
BB15C.39	963	277	3.47	0.013975	3.344	0.090739	6.821	0.047093	7.176	89.5	3.0	88.19	5.8	54	±171	-39.7
BB15C.40	2187	473	4.62	0.236750	2.227	2.594610	2.449	0.079484	1.278	1389.8	27.5	1299.12	18.0	1184	±25	-13.5
BB15C.41	1672	781	2.14	0.309114	1.986	4.351382	2.008	0.102096	1.269	1736.3	30.2	1703.16	16.6	1663	±23	-4.2
BB15C.43	886	497	1.78	0.176804	2.359	1.713786	2.623	0.070301	1.875	1049.5	22.8	1013.70	16.8	937	±38	-10.7
BB15C.46	3297	1012	3.26	0.075627	2.825	0.587370	3.046	0.056330	2.112	470.0	12.8	469.19	11.4	465	±47	-1.0
BB15C.47	1745	301	5.80	0.078267	2.312	0.615580	2.469	0.057043	1.959	485.8	10.8	487.07	9.6	493	±43	1.5
BB15C.48	1151	480	2.40	0.079473	2.307	0.624049	3.156	0.057676	2.454	487.0	10.8	492.38	12.3	517	±54	6.3
BB15C.49	3413	1500	2.28	0.017620	2.715	0.116417	4.175	0.047918	3.675	112.6	3.0	111.82	4.4	95	±87	-15.4
BB15C.52	1238	458	2.70	0.025291	2.455	0.167986	4.867	0.048174	4.631	161.0	3.9	157.67	7.1	108	±109	-33.0
BB15C.54	3993	1283	3.11	0.040321	2.249	0.280893	2.830	0.050526	2.515	254.8	5.6	251.37	6.3	219	±58	-14.0
BB15C.55	414	308	1.34	0.204316	2.137	2.266051	3.092	0.080439	2.933	1198.5	23.4	1201.79	21.8	1208	±58	0.8
BB15C.57	1423	1137	1.25	0.244728	1.816	3.056568	2.080	0.090584	1.715	1411.2	23.0	1421.88	15.9	1438	±33	1.9

Table : Hannold Hill Formation

Spot	[U]		[Th]		Ratios					Ages					% Disc.	
	Conc. (ppm)		U/Th	206Pb/238U	±2σ	207Pb/235U	±2σ	207Pb/206Pb	±2σ	206Pb/238U	±2σ	207Pb/235U	±2σ	207Pb/206Pb		±2σ
BB15C.58	5335	1402	3.81	0.073337	2.246	0.570545	2.281	0.056424	1.847	456.2	9.9	458.37	8.4	469	±41	2.8
BB15C.62	1239	794	1.56	0.013684	2.716	0.090858	6.337	0.048157	6.226	87.6	2.4	88.30	5.4	107	±147	22.1
BB15C.63	2387	1356	1.76	0.009722	2.308	0.062423	4.636	0.046567	4.742	62.4	1.4	61.48	2.8	27	±114	-56.6

WTX-BB 15C

**Table 3: Canoe Formation**

Spot	Conc. (ppm)		Ratios					Ages					% Disc.			
	[U]	[Th]	U/Th	<sup>206</sup> Pb/ <sup>238</sup> U	<sup>207</sup> Pb/ <sup>235</sup> U	<sup>207</sup> Pb/ <sup>206</sup> Pb	<sup>206</sup> Pb/ <sup>238</sup> U	<sup>207</sup> Pb/ <sup>235</sup> U	<sup>207</sup> Pb/ <sup>206</sup> Pb	<sup>207</sup> Pb/ <sup>235</sup> U	<sup>207</sup> Pb/ <sup>206</sup> Pb	±2σ	±2σ			
Canoe.1	893	287	3.11	0.212733	2.350204	3.692	0.080125	2.017	1243.4	31.3	1227.62	26.3	1200	±40	-3.5	
Canoe.2	1574	1050	1.50	0.013228	0.081229	9.677	0.044535	9.630	84.7	2.5	79.30	7.4	-81	±236	-195.7	
Canoe.3	1645	846	1.95	0.160006	1.622835	3.579	0.073559	1.678	956.8	26.0	979.09	22.5	1029	±34	7.6	
Canoe.4	3877	2985	1.30	0.013307	2.772	5.350	0.048110	4.408	85.2	2.3	85.89	4.4	105	±104	22.8	
Canoe.5	936	533	1.76	0.014089	0.088272	15.176	0.041746	15.971	90.2	3.2	79.17	11.6	-242	±404	-368.1	
Canoe.6	1244	803	1.55	0.013067	0.075743	13.056	0.042039	13.292	83.7	2.4	74.13	9.3	-224	±335	-367.9	
Canoe.9	593	447	1.33	0.042193	0.306938	7.487	0.052760	7.084	266.4	7.0	271.80	17.9	319	±161	19.6	
Canoe.13	398	378	1.05	0.008796	0.043361	63.349	0.035754	83.351	56.5	3.4	43.10	26.7	-650	±2290	-1250.9	
Canoe.18	742	240	3.10	0.174765	1.738718	2.731	0.072156	2.584	1038.3	19.8	1022.99	17.6	990	±53	-4.6	
Canoe.19	865	248	3.49	0.200433	2.117289	2.412	0.076614	1.895	1177.6	20.3	1154.45	16.6	1111	±38	-5.6	
Canoe.20	2266	908	2.50	0.246929	3.057470	2.341	0.089803	1.406	1422.6	25.0	1422.10	17.9	1421	±27	-0.1	
Canoe.22	2285	931	2.45	0.012708	0.071766	8.749	0.040958	8.574	81.4	2.2	70.37	5.9	-290	±219	-456.5	
Canoe.25	929	1133	0.82	0.076624	0.618969	4.010	0.058587	3.800	475.9	12.6	489.20	15.6	552	±83	15.9	
Canoe.27	889	300	2.30	0.014085	0.073884	23.040	0.038045	23.115	90.2	3.5	72.38	16.1	-482	±613	-634.7	
Canoe.29	303	348	0.87	0.542301	14.271278	4.221	0.190863	5.567	2793.1	57.7	2767.91	40.1	2750	±91	-1.6	
Canoe.32	330	133	2.47	0.257821	3.467792	9.220	0.097551	6.123	1478.7	65.1	1519.92	72.8	1578	±115	6.7	
Canoe.33	1130	667	1.69	0.025806	3.154	0.165422	7.146	7.962	164.2	5.1	155.44	10.3	23	±191	-85.9	
Canoe.37	961	983	0.98	0.099828	0.823630	3.864	0.059838	3.842	613.4	14.4	610.07	17.7	598	±83	-2.6	
Canoe.39	866	637	1.04	0.312790	4.605630	2.665	0.106791	2.823	1754.4	34.6	1750.29	22.2	1745	±52	-0.5	
Canoe.40	850	577	1.47	0.342215	4.935193	3.470	0.104593	2.281	1897.3	51.6	1808.30	29.3	1707	±262	-240.2	
Canoe.41	5566	6166	0.92	0.026480	0.181387	3.266	0.049690	2.824	168.5	3.3	169.25	5.1	180	±66	6.9	
Canoe.44	1122	260	4.31	0.034508	0.186053	7.640	0.039104	7.376	218.7	4.4	173.26	12.2	-410	±193	-287.4	
Canoe.45	257	320	0.81	0.549686	2.163	15.404390	3.020	0.203249	2.021	2823.9	49.5	2840.58	28.8	2852	±33	1.0
Canoe.51	1484	463	3.23	0.012355	2.478	0.074946	11.193	0.043995	10.652	79.2	73.38	7.9	-111	±262	-240.2	
Canoe.54	512	309	1.66	0.194269	1.666	2.015780	4.430	0.075255	3.687	1144.5	1120.84	30.1	1075	±74	-6.0	
Canoe.58	861	671	1.28	0.318825	4.485170	3.281	0.102029	2.421	1784.0	40.0	1728.23	27.2	1661	±45	-6.9	
Canoe.59	747	646	1.16	0.011954	0.071476	17.970	0.043364	19.035	76.6	2.7	70.10	12.2	-147	±472	-291.5	
Canoe.60	1960	1467	1.34	0.058289	2.398	0.434885	3.733	0.054111	2.739	365.2	366.64	11.5	376	±62	2.9	
Canoe.61	2079	1492	1.39	0.012125	2.399	0.073047	9.006	0.043694	9.042	77.7	71.59	6.2	-128	±223	-264.6	
Canoe.62	674	294	2.30	0.017563	4.524	0.099120	16.790	0.040932	15.330	112.2	95.96	15.4	-292	±391	-360.0	
Canoe.63	2803	1489	1.88	0.007667	2.487	0.046451	8.999	0.043943	8.973	49.2	46.10	4.1	-114	±221	-331.3	
Canoe.65	785	596	1.32	0.014354	0.083629	15.958	0.042255	16.904	91.9	3.2	81.55	12.5	-211	±424	-330.0	
Canoe.69	1612	654	2.46	0.276431	3.747828	4.889	0.098331	4.662	1573.4	26.0	1581.65	39.2	1593	±87	1.2	
Canoe.71	2767	771	3.59	0.075732	2.767	0.572429	4.596	0.054820	3.624	470.6	459.58	17.0	405	±81	-14.0	
Canoe.74	4075	2350	1.73	0.014759	0.092631	6.088	0.045520	5.890	94.4	1.8	89.95	5.2	-28	±143	-129.4	
Canoe.75	896	441	2.03	0.012750	0.078630	16.200	0.044726	15.775	81.7	2.8	76.86	12.0	-71	±385	-186.4	
Canoe.78	1019	560	1.82	0.012846	4.242	0.059673	21.109	0.033691	22.040	82.3	58.85	12.1	-816	±627	-1091.6	
Canoe.79	480	203	2.37	0.189687	2.865	2.179208	6.792	0.083322	10.084	1119.7	1179.42	47.3	1277	±197	14.0	
Canoe.82	533	671	0.80	0.238583	2.849	4.754	0.081387	5.911	1379.3	35.4	1322.21	35.2	1231	±116	-8.8	
Canoe.87	502	227	1.33	0.234151	3.323	2.643819	4.101	0.081891	2.704	1356.2	1312.92	30.2	1243	±53	-8.4	
Canoe.88	866	625	1.39	0.012252	5.809	0.074744	38.881	0.044244	32.609	78.5	73.19	27.5	-97	±801	-223.7	

Table : Canoe Formation

Spot	Ratios			Ages					% Disc.							
	[U]	[Th]	U/Th	206Pb/238U	±2σ	207Pb/235U	±2σ	207Pb/206Pb		±2σ						
Canoe.90	611	352	1.74	0.284456	5.042	4.005858	6.184	0.102136	2.546	1613.8	72.0	1635.38	50.3	1663	±47	3.1
Canoe.91	1466	1017	1.44	0.012329	3.571	0.071111	12.707	0.041831	12.614	79.0	2.8	69.75	8.6	-237	±318	-399.6
Canoe.92	982	802	1.22	0.011237	4.622	0.066859	18.942	0.043154	19.075	72.0	3.3	65.71	12.1	-159	±474	-320.4
Canoe.93	1817	617	2.95	0.007467	3.986	0.048259	13.061	0.046872	15.122	48.0	1.9	47.86	6.1	43	±362	-11.0
Canoe.98	248	125	1.99	0.024785	4.011	0.114203	36.694	0.033419	34.369	157.8	6.3	109.80	38.2	-839	±983	-631.6
Canoe.100	1740	644	2.70	0.013822	3.919	0.084151	11.440	0.044156	8.755	88.5	3.4	82.04	9.0	-102	±215	-215.3
Canoe.102	1571	954	1.65	0.026072	2.386	0.172088	5.456	0.047870	5.159	165.9	3.9	161.23	8.1	93	±122	-44.0
Canoe.103	1243	1062	1.17	0.007346	4.319	0.039500	32.910	0.038999	31.709	47.2	2.0	39.34	12.7	-417	±830	-983.5

**Table 4: Lower Rhyolite**

Table : Lower Rhyolite

Spot	Ratios				Ages				% Disc.							
	[U]	[Th]	U/Th	Conc. (ppm)	206Pb/238U	±2σ	207Pb/235U	±2σ		207Pb/206Pb	±2σ					
Tlr.1	392	293	1.34	0.005621	5.066	0.032759	36.681	0.042268	42.889	36.1	1.8	32.73	11.8	-211	±1077	-682.7
Tlr.2	427	332	1.29	0.005635	5.384	0.038265	26.724	0.049248	30.656	36.2	1.9	38.13	10.0	160	±717	340.8
Tlr.3	1179	533	2.21	0.005638	3.399	0.036204	14.837	0.046577	15.361	36.2	1.2	36.11	5.3	28	±368	-23.9
Tlr.4	954	394	2.43	0.005640	3.592	0.037423	21.855	0.048125	18.390	36.3	1.3	37.31	8.0	105	±435	190.8
Tlr.5	1566	838	1.87	0.005360	2.755	0.031967	11.484	0.043258	10.517	34.5	0.9	31.95	3.6	-153	±261	-543.2
Tlr.6	204	73	2.79	0.021940	34.430	0.850884	43.925	0.281278	22.033	139.9	47.7	625.13	207.9	3370	±344	2308.8
Tlr.7	472	186	2.53	0.005417	4.109	0.037202	29.080	0.049813	28.037	34.8	1.4	37.09	10.6	186	±653	435.0
Tlr.8	239	151	1.58	0.005384	7.340	0.023636	58.072	0.031841	93.760	34.6	2.5	23.72	13.6	-980	±2767	-2930.2
Tlr.9	191	123	1.56	0.005232	7.105	0.045893	175.002	0.063614	98.447	33.6	2.4	45.56	78.1	729	±2087	2066.4
Tlr.10	256	171	1.50	0.005246	6.425	0.020110	54.846	0.027801	114.294	33.7	2.2	20.22	11.0			
Tlr.11	854	414	2.06	0.005917	3.427	0.037772	16.047	0.046301	16.296	38.0	1.3	37.65	5.9	13	±392	-65.0
Tlr.12	902	523	1.72	0.005623	3.159	0.032033	14.415	0.041315	15.848	36.1	1.1	32.02	4.5	-268	±402	-841.8
Tlr.13	96	40	2.41	0.005827	12.653	-0.118995	488.890	-0.148104	113.342	37.5	4.7	-128.64	805.6			
Tlr.15	622	311	2.00	0.005275	3.573	0.035125	24.521	0.048297	26.547	33.9	1.2	35.05	8.4	114	±626	235.6
Tlr.16	459	196	2.34	0.005579	3.764	0.058212	19.521	0.075673	19.503	35.9	1.3	57.45	10.9	1086	±391	2929.2
Tlr.17	88	52	1.69	0.005617	17.579	0.190128	81.039	0.245484	180.002	36.1	6.3	176.74	132.2	3156	±2856	8639.7
Tlr.18	118	74	1.59	0.005370	10.010	0.029060	437.501	0.039248	350.001	34.5	3.4	29.09	126.1	-400	±9129	-1259.2
Tlr.19	153	99	1.54	0.005657	8.273	0.009943	625.001	0.012746	546.155	36.4	3.0	10.05	62.6			
Tlr.20	306	220	1.39	0.005684	5.558	0.039926	32.368	0.050949	38.477	36.5	2.0	39.75	12.6	239	±887	552.9

**Table 5: Hogeve Tuff**

Spot	Conc. (ppm)				Ratios				Ages				% Disc.			
	[U]	[Th]	U/Th	206Pb/238U	±2σ	207Pb/235U	±2σ	207Pb/206Pb	WTX-INDIO 5A, 5B, 7B	±2σ	206Pb/238U	±2σ	207Pb/235U	±2σ	207Pb/206Pb	±2σ
5A_1	39678	24414	1.63	0.005776	2.630	0.037521	2.678	0.047114	2.234	37.1	1.0	37.37	1.0	51	±53	37.1
5A_2	14231	8645	1.65	0.006017	2.879	0.050400	6.703	0.060747	4.491	38.7	1.1	49.88	3.3	626	±97	1518.4
5A_3	7488	3645	2.11	0.005755	2.461	0.039318	4.372	0.049546	4.451	37.0	0.9	39.12	1.7	170	±104	358.4
5A_4	6163	3641	1.69	0.005681	3.034	0.039366	4.951	0.050253	5.560	36.5	1.1	39.17	1.9	203	±129	454.5
5A_5	11879	5772	2.06	0.005879	2.591	0.040002	2.962	0.049344	3.117	37.8	1.0	39.79	1.2	160	±73	323.5
5A_6	11928	4979	2.40	0.005776	2.841	0.041873	4.794	0.052574	4.627	37.1	1.1	41.62	2.0	306	±105	724.7
5A_7	26010	11749	2.21	0.005898	2.871	0.048168	4.303	0.059234	3.227	37.9	1.1	47.73	2.0	571	±70	1407.1
5A_8	458	2800	0.16	0.016095	3.796	1.269744	3.371	0.572153	4.087	102.9	3.9	831.57	19.1	4432	±60	4205.4
5A_9	11829	9749	1.21	0.006020	2.979	0.052853	7.098	0.063674	6.265	38.7	1.1	52.25	3.6	726	±133	1777.3
5A_10	6045	2525	2.39	0.005670	2.943	0.040708	4.245	0.052069	4.421	36.4	1.1	40.48	1.7	284	±101	679.8
5A_11	5036	2183	2.31	0.005708	3.493	0.042408	6.348	0.053885	5.706	36.7	1.3	42.14	2.6	362	±129	886.6
5A_12	4208	2614	1.61	0.007092	4.507	0.152948	10.840	0.156409	8.460	45.6	2.0	144.39	14.6	2412	±143	5193.7
5A_13	63452	47495	1.34	0.005951	2.499	0.038188	3.802	0.046539	1.933	38.3	1.0	38.02	1.4	22	±46	-43.7
5A_14	17346	7395	2.35	0.005853	2.665	0.040719	4.000	0.050454	2.464	37.6	1.0	40.49	1.6	212	±57	462.9
5A_15	30135	15582	1.93	0.005898	2.799	0.042671	4.164	0.052473	4.003	37.9	1.1	42.39	1.7	302	±91	696.2
5B_1	5865	2598	2.26	0.005920	3.073	0.043407	5.488	0.053179	5.152	38.1	1.2	43.11	2.3	332	±117	773.0
5B_2	6478	3177	2.04	0.005943	3.212	0.053001	9.554	0.064683	7.516	38.2	1.2	52.39	4.9	760	±158	1888.6
5B_3	5964	2746	2.17	0.005856	2.773	0.048965	5.698	0.060646	4.538	37.6	1.0	48.50	2.7	622	±98	1553.5
5B_4	16650	7687	2.17	0.006043	2.865	0.037670	3.987	0.045207	3.190	38.8	1.1	37.51	1.5	-49	±78	-225.0
5B_5	6792	2948	2.30	0.005945	3.053	0.052443	5.160	0.063976	4.151	38.2	1.2	51.86	2.6	736	±88	1827.2
5B_6	6991	3658	1.91	0.005865	2.386	0.039983	4.779	0.049445	4.178	37.7	0.9	39.77	1.9	165	±98	337.3
5B_7	5948	3312	1.80	0.005863	3.548	0.042012	5.913	0.051968	5.173	37.7	1.3	41.75	2.4	280	±118	642.4
5B_8	11895	12707	0.94	0.005842	2.944	0.038122	4.101	0.047326	3.392	37.6	1.1	37.96	1.5	62	±81	64.0
5B_9	2765	9280	0.30	0.016985	4.562	1.347039	6.053	0.575181	2.864	108.6	4.9	865.54	35.3	4439	±42	3988.7
5B_10	454	3618	0.13	0.017098	3.624	1.422582	3.730	0.603435	3.372	109.3	3.9	897.68	22.2	4509	±49	4025.8
5B_11	744	5270	0.14	0.017884	8.139	1.398408	9.798	0.567108	4.083	114.3	9.2	887.51	58.1	4419	±60	3766.9
5B_12	9990	4679	2.14	0.005631	2.279	0.044736	3.512	0.057619	2.950	36.2	0.8	44.40	1.5	511	±65	1311.6
5B_13	1176	7495	0.16	0.032565	3.237	3.207841	4.221	0.714435	1.863	206.6	6.6	1457.81	32.7	4753	±27	2200.6
5B_14	8	17	0.46	10.657607	10.183	1189.249495	10.919	0.809289	2.474	15832.2	601.9	7184.73	111.2	4930	±35	-68.9
5B_15	2074	1194	1.74	0.006672	3.718	0.089577	7.724	0.097377	7.289	42.9	1.6	87.03	6.4	1570	±136	3561.5
7B_1	1680	837	2.01	0.007136	4.082	0.157862	10.652	0.160445	9.444	45.8	1.9	148.70	14.7	2455	±159	5255.4
7B_2	5533	11270	0.49	0.006116	3.522	0.043060	5.817	0.051060	4.763	39.3	1.4	42.77	2.4	239	±110	508.9
7B_3	487	456	1.07	0.006042	5.594	0.059687	26.553	0.071645	26.764	38.8	2.2	58.82	15.2	971	±545	2401.3
7B_4	10338	12145	0.85	0.005761	2.703	0.037033	3.432	0.048620	3.491	37.0	1.0	36.89	1.2	26	±84	-30.6
7B_5	271	1189	0.23	0.015177	4.680	1.218436	3.984	0.582244	5.736	97.1	4.5	808.37	22.2	4457	±83	4490.0
7B_6	1514	1948	0.78	0.006748	4.288	0.151160	18.446	0.162463	14.293	43.4	1.9	142.81	24.6	2476	±241	5610.7
7B_7	2008	1596	1.26	0.007665	5.978	0.285813	12.972	0.270436	9.340	49.2	2.9	255.04	29.3	3302	±146	6608.8
7B_8	1403	2287	0.61	0.011462	4.397	0.725589	7.339	0.459136	5.076	73.5	3.2	553.49	31.3	4108	±75	5491.9
7B_9	888	4252	0.21	0.012500	4.572	0.773955	7.438	0.449045	4.965	80.1	3.6	581.53	33.0	4075	±74	4988.6
7B_11	533	3506	0.15	0.013300	3.706	0.947442	3.146	0.516654	4.707	85.2	3.1	676.19	15.5	4282	±69	4927.9
7B_12	15076	6395	2.36	0.006116	3.256	0.050629	4.822	0.060041	3.737	39.3	1.3	50.11	2.4	601	±81	1428.2

Table : Hogeve Tuff

Spot	Ratios				Ages							% Disc.				
	[U]	[Th]	U/Th	206Pb/238U	±2σ	207Pb/235U	±2σ	207Pb/206Pb	±2σ	206Pb/238U	±2σ		207Pb/235U	±2σ	207Pb/206Pb	±2σ
7B_13	2750	1791	1.54	0.006193	2.774	0.084616	5.144	0.099093	5.728	39.8	1.1	82.41	4.1	1602	±107	3925.5
7B_14	8731	3395	2.57	0.126717	2.947	1.514465	3.517	0.086681	2.732	769.1	21.4	935.45	21.5	1349	±53	75.3
7B_15	45	117	0.38	1.214994	2.737	142.167690	2.675	0.848644	1.864	5126.5	96.8	5036.08	27.0	4998	±26	-2.5
7B_11	2982	1235	2.41	0.188656	2.423	1.967045	2.401	0.075621	1.403	1114.1	24.8	1103.36	16.2	1080	±28	-3.0

WTX-INDIO 5A, 5B, 7B

**Table 6: Bell Valley Andesite**

Table : Bell Valley Andesite

Spot	[U]	[Th]	Ratios			Ages			% Disc.							
			U/Th	206Pb/238U	207Pb/235U	±2σ	207Pb/206Pb	±2σ		207Pb/235U	±2σ					
Indio1.1	2648	740	3.58	0.005479	2.616	0.036315	6.189	0.048071	6.593	35.2	0.9	36.22	2.2	103	±156	191.7
Indio1.2	41	16	2.50	0.005958	28.020	-0.072191	333.334	-0.087873	255.558	38.3	10.7	-76.08	269.5			
Indio1.3	2077	721	2.88	0.005963	2.808	0.053807	8.884	0.065448	8.547	38.3	1.1	53.22	4.6	789	±179	1958.2
Indio1.4	943	354	2.66	0.005596	3.196	0.034143	15.656	0.044248	15.457	36.0	1.1	34.09	5.2	-97	±380	-389.2
Indio1.5	1090	425	2.56	0.005555	3.020	0.042046	11.857	0.054900	11.752	35.7	1.1	41.82	4.9	408	±263	1043.0
Indio1.6	1433	584	2.45	0.005659	2.973	0.042239	7.843	0.054137	7.440	36.4	1.1	42.01	3.2	377	±167	935.8
Indio1.7	637	229	2.78	0.005626	3.790	0.036172	21.998	0.046630	22.937	36.2	1.4	36.08	7.8	30	±550	-16.1
Indio1.8	832	295	2.82	0.005845	3.469	0.060648	11.651	0.075256	12.168	37.6	1.3	59.79	6.8	1075	±244	2762.3
Indio1.10	1066	633	1.68	0.005802	2.896	0.050464	11.242	0.063080	11.741	37.3	1.1	49.99	5.5	711	±250	1806.2

**Table 7: Huelster Formation**

Conc. (ppm)	Ratios					Ages					% Disc.				
	Spot	[U]	[Th]	U/Th	206Pb/238U ±2σ	207Pb/235U ±2σ	207Pb/206Pb ±2σ	WTX#NDAVIS 1B	206Pb/238U ±2σ	207Pb/235U ±2σ		207Pb/206Pb ±2σ			
Huel.1	647	578	1.12	0.005812	2.772	0.047084	9.159	0.058756	9.456	37.4	1.0	46.72	4.2	558 ±206	1393.8
Huel.2	949	1039	0.91	0.005698	2.613	0.037549	6.704	0.047794	6.675	36.6	1.0	37.43	2.5	89 ±158	143.2
Huel.3	1111	1152	0.96	0.005924	2.527	0.067271	4.706	0.082353	4.647	38.1	1.0	66.11	3.0	1254 ±91	3193.0
Huel.4	82	128	0.65	0.005785	7.901	0.054347	54.060	0.068132	63.77	37.2	2.9	53.74	28.3	873 ±1321	2246.5
Huel.5	452	929	0.49	0.005243	3.007	0.054176	10.679	0.074944	10.835	33.7	1.0	53.57	5.6	1067 ±218	3065.3
Huel.6	124	89	1.40	0.007144	6.931	0.210068	20.017	0.213263	17.612	45.9	3.2	193.61	35.3	2931 ±285	6286.0
Huel.7	671	1225	0.55	0.005115	3.313	0.031891	11.523	0.045218	11.819	32.9	1.1	31.88	3.6	-44 ±287	-233.4
Huel.8	1685	2470	0.68	0.006059	2.650	0.039262	5.191	0.046994	5.330	38.9	1.0	39.10	2.0	49 ±127	25.7
Huel.9	111	136	0.82	0.005983	5.983	0.058641	44.464	0.071082	43.068	38.5	2.3	57.86	25.0	960 ±880	2395.8
Huel.10	155	255	0.61	0.004925	6.234	0.045584	29.435	0.067132	32.367	31.7	2.0	45.26	13.0	842 ±674	2558.3
Huel.11	1813	3326	0.55	0.005598	2.330	0.037186	4.474	0.048173	4.391	36.0	0.8	37.07	1.6	108 ±104	199.5
Huel.12	399	707	0.56	0.005263	3.490	0.031662	16.012	0.043631	17.443	33.8	1.2	31.65	5.0	-131 ±431	-488.5
Huel.13	375	381	0.99	0.005388	3.439	0.036009	15.353	0.048467	15.098	34.6	1.2	35.92	5.4	122 ±356	252.6
Huel.14	2502	4057	0.62	0.005704	2.410	0.039592	3.876	0.050341	3.454	36.7	0.9	39.43	1.5	211 ±80	474.9
Huel.15	125	201	0.62	0.005501	5.126	0.037432	54.556	0.049353	82.005	35.4	1.8	37.31	20.0	165 ±1917	365.6
Huel.16	224	189	1.19	0.006380	5.606	0.090299	28.415	0.102647	21.172	41.0	3.3	87.78	23.9	1673 ±391	3979.4
Huel.17	65	104	0.62	0.005272	9.832	-0.029417	208.336	-0.040466	219.514	33.9	3.3	-30.32	64.2	#NUM!	#NUM!
Huel.18	633	1192	0.53	0.005335	3.246	0.030490	14.336	0.041452	15.031	34.3	1.1	30.50	4.3	-260 ±381	-857.3
Huel.19	28	3	10.71	0.006165	22.472	0.109052	220.003	0.128299	192.311	39.6	8.9	105.10	223.2	2075 ±3387	5137.0
Huel.20	125	180	0.70	0.005195	6.619	0.028864	76.478	0.037502	78.954	33.4	2.2	26.92	20.3	-520 ±2111	-1657.8
Huel.21	950	902	1.05	0.006125	6.043	0.076972	32.450	0.076972	21.812	39.4	2.4	63.95	20.1	1120 ±435	2746.5
Huel.22	32	264	0.12	0.002489	5.650	2.486643	4.657	0.724307	8.085	158.5	8.8	1268.15	33.7	4780 ±116	2914.5
Huel.23	1934	2452	0.79	0.005707	2.366	0.036650	4.517	0.046575	4.764	36.7	0.9	36.55	1.6	27 ±114	-25.1
Huel.24	320	173	1.85	0.006010	3.724	0.087486	11.150	0.105580	11.258	38.6	1.4	85.16	9.1	1724 ±207	4364.6
Huel.25	60	50	1.19	0.005745	9.895	0.218072	33.345	0.275292	35.137	36.9	3.6	200.30	60.7	3336 ±650	8934.5
Huel.26	88	337	0.26	0.014013	7.766	1.075171	11.023	0.556460	10.849	89.7	6.9	741.27	58.1	4398 ±159	4802.8
Huel.27	319	537	0.59	0.005165	4.235	0.032882	20.165	0.046173	20.957	33.2	1.4	32.85	6.5	7 ±505	-79.9
Huel.28	137	220	0.62	0.005453	5.830	0.085308	21.896	0.113456	20.883	35.1	2.0	83.12	17.5	1855 ±377	5192.5
Huel.29	12	88	0.13	0.068725	5.029	8.534986	4.003	0.900713	6.188	428.5	20.8	2289.66	36.4	5090 ±87	1087.9
Huel.30	519	817	0.64	0.005691	3.633	0.038240	14.601	0.048734	15.402	36.6	1.3	38.10	5.5	135 ±362	269.2
Huel.31	123	128	0.96	0.005476	5.796	0.089631	21.079	0.117387	24.381	35.2	2.0	86.23	17.4	1917 ±437	5344.9
Huel.32	1008	869	1.16	0.005589	2.827	0.037852	7.493	0.049124	7.066	35.9	1.0	37.73	2.8	154 ±165	328.0
Huel.33	30	333	0.09	0.025492	5.492	2.777058	4.798	0.790106	7.284	162.3	8.8	1349.39	35.8	4904 ±104	2922.1
Huel.34	959	1897	0.51	0.006906	4.811	0.192541	17.649	0.202207	14.655	44.4	2.1	178.80	28.9	2844 ±239	6310.5
Huel.35	590	993	0.59	0.005223	3.002	0.039067	9.019	0.054249	8.575	33.6	1.0	38.91	3.4	381 ±193	1035.8
Huel.36	838	886	0.95	0.005523	2.634	0.037026	7.229	0.048624	6.529	35.5	0.9	36.92	2.6	130 ±154	265.3
Huel.37	468	591	0.79	0.005598	3.247	0.058460	7.582	0.075744	7.196	36.0	1.2	57.69	4.3	1088 ±144	2924.4
Huel.38	168	234	0.72	0.005221	4.650	0.051824	19.340	0.071995	20.562	33.6	1.6	51.30	9.7	986 ±418	2836.8
Huel.39	10	83	0.11	0.080311	5.995	9.533646	4.249	0.860957	6.689	498.0	28.7	2390.80	39.1	5026 ±95	909.3
Huel.40	185	292	0.63	0.005383	4.718	0.056359	19.458	0.075936	24.685	34.6	1.6	55.67	10.5	1093 ±494	3059.4
Huel.41	410	973	0.42	0.006360	5.575	0.103762	24.511	0.118332	19.176	40.9	2.3	100.24	23.4	1931 ±343	4625.5

Table : Huelster Formation

Spot	Ratios										Ages										% Disc.
	206Pb/238U					207Pb/235U					206Pb/238L					207Pb/235L					
	[U]	[Th]	U/Th	±2σ	±2σ	±2σ	±2σ	±2σ	±2σ	±2σ	±2σ	±2σ	±2σ	±2σ	±2σ	±2σ	±2σ	±2σ	±2σ		
Huel.46	1849	3306	0.56	0.005839	2.097	0.042939	4.214	0.053337	4.281	37.5	0.8	42.69	1.8	343 ±97	814.4						
Huel.47	405	1145	0.35	0.005515	3.284	0.031409	17.646	0.041308	17.430	35.5	1.2	31.40	5.5	-269 ±443	-857.5						
Huel.48	458	884	0.52	0.005464	3.332	0.030673	13.881	0.040715	14.055	35.1	1.2	30.68	4.2	-305 ±360	-969.4						
Huel.49	622	843	0.74	0.006341	3.300	0.049556	9.947	0.056684	9.406	40.7	1.3	49.11	4.8	479 ±208	1076.3						
Huel.50	468	942	0.50	0.005212	3.226	0.039533	13.734	0.055007	13.826	33.5	1.1	39.37	5.3	413 ±309	1130.9						
Huel.51	572	992	0.58	0.005249	3.452	0.042158	9.788	0.058256	9.684	33.7	1.2	41.93	4.0	539 ±212	1498.4						
Huel.52	180	261	0.69	0.005185	4.833	0.042285	43.522	0.059142	38.343	33.3	1.6	42.05	17.9	572 ±834	1616.5						
Huel.53	305	590	0.52	0.005423	4.267	0.030586	19.190	0.040905	20.265	34.9	1.5	30.59	5.8	-294 ±517	-941.8						
Huel.54	9	69	0.13	0.079898	6.342	9.316342	4.414	0.845685	7.083	495.5	30.2	2369.63	40.5	5001 ±101	909.2						
Huel.55	654	776	0.84	0.005760	3.585	0.051977	13.094	0.065445	11.789	37.0	1.3	51.45	6.6	789 ±247	2030.1						
Huel.56	1481	1961	0.76	0.006009	2.733	0.063609	6.543	0.076774	5.988	38.6	1.1	62.62	4.0	1115 ±120	2787.9						
Huel.57	801	1238	0.65	0.005645	2.858	0.046795	8.621	0.060117	8.582	36.3	1.0	46.44	3.9	608 ±186	1574.8						
Huel.58	336	653	0.52	0.005845	3.985	0.050038	19.604	0.062087	17.497	37.6	1.5	49.58	9.5	677 ±374	1702.2						
Huel.59	121	144	0.84	0.005319	7.932	0.064323	24.602	0.087707	37.096	34.2	2.7	63.30	15.1	1376 ±713	3923.9						
Huel.60	162	203	0.80	0.005456	5.921	0.059303	26.893	0.078834	27.518	35.1	2.1	58.50	15.3	1168 ±545	3230.0						
Huel.61	327	836	0.39	0.005417	3.549	0.063289	12.880	0.084740	12.821	34.8	1.2	62.31	7.8	1310 ±249	3660.6						
Huel.62	1505	1660	0.91	0.005691	3.016	0.034408	5.762	0.043847	5.464	36.6	1.1	34.35	1.9	-119 ±135	-426.0						
Huel.63	241	383	0.63	0.005103	4.941	0.032583	28.164	0.046309	27.677	32.8	1.6	32.56	9.0	14 ±665	-58.1						
Huel.64	67	71	0.94	0.005065	10.257	0.124543	34.772	0.178335	41.448	32.6	3.3	119.18	39.1	2637 ±688	7998.0						
Huel.65	895	845	1.06	0.005815	2.966	0.038153	8.920	0.047588	8.742	37.4	1.1	38.02	3.3	79 ±208	110.9						
Huel.66	224	475	0.47	0.005288	4.055	0.035917	27.897	0.049259	30.013	34.0	1.4	35.83	9.8	160 ±702	371.1						
Huel.67	115	136	0.85	0.005750	6.049	0.039054	37.189	0.049258	46.009	37.0	2.2	38.90	14.2	160 ±1076	333.2						
Huel.68	1108	170	6.52	0.105997	3.222	1.158995	3.183	0.079303	1.696	649.5	19.9	781.48	17.4	1180 ±34	81.6						
Huel.69	238	318	0.75	0.005224	4.438	0.031223	24.897	0.043345	29.567	33.6	1.5	31.22	7.7	-148 ±733	-539.9						
Huel.70	73	77	0.95	0.006024	8.033	0.010636	163.650	0.012806	300.002	38.7	3.1	10.74	17.5	-711 ±362	-2076.6						
Huel.71	558	630	0.88	0.005597	3.129	0.026987	13.086	0.034968	12.990	36.0	1.1	27.04	3.5	-390 ±911	-1284.7						
Huel.72	606	685	0.88	0.005122	4.451	0.027825	31.319	0.039399	35.012	32.9	1.5	27.87	8.6	752 ±218	2009.3						
Huel.73	583	1017	0.57	0.005546	3.367	0.049186	10.431	0.064318	10.308	35.7	1.2	48.75	5.0	4983 ±93	854.9						
Huel.74	9	118	0.08	0.084313	6.155	9.709537	5.239	0.835225	6.560	521.8	30.9	2407.61	48.3	5058 ±94	745.0						
Huel.75	9	88	0.10	0.097295	6.090	11.812041	4.644	0.880510	6.666	598.5	34.8	2589.62	43.5	4293 ±99	5455.6						
Huel.76	99	161	0.62	0.005244	7.297	0.010681	222.233	0.014772	293.335	33.7	2.5	10.79	23.9	672 ±127	1667.3						
Huel.77	77	706	0.11	0.012060	5.089	0.861339	5.472	0.518001	6.720	77.3	3.9	630.85	25.7	58 ±131	51.9						
Huel.78	90	101	0.89	0.005468	8.129	0.018560	76.206	0.024619	132.001	35.2	2.8	18.67	14.1								
Huel.79	1826	2344	0.78	0.005917	2.760	0.050529	7.029	0.061940	5.917	38.0	1.0	50.05	3.4								
Huel.80	1311	2746	0.48	0.005916	3.035	0.038475	5.374	0.047168	5.477	38.0	1.2	38.33	2.0								

Table : Huelster Formation

Spot	[U]	[Th]	Ratios					Ages					% Disc.		
			U/Th	<sup>206</sup> Pb/ <sup>238</sup> U	<sup>207</sup> Pb/ <sup>235</sup> U	<sup>±2σ</sup>	<sup>207</sup> Pb/ <sup>206</sup> Pt	<sup>±2σ</sup>	<sup>206</sup> Pb/ <sup>238</sup> L	<sup>±2σ</sup>	<sup>207</sup> Pb/ <sup>235</sup> L	<sup>±2σ</sup>		<sup>07</sup> Pb/ <sup>206</sup> P	<sup>±2σ</sup>
Huel.81	2751	4524	0.61	0.005702	2.710	0.041030	4.297	0.052186	3.859	36.7	1.0	40.83	1.7	294 ±88	700.9
Huel.82	14	120	0.11	0.075233	5.861	9.416951	4.157	0.907820	6.773	467.6	26.4	2379.48	38.2	5101 ±96	990.9
Huel.83	82	103	0.80	0.005402	8.508	0.026398	65.436	0.035445	111.115	34.7	2.9	26.46	17.1	-674 ±3068	-2039.8
Huel.84	500	776	0.65	0.006062	3.576	0.080648	13.193	0.096486	11.260	39.0	1.4	78.75	10.0	1557 ±211	3897.0
Huel.85	98	115	0.86	0.010327	6.767	0.553741	10.330	0.388889	8.906	66.2	4.5	447.44	37.4	3867 ±134	5738.1
Huel.86	541	911	0.59	0.007157	13.190	0.057998	19.119	0.058772	10.591	46.0	6.0	57.25	10.6	559 ±231	1115.2
Huel.87	420	836	0.50	0.005598	3.510	0.041716	10.612	0.054045	11.331	36.0	1.3	41.50	4.3	373 ±255	936.3
Huel.88	103	186	0.55	0.005884	6.962	0.043129	69.269	0.053158	51.863	37.8	2.6	42.87	29.1	336 ±1175	787.2
Huel.89	107	131	0.82	0.005871	6.978	0.058173	34.784	0.071860	41.114	37.7	2.6	57.41	19.4	982 ±837	2502.1
Huel.90	64	426	0.15	0.012128	6.369	0.869101	6.294	0.519739	8.234	77.7	4.9	635.08	29.7	4298 ±121	5431.0
Huel.91	776	983	0.79	0.006305	3.540	0.090697	12.586	0.104332	11.386	40.5	1.4	88.15	10.6	1703 ±210	4102.2
Huel.92	355	705	0.50	0.005445	3.934	0.042337	15.631	0.056397	17.311	35.0	1.4	42.10	6.4	468 ±383	1237.1
Huel.93	1954	2233	0.88	0.005905	2.837	0.039827	4.975	0.048915	4.205	38.0	1.1	39.65	1.9	144 ±99	278.8
Huel.94	1253	1823	0.69	0.006091	2.779	0.044885	6.736	0.053441	6.560	39.1	1.1	44.58	2.9	348 ±148	787.9
Huel.95	26	311	0.08	0.038112	5.166	3.909669	4.635	0.744013	5.817	241.1	12.2	1615.68	37.5	4818 ±83	1898.3

**Table 8: Buckshot Ignimbrite**

Table : Buckshot Ignimbrite

Spot	[U]		[Th]		U/Th		Ratios				Ages				% Disc.	
	[U]	[Th]	[U]	[Th]	206Pb/238U	±2σ	207Pb/235U	±2σ	207Pb/206Pb	±2σ	206Pb/238U	±2σ	207Pb/235U	±2σ		207Pb/206Pb
Tvj.1	2089	912	2.29	0.005717	3.041	0.037689	17.993	0.047815	17.982	36.7	1.1	37.57	6.6	90	±426	145.2
Tvj.2	812	306	2.65	0.016841	4.935	1.298402	5.978	0.559169	4.971	107.7	5.3	845.02	34.3	4405	±73	3991.9
Tvj.3	1122	350	3.21	0.006268	4.882	0.072570	22.756	0.083977	22.358	40.3	2.0	71.14	15.6	1292	±435	3107.8
Tvj.4	1710	640	2.67	0.005759	4.127	0.037660	24.299	0.047428	22.922	37.0	1.5	37.54	9.0	71	±545	91.3
Tvj.5	2288	1127	2.03	0.005842	3.527	0.027459	21.544	0.034090	23.193	37.5	1.3	27.51	5.8	-782	±656	-2183.9
Tvj.6	1315	615	2.14	0.005831	5.490	0.027808	52.189	0.034586	48.575	37.5	2.1	27.85	14.3	-742	±1361	-2079.2
Tvj.7	1708	914	1.87	0.006276	3.372	0.090639	11.084	0.104753	11.339	40.3	1.4	88.10	9.4	1710	±209	4140.1
Tvj.8	3628	4083	0.89	0.008039	4.228	0.107350	17.962	0.096855	13.281	51.6	2.2	103.54	17.7	1564	±249	2931.1
Tvj.10	1208	411	2.94	0.014122	3.742	0.975933	4.448	0.501222	3.414	90.4	3.4	691.52	22.3	4245	±50	4595.7
Tvj.11	5015	3698	1.36	0.005615	3.137	0.045766	11.040	0.059115	9.241	36.1	1.1	45.44	4.9	571	±201	1482.8
Tvj.12	1652	598	2.76	0.005927	3.882	0.049369	20.828	0.060415	22.962	38.1	1.5	48.93	10.0	618	±496	1523.6

**Table 9: Tascotal Formation**

Table : Tascotal Formation

Spot	[U]	[Th]	Ratios			Ages			% Disc.							
			U/Th	206Pb/238U	207Pb/235U	±2σ	207Pb/206Pb	206Pb/238U	±2σ	207Pb/235U	±2σ	207Pb/206Pb	±2σ			
Tas.1	2566	2141	1.20	0.004881	3.554	0.039997	11.778	0.059435	11.868	31.4	1.1	39.82	4.6	583	±258	26.9
Tas.2	1690	1837	0.92	0.005174	3.370	0.039926	17.098	0.059966	16.795	33.3	1.1	39.75	6.7	451	±373	19.5
Tas.9	4506	3822	1.18	0.005186	3.254	0.035935	8.678	0.050251	8.632	33.3	1.1	35.85	3.1	207	±200	7.5
Tas.10	6859	2914	2.35	0.005066	3.458	0.029624	6.467	0.042410	5.742	32.6	1.1	29.64	1.9	-202	±144	-9.0
Tas.15	8161	4418	1.85	0.004783	2.526	0.031853	6.151	0.048297	5.445	30.8	0.8	31.84	1.9	114	±128	3.5
Tas.19	2634	1058	2.49	0.004754	3.804	0.021899	17.589	0.033410	17.882	30.6	1.2	22.00	3.8	-840	±512	-28.1
Tas.29	1267	1385	0.91	0.005262	3.822	0.029480	32.250	0.032360	30.201	33.8	1.3	23.57	7.5	-932	±882	-30.4
Tas.32	1779	1379	1.29	0.005193	3.598	0.026245	24.435	0.036657	23.142	33.4	1.2	26.30	6.3	-582	±627	-21.2
Tas.35	4471	3427	1.30	0.005671	2.966	0.039809	6.717	0.050913	6.613	36.5	1.1	39.64	2.6	237	±153	8.7
Tas.36	576	807	0.71	0.004533	5.815	0.015572	108.351	0.024914	104.014	29.2	1.7	15.69	16.9	49	±168	-46.2
Tas.46	4862	4564	1.07	0.005134	2.624	0.033270	7.803	0.046999	7.036	33.0	0.9	33.23	2.6	49	±168	0.7
Tas.49	883	715	1.24	0.005774	5.168	0.046882	27.561	0.058889	27.126	37.1	1.9	46.52	12.5	563	±591	25.3
Tas.52	3022	2225	1.36	0.005726	2.666	0.031615	13.062	0.040040	13.230	36.8	1.0	31.60	4.1	-348	±341	-14.1
Tas.60	2795	2996	0.93	0.004996	2.870	0.040407	8.582	0.058661	8.538	32.1	0.9	40.22	3.4	555	±186	25.2
Tas.64	1656	858	1.93	0.004933	4.369	0.037408	18.964	0.054996	18.197	31.7	1.4	37.29	6.9	412	±407	17.5
Tas.70	6196	2202	2.81	0.005317	2.891	0.034771	6.363	0.047434	5.771	34.2	1.0	34.71	2.2	71	±137	1.5
Tas.71	3623	2562	1.41	0.005388	3.049	0.029967	10.785	0.040338	10.755	34.6	1.1	29.98	3.2	-329	±277	-13.4
Tas.74	26176	27018	0.97	0.004978	2.425	0.033262	3.521	0.048457	2.642	32.0	0.8	33.22	1.2	122	±62	3.8
Tas.75	2526	962	2.63	0.004727	3.338	0.034062	13.170	0.052266	12.504	30.4	1.0	34.01	4.4	297	±285	11.9
Tas.79	5981	7916	0.76	0.004825	3.168	0.030124	8.250	0.045280	8.726	31.0	1.0	30.14	2.4	-41	±212	-2.9
Tas.83	1885	1479	1.27	0.004676	3.744	0.027466	20.834	0.042597	20.319	30.1	1.1	27.51	5.7	-191	±508	-8.5
Tas.84	5815	3279	1.77	0.005132	3.396	0.034327	7.236	0.048514	6.072	33.0	1.1	34.27	2.4	124	±143	3.9
Tas.85	2707	2173	1.25	0.005531	3.562	0.029278	13.989	0.038393	13.702	35.6	1.3	29.30	4.0	-458	±362	-17.6
Tas.87	3360	2468	1.36	0.004952	3.489	0.027594	11.957	0.040412	11.781	31.8	1.1	27.64	3.3	-325	±303	-13.2
Tas.88	3106	2939	1.06	0.005228	3.543	0.034481	10.695	0.047837	11.028	33.6	1.2	34.42	3.6	91	±261	2.4
Tas.89	3921	3687	1.06	0.004892	3.339	0.033215	7.656	0.049244	7.122	31.5	1.0	33.18	2.5	159	±167	5.5

**Table 10: Morita Ranch Formation**

Table : Morita Ranch Formation

Spot	Ratios			Ages					% Disc.						
	[U]	[Th]	U/Th	206Pb/238U	$\pm 2\sigma$	207Pb/235U	$\pm 2\sigma$	207Pb/206Pb		$\pm 2\sigma$					
BB11A.1	59	102	0.58	0.005022	19.169	0.067136	279.168	0.096947	270.002	32.3	6.2	65.98	180.2	1566 $\pm$ 5060	4749.5
BB11A.2	61	103	0.59	0.005109	20.284	-0.211667	136.002	-0.300504	280.647	32.8	6.6	-241.49	388.7		
BB11A.4	63	109	0.58	0.006280	15.369	-0.050352	516.667	-0.058154	416.667	40.4	6.2	-52.46	285.5		
BB11A.5	404	426	0.95	0.005440	4.154	0.043616	28.494	0.058152	26.680	35.0	1.4	43.35	12.1	535 $\pm$ 584	1431.2
BB11A.6	241	169	1.42	0.005593	6.785	0.054570	67.900	0.070759	108.222	36.0	2.4	53.95	30.4	950 $\pm$ 2215	2543.3
BB11A.7	261	234	1.11	0.005813	6.539	0.049724	67.652	0.062040	54.694	37.4	2.4	49.27	32.6	676 $\pm$ 1169	1707.9
BB11A.9	273	241	1.13	0.005723	5.490	0.031372	55.181	0.039759	68.301	36.8	2.0	31.37	17.0	-367 $\pm$ 1769	-1096.5
BB11A.10	287	276	1.04	0.005605	5.186	0.021736	73.691	0.028128	93.110	36.0	1.9	21.83	15.9		
BB11A.11	353	334	1.06	0.006108	4.429	0.108726	15.587	0.129098	15.827	39.3	1.7	104.80	15.5	2086 $\pm$ 278	5213.1
BB11A.12	275	295	0.93	0.007042	6.370	0.163103	14.777	0.167972	13.916	45.2	2.9	153.42	21.0	2538 $\pm$ 233	5509.1
BB11A.14	431	492	0.88	0.005490	4.670	0.030169	30.053	0.039858	31.726	35.3	1.6	30.18	8.9	-360 $\pm$ 821	-1120.5
BB11A.15	208	209	0.99	0.006257	7.485	0.100693	26.406	0.116721	38.358	40.2	3.0	97.42	24.5	1907 $\pm$ 689	4641.9

**Table 11: Chisos Formation**

Spot	Ratios										Ages					% Disc.
	[U]	[Th]	U/Th	206Pb/238U	±2σ	207Pb/235U	±2σ	207Pb/206Pb	±2σ	206Pb/238U	±2σ	207Pb/235U	±2σ	207Pb/206Pb	±2σ	
BB19.1	2343	519	4.52	0.005072	3.576	0.035816	7.918	0.051218	7.965	32.6	1.2	35.73	2.8	251	±183	668.6
BB19.2	1571	351	4.48	0.004980	4.119	0.037466	8.645	0.054568	9.096	32.0	1.3	37.35	3.2	395	±204	1132.2
BB19.3	1271	398	3.19	0.004816	4.418	0.036760	12.510	0.055357	13.570	31.0	1.4	36.66	4.5	427	±303	1277.6
BB19.4	1597	541	2.95	0.004801	3.640	0.032802	8.976	0.049548	9.215	30.9	1.1	32.77	2.9	174	±215	463.1
BB19.5	1638	371	4.42	0.005722	3.624	0.104918	8.556	0.132986	8.961	36.8	1.3	101.31	8.2	2138	±157	5712.2
BB19.6	1132	295	3.84	0.007975	4.666	0.378053	9.947	0.343832	6.703	51.2	2.4	325.60	27.7	3680	±102	7086.8
BB19.7	1967	644	3.06	0.004965	2.676	0.037901	8.671	0.055369	7.924	31.9	0.9	37.77	3.2	427	±177	1238.0
BB19.8	767	506	1.52	0.278892	16.742	30.233053	16.728	0.786222	2.565	1585.8	235.5	3494.42	165.9	4897	±37	208.8
BB19.9	2089	558	3.75	0.004993	3.139	0.059151	10.710	0.085915	9.710	32.1	1.0	58.35	6.1	1336	±188	4061.6
BB19.10	1643	305	5.39	0.005103	2.841	0.032793	9.410	0.046604	9.173	32.8	0.9	32.76	3.0	29	±220	-11.7
BB19.11	1136	306	3.71	0.004767	3.347	0.033420	11.558	0.050847	13.615	30.7	1.0	33.38	3.8	234	±314	662.9
BB19.12	3849	1756	2.19	0.005009	3.013	0.055598	6.817	0.080509	6.468	32.2	1.0	54.94	3.6	1209	±127	3655.3
BB19.13	2571	710	3.62	0.005048	2.543	0.036833	7.042	0.052919	6.802	32.5	0.8	36.73	2.5	325	±154	902.3
BB19.14	1665	377	4.42	0.005002	3.020	0.035206	8.893	0.051048	8.190	32.2	1.0	35.13	3.1	243	±189	655.5
BB19.15	1705	378	4.51	0.004955	3.047	0.032657	8.814	0.047797	8.328	31.9	1.0	32.63	2.8	89	±197	180.0
BB19.20	1890	1941	0.97	0.027224	2.178	0.182165	4.715	0.048531	3.286	173.1	3.7	169.92	7.4	125	±77	-27.7

WTX-BB 19

**Table 12: South Rim Formation**

Table 12: South Rim Formation

Spot	Conc. (ppm)		Ratios					Ages					% Disc.			
	[U]	[Th]	U/Th	206Pb/238U	±2σ	207Pb/235U	±2σ	207Pb/206Pb	±2σ	206Pb/238U	±2σ	207Pb/235U		±2σ	207Pb/206Pb	±2σ
BB18.1	1451	305	4.76	0.004750	3.315	0.033710	9.867	0.051474	9.421	30.5	1.0	33.66	3.3	262	±216	758.1
BB18.2	3115	2041	1.53	0.005032	3.368	0.069653	9.841	0.100392	9.854	32.4	1.1	68.37	6.5	1631	±183	4941.7
BB18.3	2309	1106	2.09	0.006766	5.042	0.229544	13.737	0.246067	10.049	43.5	2.2	209.82	26.0	3160	±159	7169.0
BB18.4	3414	1358	2.51	0.005096	2.918	0.040801	8.814	0.058073	7.187	32.8	1.0	40.61	3.5	533	±157	1525.3
BB18.5	2757	931	2.96	0.005000	2.757	0.035894	6.622	0.052070	6.690	32.1	0.9	35.81	2.3	288	±153	797.3
BB18.6	4061	2219	1.83	0.004910	2.829	0.041453	7.867	0.061235	6.663	31.6	0.9	41.24	3.2	647	±143	1950.8
BB18.8	1397	403	3.46	0.005284	3.676	0.054294	9.361	0.074529	9.182	34.0	1.2	53.68	4.9	1056	±185	3008.0
BB18.9	1483	310	4.79	0.005092	3.151	0.029790	10.037	0.042434	10.978	32.7	1.0	29.81	2.9	-201	±275	-713.0
BB18.10	3163	1373	2.30	0.006981	4.147	0.240701	12.359	0.250082	7.971	44.8	1.9	218.99	24.3	3185	±126	7003.1
BB18.11	2618	1525	1.72	0.006501	5.414	0.183597	14.455	0.204816	11.156	41.8	2.3	171.15	22.8	2865	±181	6758.2
BB18.12	908	329	2.76	0.005366	4.684	0.059743	20.692	0.080747	15.922	34.5	1.6	58.92	11.8	1215	±313	3422.6
BB18.13	1488	337	4.41	0.004970	3.703	0.035291	10.168	0.051502	10.052	32.0	1.2	35.22	3.5	263	±231	724.0
BB18.14	1690	351	4.81	0.004891	3.538	0.038853	8.187	0.057608	8.842	31.5	1.1	38.70	3.1	515	±194	1536.9
BB18.15	1867	421	4.43	0.004837	3.572	0.037304	8.416	0.055935	8.926	31.1	1.1	37.19	3.1	450	±198	1346.0

WTX-BB 18